BUCKLING BEHAVIOUR OF DELAMINATED COMPOSITE PLATES USING EXACT STIFFNESS ANALYSIS

MAHDI DAMGHANI

Ph.D. 2009

ProQuest LLC
789 East Eisenhower Parkway
P.O. Box 1346
Ann Arbor, MI 48106-1346

BUCKLING BEHAVIOUR OF DELAMINATED COMPOSITE PLATES USING EXACT STIFFNESS ANALYSIS

by

Mahdi Damghani

Thesis submitted to

Cardiff University in candidature

for the degree of

Doctor of Philosophy.

October 2009

Division of Structural Engineering,

Cardiff School of Engineering,

Cardiff University.

Declaration

This work has not previously been accepted in substance for any degree and is not concurrently submitted in candidature for any other higher degree.

Signed:.....  ....(Candidate) Date:.....16/12/09.....

Statement 1

This thesis is being submitted in partial fulfilment of the requirements for the degree of ..Ph.D.....(insert as appropriate PhD, MPhil, EngD)

Signed:..... 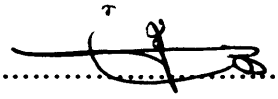 ....(Candidate) Date:....16/12/09.....

Statement 2

This thesis is the result of my own independent work/investigation, except where otherwise stated. Other sources are acknowledged by explicit references.

Signed:..... 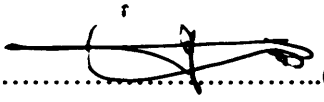 .....(Candidate) Date:....16/12/09.....

Statement 3

I hereby give consent for my thesis, if accepted, to be available for photocopying, inter-library loan and for the title and summary to be made available to outside organisations.

Signed:..... 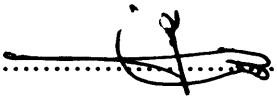 .....(Candidate) Date:..16/12/09.....

ACKNOWLEDGEMENTS

Foremost, I would like to express my deepest gratitude to ''Allah'' the creator of mankind, the creator of life and death and the creator of seven heavens and the earth, who imparted unto me articulate thought and speech.

I express my sincere gratitude to my supervisors Prof. David Kennedy and Dr Carol Featherston for the continuous support of my Ph.D study and research, for their patience, motivation, enthusiasm, and immense knowledge. Their guidance helped me in all the time of research and writing of this thesis.

My deepest gratitude goes to my family for their unflagging love and support throughout my life; this thesis is simply impossible without them. I am immensely indebted to my father, Hossein Damghani, and mother, Dr Shahnaz Shirbazu, for their care and love. As a typical father in an Iranian family, he worked industriously to support the family and spare no effort to provide the best possible environment for me to grow up and attend school. He had never complained in spite of all the hardships in his life. I cannot ask for more from my mother, as she is simply perfect. I have no suitable word that can fully describe her everlasting love to me. I remember many sleepless nights with her accompanying me when I was suffering from Leukaemia. I remember her constant support when I encountered difficulties and I remember, most of all, her tears when I was in hospital. Mother, I love you.

I am grateful to my wife, Maryam Damghani, for her immense and endless support throughout my Ph.D. I remember her patient love and the sacrifice she made in her career which gave the opportunity to complete this work. I thank her for giving birth to my beautiful son, Ibrahim Damghani, who was my motivation when I would face difficulty.

Last but not the least, many thanks go to my mother-in-law, Afsaneh Derakhshan, and father-in-law, Dr Reza Afzal, for supporting me in all the time of research.

SUMMARY OF THESIS

The aim of this thesis is to investigate the local and global buckling behaviour of delaminated composite plates using exact stiffness analysis. Several attempts are made to model delamination with the accuracy of detailed 3D finite element analysis (FEA) but substantially improved computational efficiency.

Investigation of local buckling behaviour is performed using the exact stiffness program VICONOPT, giving good comparative results and substantially less solution times compared to those of FEA. Extending this approach to global buckling behaviour poses limitations and difficulties in retaining computational efficiency. Several techniques are introduced to study global buckling behaviour while requiring less solution time than FEA. The advantages and disadvantages of these techniques are discussed.

Finally, an improved smeared stiffness method is derived which results from simplification of the total potential energy expression for the plate. This simplification avoids expensive computational effort while maintaining results of good accuracy (within 2%-3% of FEA results). This method can be employed for modelling delaminations of different shape and size located anywhere in the composite plate.

TABLE OF CONTENTS

Page no

Title

DECLARATION, STATEMENT 1, STATEMENT 2 & STATEMENT 3 i

ACKNOWLEDGEMENTS ii

SUMMARY OF THESIS iii

CONTENTS iv

CONTENTS

CHAPTER 1

INTRODUCTION TO COMPOSITE MATERIALS AND PLATES

1.1 Introduction.....1

1.2 Composite Materials.....1

1.3 Laminae and Laminates.....3

1.4 Examples of laminated structures.....5

1.5 Imperfections.....6

1.6 Delamination.....6

1.6.1 The Origin of Delaminations.....7

1.6.2 Types of Delamination.....8

1.7 Compressive load and delaminated composite plates.....12

1.8 Thesis outline.....19

1.9 References.....21

CHAPTER 2

ANALYSIS OF COMPOSITE PLATE STRUCTURES

2.1 Introduction.....34

2.2 Exact stiffness analysis.....35

2.2.1 Composite laminates stiffness matrices.....36

2.2.2 Theory and formulation used in VIPASA analysis.....39

2.2.3 Theory and formulation used in VICON analysis.....43

2.3 Multi-level sub-structuring.....45

2.4 References.....48

CHAPTER 3

CRITICAL BUCKLING OF DELAMINATED COMPOSITE PLATES USING EXACT STIFNESS ANALYSIS

3.1 Introduction.....55

3.2 Through-the-length delamination model.....55

3.3 Numerical examples.....56

3.3.1 Example 3.1: single mid-width delamination.....58

3.3.2 Examples 3.2–3.4: single mid-width delamination at varying depth.....59

3.3.3 Example 3.5: double mid-width delamination.....60

3.3.4 Example 3.6: single edge delamination.....60

3.3.5 Example 3.7: effect of edge conditions.....61

3.3.6 Residual buckling strength.....61

3.4 Conclusions and further work.....62

3.5 References.....64

CHAPTER 4

MULTI-STRUCTURE MODELLING OF PERFECT PLATES

4.1 Introduction.....76

4.2 Theory and Formulation.....77

4.3 Material properties.....79

4.4 Methodology.....79

4.5 Results and discussion.....81

4.6 Conclusions.....84

4.7 References.....86

CHAPTER 5

MULTI-STRUCTURE MODELLING OF DELAMINATED PLATES

5.1 Introduction.....96

5.2 Material properties.....96

5.3 Methodology.....97

5.3.1 VICONOPT modelling.....97

5.3.2 FE modelling.....98

5.4 Results and discussion.....99

5.5 Conclusions.....100

CHAPTER 6

NEGATIVE STIFFNESS MODELLING OF DELAMINATED STRUCTURES

6.1 Introduction.....112

6.2 Delaminated beam model.....112

6.3 Methodology.....113

6.4 Theory and formulation.....115

6.5 Results.....124

6.6 Conclusions.....125

6.7 References.....127

CHAPTER 7

SUB-STRUCTURING APPROACH FOR DELAMINATION MODELLING

7.1 Introduction.....132

7.2 Theory and formulation.....132

7.3 Methodology.....136

7.4 Results.....137

7.5 Conclusions.....138

7.6 References.....139

CHAPTER 8

SIMPLE SMEARING METHOD FOR DELAMINATION MODELLING

8.1 Introduction.....144

8.2 Theory.....145

8.3 Examples.....149

8.4 Results and discussion.....150

8.5 Conclusion.....152

8.6 References.....153

CHAPTER 9

IMPROVED SMEARING METHOD FOR DELAMINATION MODELLING

9.1 Introduction.....160

9.2 Problem definition and theory.....161

9.2.1 Physical basis.....161

9.2.2 Theory.....161

9.2.3 Problem definition and theory application.....165

9.3 Numerical study.....167

9.3.1 Properties of the composite plate and delamination.....167

9.3.2 Validation analysis.....168

9.3.3 FE analysis.....168

9.4 Results and discussion.....170

9.4.1 Effects of approximating $\mathbf{K}_{(eq)}$ by $\mathbf{K}_{(approx)}$.....170

9.4.2 Effects of width and depth of delamination.....171

9.4.3 Effects of length and depth of delamination.....172

9.4.4 Effects of the lengthwise position and depth of delamination.....173

9.4.5 Effects of the widthwise position and depth of delamination.....174

9.5 Conclusions.....174

9.6 References.....176

CHAPTER 10

OVERALL CONCLUSIONS AND FUTURE WORK

10.1 Summary of conclusions.....194

10.2 Future work.....195

APPENDIX

Appendix 1.....197

Appendix 2.....200

CHAPTER 1

INTRODUCTION TO COMPOSITE MATERIALS AND PLATES

1.1 Introduction

The benefits and advantages of using lightweight structures in industries such as aerospace and the automotive sector have directed engineers to the use of new materials. These new materials require detailed testing to understand their behaviour followed by the development of appropriate design, analysis, fabrication and manufacturing techniques. Composite materials are one of many such new man-made materials which can be tailored for specific applications. With the use of composite materials, however certain new material imperfections can be encountered. One of these imperfections is delamination. The existence of delaminations and their effects on the structural response of a system has been paramount in many cases [1.1]. It is necessary in this case to try to quantify these effects.

1.2 Composite Materials

Composite materials are formed by uniting two or more materials differing in form or composition on a macroscale. The constituents keep their properties and identities, i.e. they do not dissolve or merge completely into one another whilst performing in harmony. This allows the newly formed material to exhibit better engineering behaviour and properties than its constituents. Among the potentially improved properties are stiffness, strength, weight reduction, corrosion resistance, thermal properties, fatigue life, and wear resistance.

The majority of man-made composite materials can be categorised into three main types depending on geometry:

1) fibrous composites

2) particulate composites

3) laminated composites

Fibrous composite materials are generally composed of two materials: a reinforcement material called *fibre* and a base material called *matrix* material. In these composites, fibres of a reinforcement material are embedded into a matrix of another material. Depending on the length of fibres used, this type of composite can be further categorised as short or continuous fibre-reinforced. Short fibre-reinforced materials are those in which the ratio of fibre length (l) to fibre diameter (d) is approximately 100, i.e. $l/d \sim 100$ whilst this ratio approaches infinity for continuous fibre-reinforced materials, i.e. $l/d \sim \infty$. The high stiffness and strength of fibrous composites stems from the fibres while the matrix keeps the fibres in place, transfers load to the fibres and acts as a cover for fibres which protects them from being exposed to the environment. Matrix materials have bulk-form properties whereas fibres have directionally dependent properties. An example of a fibre material used in continuous fibre-reinforced composites is carbon fibre. Another example for these composites is fibre reinforced concrete [1.1-1.4].

In particulate composites macro size particles of one material which are usually roughly spherical are impregnated in a matrix of another material. An example of such materials is concrete where cement serves as a matrix with sand acting as the filler [1.1-1.4].

Laminated composites comprise layers of different materials, possibly including the two previously mentioned composites, stacked on top of each other. Filler in this type of composites is in the form of a sheet as opposed to fibres or particulates. The matrix material is normally a phenolic type thermoset polymer. An example of this type of composites is glass filled phenolic [1.1-1.4].

1.3 Laminae and Laminates

A *lamina* or *ply* is a single layer of composite material. A fibre-reinforced lamina includes many fibres embedded in a matrix material, which can be a metal such as aluminium or a non-metal like a thermosetting or thermoplastic polymer. Generally, coupling agents and additives are added to improve adhesion and compatibility between the fibres and the matrix material which subsequently will lead to improved properties of the composite system.

There are various types of fibre-reinforced composite laminae as follows (Figure 1.1):

1) Unidirectional

2) Bi-directional

3) Discontinuous fibre

4) Woven

Unidirectional fibre-reinforced laminae display maximum strength and stiffness in the direction of the fibres while having very low strength and stiffness in the direction transverse to the fibres.

Bi-directional laminae are those which contain parallel, continuous fibres aligned along mutually perpendicular directions.

Discontinuous laminae are those which contain random in-plane discontinuous fibres embedded in a matrix. Composites containing such laminae have lower strength and modulus than continuous fibre-reinforced composites.

Woven fibres result from twisting thousands of fibres together in the mutually orthogonal warp and fill directions. Woven fibres will form a fabric which is then combined with a matrix to form woven fibre laminae. This type of laminae can also be treated as bi-directional laminae.

A *laminate* is the resultant of stacking two or more unidirectional laminae or plies. Each of the stacked laminae can have its own orientation depending on the designed structural stiffness and strength of the laminate. The laminae (plies) can have various thicknesses and comprise different or the same materials. The sequence of various orientations of the fibre-reinforced composite layers in a laminate is called the *stacking sequence* (Figure 1.2) [1.1-1.4].

The stacking sequence describes the angle of each ply from the laminate axis. It is normally denoted as angles in degrees by enclosing a series of ply angles separated from each other by commas within parentheses( ) or brackets[ ]. The first entry is usually the angle of the top ply. As an example the stacking sequence for Figure 1.2 is defined as $(0,\theta,90,-\theta)$. In practical applications the stacking sequence (lay-up) has plies of equal thickness and is often balanced, and either symmetric or anti-symmetric. A *balanced lay-up* is where, for $0 < \theta < 90$, there is an equal number of $+\theta$ and $-\theta$ plies, eg. (0,+45,–45,90,90,–45,0,+45) In a symmetric lay-up, the layers in the top half

of the laminate are repeated in reverse order in the bottom half, eg. (+30,+45,–45,90,90,–45,+45,+30). In an anti-symmetric stacking sequence, the top layers are repeated in the same order in the bottom half, e.g. (+30,+45,–45,90,+30,+45,–45,90).

1.4 Examples of laminated structures

Some of the most commonly used and best known examples of multilayered structures are fibre-reinforced composite panels and plates. However, these materials are used in many forms in numerous fields of industry such as,

1- Robotised machinery where high strength and stiffness at low weight contributes to the life span of the machine.

2- Healthcare where they can be used to manufacture implants ranging from hip joints to heart valves. Laminates are also used as biomedical retinas.

3- Aerospace where the use of materials with high stiffness to weight ratio is of paramount importance. Examples of this are the Airbus A380 and Boeing 777 and 787 aircraft which have high composite contents.

4- Military aircraft and other applications where the high strength and impact resistance of composite materials makes them an attractive solution for armoured vehicles. They are also used in radomes due to their transparency to radio waves.

5- Sporting where equipment with high strength yet light weight is essential. Examples of this are Corima bikes, tennis rockets, golf clubs and swimming flippers.

In Tables 1.1 and 1.2, information about the application of composite plates in different branches of industry accompanied with their advantages and disadvantages is given.

1.5 Imperfections

As mentioned earlier, composite materials are prone to various internal imperfections, each of which compromise mechanical performance to a differing degree. Examples of some of these imperfections include:

1- Fibre breakage.

2- Fibre debonding.

3- Delamination.

4- Cracks in the matrix.

5- Existence of small voids and flaws.

6- Foreign inclusions.

The present work will focus on damage due to delamination.

1.6 Delamination

Delamination is the inter-laminar failure mode of composite materials, in which an interlayer crack is generated between the laminae of a laminate caused by the bonding stiffness mismatch of neighbouring layers. Delaminations can be the result of low-velocity impact, fatigue load, air entrapments caused by manufacturing processes (manufacturing defects), or stress concentrations at free edges (free edge effects).

Application of such effects causes adjacent plies with different lay-up angles to debond from each other. Since at least two different lay-up angles are generally used in composite laminates, e.g. cross-ply (0, 90, 90, 0) or quasi-isotropic (0, 45, −45, 90) or (65, −70, −25, 20) laminates, delaminations can appear at several interfaces. Many experimental studies have been performed, for example to analyze the characteristics of the delaminations induced by low-velocity impact, i.e. Barely Visible Impact Damage (BVID).

Delaminations are known to degrade the overall stiffness and strength of a structure. In particular, they may severely reduce the load-carrying capacity of the laminates under compressive loads. The level of reduction in load-bearing capacity depends on the shape, area, orientation and position of the delamination and the type of loading and boundary conditions.

With the increasing use of composite laminates, the compression behaviour of delaminated composite structures in particular has attracted increasing attention in recent years. When a delaminated composite plate is subjected to uniaxial in-plane compression, local mode buckling of the delaminated region or mixed mode buckling (a combination of local and global mode buckling) may occur before global mode buckling, as shown in Figure 1.3. This results in the delaminated composite plate having a lower ability to resist compressive loads.

1.6.1 The Origin of Delaminations

Delaminations can originate in the following situations:

1- At the manufacturing stage, e.g., adhesion failures and shrinkage cracks.

2- At the stage of transportation and installation, when the loads and actions may differ in character and level from the design ones, e.g. impacts upon the surface of the structure such as tool drop. Even relatively light impacts can lead to the delamination of the near-surface layers. Low velocity impact of foreign objects is the most important cause of delamination. It can create multiple delaminations which increase in size away from the point of impact.
3- At the stage of operation as a result of off-design situations or of an inadequate design [1.6].

1.6.2 Types of Delamination

In describing the location of delaminations through the thickness of a composite plate, two categories need to be distinguished [1.6]:

1- Internal delaminations.
2- Near-surface delaminations.

Internal delaminations are those with sub-laminate thicknesses h_1 and h_2 which are comparable to half the thickness of the laminate, i.e. h (Figure 1.4a). Internal delaminations are sometimes regarded as cracks and are mostly investigated within the area of classical fracture mechanics, although there are situations in which internal delaminations affect global stability in compression and reduce load carrying capacity such as in the case of shells and plates.

Near-surface delaminations are more complicated imperfections as their deformation does not necessarily follow that of the base structure. As an example, if the delaminated composite plate of Figure 1.3 is considered under longitudinal compression

load, the deformation of the delamination is ruled by the deformation of the base plate with mutual interaction between the two. The amount of interaction depends on the depth and size of the delamination compared the dimensions of the structure and can lead to the following modes

1- The shape of Figure 1.3a, in which the midpoints of top and bottom sub-laminates in delaminated region move in opposite directions as the buckling develops, is regarded as the ''opening'' mode shape. The opening mode shape is found to be dominant in the post-buckling regime [1.7].
2- The shape of Figure 1.3b in which the two sub-laminates move in the same directions and separate from each other is referred to as the ''closing'' mode shape. The closing mode shape is known to occur at a lower critical buckling load than the opening mode shape [1.7].
3- The shape of Figure 1.3c in which the two sub-laminates reach a state where they are in contact with each other. This mode shape is referred as ''overall'' or ''global'' mode shape [1.7].
4- The shape of Figure 1.3d in which the top sub-laminate separates from the bottom sub-laminate with almost zero displacement in the base structure. This mode shape is regarded as ''local'' mode shape [1.7].

In all cases mentioned above, there are always two important constraints at the ends of the delaminated region as follow [1.7]

1- Undelaminated part and each of the top and bottom sub-laminates must have equal rotations.
2- There must be no relative shear movement between the interfaces of the top and bottom sub-laminates.

Various problems pertaining to the behaviour of near-surface delaminations can be differentiated [1.6],

1- The situation where the delamination behaves in harmony with the base structure, i.e. the delamination has a deformation similar to that of the base structure (Figure 1.3c and Figure 1.5a). This situation normally occurs before the critical buckling of the delamination (local buckling) and is investigated within the area of stability theory.

2- The situation in which post critical behaviour (post-local-buckling) is determined under the condition that the delamination does not grow (Figure 1.5b). The initial post-buckling response is ruled by the buckling of the thinner sub-laminate alone which is known as thin-film buckling. Post-buckling behaviour can be either stable or unstable. In stable post-buckling, local buckling occurs (Figure 1.3d) at the onset of initial buckling and then the shape changes to an opening mode shape (Figure 1.3a) in the post-buckling path. Another example of stable post-buckling is when buckling is initiated with a closing mode shape (Figure 1.3b) and shifts to a state where the top and the bottom sub-laminates contact each other (Figure 1.3c). This situation is also known as overall buckling. Unstable post-buckling occurs when initial buckling is triggered with a closing mode shape (Figure 1.3b) and then shifts to an opening mode shape (Figure 1.3a) in the post-buckling path. This situation is known as mixed-mode buckling (see Table 1.3). Like the first problem, this type of problem is addressed in the area of stability theory [1.7].

3- The situation in which the delamination propagates under quasi-static loading (Figure 1.5c). This type of problem is dealt with within the scope of fracture mechanics theory.

Studying near-surface delaminations within the third class of problems will lead to problems such as determining [1.6]

- The load at which the delamination starts to propagate.
- Whether the delamination grows in a stable manner (i.e. follows the loading level) or in an unstable way.
- Whether the delamination front moves to a new position or the delamination separates from the base structure.

Delaminations are further categorised based on their geometric shape. The shape of the delamination is a function of various factors such as impact energy, material properties, and stacking sequence etc, and can be

1- A discontinuous delamination (Figure 1.6a) which usually originates when it is applied under tension in the direction of its growth [1.6].
2- A continuous compression-caused delamination (Figure 1.6b) [1.6].
3- An elliptical embedded delamination (Figures 1.6c and 1.6d), which can be either continuous or discontinuous. Discontinuous elliptical delaminations normally occur when the structure is under tension [1.6].
4- A pocket-like delamination (Figure 1.6e), which is located at the edge of a plate structure. On some occasions as the delamination grows transverse cracks can occur as shown in Figure 1.6f [1.6].
5- A through-the-width delamination (strip delamination).

6- A circular embedded delamination.

7- A rectangular embedded delamination.

8- A triangular embedded delamination.

1.7 Compressive load and delaminated composite plates

The mechanisms related to strength degradation in laminates have been the subject of intense research and it has been found that different mechanisms may dominate in different failure modes. Current research is concerned mainly with failure modes due to in-plane compressive loads. Although the details of the initial degradation process in such a case are not completely understood, it is generally believed that the strength degradation under compressive in-plane loading is primarily the result of delamination buckling and its growth.

Two basic questions arise in understanding the behaviour of laminates under compressive loading

1- What is the maximum compressive load a laminate can carry when it contains a delamination prior to the loading process?

2- What will the level of degradation in the compressive load-carrying ability of a laminate be, if a delamination is introduced into a compressively stressed laminate?

The answer to the above questions depends on various parameters such as

1- The size of the delamination.

2- The number of delaminations.

3- The location of the delamination (through the thickness, along the length and across the width of the structure).

4- The laminate stiffness (i.e. the **A, B, D** matrices defined in chapter 2).

5- The laminate boundary conditions.

6- The laminate stacking sequence.

7- The thermal cool-down effects arising out of the manufacturing process (i.e. residual stresses).

Extensive analytical, numerical and experimental studies have been conducted over the past two decades [1.9-1.32] modelling the buckling and post-buckling behaviour of delaminated composite laminates with different shapes of delamination including:

1- Through-the-width delamination (strip delamination) [1.9-1.11, 1.12-1.15, 1.20-1.21, 1.26-1.28, 1.30]

2- Circular embedded delamination [1.12, 1.24]

3- Elliptical embedded delamination [1.31]

4- Rectangular embedded delamination [1.17-1.18, 1.23-1.24]

5- Triangular embedded delamination [1.23]

Karihaloo and Stang [1.9] examined the pre- and post- buckling response of a strip delamination in a composite laminate analytically and experimentally. They also developed guidelines for assessing whether or not it poses a threat to the safe operation of the laminate. Lee and Park [1.10] studied the interaction between local and global buckling behaviours of composite laminates. They investigated the effect of various parameters, such as delamination size, aspect ratio, width-to-thickness ratio and stacking sequence on through-the-width delaminations and also the effects of location

of delamination and the existence of multiple delaminations on embedded rectangular delaminations. Riccio and Gigliotti [1.11] presented a fast numerical method for simulation of delamination growth in delaminated composite panels using four linear analyses. The work was validated against two finite element models, with through-the-width and embedded delaminations, respectively. The numerical results obtained were compared to two- and three-dimensional numerical results. Butler et al [1.12] presented a new model which could predict the compressive fatigue limit strain of composites containing BVID. The method was based on a combination of 2D and 1D models and represented the complexity of the morphology and progression of damage during static growth of a single delamination at a critical depth within the sample. The results obtained using this method, were compared with two sets of experimental results, involving the use of different materials, different stacking sequences and different levels of impact energy. They also presented an enhanced version of the model for predicting the magnitude of fatigue strain required to propagate an area of BVID at a critical delamination level [1.13]. The new enhanced model uses an updated propagation approach based on plate bending energy together with damage principles.

Capello and Tumino [1.14] carried out a study considering the influence of the length of a delamination, its position through the thickness and stacking sequence on the critical load and the threshold value between global and mixed, and mixed and local behaviour, in unidirectional and cross ply composite laminated plates with multiple delaminations This was examined for symmetrical and non-symmetrical cases. Pekbey and Sayman [1.15] conducted experimental measurements and determined numerical solutions for the buckling of glass-fiber rectangular plates containing a single delamination. In addition, the effects of variation in structural configuration, such as ply stacking sequence, the width of the delamination and specimen geometry (width to

unsupported length), were considered. In all cases, the delamination was centrally placed through-the-thickness of the laminate. Compression tests were carried out on EP GC 203 glass/epoxy woven composites with a single embedded delamination built in, in order to evaluate critical buckling load. Finite element modelling was used to gain further understanding of the critical buckling load.

Zor et al [1.16] investigated the effects of a square delamination around a square hole on the buckling loads of simply supported and clamped composite plates. They performed linear buckling analyses of a square laminated plate for different fibre angles, using a 3D finite element method. Li et al [1.17] used a semi-analytical, semi-exact method, namely the strip transfer function method based on Mindlin's first-order shear deformation theory to analyze the buckling problems of a laminated plate with a built-in rectangular delamination. The delaminated plate was divided into two kinds of rectangular super-units. In the lateral direction, these super-units were divided into many strip elements. In contrast to FEM, this technique interpolated the displacement field of the super-units using polynomials written in terms of the nodal line displacements, which were functions of the strip's longitudinal coordinate. The strip distributed transfer function method was used to get the exact and closed-form solutions for the super-units along the strip longitudinal direction. Finally, the buckling load and mode of the delaminated plate were computed with higher accuracy and efficiency through a special treatment for the super-units with a delamination and a synthesized method. Possible contact between delamination surfaces was not taken into consideration. Wang et al [1.18] conducted an investigation into the effect of the through-thickness position of single and double rectangular embedded delaminations on the buckling response and compressive failure load of GFRP panels. They carried out a three dimensional finite element analysis to determine buckling and post-buckling

behaviour, and compared predicted failure loads with those measured experimentally. Hwang and Huang [1.19] evaluated the interaction between a long through-the-width delamination and a short through-the-width delamination in the post-buckling stage. They carried out nonlinear buckling analyses using the finite element method to predict the effects of this interaction on post-buckling behaviour. In addition, the possible fracture mode of delamination was discussed.

Kucuk [1.20] conducted a buckling analysis on a woven steel fibre reinforced low-density polyethylene thermoplastic plate with a strip shaped lateral delamination. Linear buckling analyses of a square laminated plate were performed for different fibre angles and simply supported boundary conditions, by using three dimensional finite element methods. Zor et al [1.21] prepared three dimensional models of low-density polyethylene thermoplastic plates reinforced by woven steel fibres which included vertical and horizontal strip delaminations and the critical loads caused by buckling (local buckling) were determined for various stacking sequences with simple supported boundary conditions.

Bai and Chen [1.22] established a numerical model and method for simulating multiple compressive failure modes, including initial buckling, post-bucking and delamination propagation. A model was constructed which used a Griffith-type crack growth criterion to describe failure characteristics and a self-adaptive grid moving technology to analyze delamination onset and propagation. A GAP interface element was employed to avoid overlap and penetration between the upper and lower sub-laminated portions (GAP elements are used in MSC/NASTRAN to simulate unidirectional point-to-point contact problems [1.23]). Furthermore, a global-local nonlinear analysis technique and modified incremental strategy were developed for use in the nonlinear numerical iterative procedure to reduce computation cost. Numerical

results were presented to illustrate the method, and the influence of features such as the distribution and location of stiffeners, the configuration and size of the delamination and the effects of boundary conditions and contact upon the delamination growth behaviour of a series of stiffened plates. Some useful conclusions were obtained.

Wang and Lu [1.24] utilized an energy method to investigate the buckling behaviours of rectangular and triangular local delaminations near the surface of laminated plates under mechanical and thermal coupling loads. They also performed experiments to investigate the mechanism of delamination buckling failure for plates under mechanical compression load only. Analytical predictions for delamination buckling loads were shown to correlate well with experimental results for a number of different delamination shapes.

Kim and Cho [1.25] outlined in their paper the development of a four-noded plate bending element for an efficient higher-order zig-zag theory for multiple delaminations. Zig-zag formulations were applied to classical laminate theory (CLT) and first order shear deformation theory (FSDT). Patch tests for the proposed element were developed and performed. Delamination buckling analyses for both circular and rectangular embedded delaminations were carried out and compared with available results from previously reported models to assess the accuracy of the element. Hwang and Liu [1.26] observed the buckling and post-buckling behaviours of composite laminates with multiple delaminations under uniaxial compression. The shape of multiple delaminations used was related to impact damage. A nonlinear buckling analysis using FEA was also used to predict buckling loads which were compared with experimental results. The critical delamination growth loads of multiple delaminations were obtained from post-buckling testing. The difference between single and multiple delaminations on buckling and post-buckling behaviour was also discussed. Zor [1.27]

studied the effect of single strip delaminations on the buckling loads of a carbon/epoxy woven-fibre system. He carried out linear buckling analyses of a square laminated plate with different fibre angles and simply supported boundary conditions using a 3D finite element method, and evaluated critical delamination lengths for all cases.

Short et al [1.28] described a preparatory investigation into the effect of curvature on the compressive failure load of glass fibre reinforced plastic (GFRP) laminates containing embedded delaminations, where the plane of curvature was normal to the loading direction. They obtained experimental results for flat and curved laminates containing delaminations having different sizes and through thickness positions. Three dimensional finite element analyses were also carried out in order to compare predicted failure loads with those measured experimentally.

Hwang and Liu [1.29] investigated the interaction of multiple delaminations upon buckling loads and modes. They considered different shapes of multiple delaminations. They also performed nonlinear FE analyses to predict buckling behaviour and eventually discussed the differences between obtained buckling loads and mode shapes. Nilsson et al [1.30] presented a combined experimental/numerical study for rectangular panels with delaminations inserted at three different depths. Their objective was to study the interaction between buckling of the delaminated member and global panel buckling. Their computational model for general delamination shapes was extended to include the effect of global bending. Hwang and Mao [1.31] studied the buckling loads, buckling modes, post-buckling behaviour and critical loads for delamination growth in unidirectional carbon/epoxy composites. Delaminations were limited to a through-the-width strip shape. To predict buckling loads precisely, a refined FE method, involving nonlinear buckling analysis, was used. Geometric nonlinearity and the physically impossible situation of overlapping were prevented by using contact

elements between the delamination surfaces. Finally, the results of these analyses were compared with experimental ones, and the failure of delaminated composite plates was assessed.

Sekine et al [1.32] obtained the buckling load and mode of an elliptically delaminated plate by solving the eigenproblem. They added constraints to prevent layer overlaps by a penalty function method. They also studied the effects of different parameters such as delamination size, shape, position and the fibre angle of the delaminated layer on the buckling loads and modes.

Numerous studies have therefore been performed to determine buckling behaviour of delaminated composite plates using the finite element method. Finite element methods are suitable for any shape of delaminations and boundary conditions with no limitation, but they embrace some drawbacks such as:

1- They are computationally intensive.

2- They need large amount of computer memory so increase the time of analysis.

3- They do not provide explicit and closed-form solutions.

The aim of the work presented in this thesis will be to develop a technique for predicting this behaviour which addresses as many as possible of these points.

1.8 Thesis outline

In this thesis, the focus is to quantify the effects of delamination on the buckling behaviour of delaminated composite plates using exact stiffness analysis. Therefore, several approaches are taken in the following chapters to obtain these effects.

The second chapter reviews the theory used for analysis of composite plates including the definition of composite plate stiffness matrices, stress and strain relationship equations, exact stiffness analysis, the Wittrick-William algorithm and the

theory of the computer program VICONOPT, highlighting the features which are essential in understanding the rest of the thesis.

The third chapter models through-the-length delamination under longitudinal, transverse and shear loading using the existing code of VICONOPT.

Chapters 4 and 5 examine a potential method for expanding analysis to cover more generally shaped delaminations. The multi-structure approach in VICONOPT is employed in an attempt to model the effects of delamination on critical buckling behaviour of composite plates. Limitations of this method led to the feasibility study described in Chapter 6, which considers the combination of positive and negative stiffness regions to model a delamination.

In Chapter 7, a further existing feature of VICONOPT, multi-level sub-structuring, is used to model delamination, but proves to be inefficient.

The most important advance in this thesis is described in Chapters 8 and 9. Here, an efficient method for modelling a rectangular delamination located in numerous positions and loaded longitudinally is devised and subsequently good results are obtained.

Finally, Chapter 10 provides an overall conclusion of the different methods used and potential future work.

1.9 References

[1.1] G.J. Turvey and I.H.Marshall, Buckling and Postbuckling of Composite Plates Chapter 9, 299-301 (1995).

[1.2] Reddy, J. N. (Junuthula Narasimha), Mechanics of Laminated Composite Plates and Shells: theory and analysis, 2nd ed, (1997).

[1.3] Jones, R.M., Mechanics of Composite Materials, *Hemisphere Publishing Corporation, New York*, 1-92 (1975).

[1.4] Carlsson ,L.A., Pipes, R.B., Experimental Characterization of Advanced Composite Materials, *Prentice-Hall, Inc., New Jersey*, 91-93 (1987).

[1.5] H.Altenbach, Theories for laminated and sandwich plates. A review, *Mechanics of Composite Materials*, **34**, NO. 3, 333-348 (1998).

[1.6] G. W. Hunt, B. Hu, R. Butler, D. P. Almond and J. E. Wright, Nonlinear modeling of delaminated struts, *AIAA Journal*, **42** (11), 2364-2371 (2004).

[1.7] Bolotin, V.V., Delaminations in composite structures: its origin, buckling, growth and stability Composites Part B, *Engineering*, **27**, Issue 2,129-145 (1996).

[1.8] Bolotin, V.V., Delaminations in composite structures: its origin, buckling, growth and stability Composites Part B, *Engineering*, **27**, Issue 2,129-145 (1996).

[1.9] B.L. Karihaloo, H. Stang, Buckling-driven delamination growth in composite laminates: Guidelines for assessing the threat posed by interlaminar matrix delamination, *Composites: Part B*, **39**, 386-395 (2008).

[1.10] Sang-Youl Lee, Dae-Yong Park, Buckling analysis of laminated composite plates containing delaminations using the enhanced assumed strain solid element, *International Journal of Solids and Structures*, **44**, 8006–8027 (2007).

[1.11] Aniello Ricci, Marco Gigliotti, A Novel Numerical Delamination Growth Initiation Approach for the Preliminary Design of Damage Tolerant Composite Structures, *Journal of Composite Materials*, **41**, 1939-1960 (2007).

[1.12] R. Butler, D.P. Almond, G.W. Hunt, B. Hu, N. Gathercole, Compressive fatigue limit of impact damaged composite laminates, *Composites: Part A*, **38**,1211-1215 (2007).

[1.13] A.T. Rhead, R. Butler, G.W. Hunt, Post-buckled propagation model for compressive fatigue of impact damaged laminates, *International Journal of Solids and Structures*, **45**, 4349–4361 (2008).

[1.14] F.Capello, D. Tumino, Numerical analyses of composite plates with multiple delaminations subjected to uniaxial buckling load, *Composite Science and Technology*, **66**, 264-272 (2006).

[1.15] Y.Pekbey, O.Sayman, A Numerical and experimental Investigation of Critical Buckling Load of Rectangular Laminated Composite Plates with Strip Delamination, *Journal of Reinforced Plastics and Composites*, **25**, 685-697 (2006).

[1.16] Mehmet Zor, Faruks_En , M. Evren Toygar, An Investigation of Square Delamination Effects on the Buckling Behaviour of Laminated Composite Plates with a Square Hole by using Three-dimensional FEM Analysis, *Journal of Reinforced Plastics and Composites*,**24**,1119-1130 (2005).

[1.17] D. Li, G. Tang, J. Zhou, and Y. Lei, Buckling analysis of a plate with built-in rectangular delamination by strip distributed transfer function method, *Acta Mechanica*, **176**, 231–243 (2005).

[1.18] X.W. Wang, I. Pont-Lezica, J.M. Harris, F.J. Guild, M.J. Pavier, Compressive failure of composite laminates containing multiple delaminations, *Composites Science and Technology*, **65**, 191–200 (2005).

[1.19] Shun-Fa Hwang, Shu-Mei Huang, Postbuckling behaviour of composite laminates with two delaminations under uniaxial compression, *Composite Structures*, **68**,157–165 (2005).

[1.20] Mu Min Kucuk, An Investigation on Buckling Behaviour of Simply Supported Woven Steel Reinforced Thermoplastic Laminated Plates with Lateral Strip Delamination, *Journal of Reinforced Plastics and Composites,* **23**, 209-216 (2004).

[1.21] Mehmet Zor, Hasan Çallioglu and Hamit Akbulut, Three-dimensional Buckling Analysis of Thermoplastic Composite Laminated Plates with Single Vertical or Horizontal Strip Delamination, *Journal of Thermoplastic Composite Materials,* **17**, 557-568 (2004).

[1.22] Bai Rui-xiang, CHEN Hao-ran, numerical analysis of delamination growth for stiffened composite laminated plates, *Applied Mathematics and Mechanics*, **25**, 405-417 (2004).

[1.23] MSC.Nastran, Linear Static Analysis User's Guide, MSC softwarte corporation (2003).

[1.24] X. Wang, G. Lu, Local buckling of composite laminar plates with various delaminated shapes, *Thin-Walled Structures*, **41**, 493–506 (2003).

[1.25] Jun-Sik Kim, Maenghyo Cho, Buckling analysis for delaminated composites using plate bending elements based on higher-order zig-zag theory, *International Journal of Numerical Methods in Engineering*, **55**, 1323–1343 (2002).

[1.26] Shun-Fa-Hwang, Guu-Huann-Liu, Experimental Study for Buckling and Postbuckling Behaviors of Composite Laminates with Multiple Delaminations, *Journal of Reinforced Plastics And Composites*, **21**, 333-349 (2002).

[1.27] Mehmet Zor, Delamination Width Effect on Buckling Loads of Simply Supported Woven-Fabric Laminated Composite Plates Made of Carbon/Epoxy, *Journal of Reinforced Plastics and Composites*, **22**,1535-1546 (2003).

[1.28] G.J. Short, F.J. Guild, M.J. Pavier , Delaminations in flat and curved composite laminates subjected to compressive load, *Composite Structures*, **58**, 249–258 (2002).

[1.29] Shun-Fa Hwang, Guu-Huann Liu, Buckling behaviour of composite laminates with multiple delaminations under uni-axial compression, *Composite Structures*, **53**, 235-243 (2001).

[1.30] K.F. Nilsson, L.E. Asp, J.E. Alpman, L. Nystedt, Delamination buckling and growth for delaminations at different depths in a slender composite panel, *International Journal of Solids and Structures*, **38**, 3039-3071 (2001).

[1.31] Shun-fa Hwang, Ching-ping Mao, Failure of Delaminated Carbon/Epoxy Composite Plates under Compression, *Journal of Composite Materials*, **35**, 1634-1653 (2001).

[1.32] H. Sekine, N. Hu and M. A. Kouchakzadeh, Buckling Analysis of Elliptically Delaminated Composite Laminates with Consideration of Partial Closure of Delamination, *Journal of Composite Materials*, **34**, 551-574 (2000).

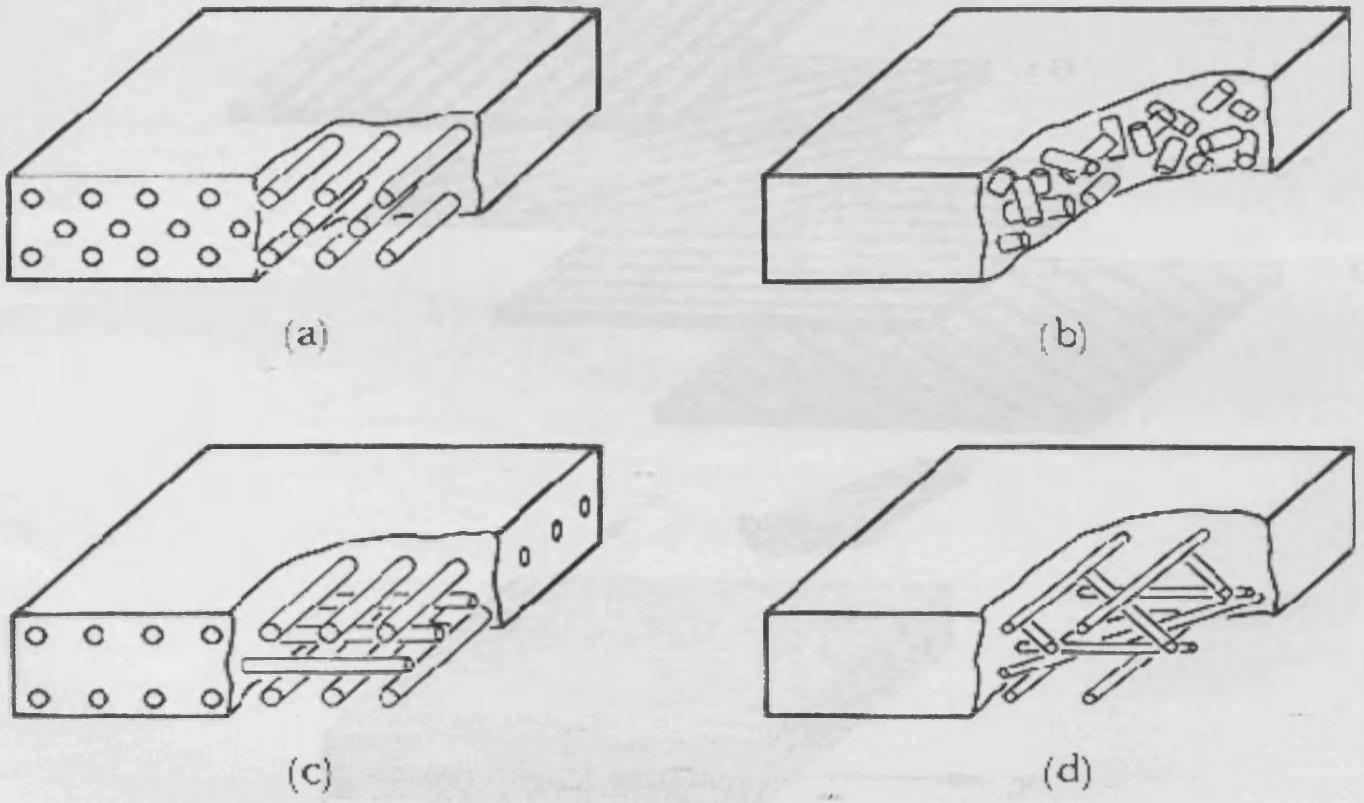

Figure 1.1: Various types of fibre-reinforced composite laminae. a) Unidirectional, b) Discontinuous fibre, c) Bi-directional, d) Woven [1.2]

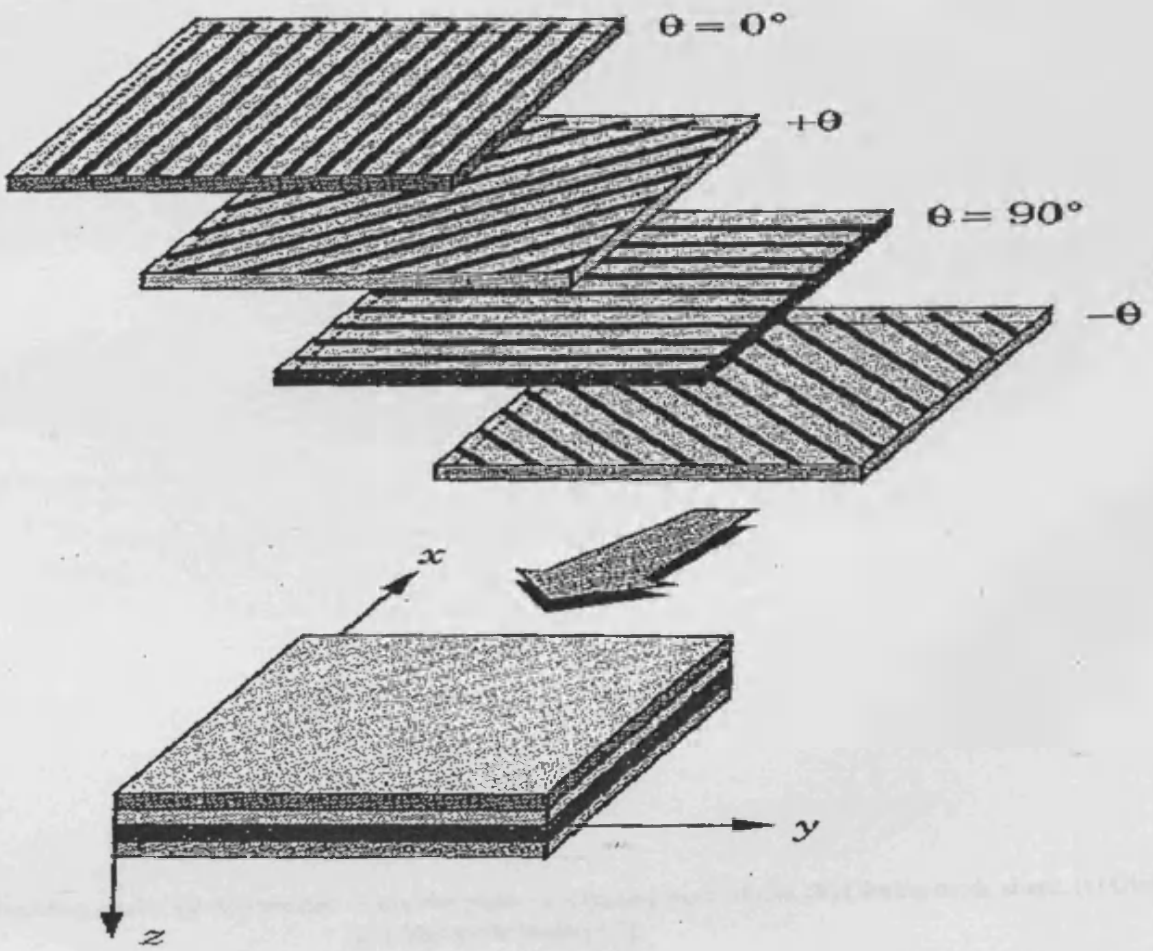

Figure 1.2: A laminate made up of laminae with different fibre orientations [1.2]

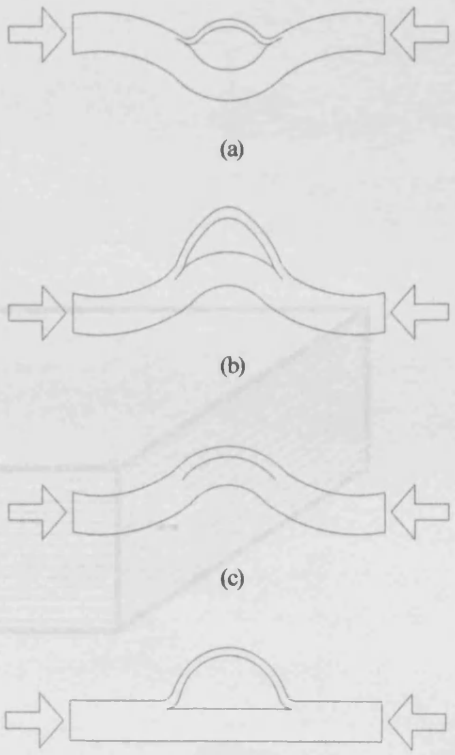

Figure 1.3: Different possible buckling modes for delaminated composite plates (a) Opening mode shape, (b) Closing mode shape, (c) Global mode shape, (d) Local mode shape [1.7].

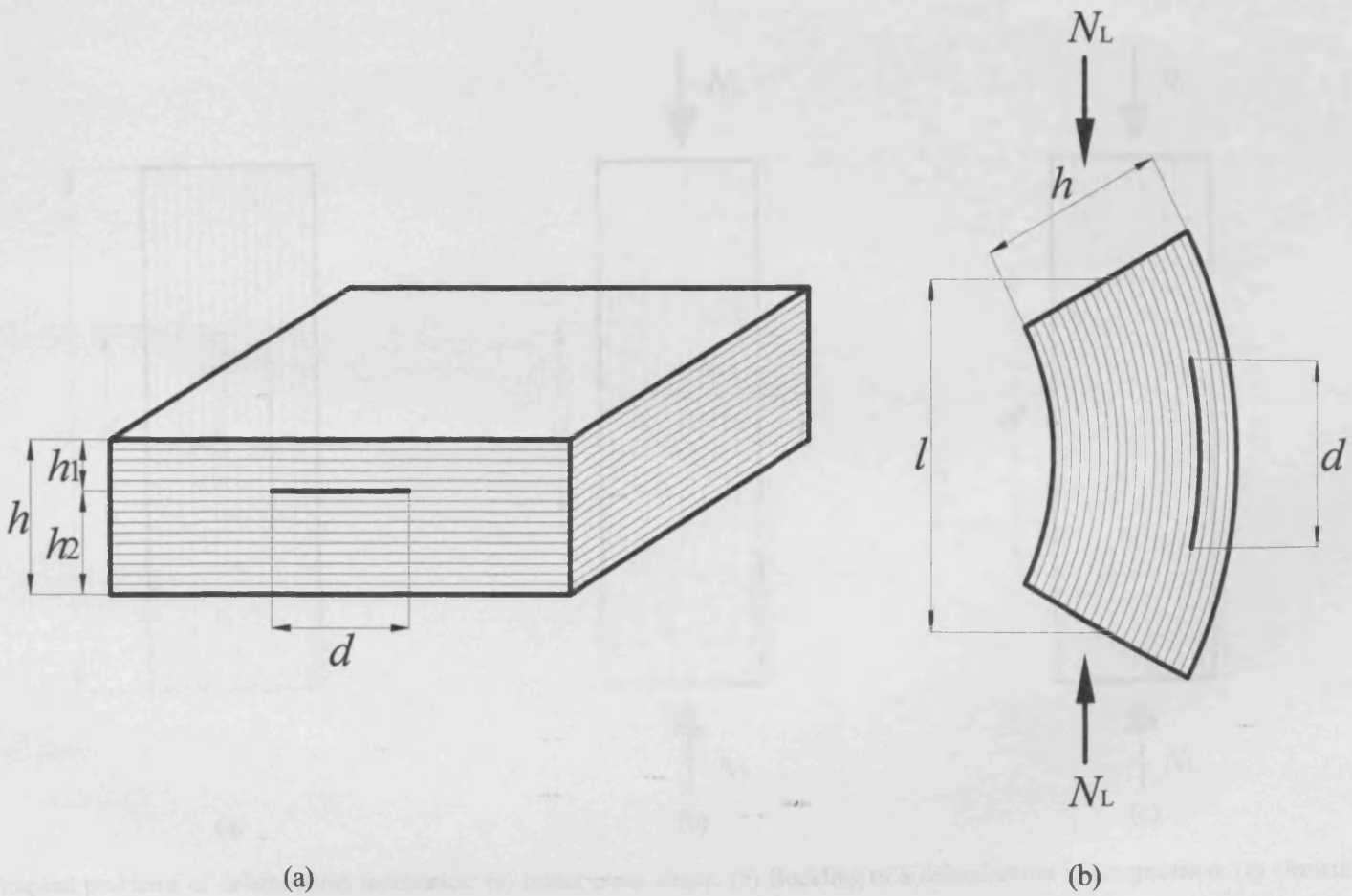

Figure 1.4: Internal delamination: (a) Disposition across the plate thickness, (b) Buckling of the plate under delamination.

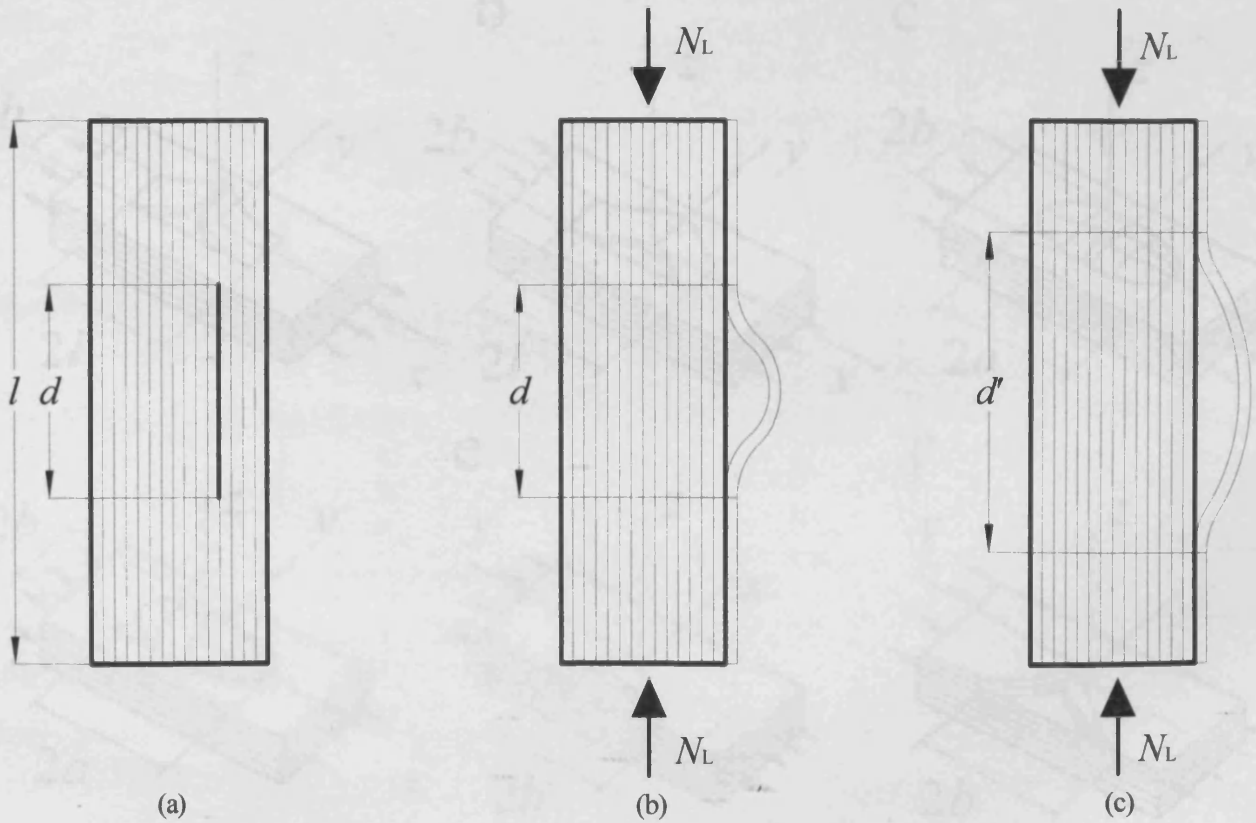

Figure 1.5: Simplest problems of delamination mechanics: (a) Initial plane shape. (b) Buckling of a delamination in compression. (c) Growth of a buckled delamination, and N_L is compressive longitudinal load.

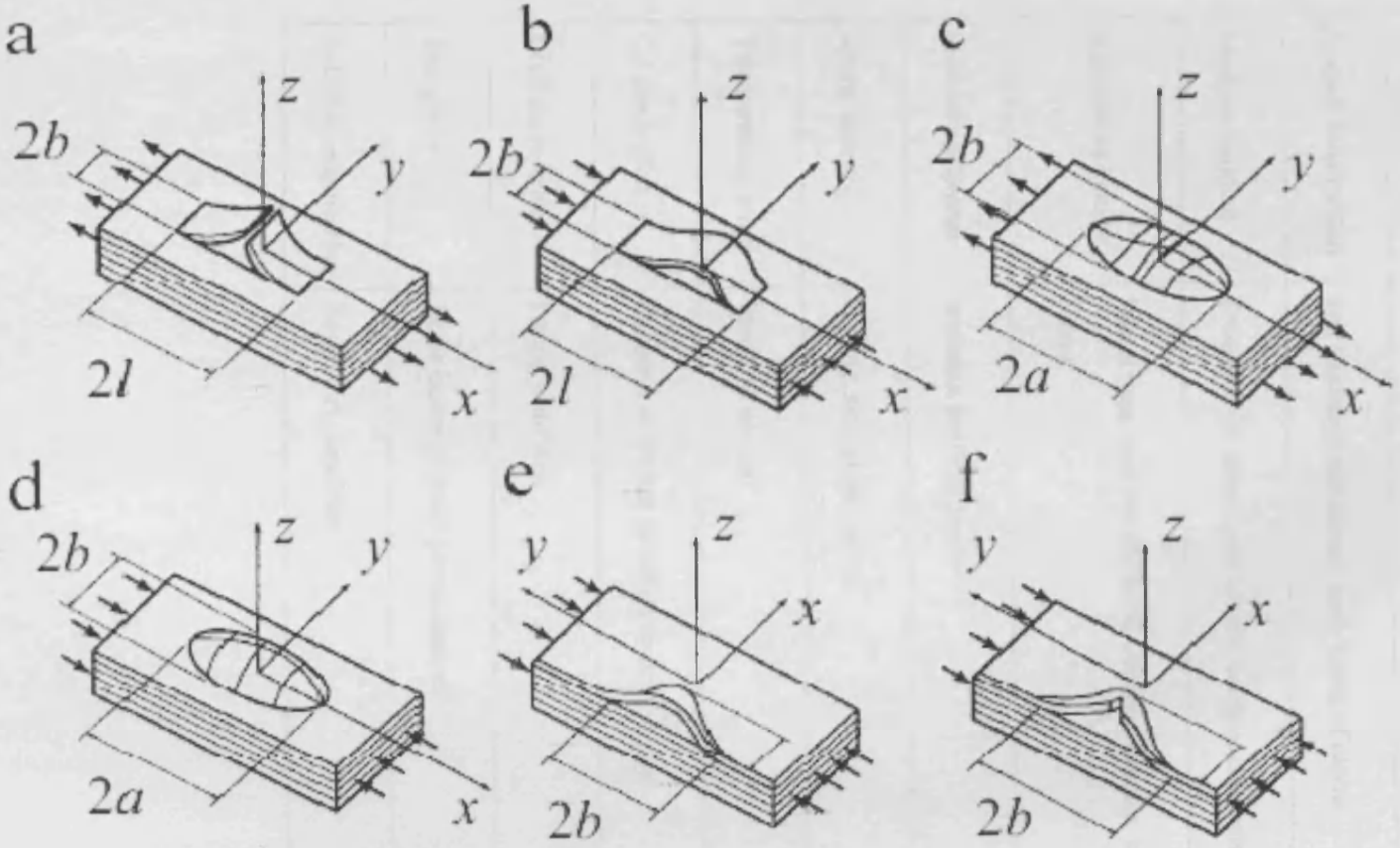

Figure 1.6: Typical surface delaminations: (a) Discontinuous in tension, (b) Continuous in compression, (c) Discontinuous quasi-elliptic, (d) Continuous elliptic, (e) Pocket-like, (f) Pocket-like with a transverse crack [1.6].

Table 1.1: Application of composite plates in different branches of industry [1.5]

Branch of industry	**Application**
Rocket construction	Load-carrying structural elements, fuels tanks, aerial elements
Aircraft construction	Tail assembly, stabilisers, inner lining of cabins
Machine building	Transmission cases, gear wheels, machine elements
Automotive industry	Wheel rims, tank covers, hood, steering columns, inner lining of cabins
Medical equipment	Implants, artificial joints
Sports industry	Surfing, skis, clubs, canoes
Telecommunication	Parabolic aerials
Oil production	Elements of frames for offshore drilling rigs
Civil engineering	Facing materials
Energetics	Rotor blades of wind power stations
Industrial engineering	Reservoirs, pipelines

Table 1.2: advantages and disadvantages of composite plates [1.5]

Disadvantages	**Advantages**
High rigidity characteristics relative to mass	Loss of strength due to aging of adhesive joints
Thermo insulation	High technological requirements to the accuracy of production
Sound-proofing	Necessity of modifying the methods of non-destructive testing of structures
High fatigue characteristics	High sensitivity to impact loads
High corrosive resistance	Brittleness
Low tendency to loss of stability	----------
Decrease in the number of assembling	----------

Table 1.3: Various post-buckling responses for delaminated composite plates

Stable post-buckling		**Unstable post-buckling**	
MB*	**MPB****	**MB**	**MPB**
Thin film buckling		**Mixed-mode buckling**	
			
Overall buckling			
			

*Mode shape at the point of buckling
**Mode shape in post-buckling path

CHAPTER 2

ANALYSIS OF COMPOSITE PLATE STRUCTURES

2.1 Introduction

Various techniques have been investigated by many researchers for obtaining the critical buckling loads of prismatic structures that are assembled by joining plates rigidly along their longitudinal edges. The use of exact stiffnesses obtained from analytical solutions (closed form solutions) of the member stiffness equations for each of the constituent plates of the assembly prevents the approximation errors stemming from discretising the entire assembly into finite strips or finite elements (numerical solutions) as is the case for Finite Strip Method (FSM) and Finite Element Analysis (FEA), respectively. On the other hand, employing exact stiffnesses results in highly non-linear (transcendental) eigenproblems, i.e. the elements of the stiffness matrix will include transcendental functions (sin, cos, exp, log etc) of the eigenparameter.

The Wittrick–Williams (W–W) algorithm was developed in 1970 [2.1] to calculate the eigenvalues (natural frequencies in free vibration problems or critical load factors in buckling problems) of transcendental eigenproblems with certainty to any required accuracy, as opposed to alternative methods which can miss eigenvalues. The W–W algorithm is a method which can produce exact solutions to structural eigenproblems with the certainty by which these fast solutions are obtained. This makes the method suitable for processes such as initial aircraft design, where eigenvalues must be found for many alternative configurations. The algorithm obtains the eigenvalues indirectly by calculating a parameter called J. J is the number of eigenvalues exceeded by a trial value φ_t of the eigenvalue. In other words, an interval with lower limit of zero and upper limit of φ_t would enclose J eigenvalues. The length of the interval is

repeatedly reduced using iterative computation to converge on the required eigenvalue to any desired accuracy. The algorithm has many other applications such as Sturm-Liouville problems and permits exact sub-structuring. The latter will be detailed later in this Chapter [2.1-2.3].

2.2 Exact stiffness analysis

The W–W algorithm is used in the computer program VIPASA [2.4] for the analysis of plate structures in which the mode of buckling or vibration is assumed to vary sinusoidally in the longitudinal direction with half-wavelength λ. Figure 2.1 shows, for an individual plate, its Cartesian axis system xyz, displacement amplitudes u, v and w and its basic in-plane force system, where N_L, N_T and N_S are, respectively, uniform longitudinal, transverse and shear stress resultants (i.e. forces per unit width). Eigenvalues and modes can be obtained for any half-wavelength λ specified by the user. When all plates of the plate assembly are isotropic or orthotropic and have $N_S = 0$, the nodal lines are straight and perpendicular to the longitudinal (x) direction. In these cases VIPASA gives exact solutions for plate assemblies with simply supported ends, so long as λ divides exactly into the length l. When anisotropy or shear load are present the nodal lines are skewed, as shown in the contour plot of Figure 2.2, and hence there are spatial phase differences across the widths of the plates. The solutions therefore only approximate simply supported ends, being quite accurate for short wavelength buckling, i.e. $\lambda << l$, but becoming substantial underestimates as λ approaches l, i.e. they are very conservative for overall modes [2.5].

This limitation is overcome in the computer program VICON [2.6] by coupling together the VIPASA stiffness matrices for different half wavelengths λ using the method of Lagrangian multipliers. VICON retains the guarantee of convergence on all

required eigenvalues [2.7], and applies constraints to represent arbitrarily located point supports, or point connections of the plate assembly to simple elastic supporting structures consisting of transverse beam-columns. This analysis has been extended to allow point connections between two or more plate assemblies, e.g. to model riveted connections [2.8]. All such constraints are assumed to repeat at intervals of l to give an infinitely long plate assembly for which the buckling mode repeats over some multiple of l. The infinitely long model thus represents continuity with adjacent parts of the structure and also gives approximate solutions for a plate assembly of finite length l.

The design software VICONOPT [2.9, 2.10] incorporates both the VIPASA and VICON forms of analysis, and also has postbuckling and optimisation capabilities.

2.2.1 Composite laminates stiffness matrices

Prior to introducing the theory and formulation used in VIPASA.

Figure 2.3 shows a typical composite laminate and Figure 2.4 illustrates the free body diagram showing the forces and moments acting on a typical composite laminate. In order to obtain the forces and moments that a laminate is subjected to, recourse needs to be made to the elasticity law of laminates as [2.11]

$$\begin{bmatrix} n_x \\ n_y \\ n_{xy} \\ m_x \\ m_y \\ m_{xy} \end{bmatrix} = \begin{bmatrix} A_{11} & A_{12} & A_{16} & B_{11} & B_{12} & B_{16} \\ A_{12} & A_{22} & A_{26} & B_{12} & B_{22} & B_{26} \\ A_{16} & A_{26} & A_{66} & B_{16} & B_{26} & B_{66} \\ B_{11} & B_{12} & B_{16} & D_{11} & D_{12} & D_{16} \\ B_{12} & B_{22} & B_{26} & D_{12} & D_{22} & D_{26} \\ B_{16} & B_{26} & B_{66} & D_{16} & D_{26} & D_{66} \end{bmatrix} \begin{bmatrix} {\varepsilon^0}_x \\ {\varepsilon^0}_y \\ {\gamma^0}_{xy} \\ \kappa_x \\ \kappa_y \\ \kappa_{xy} \end{bmatrix} \tag{2.1}$$

where n_x, n_y, n_{xy} and m_x, m_y, m_{xy} are stress ([**n**]) and moment ([**m**]) resultants, respectively. A_{ij}, B_{ij} and D_{ij} are elements of membrane ([**A**]), coupling ([**B**]) and out-of-plane bending ([**D**]) stiffness matrices. ${\varepsilon^0}_x$, ${\varepsilon^0}_y$, ${\gamma^0}_{xy}$ and κ_x, κ_y, κ_{xy} are strains ([ε^0])

and curvatures ([κ]) at the mid-surface of the laminate. The stiffness matrix elements are calculated as

$$A_{ij} = -\sum_{k=1}^{N} (\overline{Q}ij)_k (Z_k - Z_{k-1})$$

$$B_{ij} = \frac{1}{2}\sum_{k=1}^{N} (\overline{Q}ij)_k (Z_k{}^2 - Z_{k-1}{}^2)$$

$$D_{ij} = -\frac{1}{3}\sum_{k=1}^{N} (\overline{Q}ij)_k (Z_k{}^3 - Z_{k-1}{}^3) \qquad (2.2)$$

where $i, j = 1, 2, 6$. z_k and z_{k-1} are the coordinates of the top and bottom surface of ply k and N is the number of plies within the laminate (Figure 2.3). $\overline{Q}_{ij}$ is the *transformed reduced stiffness matrix* which is obtained as follows.

The *Reduced stiffness matrix* is the stiffness matrix for a single orthotropic lamina which is represented by the 3 × 3 matrix [2.11]

$$Q_{ij} = \begin{bmatrix} Q_{11} & Q_{12} & 0 \\ Q_{21} & Q_{22} & 0 \\ 0 & 0 & Q_{66} \end{bmatrix} \qquad (2.3)$$

where

$$Q_{11} = \frac{E_{11}}{1 - \nu_{12}\nu_{21}}$$

$$Q_{22} = \frac{E_{22}}{1 - \nu_{12}\nu_{21}}$$

$$Q_{12} = \frac{\nu_{21}E_{11}}{1 - \nu_{12}\nu_{21}} = \frac{\nu_{12}E_{22}}{1 - \nu_{12}\nu_{21}}$$

$$Q_{66} = G_{12} \qquad (2.4)$$

E_{11} and E_{22} are Young's moduli parallel and normal to the fibre direction, G_{12} is the shear modulus and ν_{12} is Poisson's ratio.

Equation (2.3) represents the ply properties for a single lamina oriented in the direction of its material axis. To obtain the ply properties of a lamina rotated θ clockwise from the material axis, the values of matrix of Eq (2.3) must be rotated using the tensor transformation matrix. The resulting matrix is called the *transformed reduced stiffness matrix* [2.11]

$$[\overline{Q}_{ij}] = \begin{bmatrix} \overline{Q}_{11} & \overline{Q}_{12} & \overline{Q}_{16} \\ \overline{Q}_{21} & \overline{Q}_{22} & \overline{Q}_{26} \\ \overline{Q}_{16} & \overline{Q}_{26} & \overline{Q}_{66} \end{bmatrix} \tag{2.5}$$

To obtain elements of $[\overline{Q}_{ij}]$ the following definitions are introduced

$$U_1 = \frac{1}{8}[3Q_{11} + 3Q_{22} + 2Q_{12} + 4Q_{66}]$$

$$U_2 = \frac{1}{2}[Q_{11} - Q_{22}]$$

$$U_3 = \frac{1}{8}[Q_{11} + Q_{22} - 2Q_{12} - 4Q_{66}]$$

$$U_4 = \frac{1}{8}[Q_{11} + Q_{22} + 6Q_{12} - 4Q_{66}]$$

$$U_5 = \frac{1}{8}[Q_{11} + Q_{22} - 2Q_{12} + 4Q_{66}] \tag{2.6}$$

The explicit form for $[\overline{Q}ij]$ is expressed as

$$\begin{bmatrix} \overline{Q}_{11} \\ \overline{Q}_{22} \\ \overline{Q}_{12} \\ \overline{Q}_{66} \\ \overline{Q}_{16} \\ \overline{Q}_{26} \end{bmatrix} = \begin{bmatrix} U_1 & cos2\theta & cos4\theta \\ U_1 & -cos2\theta & cos4\theta \\ U_4 & 0 & -cos4\theta \\ U_5 & 0 & -cos4\theta \\ 0 & sin2\theta/2 & sin4\theta \\ 0 & sin2\theta/2 & -sin4\theta \end{bmatrix} \begin{bmatrix} 1 \\ U_2 \\ U_1 \end{bmatrix} \quad (2.7)$$

2.2.2 Theory and formulation used in VIPASA analysis

VIPASA analysis uses a stiffness matrix method based on exact classical thin plate theory (CLT). The following assumptions are made

1- Orthotropic layers are assumed to be perfectly bonded together with a non-shear-deformable infinitely thin line bond.

2- The coupling stiffness matrix [**B**] is zero.

3- A_{16} and A_{26} are zero, i.e. it assumes orthotropic in-plane material properties for the laminate.

The out-of-plane and in-plane elastic properties of an anisotropic plate are then given by [2.12]

$$\begin{bmatrix} m_x \\ m_y \\ m_{xy} \end{bmatrix} = - \begin{bmatrix} D_{11} & D_{12} & D_{16} \\ D_{12} & D_{22} & D_{26} \\ D_{16} & D_{26} & D_{66} \end{bmatrix} \begin{bmatrix} \kappa_x \\ \kappa_y \\ 2\kappa_{xy} \end{bmatrix} \quad (2.8)$$

$$\begin{bmatrix} n_x \\ n_y \\ n_{xy} \end{bmatrix} = \begin{bmatrix} A_{11} & A_{12} & 0 \\ A_{12} & A_{22} & 0 \\ 0 & 0 & A_{66} \end{bmatrix} \begin{bmatrix} \varepsilon^0{}_x \\ \varepsilon^0{}_y \\ \gamma^0{}_{xy} \end{bmatrix} \quad (2.9)$$

The sign convention used for the bending moments and membrane forces is shown in Figure 2.5.

In VIPASA, the amplitudes of the perturbation forces and displacements shown in Figure 2.5 can be complex, to allow for the possibility of (spatial) phase differences between them. In Figure 2.5, ω is the free vibration frequency and is taken as zero if a buckling problem is intended. Perturbation force and displacement vectors $\mathbf{p}_n$ and $\mathbf{d}_n$ at edge n (n = 1 or 2) are defined as [2.17]

$$\mathbf{p}_n = [m_n, p_{zn}, p_{yn}, ip_{xn}]^T,\ \mathbf{d}_n = [\psi_n, w_n, v_n, iu_n]^T \tag{2.10}$$

where superscript T denotes transpose, so that the complex member stiffness matrices $\mathbf{k}_{mn}$ (m, n =1, 2) are defined as

$$\mathbf{p}_1 = \mathbf{k}_{11}\mathbf{d}_1 + \mathbf{k}_{12}\mathbf{d}_2\ ,\ \ \mathbf{p}_2 = \mathbf{k}_{21}\mathbf{d}_1 + \mathbf{k}_{22}\mathbf{d}_2 \tag{2.11}$$

or

$$\mathbf{p} = \mathbf{k}\mathbf{d}\ ,\ \mathbf{p} = \begin{bmatrix}\mathbf{p}_1\\ \mathbf{p}_2\end{bmatrix},\ \mathbf{d} = \begin{bmatrix}\mathbf{d}_1\\ \mathbf{d}_2\end{bmatrix} \tag{2.12}$$

Once $\mathbf{k}$ is determined for each member relative to its own local axis, it needs to be transformed to a global axis system. In other words, transformation is used to accomplish the following

1- To relate the edge forces and displacements to a set of global axes x', y' and z'.
2- To align the members according to the global axes since each member may be rotated and/or have offsets at each end.

Once necessary transformations are made, the overall system equation is assembled in the form

$$\mathbf{K}(Q)\mathbf{D} = \mathbf{P} \tag{2.13}$$

where **D** is the displacement amplitude vector and **K** is the global transcendental stiffness matrix which is a function of half-wavelength (λ) and the frequency or load factor (Q). **K** becomes real and symmetric in the following cases

1- All the plates are isotropic.

2- All the plates are orthotropic, i.e. $_{16} = D_{26} = 0$, and are not under shear loading, i.e. $N_S = 0$.

Otherwise **K** is complex and Hermitian.

In an eigenproblem the goal is to obtain the eigenvalues. This means that Eq (2.13) will take the form

$$\mathbf{K}(Q)\mathbf{D} = \mathbf{0} \tag{2.14}$$

To obtain eigenvalues the determinant of the stiffness matrix should usually become zero leading to

$$|\mathbf{K}(Q)| = \mathbf{0} \tag{2.15}$$

Equation (2.15) is a highly non-linear function of the eigenparameter (Q). In order to obtain Q's which satisfy Eq (2.15), the W-W algorithm is used.

The W-W algorithm calculates J, the number of eigenvalues, which lie between zero and any trial value of Q. In its general form the W–W algorithm can be stated as

$$J = J_0 + s\{\mathbf{K}\} \tag{2.16}$$

where s{**K**} is known as the sign count of **K**, and is equal to the number of negative leading diagonal elements of the upper triangular matrix $\mathbf{K}^{\Delta}$ obtained by applying conventional Gauss elimination, without pivoting, to the matrix **K**. J_0 is the value J would have if all the degrees of freedom corresponding to **K** were clamped. J_0 can be calculated as

$$J_0 = \sum_m J_m \tag{2.17}$$

where the summation is over all members m of the structure, and J_m is calculated for each member as the number of critical load factors or natural frequencies exceeded by the trial value, when the member ends are clamped.

It should be noted that when {**D**} is null the structure will degenerate into a set of individual plates, each having their longitudinal edges clamped. Thus J_0 simply becomes the sum of the eigenvalues below the trial value, for each of the constituent plates.

Eigenvectors are obtained by substituting the approximation of the eigenvalues Q_t into Eq (2.13) and giving an arbitrary force vector $\mathbf{P}_t$. Solving the Eq (2.13) for given values gives

$$\mathbf{D}_t = \mathbf{P}_t\mathbf{K}^{-1}(Q_t) \tag{2.18}$$

Once the displacement vector $\mathbf{D}_t$ is obtained, it is normalised to represent the mode shape of the structure corresponding to the eigenvalue Q_t.

2.2.3 Theory and formulation used in VICON analysis

In VICON analysis, deflections of infinitely long plate assemblies are assumed in terms of Fourier series as

$$\mathbf{D}_a = \sum_{m=-\infty}^{\infty} \mathbf{D}_m \exp(\frac{i\pi x}{\lambda_m}) \tag{2.19}$$

The nodal deflections $\mathbf{D}_a$ of the plate assemblies are stated as the coupling the modes $\mathbf{D}_m$ from a series of VIPASA analyses. The deflections are then used to obtain forces at each node as

$$\mathbf{P}_a = \sum_{m=-\infty}^{\infty} \mathbf{K}_m \mathbf{D}_m \exp(\frac{i\pi x}{\lambda_m}) \tag{2.20}$$

where $\mathbf{K}_m$ is the VIPASA stiffness matrix of Eq (2.13) for $\lambda = \lambda_m$ and

$$\lambda_m = \frac{l}{\xi + 2m}, (0 \le \xi \le 1; m = 0, \pm 1, \pm 2, ..., \pm q) \tag{2.21}$$

where the mode shapes of the plate structure repeats at intervals of $L = \frac{2l}{\xi}$.

In order to get an explicit term for the stiffness matrix, the total energy of a length L of plate assemblies is minimized, subject to constraints. It is worth noting that the L is in general different from the length of the plate assembly (l).

Minimising the total energy gives

$$L\mathbf{K}_m\mathbf{D}_m + \mathbf{E}^H{}_m\mathbf{P}_L = 0 \tag{2.22}$$

$$\sum_{m=-\infty}^{\infty}\mathbf{E}_m\mathbf{D}_m = \mathbf{0} \tag{2.23}$$

where m has all integer values for Eq (2.22); Eq (2.23) is the constraint equations; H denotes the Hermitian transpose of a matrix; $\mathbf{E}_m$ are the constraint matrices; and $\mathbf{P}_L$ is the vector of real Lagrangian multipliers (forces acting on the panel due to the constraints). Solutions for all the possible modes are obtained when Eq (2.22) and (2.23) are simultaneously satisfied, i.e. by solving

$$\begin{bmatrix} L\mathbf{K}_0 & & & & & & \mathbf{E}_{0H}{}^{\mathrm{T}} \\ & L\mathbf{K}_1 & & & & & \mathbf{E}_{1H} \\ & & L\mathbf{K}_{-1} & & & & \mathbf{E}_{-1H} \\ & & & L\mathbf{K}_2 & & & \mathbf{E}_{2H} \\ & & & & L\mathbf{K}_{-2} & & \mathbf{E}_{-2H} \\ & & & & & \ddots & \vdots \\ \mathbf{E}_0 & \mathbf{E}_1 & \mathbf{E}_{-1} & \mathbf{E}_2 & \mathbf{E}_{-2} & & 0 \end{bmatrix} \begin{bmatrix} \mathbf{D}_0 \\ \mathbf{D}_1 \\ \mathbf{D}_{-1} \\ \mathbf{D}_2 \\ \mathbf{D}_{-2} \\ \vdots \\ \mathbf{P}_L \end{bmatrix} = 0 \tag{2.24}$$

Terms of Eq (2.24) which have negative subscripts are the complex conjugates of those with the same subscript but with positive sign (for example $\mathbf{D}_{-1}$ is the complex conjugate of $\mathbf{D}_1$). The inclusion of terms with both positive and negative subscripts ($\mathbf{D}_m$ and $\mathbf{D}_{-m}$) is due to separate contributions of half-wavelength λ_m to the mode shape but having a 180° phase difference. The terms with a zero subscript are related to rigid body contributions ($\mathbf{D}_0$).

In VICON analysis, the W-W algorithm takes the form

$$J = \sum_{m} (J_{0m} + s\{\mathbf{K}_m\}) + s\{\mathbf{R}\} - r \tag{2.25}$$

where J_{0m} is the number of eigenvalues which would be exceeded for $\lambda = \lambda_m$ if all of the degrees of freedom nodes between the plates of the assembly were to be clamped. Here r is the number of constraints and so is also the order of the matrix **R**, which replaces the null matrix of Eq (2.24) when Gauss elimination is applied and is obtained after all rows except those in **R** have been pivotal. Matrix **R** takes the form

$$\mathbf{R} = \mathbf{R}_0 - \frac{1}{L} \sum_{-\infty}^{\infty} \mathbf{E}_m \mathbf{K}^{-1}{}_m \mathbf{E}^H{}_m \tag{2.26}$$

where $\mathbf{R}_0 = \mathbf{0}$ when the constraints are rigid [2.12-2.16].

Convergence on the buckling load factor is achieved by calculating J at appropriately chosen successive values of the load factor.

2.3 Multi-level sub-structuring

In structural analysis, computational efficiency for complex problems is often achieved by sub-structuring. In this way, a large and complex problem is divided into several smaller problems. In other words, instead of solving the complex structure directly, small problems which are sub-divisions of complex structure are solved. This procedure is called sub-structuring. This causes the matrix of equilibrium equations to be partitioned properly which would save time in iterative computing. Sub-structuring

approach in VICONOPT gives identical results to full analysis unlike sub-structuring in FE which introduces some approximations.

VICONOPT is capable of dealing with two types of sub-structures (Figure 2.6)

1- Doubly connected sub-structure.

2- Singly connected sub-structure.

A doubly connected sub-structure can consist of any number of nodes, but has the following restrictions.

a) The nodes must form a chain in the sense that each node is connected only to the immediately preceding and immediately following nodes.

b) Each node can be connected to the immediately preceding and following nodes by any number of different doubly connected sub-structures and individual plates, and any number of singly connected sub-structures can be attached to the node.

c) When a doubly connected sub-structure is incorporated in another sub-structure or in the final structure, the nodes at each end of the chain are connected to two nodes of the parent structure.

A singly connected sub-structure has the same rules, except that only the final node of the chain is attached to a node of another sub-structure or of the final structure (Figure 2.6).

In order to employ Eq (2.25) to include multi-level sub-structuring, it is noted that each sub-structure contributes to J_{om} only, i.e. sub-structures do not affect $s\{\mathbf{K}_m\}$, $s\{\mathbf{R}\}$ and r, where $\mathbf{K}_m$ is the stiffness matrix of the parent structure in Eq (2.25). As an example, if the modelling configuration of Figure 2.6b is considered, then $\mathbf{K}_m$ relates to degrees of freedom of nodes 1, 2, 3 and 4. The contribution of sub-structures to the

overall J_o is calculated as the J given by the prior application of Eq (2.25) to the sub-structure with its points of connection to the parent structure clamped. i.e.

$$J_0 = \sum_s \sum_{m'} J_{0m's} + \sum_{\bar{m}} J_{0\bar{m}} \tag{2.27}$$

where subscript s denotes summation over all sub-structures within the parent structure. Subscript m' denotes members belonging to subscript s, and subscript $\bar{m}$ denotes members belonging directly to the parent structure.

It needs to be mentioned that the procedure outlined above is applicable when there are no constraints within the sub-structures but the parent structure can have any number of point constraints. [2.15, 2.17]. Further development of the sub-structuring approach to include constraints within the sub-structures was performed by Powell et al [2.17], detail of which is given in Chapter 7.

Considering what is outlined above, it can be seen that VICONOPT presents a comprehensive suite of techniques for the analysis of plate assemblies. This coupled with the use of W-W algorithm makes VICONOPT very suitable for initial design and parametric study procedures as it is extremely efficient computationally compared to FEA (see Chapter 9).

2.4 References

[2.1] F.W. Williams, W.H. Wittrick, An automatic computational procedure for calculating natural frequencies of skeletal structures, *International Journal of Mechanical Sciences* ,**12**, 781–791 (1970).

[2.2] W.H. Wittrick, F.W. Williams, A general algorithm for computing natural frequencies of elastic structures, *Quarterly Journal of Mechanics and Applied Mathematics*, **24**, 263–284 (1971).

[2.3] W.H. Wittrick, F.W. Williams, An algorithm for computing critical buckling loads of elastic structures, *Journal of Structural Mechanics*, **1**,497–518 (1973).

[2.4] Wittrick WH, Williams FW. Buckling and vibration of anisotropic or isotropic plate assemblies under combined loadings. *International Journal of Mechanical Sciences*, **16**(4), 209-239 (1974).

[2.5] Stroud WJ, Greene WH, Anderson MS. Buckling loads of stiffened panels subjected to combined longitudinal compression and shear: results obtained with PASCO, EAL, and STAGS computer programs. *NASA Technical Paper* 2215 (1984).

[2.6] Williams FW, Anderson MS. Incorporation of Lagrangian multipliers into an algorithm for finding exact natural frequencies or critical buckling loads. *International Journal of Mechanical Sciences*, **25**(8), 579-584 (1983).

[2.7] Anderson MS, Williams FW, Wright CJ. Buckling and vibration of any prismatic assembly of shear and compression loaded anisotropic plates with an arbitrary supporting structure. *International Journal of Mechanical Sciences*, **25**(8), 585-596 (1983).

[2.8] Lam DH, Williams FW, Kennedy D. Critical buckling of stiffened panels with discrete point connections. *International Journal of Mechanical Sciences*, **39**(9), 991-1008 (1997).

[2.9] Williams FW, Kennedy D, Butler R, Anderson MS.VICONOPT: program for exact vibration and buckling analysis or design of prismatic plate assemblies. *AIAA Journal*, **29**(11), 1927-1928 (1991).

[2.10] Kennedy D, Fischer M, Featherston CA. Recent developments in exact strip analysis and optimum design of aerospace structures. Proceedings of the Institution of Mechanical Engineers, Part C: *Journal of Mechanical Engineering Science*, **221**(4), 399-413 (2007).

[2.11] Stephan W. Tsai, H.Thomas Hahn, Introduction to composite materials, *Technomic Pub Co*, 65-80 (1980).

[2.12] W.H. Wittrick, F.W. Williams, Buckling and vibration of anisotropic or isotropic plate assemblies under combined loadings, *International Journal of Mechanical Sciences*, **16**, 209–239 (1974).

[2.13] F.W. Williams, Natural frequencies of repetitive structures, *Quarterly Journal of Mechanics and Applied Mathematics,* **24**,285–310 (1971).

[2.14] W.J. Stroud, W. H. Greene and M.S. Anderson, Buckling loads of stiffened panels subjected to combined longitudinal compression and shear: results obtained with PASCO, EAL, and STAGS computer programs, *NASA Technical Paper 2215* (1984).

[2.15] D. H. Lam, F. W. Williams and D. Kennedy, Critical buckling of stiffened panels with discrete point connections, *Int J. Mech. Sci*,**39** , No. 9, 991 1009 (1997).

[2.16] M.S. Anderson, F.W. Williams and C.J. Wright, Buckling and vibration of any prismatic assembly of shear and compression loaded anisotropic plates with an arbitrary supporting structure, *International Journal of Mechanical Sciences*, **25**(8), 585-596 (1983).

[2.17] S. M. Powell, D. Kennedy and F. W. Williams, Efficient multi-level sub-structuring with constraints for buckling and vibration analysis of prismatic plate assemblies, *Int. J. Mech. Sci.***39**, No. 7, 795 805 (1997).

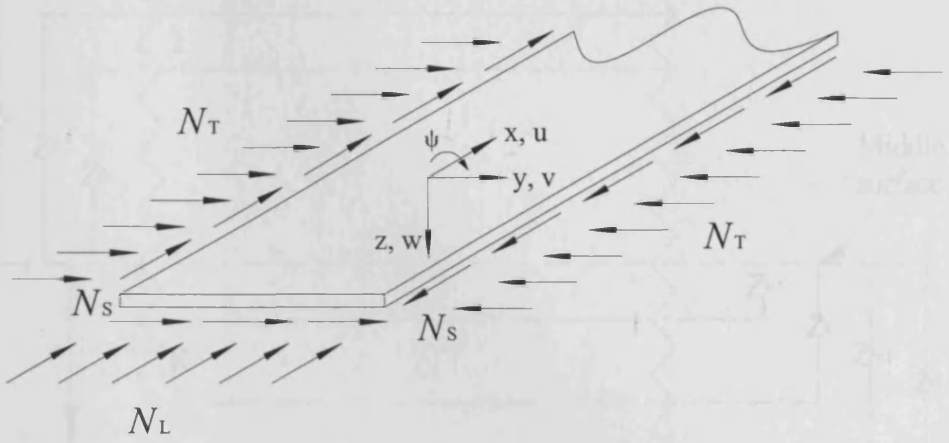

Figure 2.1: Force and axis system of a plate component.

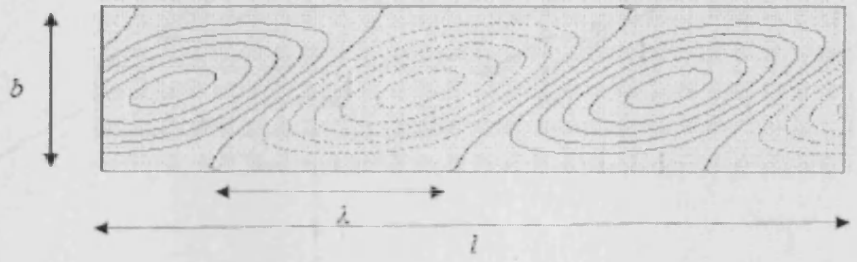

Figure 2.2: Buckling mode of a shear-loaded composite plate.

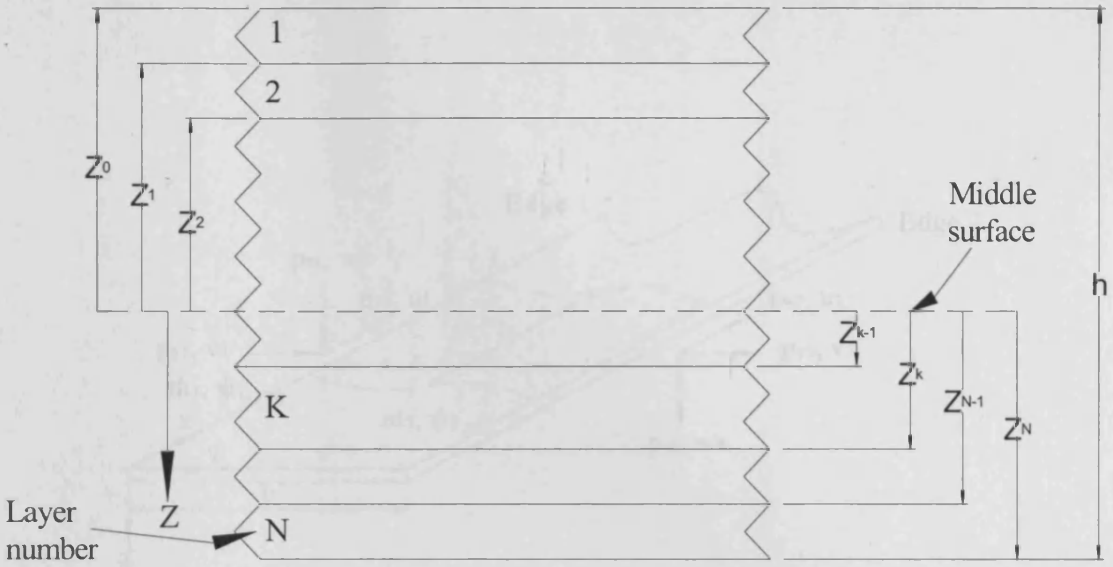

Figure 2.3: Geometry of an N-layer laminate.

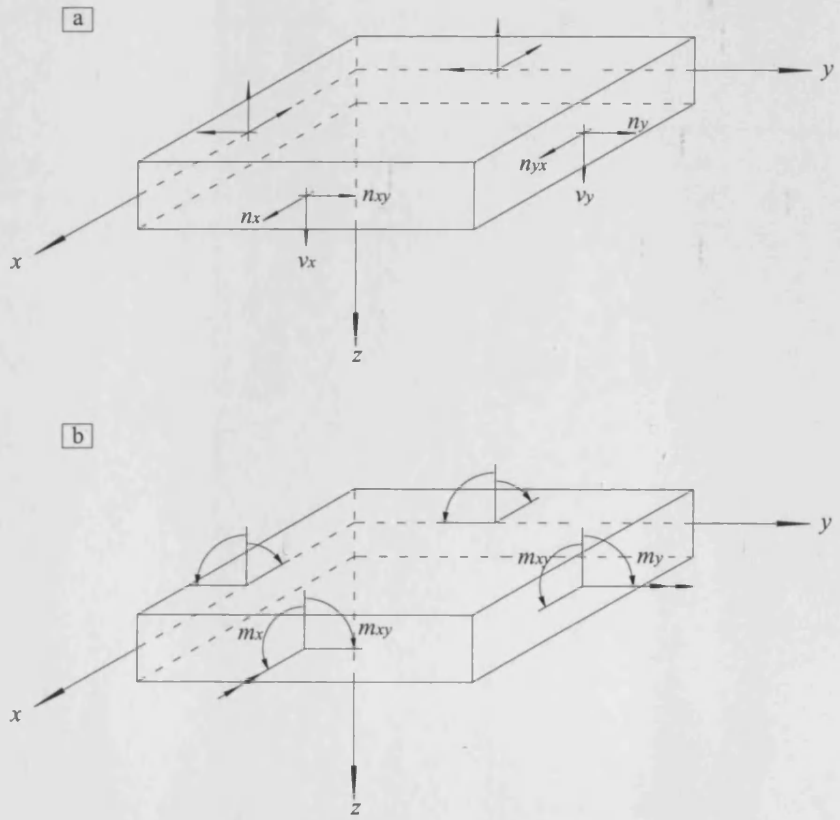

Figure 2.4: Forces and moments acting on an typical element of composite laminate.

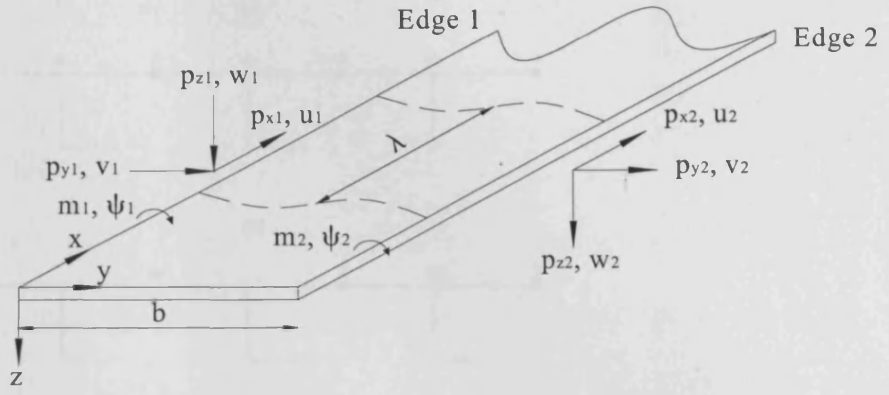

Figure 2.5: Perturbation edge forces and displacements of a component plate and its nodal lines, as shown dashed. All force and displacement amplitudes are to be multiplied by $\exp(i\pi x/\lambda)\cos 2\omega\pi t$.

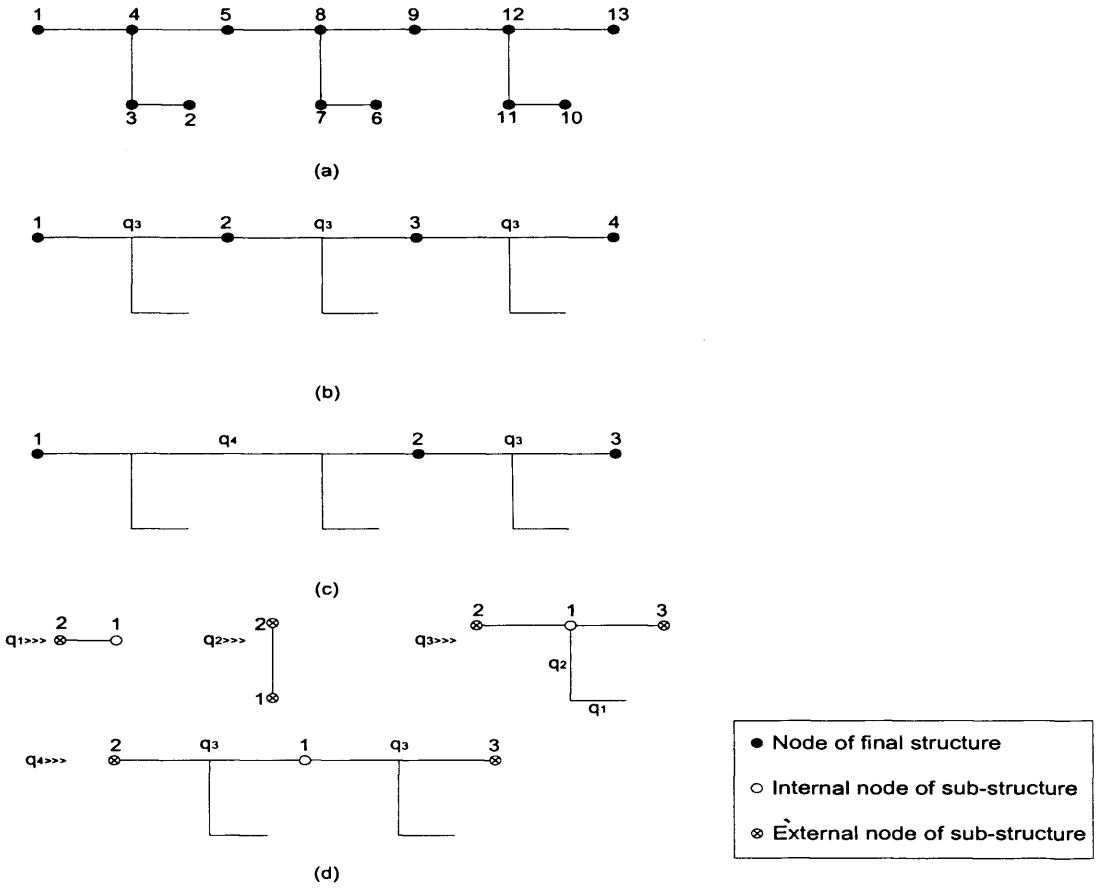

Figure 2.6: Modelling of a Z-stiffened panel using sub-structuring approach in VICONOPT, a) without using sub-structuring (parent structuring only), b) three-level sub-structuring, c) four-level sub-structuring, d) type of sub-structures used: q_1 is a singly connected sub-structure; q_2, q_3 and q_4 are doubly connected sub-structures.

CHAPTER 3

CRITICAL BUCKLING OF DELAMINATED COMPOSITE PLATES USING EXACT STIFNESS ANALYSIS

3.1 Introduction

As stated in Chapter 1, delamination is one of the most common sources of imperfections in composite plates. The presence of delaminations can bring about local buckling which may affect global buckling behaviour and cause overall degradation of the stiffness by a level which depends on the size, shape, in-plane and out-of-plane position of the delamination. This chapter outlines work carried out to investigate the use of VICONOPT to determine the global and local buckling behaviour of laminates containing through-the-length (strip) delaminations using the program VICONOPT. A parametric study is then undertaken to determine the effects of boundary conditions, width, widthwise location, depth and the number of delaminations are investigated. Transverse shear effects are taken into account. The results of such analyses are validated by ABAQUS 6.8 [3.1] and conclusions are drawn. The results described in this chapter have been presented as a conference paper [3.2] and form the basis of a further journal paper [3.3].

3.2 Through-the-length delamination model

References [3.4–3.6] considered single composite plates with through-the-width delaminations. In this chapter, delaminations are modelled as through-the-length, as illustrated in Figure 3.1, in order to satisfy the prismatic requirements of VICONOPT, namely that the geometry and loading are invariant in the longitudinal (x) direction.

The present work can therefore be compared with these earlier analyses [3.4–3.6] by supposing that the plate is rotated by $90°$. These assumptions mean that the problem could be solved using the existing capabilities of VICONOPT. Comparison is also made with the results of finite element analyses using ABAQUS 6.8.

The plate considered has length l, width B and thickness h. It is either simply supported or clamped on all four sides. Boundary conditions are satisfied exactly along edges $y = 0$ and $y = B$. The VICON analysis option of VICONOPT is employed to couple sinusoidal buckling responses, using Lagrangian multipliers to enforce the boundary conditions at intervals of $0.05B$ along the ends $x = 0$ and $x = l$. The delamination has variable width b, is at a variable depth below the top surface of the plate, and is either symmetrically located about the mid-width (as shown in Figure 3.1) or adjacent to the plate edge $y = 0$. The upper and lower portions of the delaminated region can deform independently, but their deflections and rotations must match at the edges of this region. The analysis therefore allows for both overall buckling of the plate and for local buckling of the delaminated region. However, issues of contact and penetration between the upper and lower portions are ignored, potentially giving conservative buckling predictions.

3.3 Numerical examples

Critical buckling behaviour is determined, assuming first order shear deformation theory [3.7], for a composite laminate of length $l = 100\,\text{mm}$, width $B = 100\,\text{mm}$ and thickness $h = 2\,\text{mm}$. The material has properties $E_1 = 130\,\text{kNmm}^{-2}$, $E_2 = 10\,\text{kNmm}^{-2}$, $G_{12} = 5\,\text{kNmm}^{-2}$, $\nu_{12} = 0.3$, and is laid up in 16 plies of thickness

0.125 mm in the sequence $[0/+45/-45/90/0/+45/-45/90]_S$. Through-the-length delaminations occur at various locations, and have varying width b.

VICONOPT results for single, mid-width delaminations, located at depths $h/2$, $h/4$ and $h/8$ are compared with finite element results obtained using ABAQUS, for the three cases of longitudinal, transverse and shear loading. Buckling analyses in ABAQUS consists of two steps. The first step is a general linear static analysis which provides a base state, i.e. the stiffness matrix and stresses for the next step of analysis. The second step is an eigenvalue analysis which provides results in terms of load factors (eigenvalues) and mode shapes (eigenvectors). The SC6R continuum shell elements of Figure 3.2a are used. These elements discretize an entire three-dimensional body and can be used both for linear analysis and also for complex nonlinear analyses involving contact, plasticity, and large deformations. Their thickness is determined from their element nodal geometry. Continuum shell elements have only displacement degrees of freedom at each node and from a modelling point of view look like three-dimensional continuum solids. SC6R elements are linear 6-node triangular in-plane general-purpose continuum shell wedge elements which have three displacement degrees of freedom at each node and use the reduced integration method. The boundary conditions and model mesh are shown in Figure 3.2(b).

Further VICONOPT results are presented in the non-dimensional form N/N_0, where N is the stress resultant (i.e. N_L, N_T or N_S) at critical buckling of the delaminated plate and N_0 is the corresponding value for the perfect, undelaminated plate (i.e for $b = 0$).

It is worth mentioning that for VICONOPT model, compatibility of strains for N_T and N_S and VICON static analysis for N_L are employed to determine the amount of load in each of the constituent plates of the plate assembly.

3.3.1 Example 3.1: single mid-width delamination

Initially the plate is assumed to be simply supported on all four edges and to contain a single through-the-length delamination, symmetrically located about the mid-width and at a depth $h/4$ below the top surface, i.e. between the 4th and 5th plies of the laminate. Figure 3.3 shows critical buckling results for the three load cases, as the width of the delamination increases from $b = 0$ (i.e. no delamination) to $b = B$ (i.e. delamination extending across the full width of the plate). These plots may be regarded as a datum for comparison with the subsequent results.

In VICONOPT, the three load cases for the perfect plate give critical buckling stresses of $N_L = 145.8\,\text{Nmm}^{-1}$, $N_T = 145.8\,\text{Nmm}^{-1}$ and $N_S = 405.6\,\text{Nmm}^{-1}$ respectively, which will be used as the values of N_0 for Examples 4–6. For comparison, ABAQUS gives critical buckling at $N_L = 139.7\,\text{Nmm}^{-1}$, $N_T = 139.7\,\text{Nmm}^{-1}$ and $N_S = 390.7\,\text{Nmm}^{-1}$. Figure 3.4(a) shows contour plots of the associated critical buckling modes. These have the expected appearance for buckling modes of a simply supported plate. Both ABAQUS and VICONOPT predict the same buckling behaviour.

Figure 3.3 shows that there is a negligible difference between the critical buckling loads obtained from finite element analysis and those from VICONOPT for longitudinal and transverse loadings (Maximum 4%). For all the load cases, providing the delamination width b is less than or equal to $0.2B$, the buckling modes remain similar to the global modes of Figure 3.4(a), with the upper and lower portions of the delaminated region deflecting together. As b is increased further, however the modes transform into local modes, of which contour plots are shown in Figure 3.4(b) for the case $b = 0.7B$. Here the deflections occur principally in the (thinner) upper portion of the delaminated region, with the (thicker) lower portion and the undelaminated regions

remaining essentially undeformed. It should be mentioned that since the contact effects in the delaminated region are ignored, the obtained mode shapes in which the thinner portion penetrates into the thicker portion are physically inadmissible. The limit $b = B$ corresponds to buckling of the upper portion of the delaminated region across the whole width of the plate, which occurs at a critical load much lower than that of the perfect plate. Each of the plots of Figure 3.3 may be interpreted qualitatively as the intersection of a horizontal line, corresponding to the global mode, with a decreasing parabolic curve, corresponding to the local mode (see Figure 3.5). Because VICONOPT assumes an infinitely long structure with periodically repeating simple supports, rather than a simply supported plate of finite length, its global buckling results are expected to be slightly higher than those of finite element analysis, as can be observed in Figure 3.3.

3.3.2 Examples 3.2–3.4: single mid-width delamination at varying depth

Example 3.2 is derived from Example 3.1 by moving the delamination to mid-way through the thickness, i.e. between the 8^{th} and 9^{th} plies of the laminate. Critical buckling results are shown in Figure 3.6. Here local modes involve the buckling of both the upper and lower portions of the delaminated region, which each have thickness $h/2$. Delamination causes much less degradation in buckling strength and the transition from global to local buckling is more gradual for all three load cases.

In contrast, Figure 3.7 and Figure 3.8 show that as the delamination is moved towards the top surface, so that the upper portion of the delaminated region comprises first two plies and then one ply to give Examples 3.3 and 3.4, respectively, only a very small delamination is required to trigger a rapid transition to local buckling and a catastrophic loss of buckling strength. These results are in agreement with those of Cappello and Tumino [3.6] and several other authors. For the case of delaminations

with depth of $h/8$, the sharp transitions for transverse and shear loading are accompanied by significant changes in the mode shape. For longitudinal loading, the transition is more gradual and there is less change in the shape of the critical buckling mode. When delaminations are located at the depth of $h/16$ there is an immediate sharp drop from global buckling to local buckling at the onset of delamination.

3.3.3 Example 3.5: double mid-width delamination

The original delamination at depth $h/4$ is next accompanied by one at depth $h/2$, i.e. combining the delaminations of Examples 3.1 and 3.2. Figure 3.9 shows that, apart from some small differences around the transition from global to local modes; the critical buckling behaviour is almost indistinguishable from that of Example 3.1, i.e. Figure 3.3. This is because the second delamination does not affect the global mode, where all three portions of the delaminated region deflect together. Local buckling of the upper portion, which has thickness $h/4$, is also unaffected by the second delamination, which produces central and lower portions of thickness $h/4$ and $h/2$, respectively. It is concluded that local buckling of a multiple delaminated region is likely to be dominated by local buckling of its thinnest portion providing it is near the surface.

3.3.4 Example 3.6: single edge delamination

In Example 3.6, the delamination of Example 3.1 is moved from its mid-width position to one edge of the plate, so that it runs from $y = 0$ to $y = b$. The limiting cases $b = 0$ and $b = B$ are clearly identical to those of Example 3.1. However the results in Figure 3.10 give an almost perfect match with Figure 3.3 for all delamination widths, showing that the behaviour of this laminate is not sensitive to the widthwise location of

the delamination. As in Example 3.1, if the width of the delamination is less than $0.2B$, global buckling behaviour is triggered. Again shear buckling is more sensitive to the effects of delamination than the other two loading types. This sensitivity is such that local behaviour occurs when the width of delamination is $0.1B$ or greater.

3.3.5 Example 3.7: effect of edge conditions

Finally, Example 3.7 repeats the analysis of Example 3.1, but with the edges of the plate fully clamped. With these edge conditions the perfect plate buckles at stress resultants of $N_{\mathrm{L}} = 369.2\,\mathrm{Nmm}^{-1}$, $N_{\mathrm{T}} = 369.2\,\mathrm{Nmm}^{-1}$ and $N_{\mathrm{S}} = 546.7\,\mathrm{Nmm}^{-1}$, which are used as the values of N_0 in Figure 3.11. The results again show a transition from the global mode to the local mode as the delamination width increases. For all types of loading the behaviour is qualitatively similar, with local buckling of the delaminated portion triggered at a width of $0.1B$. It seems that by using stiffer boundary conditions (i.e. switching from simple supports to clamped supports), the plate is degraded at a relatively low delamination width by a sudden transition to the local mode, despite the fact that overall load bearing capacity is increased significantly.

3.3.6 Residual buckling strength

In order to obtain the residual buckling strengths of the delaminated plates of Examples 3.1–3.3 following local buckling, the delamination is modelled as a cut-out (Figure 3.12) in VICONOPT and an initial buckling analysis is performed for such a structure.

It should be mentioned that in considering such models in VICONOPT, compressive load is distributed and applied to the mid-plane of each plate constituent

within the plate assembly. On the other hand, the operation of cutting out some portion of material from the plate assembly brings the mid-plane of the cut-out strip below the neutral axis of the plate assembly. This leads to combined longitudinal compressive load and bending moment within the cut-out region. In order to take this effect into account it is essential to consider the plate assembly under bending moment as well. This added moment works as an initial imperfection which is most suitable for post-buckling analysis.

Results for these analyses are given in Figure 3.13. As the delamination moves toward the top surface of the plate, the critical buckling load increases. Although the model gives generally conservative results due to removing material from the structure as a consequence of the cut-out (where there is actually likely to be some residual load carrying capability arising from the buckled portion), the results show the delaminated plate's capability to carry considerably higher loads after local buckling. It should be mentioned here that more reliable methods of obtaining residual buckling strength will be the focus of Chapters 8 and 9.

3.4 Conclusions and further work

Exact stiffness analysis has been used for the critical buckling analysis of composite plates with through-the-length delaminations. The usual discretisation of the finite element and finite strip methods is avoided by using analytical solutions of the member stiffness equations, the resulting transcendental eigenproblems being solved by the Wittrick-Williams algorithm. Accuracy is enhanced by coupling sinusoidal responses to give an infinitely long plate model.

Comparative results obtained from finite element analysis and VICONOPT for longitudinal, transverse and shear loading show good agreement. As delamination width is increased, there is a reduction in critical buckling load, accompanied by a transition from a global mode to a local mode of the delaminated portion. This transition tends to be sudden for shear loading, and more gradual for transverse and longitudinal loading. The local buckling load decreases as the delamination is moved towards the surface of the plate, becoming negligibly small for wide delaminations of only a few plies.

The effect of multiple through-the-length delaminations is dominated by local buckling of the thinnest portion of the delaminated region. The chosen example was insensitive to the widthwise location of the delamination, and gave qualitatively similar results for both simply supported and clamped edge conditions.

Following local buckling, the re-distribution of stress from the buckled to the unbuckled portions appears to give substantial post-buckling reserve of strength as indicated by the studies using cut-out model, and this will form the basis of further investigations in this thesis (Chapters 8 and 9). Meanwhile the buckling of plates with arbitrarily shaped embedded delaminations will be explored using multi-structure analysis [3.7] (Chapters 4 and 5), negative stiffness models (Chapter 6) and sub-structuring (Chapter 7).

Because the method incorporated in VICONOPT uses much smaller models than finite element analysis, solution times are very competitive. For example, the 33 critical buckling results plotted in Figure 3.3 were obtained in a total of 87 seconds and 693 seconds on a 2.4GHz PC for VICONOPT and finite element analysis, respectively. This approach is therefore suitable for parametric studies in the preliminary design of aerospace structures.

3.5 References

[3.1] ABAQUS theory manual. Version 6.8 Hibbitt. Pawtucket (RI): Karlsson and Sorensen, Inc.; (2008).

[3.2] M. Damghani, C. A. Featherston and D. Kennedy, Critical buckling of delaminated composite plates using exact stiffness analysis, *Proceedings of 9th International Conference on Computational Structures Technology* , CST.309 1-14 Athens, Greece ISBN 978-1-905088-23-2 (2008).

[3.3] M. Damghani, D. Kennedy and C. A. Featherston, Critical buckling of delaminated composite plates using exact stiffness analysis, submitted to *Computers and Structures*.

[3.4] S.-Y. Lee and D.-Y. Park, Buckling analysis of laminated composite plates containing delaminations using the enhanced assumed strain solid element, *International Journal of Solids and Structures*, **44** (2-4), 8006-8027 (2007).

[3.5] F. Cappello and D. Tumino, Numerical analysis of composite plates with multiple delaminations subjected to uniaxial buckling load, *Composite Science and Technology*, **66**(2), 264-272 (2006).

[3.6] Y. Pekbey and O. Sayman, A numerical and experimental investigation of critical buckling load of rectangular laminated composite plates with strip delamination, *Journal of Reinforced Plastics and Composites*, **25**(7), 685-697 (2006).

[3.7] M.S. Anderson and D. Kennedy, Transverse shear deformation in exact buckling and vibration analysis of composite plate assemblies, *AIAA Journal*, **31**(10), 1963-1965 (1993).

[3.8] D.H. Lam, F.W. Williams and D. Kennedy, Critical buckling of stiffened panels with discrete point connections, *International Journal of Mechanical Sciences*, **39**(9), 991-1008 (1997).

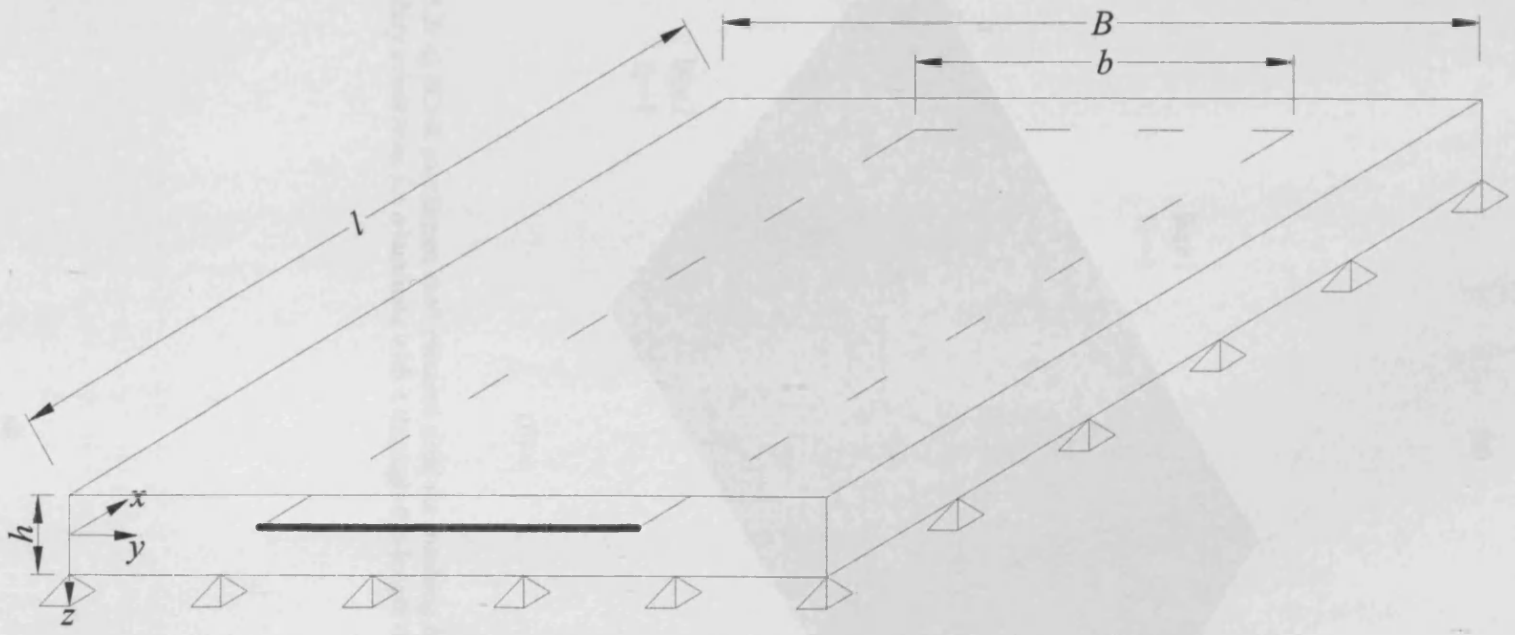

Figure 3.1: a) Composite plate of length l, width B and thickness h, having a through-the-length delamination of width b.

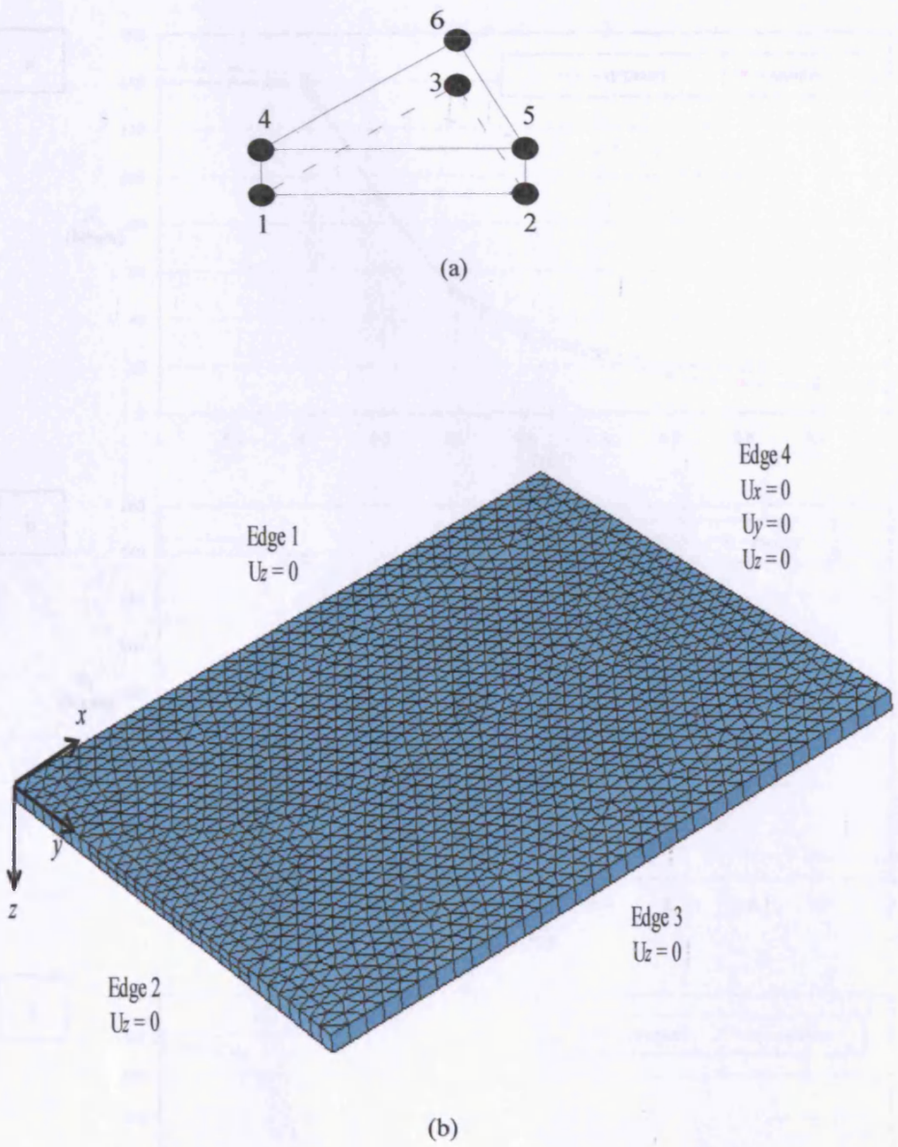

Figure 3.2: a) SC6R continuum shell element used for meshing the model, b) A typical mesh and boundary conditions for a laminate with a through-the-length delamination of width 50 mm.

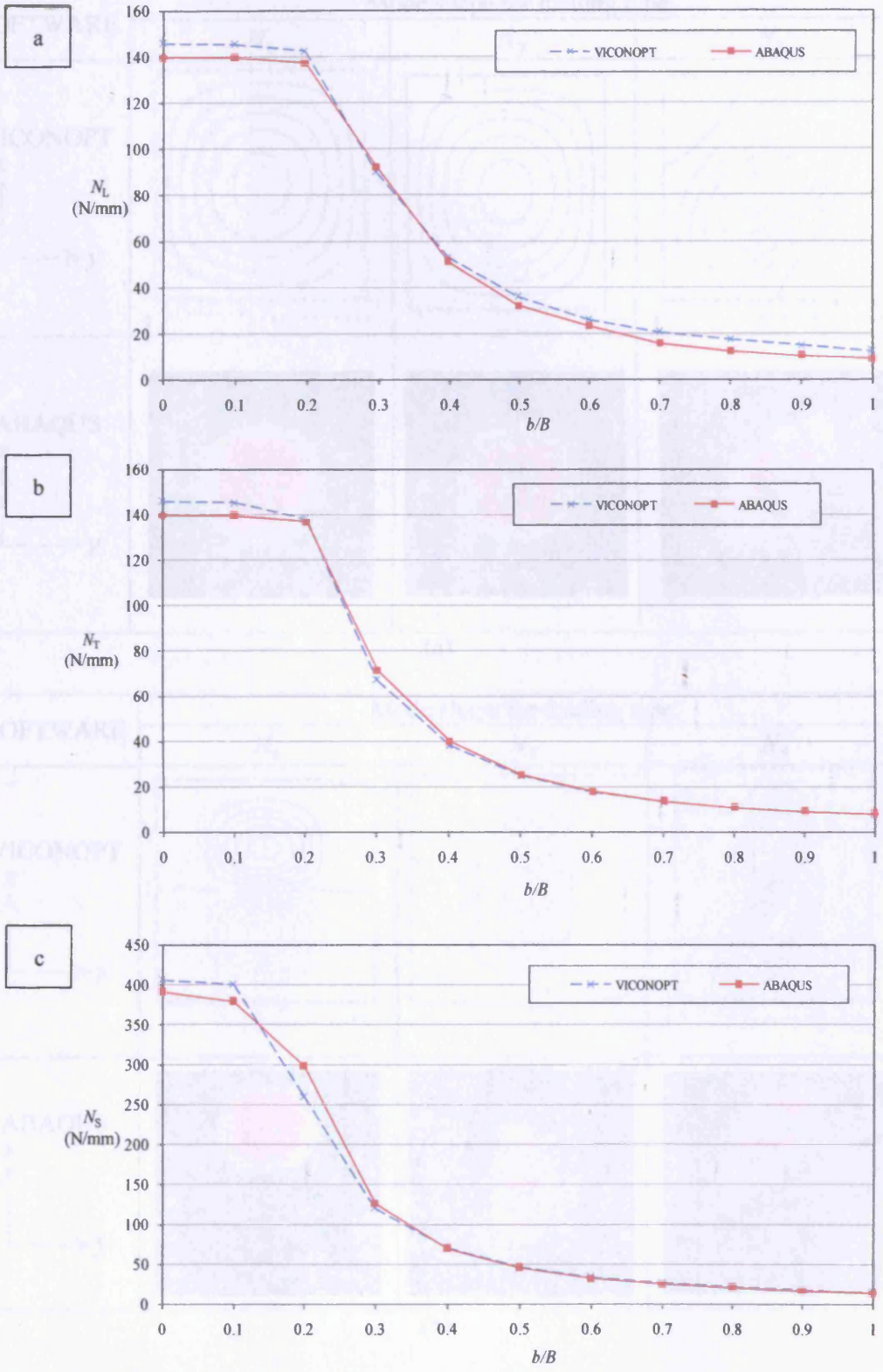

Figure 3.3: Plots of critical buckling stress resultants against delamination width b, for Example 3.1, a simply supported composite laminate of width B and thickness h, having a through-the-length delamination located at mid-width and a depth $h/4$ below the top surface (a) Longitudinal (b) Transverse (c) Shear loading.

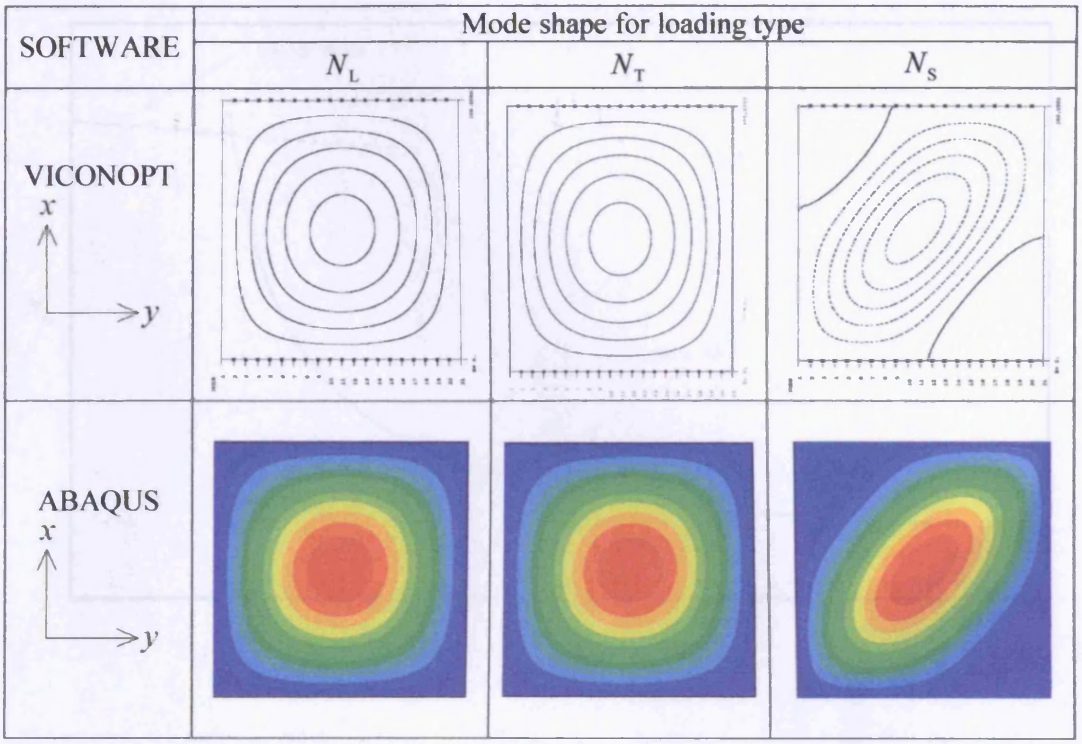

(a)

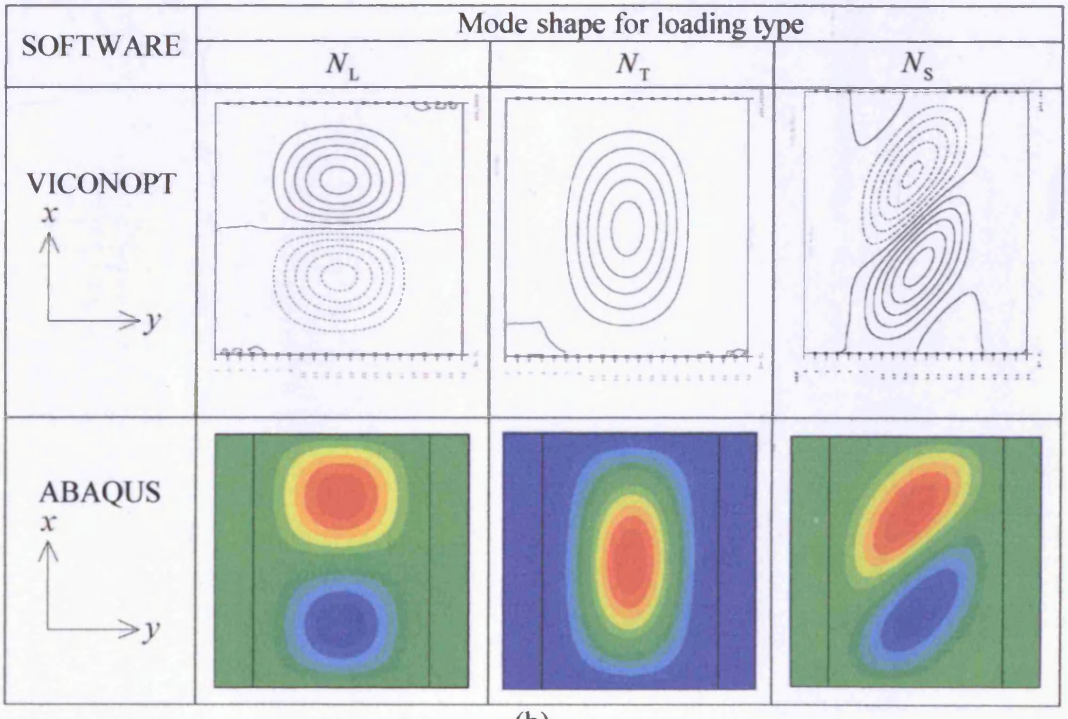

(b)

Figure 3.4: Critical buckling modes for Example 1, with longitudinal (N_L), transverse (N_T) and shear (N_S) loading. (a) $b = 0$. (b) $b = 0.7B$, with the edges of the delaminated region shown as dashed lines on the ABAQUS plots.

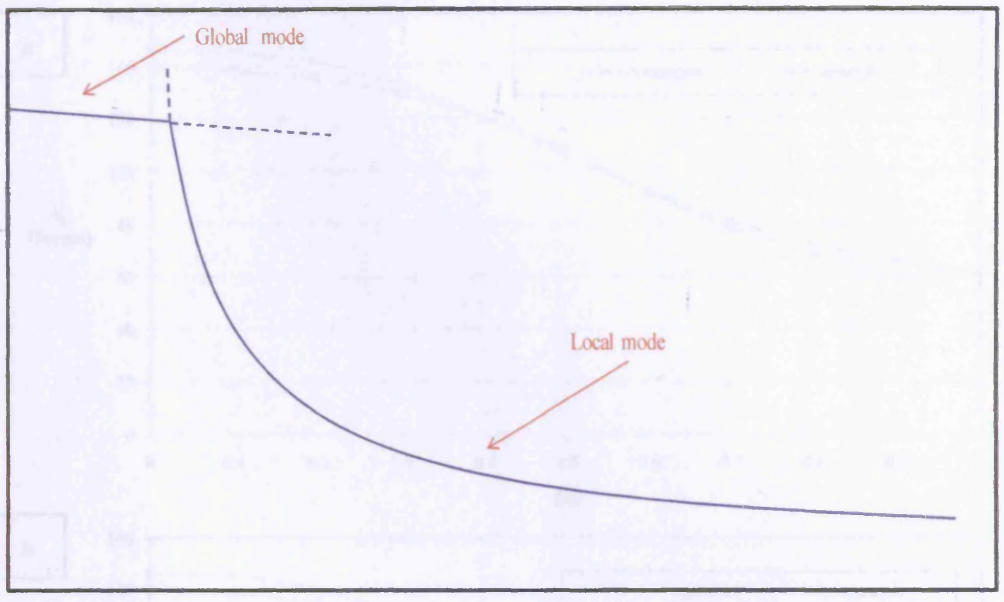

Figure 3.5: Qualitative representation of plots of Figure 3.3.

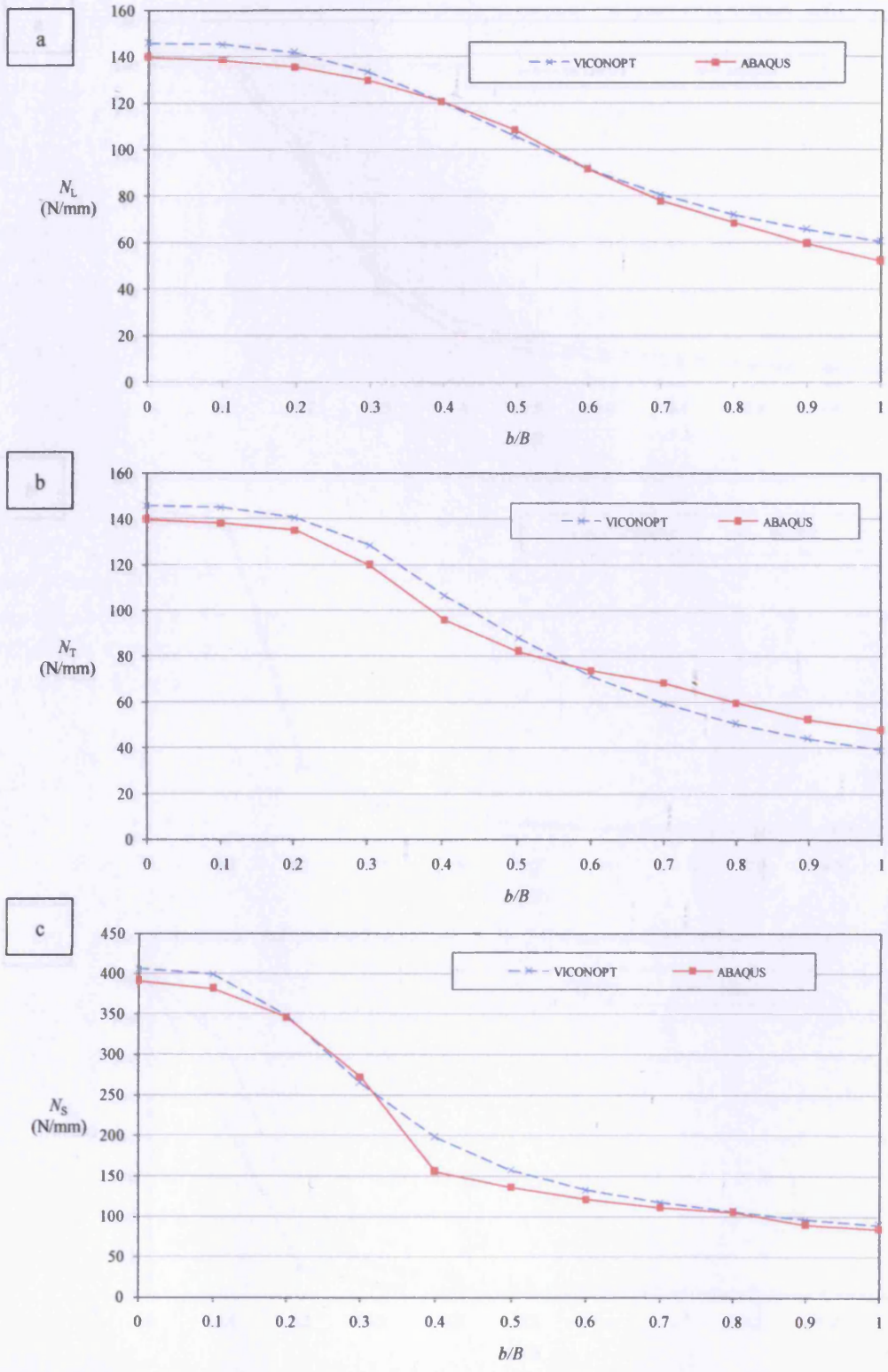

Figure 3.6: Plots of critical buckling stress resultants against delamination width b, for Example 3.2, a simply supported composite laminate of width B and thickness h, having a through-the-length delamination located at mid-width and a depth $h/2$ below the top surface (a) Longitudinal (b) Transverse (c) Shear loading.

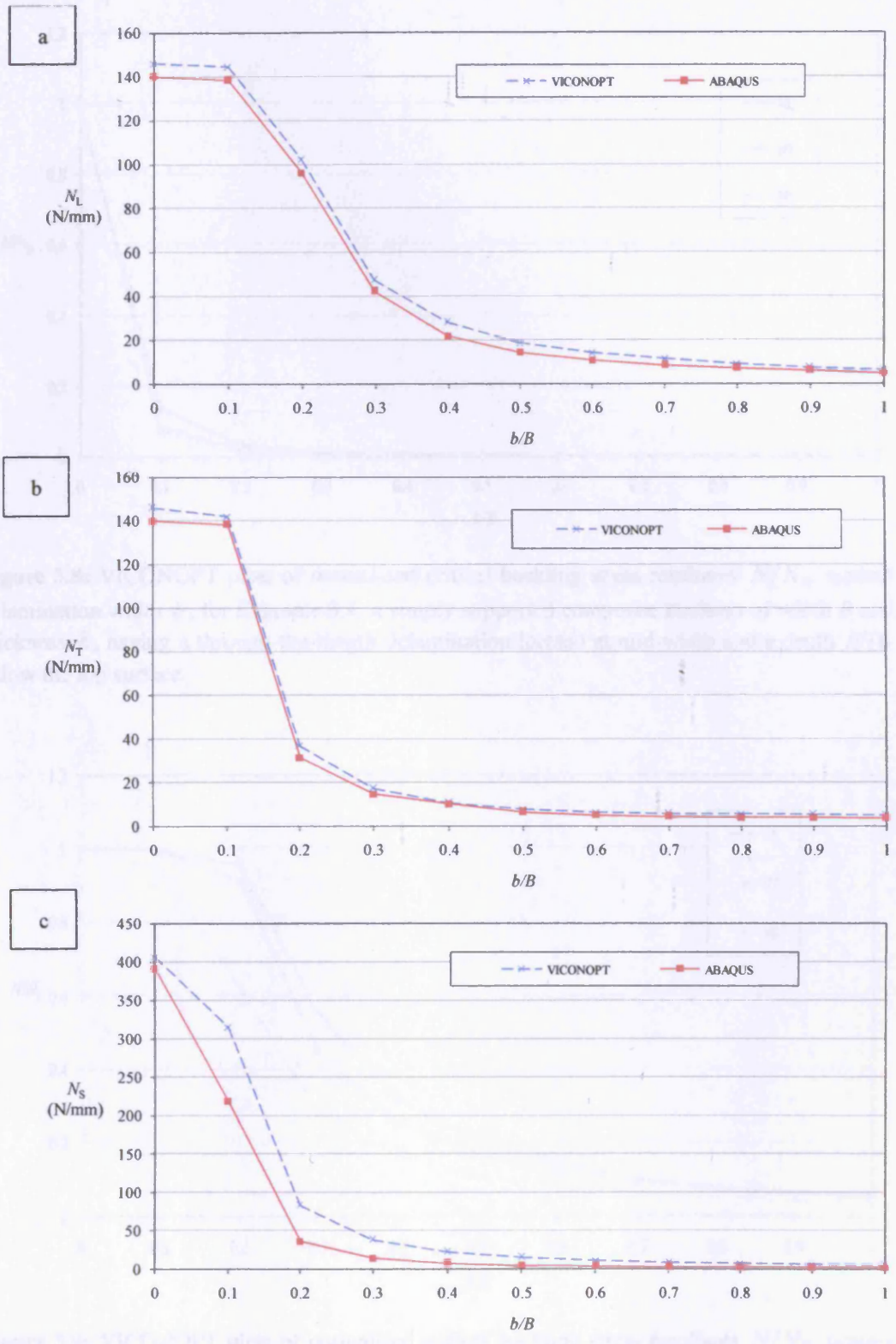

Fiugure 3.7: Plots of critical buckling stress resultants against delamination width b, for Example 3.3, a simply supported composite laminate of width B and thickness h, having a through-the-length delamination located at mid-width and a depth $h/8$ below the top surface (a) Longitudinal (b) transverse (c) Shear loading.

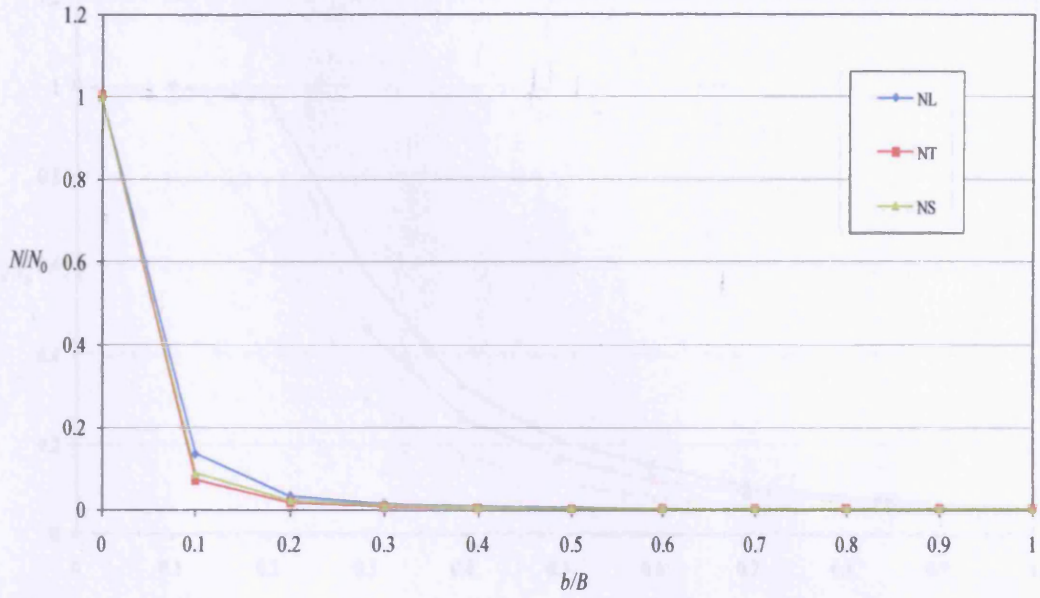

Figure 3.8: VICONOPT plots of normalised critical buckling stress resultants N/N_0 against delamination width b, for Example 3.4, a simply supported composite laminate of width B and thickness h, having a through-the-length delamination located at mid-width and a depth $h/16$ below the top surface.

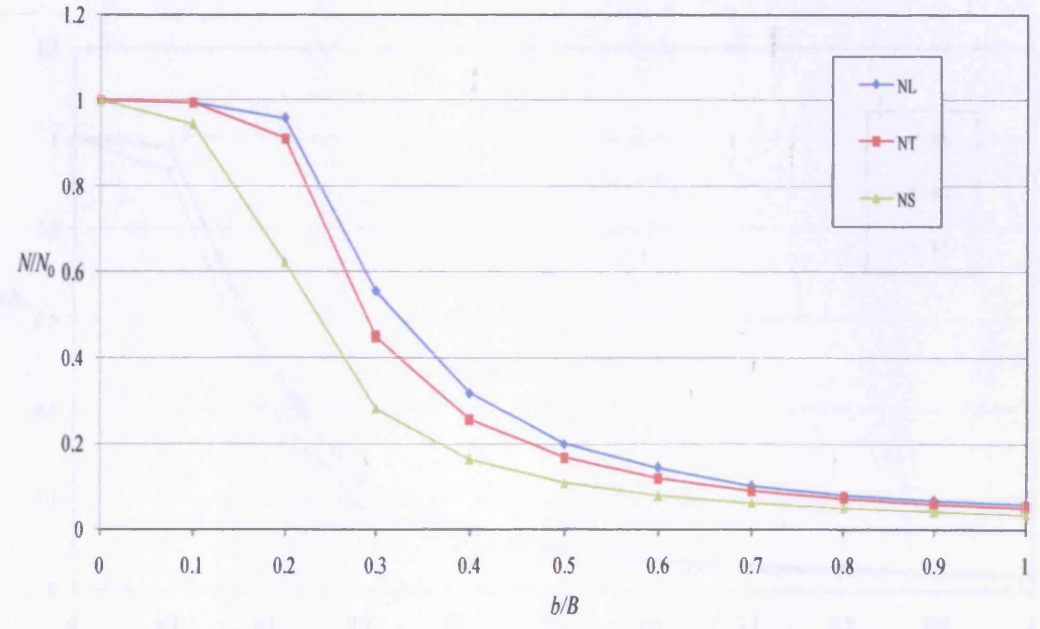

Figure 3.9: VICONOPT plots of normalised critical buckling stress resultants N/N_0 against delamination width b, for Example 3.5, a simply supported composite laminate of width B and thickness h, having through-the-length delaminations located at mid-width and depths $h/4$ and $h/2$ below the top surface.

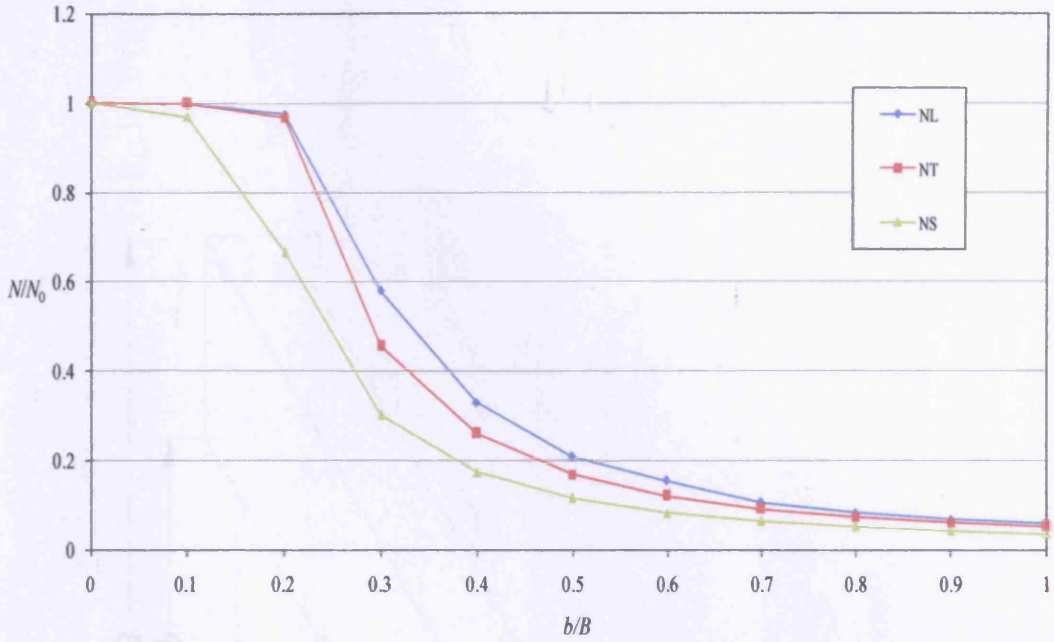

Figure 3.10: VICONOPT plots of normalised critical buckling stress resultants N/N_0 against delamination width b for Example 3.6, a simply supported composite laminate of width B and thickness h, having a through-the-length delamination located at one edge and a depth $h/4$ below the top surface.

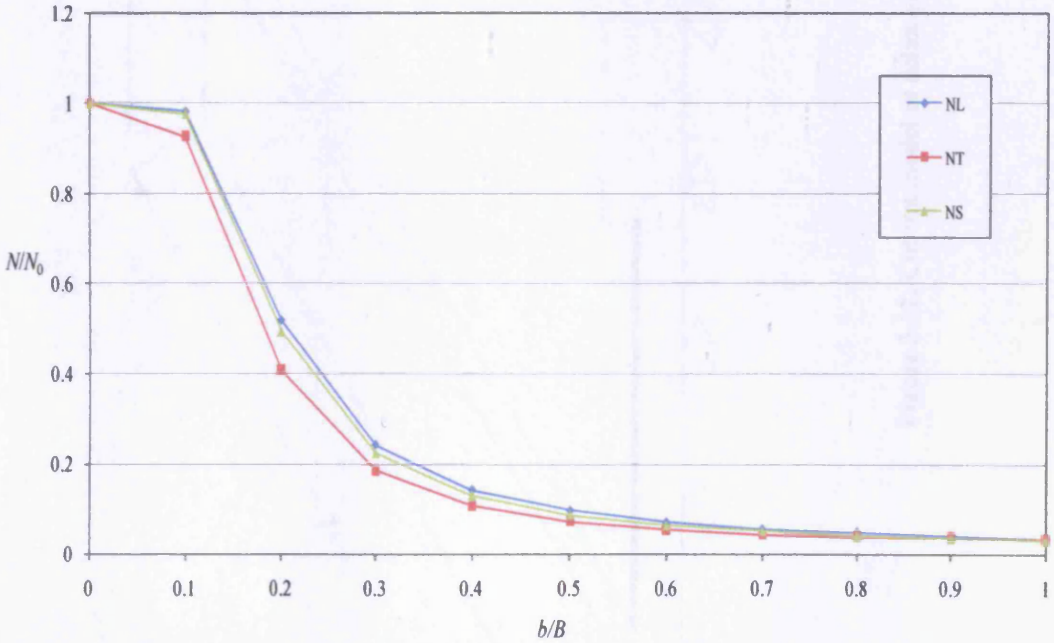

Figure 3.11: VICONOPT plots of normalised critical buckling stress resultants N/N_0 against delamination width b, for Example 3.7, a fully clamped composite laminate of width B and thickness h, having a through-the-length delamination located at mid-width and a depth $h/4$ below the top surface.

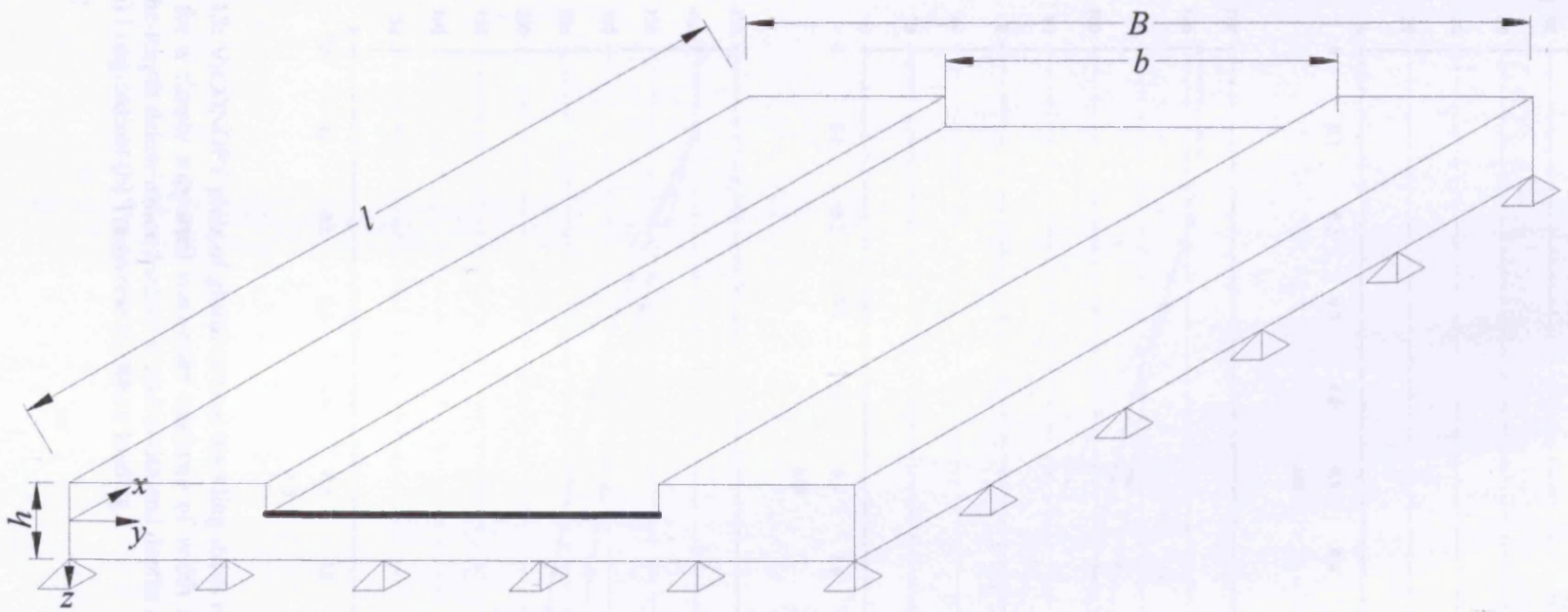

Figure 3.12: Cut-out model of delaminated composite plate.

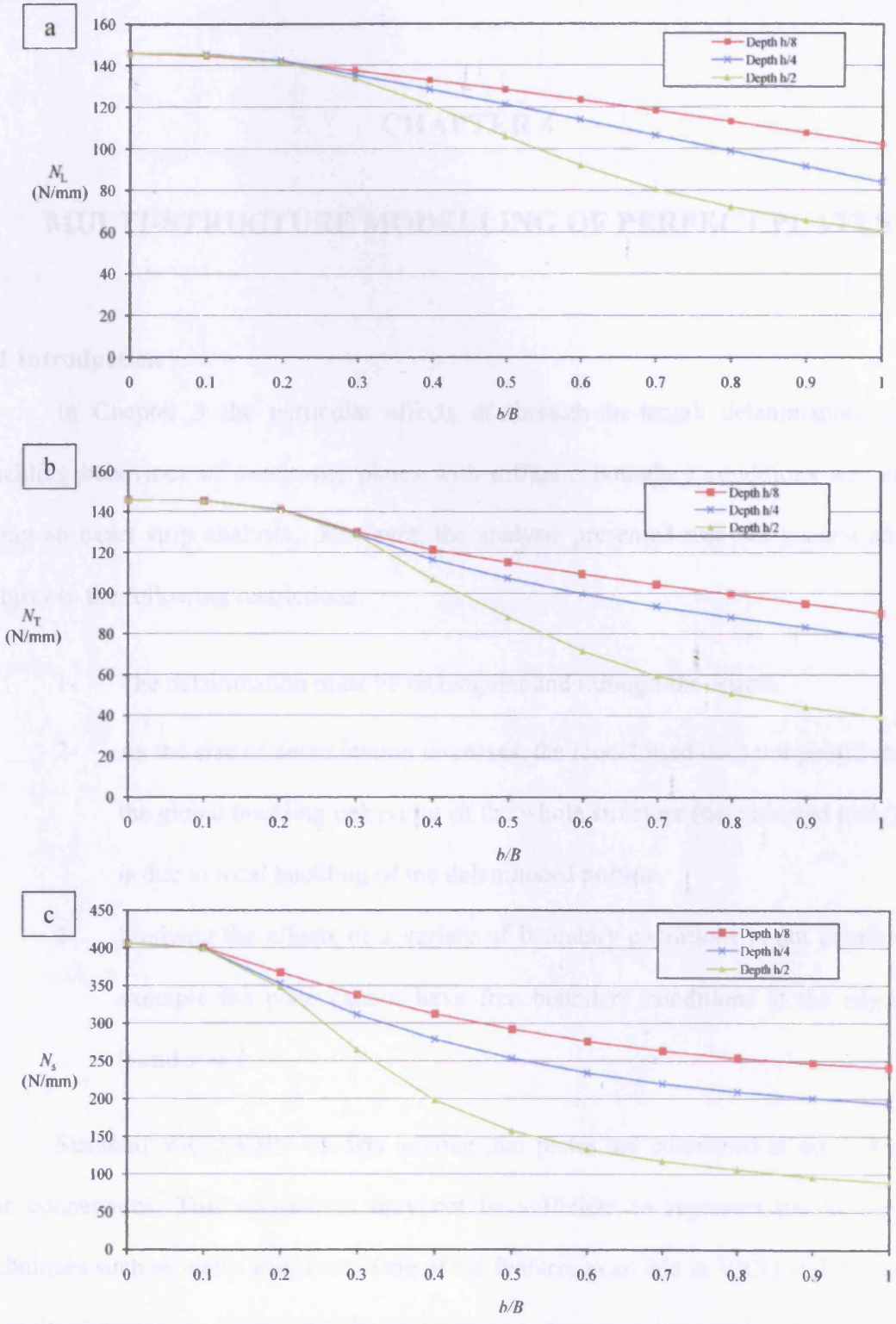

Figure 3.13: VICONOPT plots of global critical buckling stress resultants against delamination width b for a simply supported composite laminate of width B and thickness h, having a through-the-length delamination located at mid-width and depths $h/8$, $h/4$ and $h/2$ below the top surface (a) Longitudinal (b) Transverse (c) Shear loading.

CHAPTER 4

MULTI-STRUCTURE MODELLING OF PERFECT PLATES

4.1 Introduction

In Chapter 3 the particular effects of through-the-length delaminations on the buckling behaviour of composite plates with different boundary conditions was studied using an exact strip analysis. However, the analysis presented was not general and was subject to the following restrictions:

1- The delamination must be rectangular and through-the-length.

2- As the size of delamination increases, the model used does not permit study of the global buckling behaviour of the whole structure (delaminated plate). This is due to local buckling of the delaminated portion.

3- Studying the effects of a variety of boundary conditions is not possible. For example the plate cannot have free boundary conditions at the edges $x = 0$ and $x = l$.

Standard VICONOPT models assume that plates are connected at nodes by rigid line connections. This convention may not be sufficient to represent practical joining techniques such as welds and rivets. One of the features available in VICONOPT is the use of multi-structure modelling, which allows two or more structures to be attached to each other at specified 'common points', i.e. at discrete longitudinal locations in the x direction of the model. Using common points, one can constrain degrees of freedom of displacement

in the x (1), y (2) and z (3) directions and rotation about the x (4), y (5) and z (6) axes of each structure to be equal to each other. This feature was originally implemented into the program to account for welding and riveting of two structures to each other as discussed by Lam et al. [4.1].

In considering the buckling of delaminated composite plates it is desirable to obtain the global behaviour of a structure containing delaminations of any shape. However, the aim of this chapter is to use the multi-structure approach for a known perfect structure, in order to better understand the approach before using it on delaminated structures. In other words, a perfect composite plate (un-delaminated plate structure) is formed using two separate structures. These structures are attached to each other by common points to form the perfect plate. Critical buckling results from this approach are then compared to those obtained by conventional VICONOPT modelling (i.e. assembling constituent strips of the perfect structure rigidly along their longitudinal edges to form a single structure). The next chapter will focus on the modelling of composite plates containing a general rectangular delamination, again using VICONOPT.

4.2 Theory and Formulation

As stated in Chapter 2, Anderson et al. [4.2] formulated the eigenproblems of infinitely long plate assemblies for a VICON analysis in the matrix format of Eq (2.23). In a multi-structure approach the stiffness matrix and displacement vector for each structure (i) are formed using the following notation

$$\mathbf{K}^{*}{}_{i} = \begin{bmatrix} L\mathbf{K}_{0i} & & & & & & \boldsymbol{E}_{0i_H}{}^{T} \\ & L\mathbf{K}_{1i} & & & & & \boldsymbol{E}_{1i_H} \\ & & L\mathbf{K}_{-1i} & & & & \mathbf{E}_{-1i_H} \\ & & & L\mathbf{K}_{2i} & & & \boldsymbol{E}_{2i_H} \\ & & & & L\mathbf{K}_{-2i} & & \mathbf{E}_{-2i_H} \\ & & & & & \ddots & \vdots \\ \mathbf{E}_{0i} & \mathbf{E}_{1i} & \mathbf{E}_{-1i} & \mathbf{E}_{2i} & \mathbf{E}_{-2i} & & \mathbf{0} \end{bmatrix} \tag{4.1}$$

$$\mathbf{D}^{*}{}_{i} = \begin{bmatrix} \mathbf{D}_{0i} \\ \mathbf{D}_{1i} \\ \mathbf{D}_{-1i} \\ \mathbf{D}_{2i} \\ \mathbf{D}_{-2i} \\ \vdots \\ \mathbf{P}_{Li} \end{bmatrix} \tag{4.2}$$

Here, $\mathbf{K}_{mi}$ is the VIPASA stiffness matrix for structure i for half-wavelength $\lambda = \lambda_m$, and $\mathbf{D}_{mi}$ is the corresponding displacement vector. The $\mathbf{E}_{mi}$ matrices define constraints (e.g. point supports) applied solely to structure i, as described in Chapter 2. The $\mathbf{P}_{Li}$ are the associated vectors of Lagrangian multipliers. The structures are then coupled together to give a stiffness equation of the following form [4.3]

$$\begin{bmatrix} \mathbf{K}^{*}{}_{1} & \mathbf{0} & \mathbf{0} & \cdots & & \mathbf{E}^{*}{}_{1}{}^{H} \\ & \mathbf{K}^{*}{}_{2} & \mathbf{0} & & & \mathbf{E}^{*}{}_{2}{}^{H} \\ & & \mathbf{K}^{*}{}_{3} & & & \mathbf{E}^{*}{}_{3}{}^{H} \\ \vdots & & & \ddots & & \vdots \\ & & & & \mathbf{K}^{*}{}_{n} & \mathbf{E}^{*}{}_{n}{}^{H} \\ \mathbf{E}^{*}{}_{1} & \mathbf{E}^{*}{}_{2} & \mathbf{E}^{*}{}_{3} & \cdots & \mathbf{E}^{*}{}_{n} & -\epsilon\mathbf{I} \end{bmatrix} \begin{bmatrix} \mathbf{D}^{*}{}_{1} \\ \mathbf{D}^{*}{}_{2} \\ \mathbf{D}^{*}{}_{3} \\ \vdots \\ \mathbf{D}^{*}{}_{i} \\ \mathbf{P}^{*}{}_{L} \end{bmatrix} = \begin{bmatrix} \mathbf{0} \\ \mathbf{0} \\ \mathbf{0} \\ \vdots \\ \mathbf{0} \\ \mathbf{0} \end{bmatrix} \tag{4.3}$$

where the desired degrees of freedom of structures 1, 2, 3…n are coupled at locations along their length and across their width. In Eq (4.3), the $\mathbf{E}^{*}{}_{i}$ matrices define the common point constraints, $\mathbf{E}^{*}{}_{i}{}^{H}$ are their Hermitian transposes, and $\mathbf{P}^{*}{}_{L}$ is the associated vector of

Lagrangian multipliers. For more information regarding the use of above notation and matrices, the reader is referred to Chapter 2.

4.3 Material properties

The plate examined is a composite square plate with length $l = 150$ mm and width $B = 150$ mm. This is constructed from material with properties $E_1 = 128\,\text{kNmm}^{-2}$, $E_2 = 10.3\,\text{kNmm}^{-2}$, $G_{12} = 6\,\text{kNmm}^{-2}$, $\nu_{12} = 0.3$ and is laid up in 16 plies of thickness $t = 0.25\,\text{mm}$ in the symmetric sequence $(+45, 0, -45, 90, 90, -45, 0, +45)_S$ making a plate of thickness $h = 4$ mm. The plate is clamped on all four edges as shown in Figure 4.1a.

4.4 Methodology

In order to model a delaminated composite plate using common points, it is first divided into two separate structures. Structure 1 is a thin plate which includes the delaminated portion and which runs the length of the specimen. Structure 2 is the whole composite plate minus the first structure. The two structures are connected using common points at locations defined by the user. In order to verify the model and the use of common points in this application, a test analysis is conducted on a perfect plate with geometry as detailed in Figure 4.1, using two different model configurations:

1- A structure without delamination or defect, which hereafter is regarded as a perfect structure, as shown in Figure 4.1a.

2- A structure formed by superimposing and connecting two separate structures with common points with different spacings d' (as shown by cross marks in Figure 4.1b).

The two configurations above represent similar structures. In other words configuration 2 is an alternative approach to model configuration 1, and therefore it is expected that they should both exhibit similar behaviour in terms of the value of critical buckling load.

The modelling procedure for the first configuration is a fairly simple process and the node numbering and numbers of strips used to model it are shown in Figure 4.2. It is worth mentioning that the $u = 0$ constraint in Figure 4.1 is applied at the initiation of the buckling and therefore allows for compressive deformation of the plate before buckling. The reason for discretising the model of Figure 4.2 to more than one strip is to apply the clamped end conditions at $x = 0$ and $x = l$ for each node, i.e. nodes 1, 2 ... 7. Here 6 strips are defined to impose the boundary conditions at intervals of $B/6$. It is worth mentioning that decreasing the interval from $B/6$ to $B/12$ or even smaller is possible but at the expense of increased time of analysis without changing the results significantly. For example using $B/6$ and $B/12$ give critical buckling loads of 197.45 Nmm^{-1} and 197.47 Nmm^{-1}, respectively. The simulation of the perfect plate using the second configuration requires the introduction of Structures 1 and 2 which are connected along their entire length by common points. Structure 1 in Figure 4.1b has 4 plies of sequence $(+45, 0, -45, 90)$ and is 30 mm wide. Structure 2 is formed by defining 2 different plates, i.e. plate 1 and plate 2, which are then assembled and attached to Structure 1 via common points. As can be seen from Figure 4.3, plate 2 in Structure 2 (between nodes 4 and 6) has a negative z

offset whilst Structure 1 (between nodes 1 and 3) has a positive z offset, as measured from the reference surface of the plate to the nodes.

It should be noted that each line connecting successive nodes in Figures 4.2 and 4.3 represents a finite strip of length l and width equal to the distance between the two successive nodes.

In analyzing the two models, the VICON analysis option of VICONOPT is employed to couple sinusoidal buckling responses, using Lagrangian multipliers to enforce the boundary conditions at intervals of $(B-b)/6$ and $b/2$ along the ends $x=0$ and $x=l$ for plates 1 and 2 in configuration 2, respectively. It is clear that Structure 1 will inherit the boundary conditions of plate 2 of Structure 2 with similar intervals.

4.5 Results and discussion

Initial results from the buckling analysis of the plate examined using the 1996 release of VICONOPT gave much lower buckling loads for the perfect plate using the multi-structure approach (configuration 2). For the infinitely long model of VICONOPT each bay (e.g. the structure in the interval $0 \leq x \leq l$) is isolated from the next by the clamped end conditions, so the same buckling load and mode shape should have been calculated for each value of ξ. After examining the outputs for these analyses, it was noticed that the program did not give the same buckling load for all values of ξ. It was for example found that the result corresponding to $\xi = 0$ was about 20% below the results obtained with other values of ξ (including $\xi = 0.1$ and $\xi = 0.05$). An investigation found that this release of VICONOPT and all later versions had a coding error which meant point

constraints (including both regular *point supports* and *common point* attachments) applied to degrees of freedom 5 and 6 (i.e. dw/dx and dv/dx) were not set up correctly when $\xi = 0$. This caused incorrect results to be generated for problems with clamped end conditions with eigenvalues and modes being determined incorrectly, even for single structure problems, due to rotational supports (degree of freedom 5) not being applied properly. Because of the symmetry of this pattern, the critical modes should be symmetric; however although these were being identified correctly, incorrect anti-symmetric modes appeared to have smaller buckling loads and therefore the results were misleading. The code of the program was therefore modified and improved to give the correct results for a composite plate with fixed end conditions. The results found in the reminder of this chapter were calculated using the corrected version of VICONOPT.

Buckling analyses for various common point spacings (d') were carried out for both configurations of the perfect plate. The results of these analyses are shown in Figures 4.4 to 4.7.

Figure 4.4 shows the longitudinal critical buckling loads for perfect plates modelled using configurations 1 and 2. The critical buckling load determined using configuration 1 is $N_L = 197.45$ Nmm^{-1} whilst for configuration 2 the critical load varies depending on the common point spacing. It is clearly illustrated that closer common point spacing gives a higher load factor, with this factor converging toward the value for configuration 1 only as the spacing moves toward zero, which is clearly impractical for modelling.

Figure 4.5 demonstrates the time taken to complete the analysis for different common point spacings on a 2.4GHz PC. As shown, as the distance between common

points decreases the time taken increases dramatically. This is due to the increasing number of constraints required to attach the two structures of configuration 2. In addition to this factor, the use of more constraints means that more half-wavelengths λ need to be used (in this study 40 were used) in order to prevent the matrix of Eq (4.3) becoming singular. This leads to a larger and more populated stiffness matrix which requires more time to analyse. The relationship between reduced spacing and analysis time is in proportion to the cube of the number of constraints, i.e. r^3. The solution time becomes excessive for spacing $d' < 10$ mm.

Figure 4.6 shows the critical buckling mode shape for the plate achieved using configuration 1. It is clearly seen that the mode shape has one half-wavelength and is a global mode. Figure 4.7 compares mode shapes with those obtained using configuration 2, showing a variety of mode shapes depending on the common point spacing. Based on Figure 4.7, it can be seen that common point spacings of 7.5 mm and 10 mm give a global buckling mode for configuration 2 which is close to the behaviour of the perfect plate, while common point spacings of 15 mm, 25 mm and 50 mm lead to Structure 1 to buckling locally whilst Structure 2 remains undeformed. This implies that using greater spacing between common points allows buckling between these points due to insufficient constraint. The number of half-wavelengths occurring during local buckling of configuration 2 is l/d' which is 10, 6 and 3 for $d' = 15$ mm, $d' = 25$ mm and $d' = 50$ mm, respectively. This is simply because the portion of Structure 1 which lies between two successive common points acts as a plate of length d' with almost simply supported boundary conditions. This implies that Structure 1 has an approximately sinusoidal mode shape with one half-wavelength between two successive common points. Therefore the

number of half-wavelengths will be equal to the number of such portions in Structure 1 which is l/d'.

4.6 Conclusions

Exact stiffness analysis has been used for the critical buckling analysis of a clamped composite plate modelled using two different configurations, one of which involved a multi-structural approach in which two structures were joined using common points. The aim of this analysis was to determine the accuracy of such an approach prior to using it to model delamination.

The study initially identified programming errors in the 1996 release and later versions of VICONOPT. These errors were dealt with and rectified. The resulting analyses demonstrated that a relatively small common point spacing is required to obtain accurate results.

It is also observed that the smaller the spacing between common points, the greater the number of constraints in the model leading to increased times of analysis as expected. This increase is substantial, leading to excessive computational cost in obtaining solutions with reasonable accuracy.

The buckling mode varies between a global and a local mode for the same analysis depending on the distance between common points. Local buckling of the plate in the interval between two successive common points reduces the buckling load compared to that of perfect structure. The common point spacing must therefore be small enough to prevent local buckling, so as to obtain accurate global buckling results.

Considering the results obtained thus far, the study indicates that the use of common points is prohibitively expensive where a large number of constraints are required. This method could however be advantageous if only a few constraints need to be used. In order to examine whether this is possible, the next chapter studies the possibility of using the multi-structure approach for modelling of an embedded delamination.

4.7 References

[4.1] D.H. Lam, F.W. Williams and D. Kennedy, Critical buckling of stiffened panels with discrete point connections. *International Journal of Mechanical Sciences*, **39**(9), 991-1008 (1997).

[4.2] M.S. Anderson, F.W. Williams and C.J. Wright, Buckling and vibration of any prismatic assembly of shear and compression loaded anisotropic plates with an arbitrary supporting structure, *int. J. Mech. Sci*, **25** (8), 585-596 (1983).

[4.3] F.W. Williams and M.S. Anderson, Incorporation of Lagrangian multipliers into an algorithm for finding exact natural frequencies or critical buckling loads, *int. J. Mech. Sci*, **25** (8), 579-584 (1983).

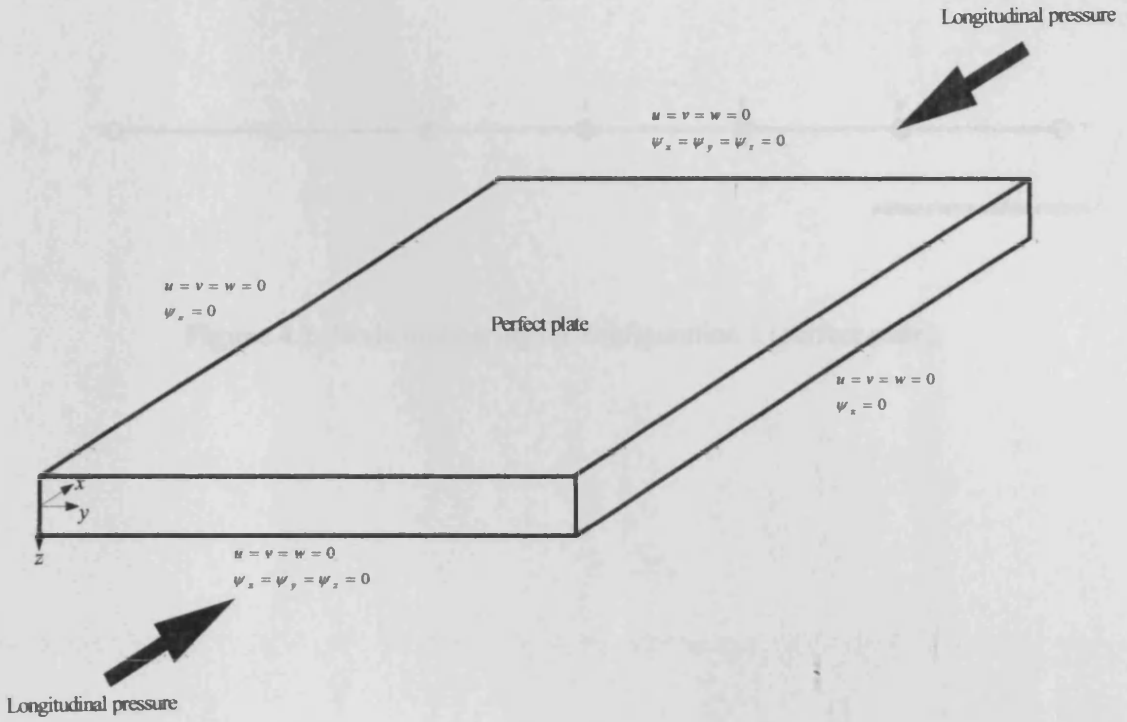

(a)

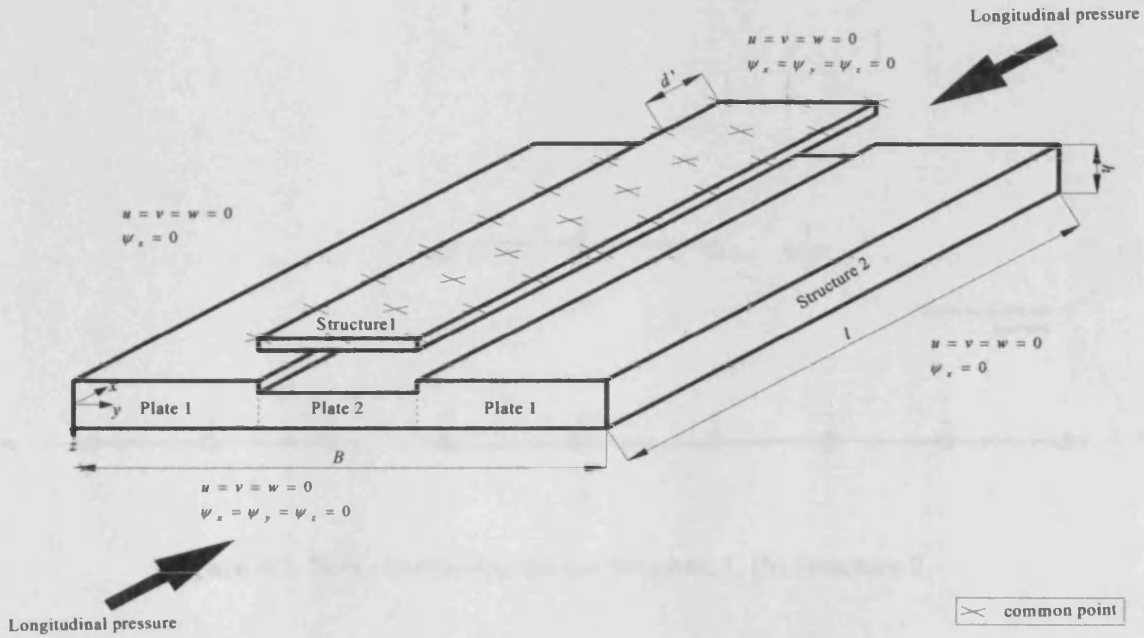

(b)

Figure 4.1: Modelling a perfect plate by (a) Configuration 1, (b) Configuration 2, with associated boundary conditions and loading.

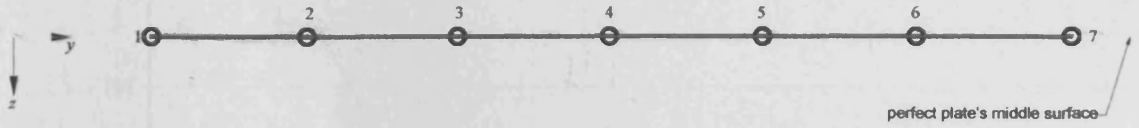

Figure 4.2: Node numbering for configuration 1 (perfect plate).

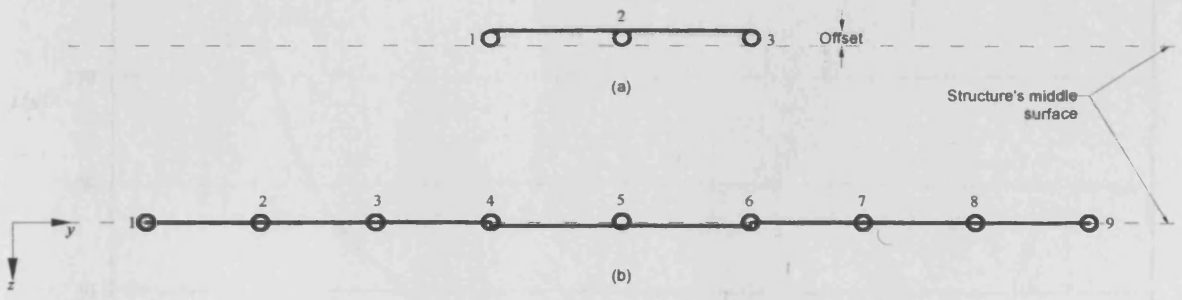

Figure 4.3: Node numbering for (a) Structure 1, (b) Structure 2.

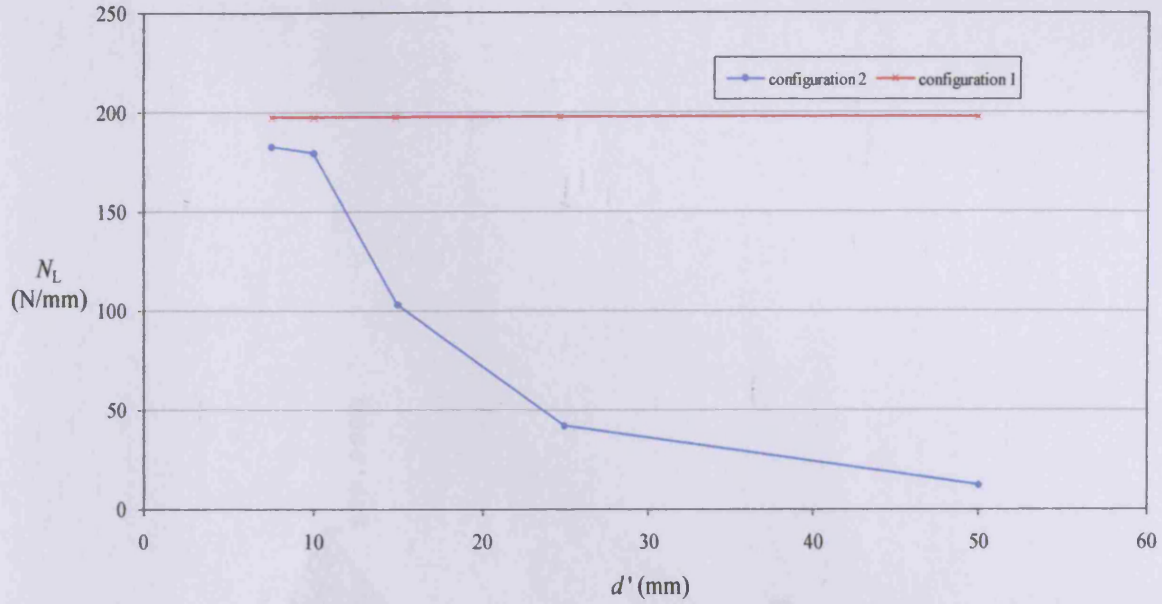

Figure 4.4: Plots of buckling load factor N_L against common point spacing d' for configurations 1 and 2.

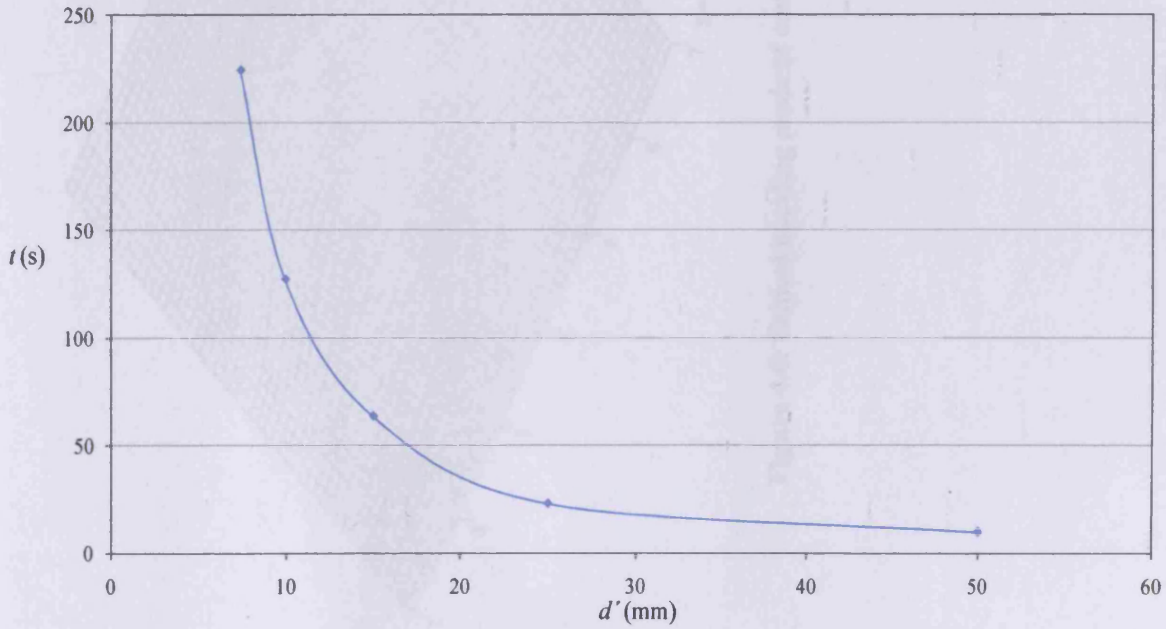

Figure 4.5: Plot of solution time against common point spacing d'.

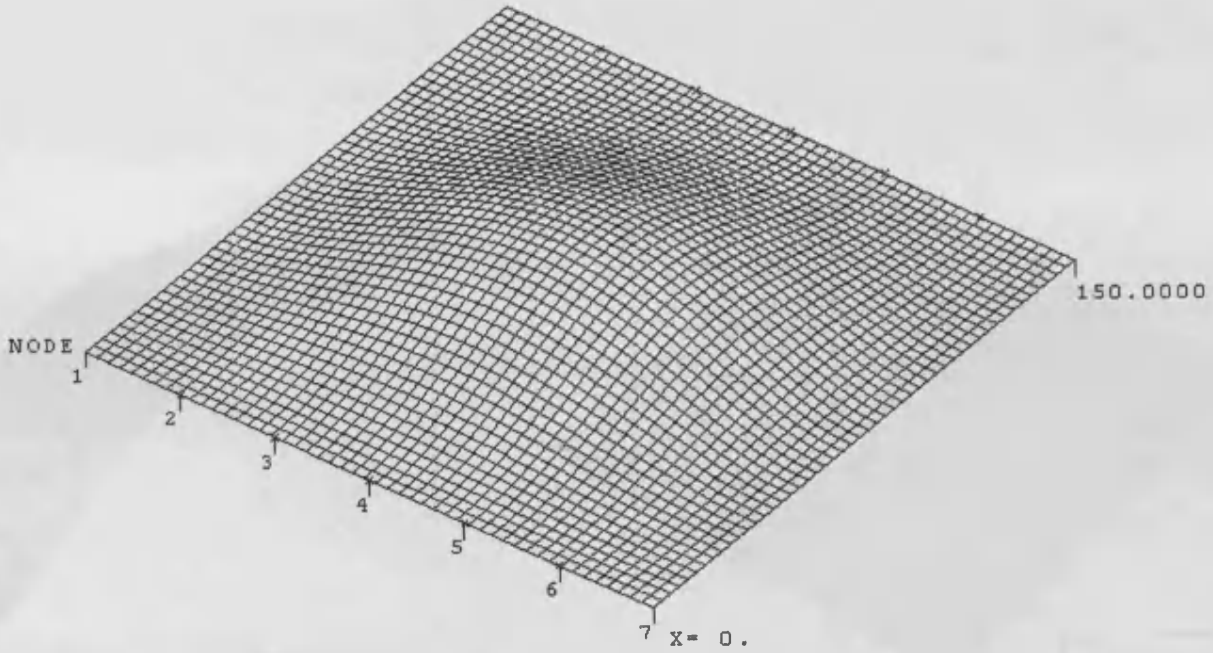

Figure 4.6: Critical buckling mode of configuration 1 (perfect plate).

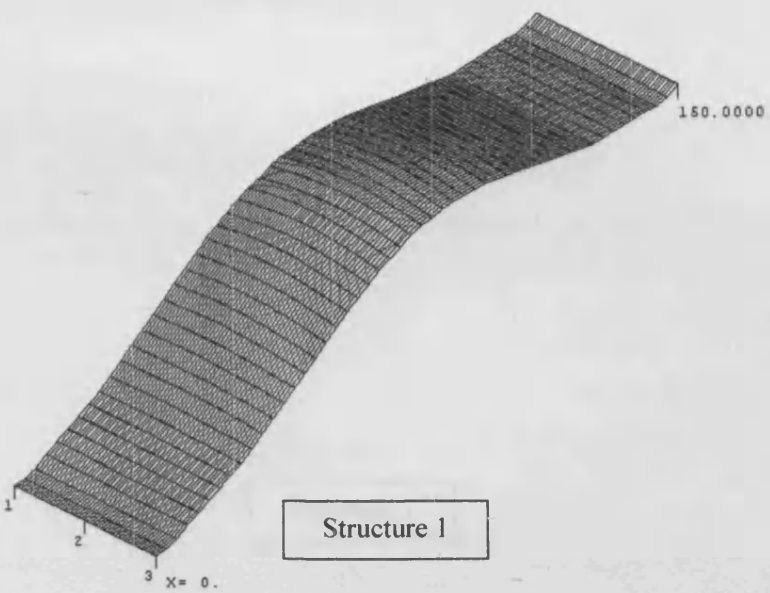

Structure 1

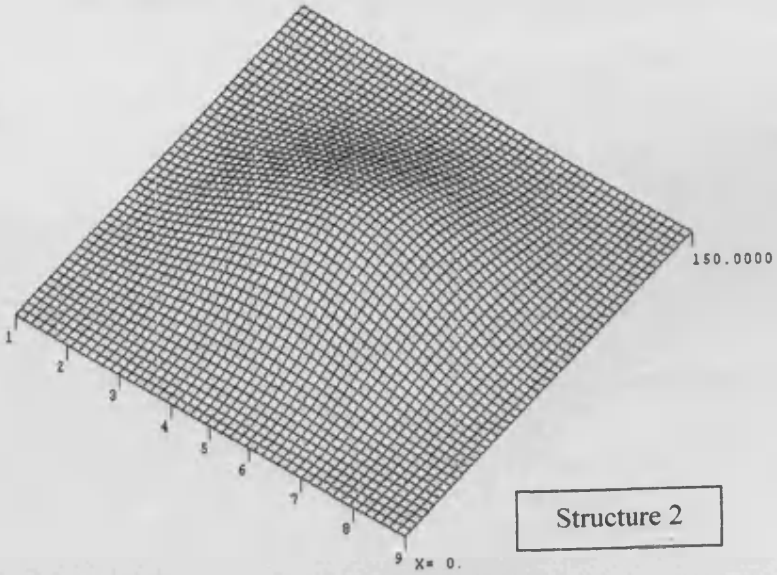

Structure 2

(a)

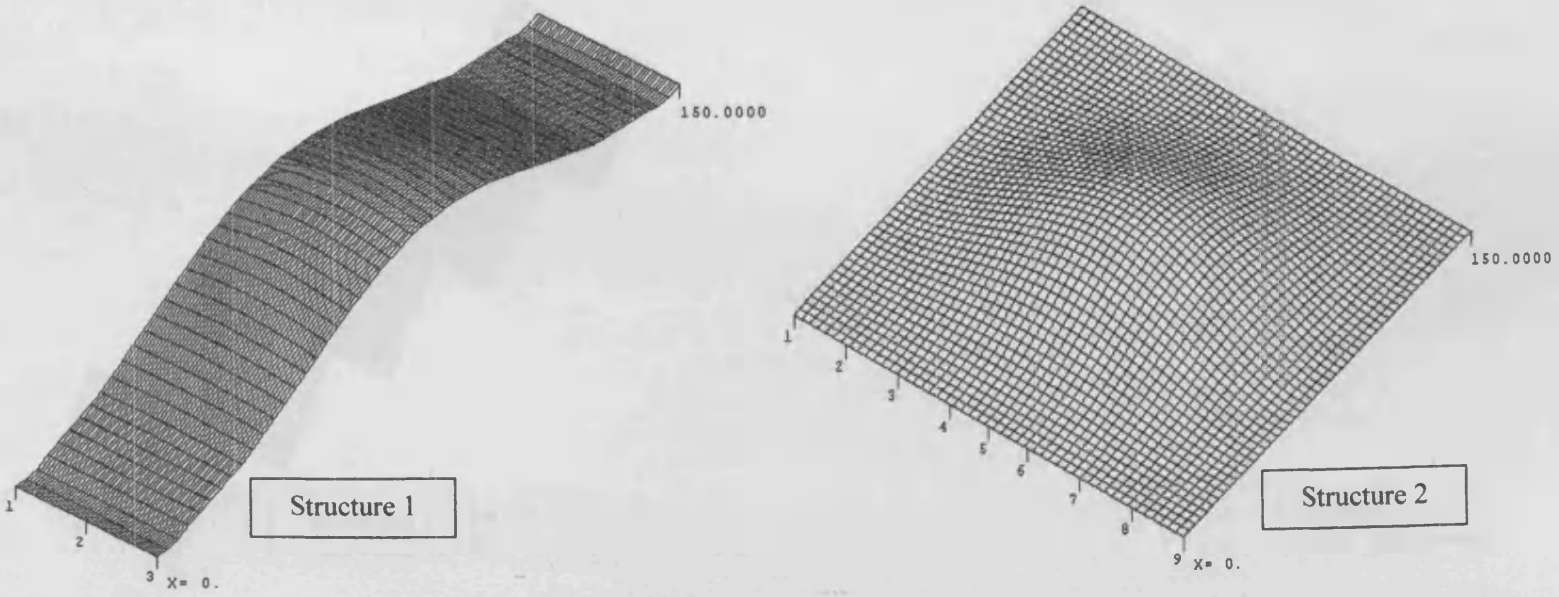
150.0000
1
2
3
X= 0.
Structure 1
150.0000
1
2
3
4
5
6
7
8
9
X= 0.
Structure 2

(b)

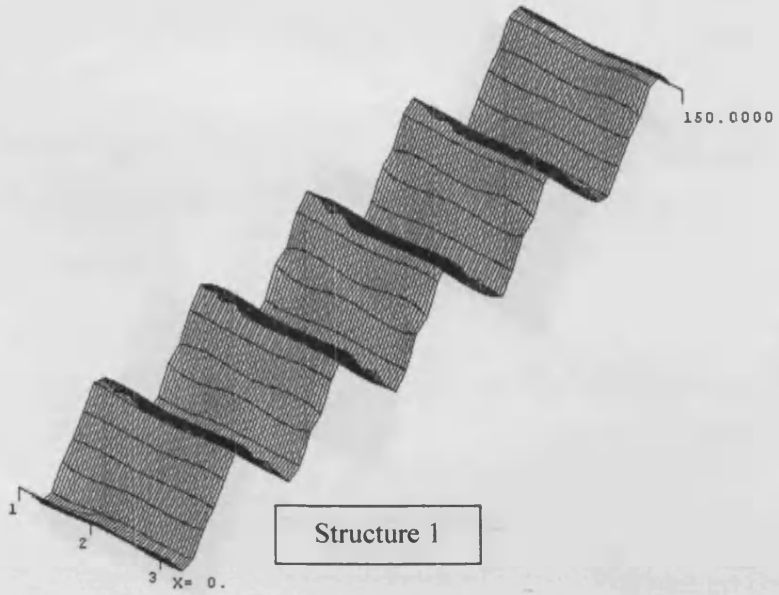

Structure 1

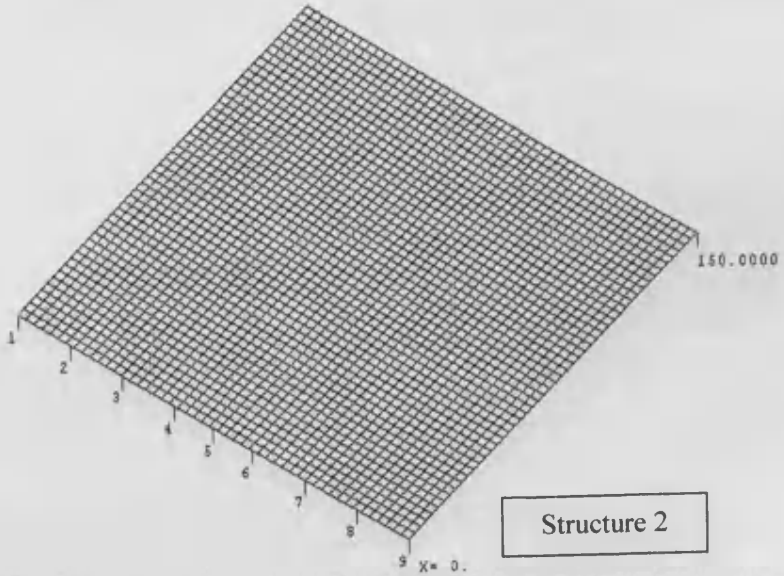

Structure 2

(c)

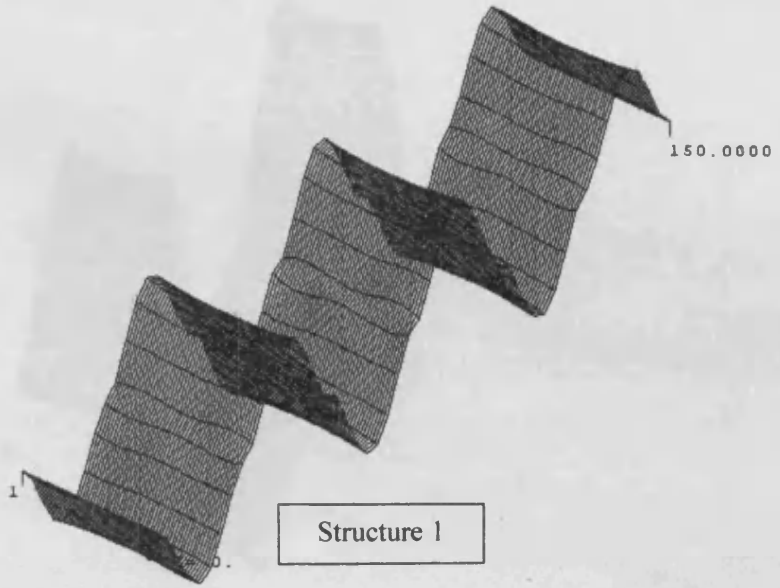

Structure 1

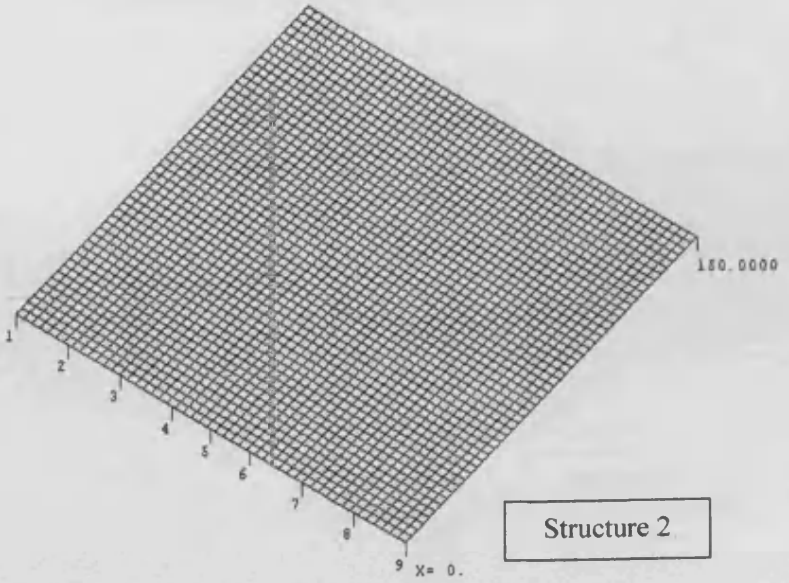

Structure 2

(d)

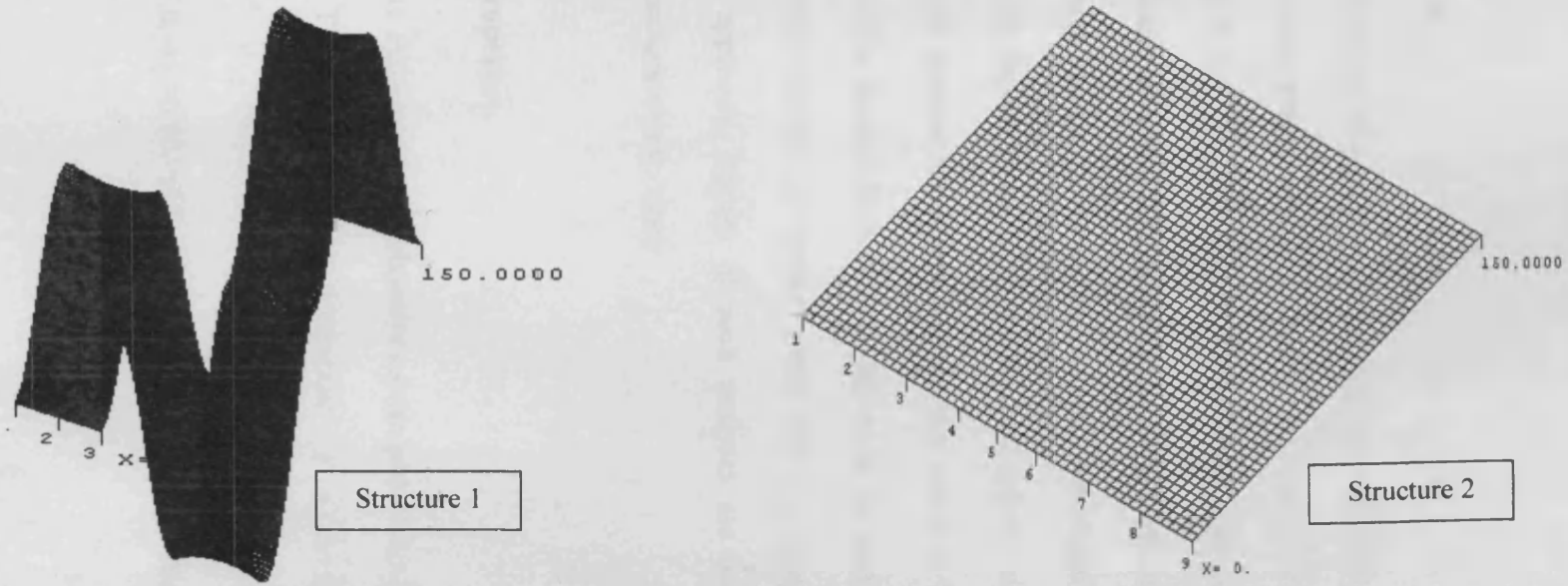

(e)

Figure 4.7: Mode shapes of configuration 2, a perfect plate modelled by the multi-structure approach for different point spacings of (a) 7.5 mm, (b) 10 mm, (c) 15 mm, (d) 25 mm and (e) 50 mm.

CHAPTER 5

MULTI-STRUCTURE MODELLING OF DELAMINATED PLATES

5.1 Introduction

In the analysis of a perfect plate using two different models (Chapter 4); it was shown that common points need to be positioned very close together to give reasonably accurate results. It was also illustrated that closer positioning of common points leads to the use of more constraints and half-wavelengths which in turn give a large and highly populated stiffness matrix, increasing the solution time significantly. Employing a multi-structure approach for delamination modelling will only be more efficient computationally if it uses a small number of constraints, but this needs to be achieved whilst retaining accurate results. The present work is an extension of the previous chapter and investigates the buckling behaviour of a composite plate with a rectangular delamination using the multi-structure approach. Results of such analyses are compared with finite element analyses and conclusions are drawn.

5.2 Material properties

The plate examined is a composite square plate with length $l = 150$ mm and width $B = 150$ mm. The material has properties $E_1 = 128\,\text{kNmm}^{-2}$, $E_2 = 10.3\,\text{kNmm}^{-2}$, $G_{12} = 6\,\text{kNmm}^{-2}$, $\nu_{12} = 0.3$, and is laid up in 16 plies of thickness $t = 0.25\,\text{mm}$ in the sequence $(+45,0,-45,90,90,-45,0,+45)_S$ making a plate of thickness $h = 4$ mm, i.e. as in

Chapter 4. The boundary conditions of the delaminated plate are shown in Figure 5.1a. There is an embedded rectangular delamination at the centre of the plate between the 4th and 5th plies. This delamination has length d and width b.

5.3 Methodology

5.3.1 VICONOPT modelling

In the plate examined, the width of delamination b maintains a constant value of 30 mm while its length d is varied from 10 mm to 70 mm in steps of 10 mm. The VICON analysis option of VICONOPT is employed to couple sinusoidal buckling responses. The modelling procedure is based on dividing the delaminated plate into two separate structures, denoted structures 1 and 2 in Figure 5.1. Structure 1 in Figure 5.1b has 4 plies of sequence $(+45,-45,0,90)$, width of $b = 30\,\text{mm}$ and contains the top sub-laminate of the delamination. Structure 2 is assembled by defining two different plates, i.e. plate 1 of sequence $(+45,0,-45,90,90,-45,0,+45)_S$ and plate 2 of sequence $(+45,0,-45,90,+45,0,-45,90,90,-45,0,+45)$ and is attached to structure 1 via common points to represent the region of no delamination. The bottom sub-laminate of the delamination is contained in structure 2. The boundary conditions are shown in Figure 5.1a and are enforced by using Lagrangian multipliers along the ends $x = 0$ and $x = l$ at intervals of $(B-b)/6$ in plate 1 and at intervals of $B/2$ in plate 2. It is worth mentioning that a small transverse compression is applied in addition to longitudinal compressive load to represent the expansion of the plate assembly due to the Poisson's ratio effects in FE model, i.e.

effects of reaction forces at edges $y = 0$ and $y = l$. The transverse compression load is obtained from a general static analysis using ABAQUS and is $N_T = 0.3N_L$.

As can be seen from Figure 5.2, plate 2 in structure 2 (between nodes 4 and 6) has a negative z offset whilst structure 1 (between nodes 1 and 3) has a positive z offset, as measured from the reference surface of the plate to the node. In order to model the delamination, structure 2 is connected to structure 1 along its edges, and also within the undelaminated regions, i.e. at points indicated by cross marks in Figure 5.1b. Compressive unit loading is applied to the plate and a buckling analysis is performed. It is worth noting that at each attachment point, all six degrees of freedoms of structure 1 are coupled with those of structure 2. In Chapter 4, a common point spacing of $d' = 7.5\,\text{mm}$ was found to give more accurate results than other spacings. Therefore, $d' < 7.5\,\text{mm}$ was adopted for present study, i.e. $d' = 6.3636\,\text{mm}$ for delamination of length $d = 10\,\text{mm}$ and $d' = 5\,\text{mm}$ for delamination length of $d = 20,30,40,50,60$ and $70\,\text{mm}$.

5.3.2 FE modelling

The plate was also modelled with ABAQUS 6.8. The SC6R continuum shell elements of Figure 5.3a were used to discretise the entire three-dimensional body. These elements take into account the effects of transverse shear. A buckling analysis was performed on the structure. Further information regarding SC6R elements and buckling analysis features is given in Chapter 3. Figure 5.3b illustrates this mesh and the boundary conditions for the FE model.

5.4 Results and discussion

VICONOPT and ABAQUS initial buckling load and mode shapes were obtained for a composite plate containing a rectangular delamination. Figure 5.4 illustrates that there is an almost perfect match between VICON and FE analysis results. where local buckling occurs, i.e. for $d/l \geq 0.15$. However for the global buckling mode which is found for $d/l \leq 0.15$ there is negligible discrepancy of up to 4% between VICON and FE analyses. This discrepancy can be explained as follows

1- VICONOPT is unable to take transverse shear effects fully into account when the multi-structure approach is used.

2- VICONOPT mode shapes repeat over several successive bays, potentially giving a stiffer model, while ABAQUS mode shapes occur in just one bay.

Taking the above factors into account, VICONOPT slightly overestimates the buckling load factor compared to FE analysis.

Figure 5.5 shows the time taken to complete each analysis. Although there is very good agreement between the VICON and FE analyses for local buckling behaviour, the VICON analyses are very expensive computationally. As the length of delamination decreases, more common points are required to attach structure 1 to structure 2 and the time of analysis increases significantly.

Figures 5.6 shows good qualitative agreement between VICONOPT and ABAQUS in predicting buckling mode shapes except for Figure 5.6c. This mode shape is related to the transition point for one to two half-waves of local buckling; ABAQUS plot shows the beginnings of a second buckle; the VICONOPT mode repeats over several longitudinal

bays, and the figure shows that it predicts one buckle in some bays and two buckles in other bays.

5.5 Conclusions

The buckling behaviour of a composite plate with a central rectangular delamination has been studied using VICONOPT and ABAQUS. Predicted mode shapes are in good agreement. Buckling loads are also in good agreement for local buckling behaviour. VICONOPT overestimates global buckling loads by up to 21.5% due to its intrinsic limitations such as the way in which it models the boundary conditions and the fact that transverse shear effects cannot be considered for a multi-structure approach. However, the multi-structure approach is not competitive (against FEA) since it is very expensive computationally. Hence it is essential to either improve the common point model (multi-structure approach) or look for a replacement method to model delamination, in order to get reliable results for a parametric study of delaminated composite plates.

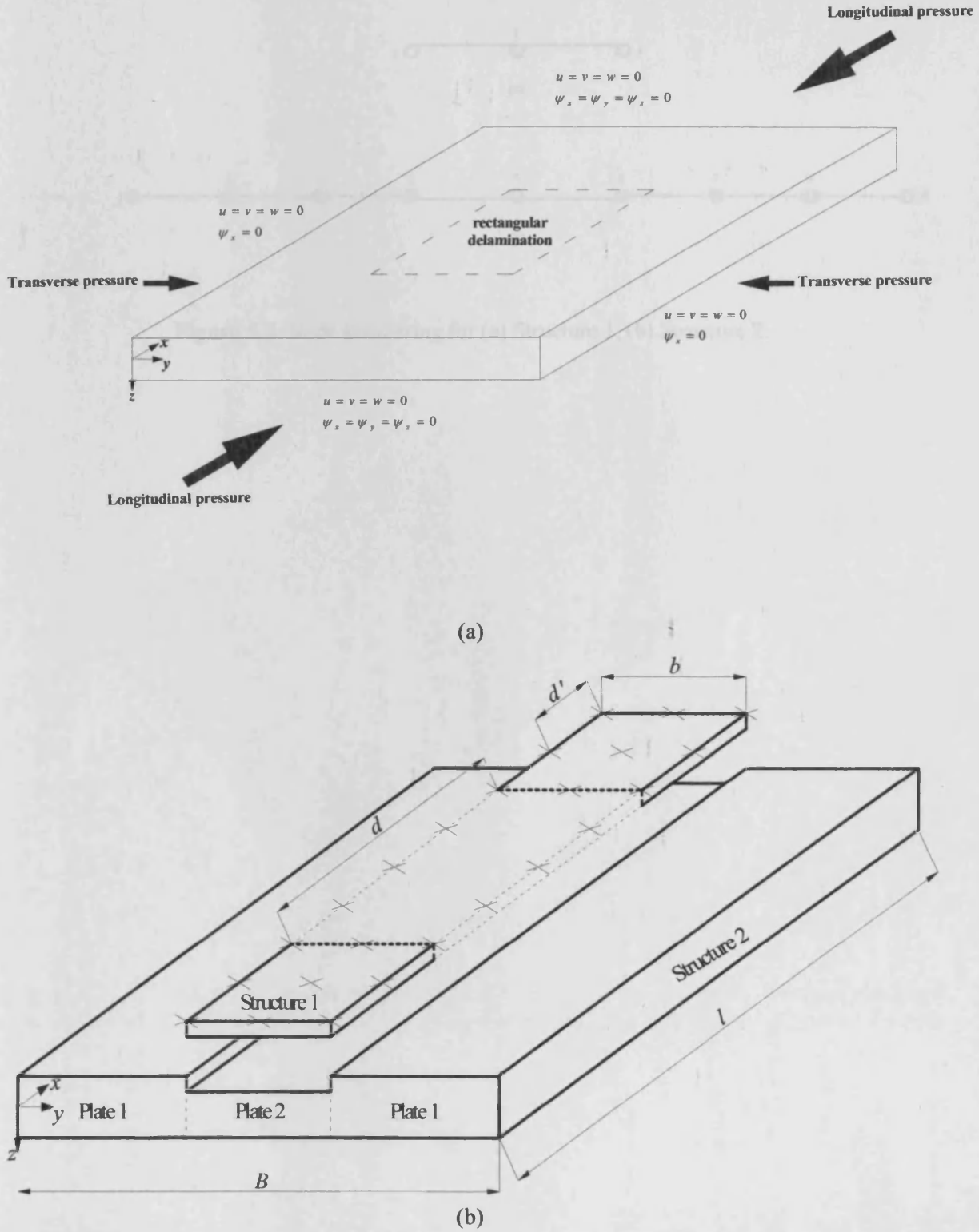

Figure 5.1: VICONOPT modelling of delamination (a) Boundary conditions and loading. (b) Common points and dimensions of structures 1 and 2.

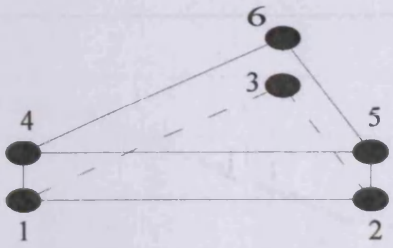

(a)

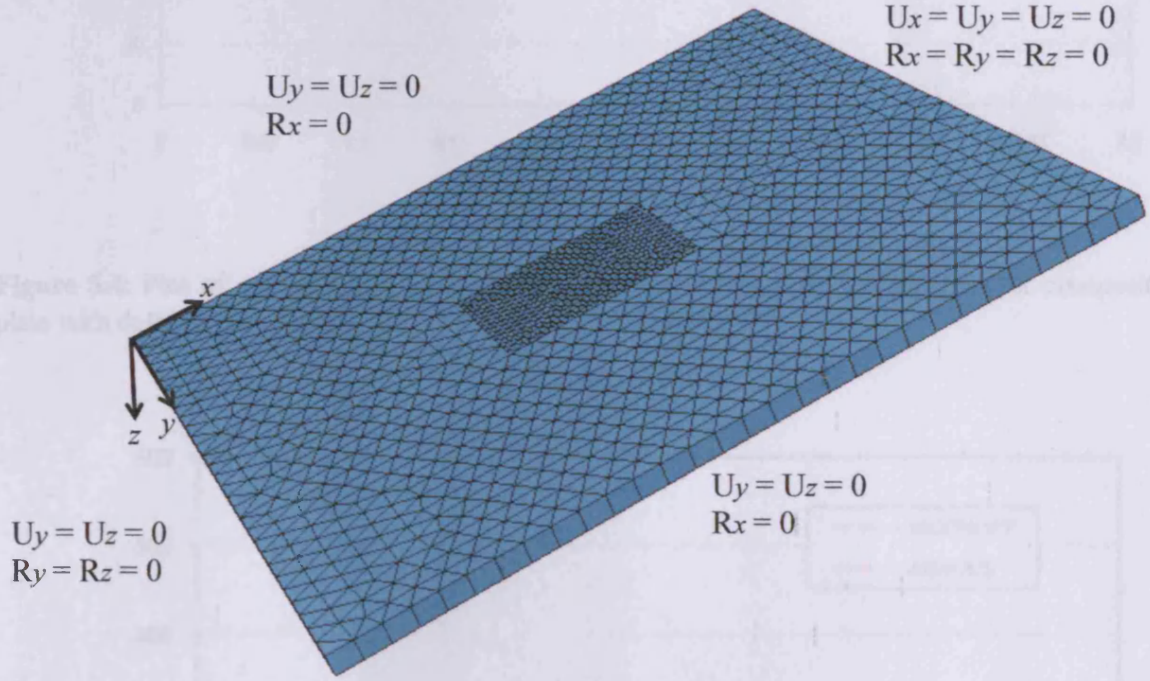

(b)

Figure 5.3: a) SC6R continuum shell element used for meshing the model, b) A typical mesh and boundary conditions for a laminate with a rectangular delamination of width b = 30 mm and length d = 40 mm.

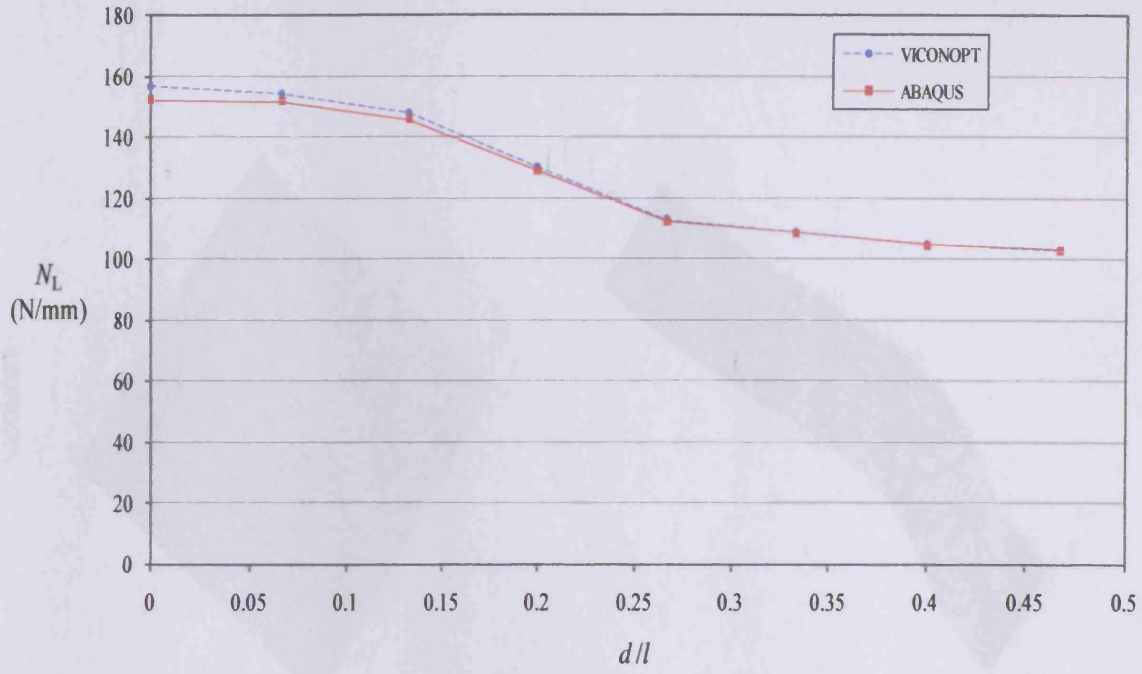

Figure 5.4: Plot of critical buckling stress resultant against length of delamination for composite plate with delamination width of $b = 0.2B$ and $h_1 = 0.25h$.

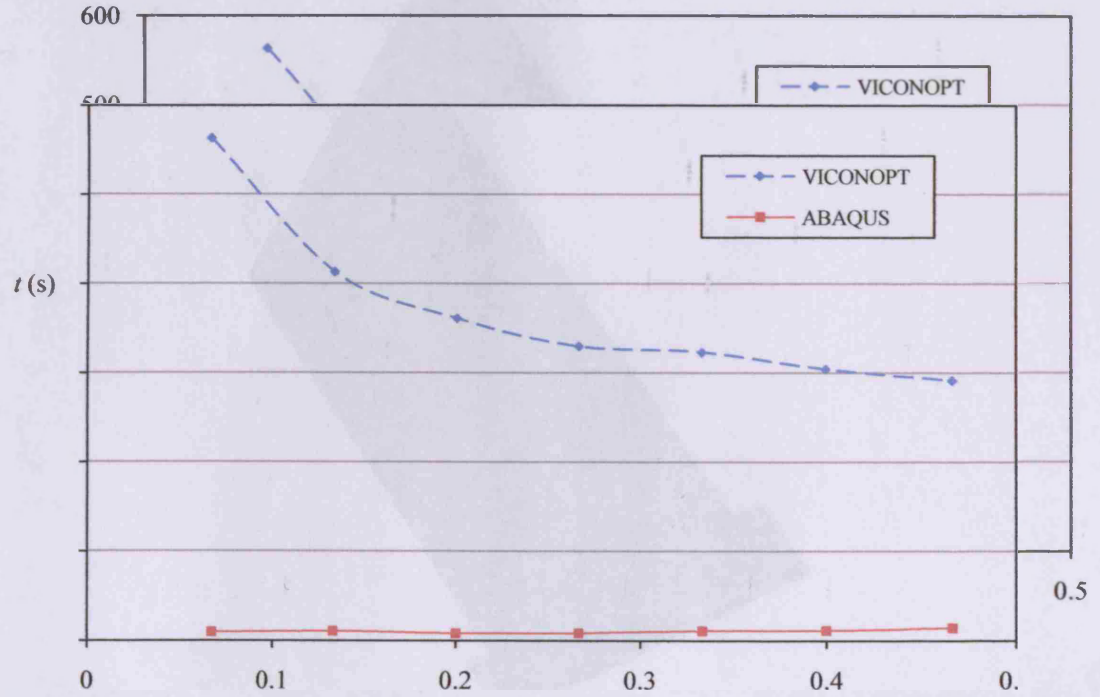

Figure 5.5: Time of analysis versus length of delamination for composite plate with delaminated width of $b = 0.2B$ and $h_1 = 0.25h$.

ABAQUS

VICONOPT

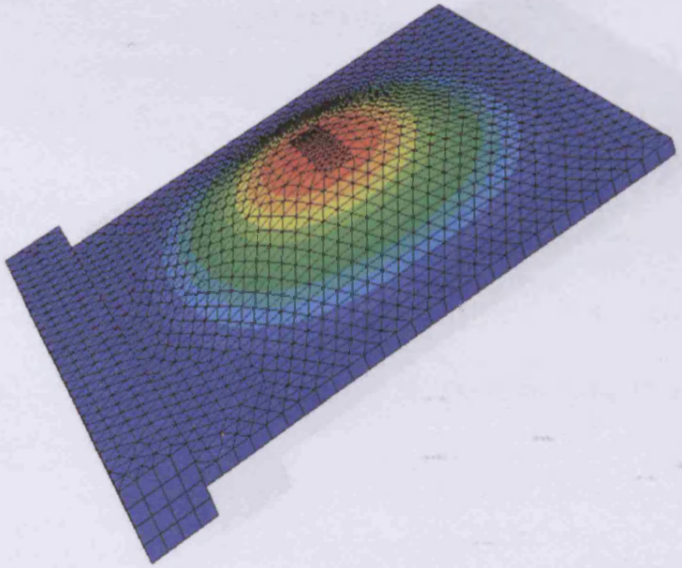

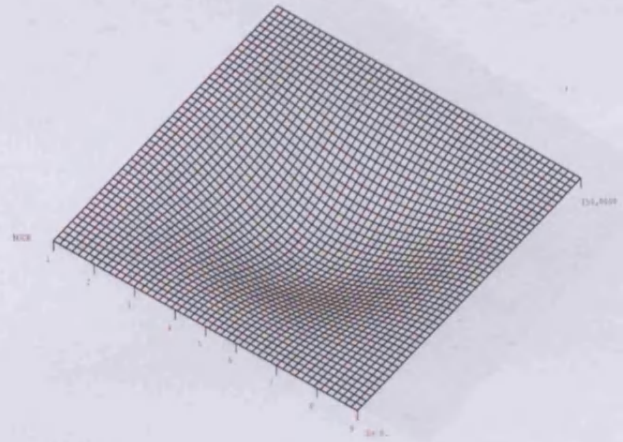

(a)

ABAQUS

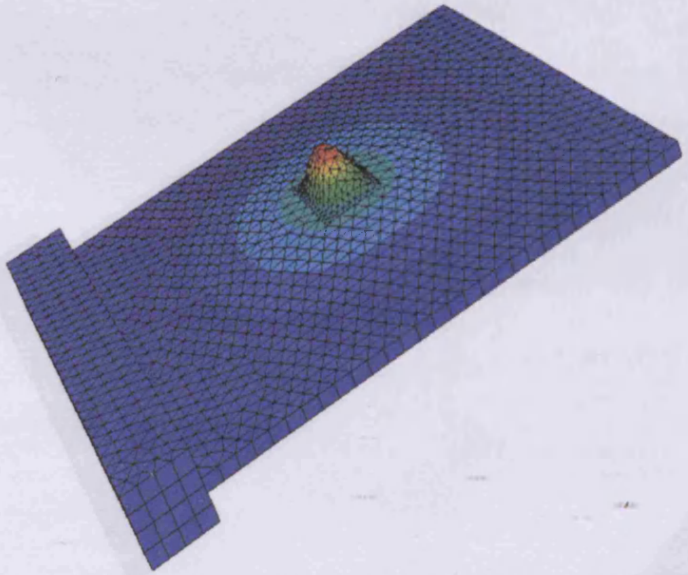

VICONOPT

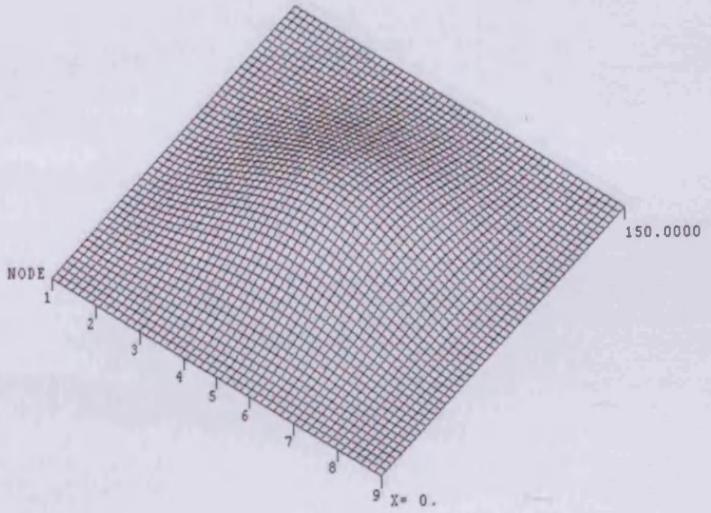

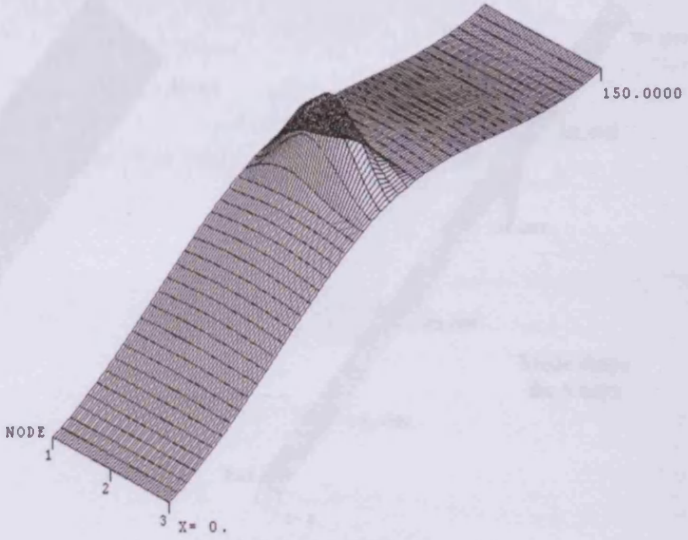

(b)

ABAQUS

VICONOPT

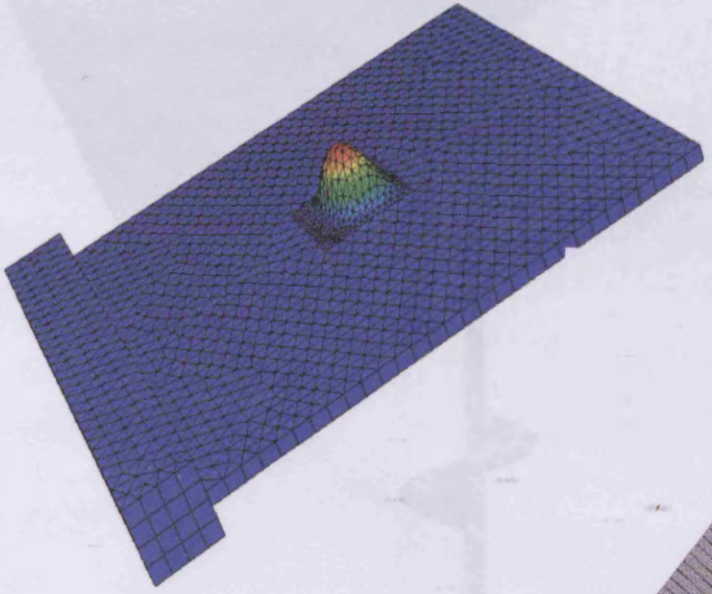

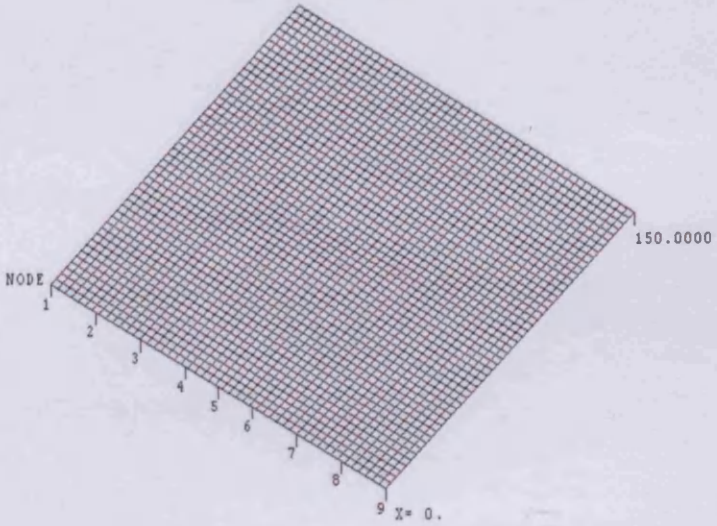

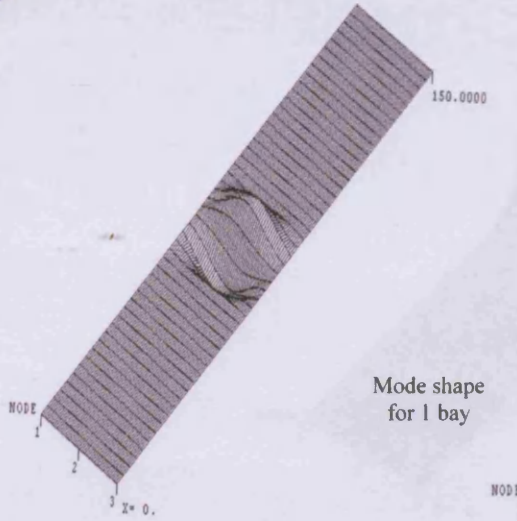

Mode shape
for 1 bay

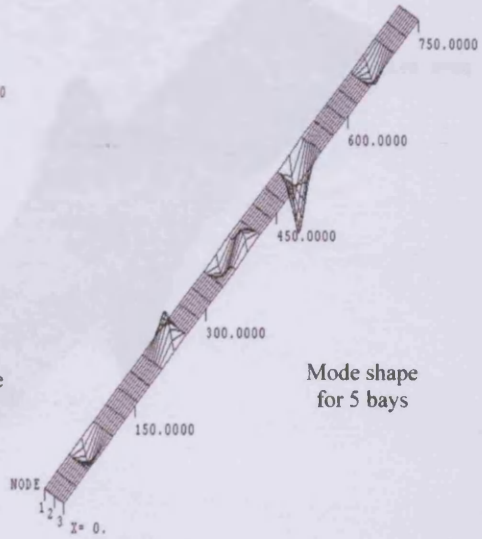

Mode shape
for 5 bays

(c)

ABAQUS

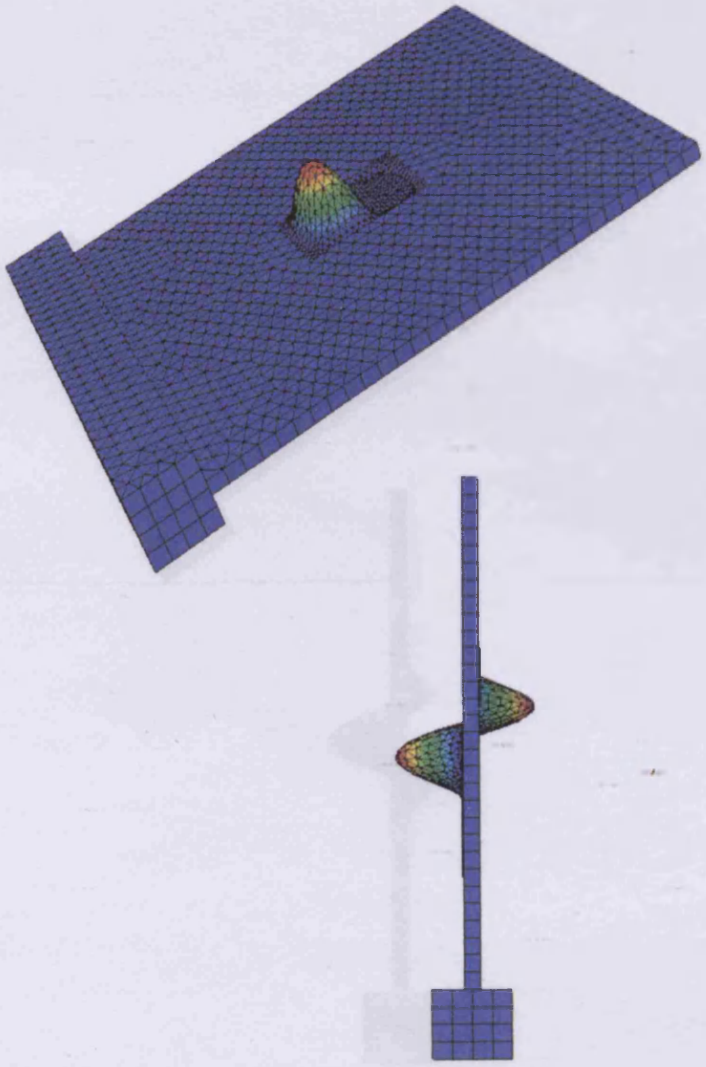

VICONOPT

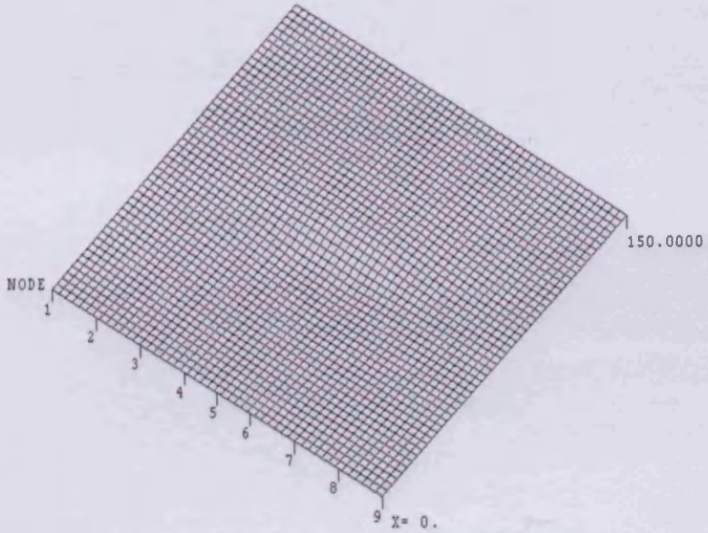

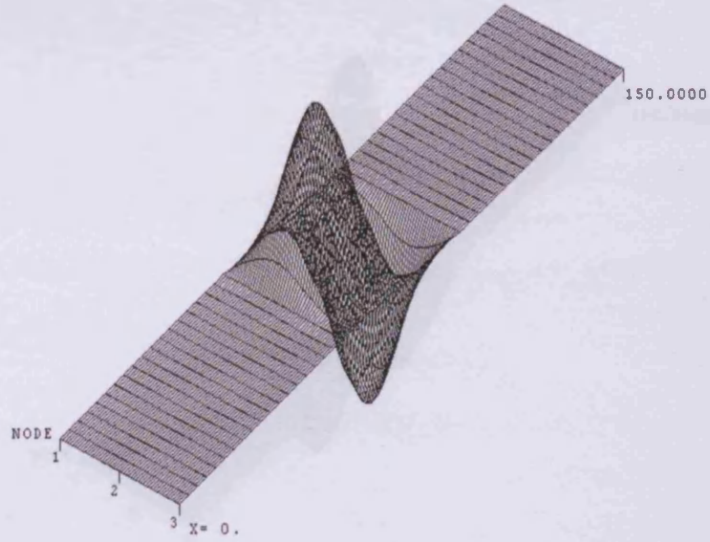

(d)

ABAQUS

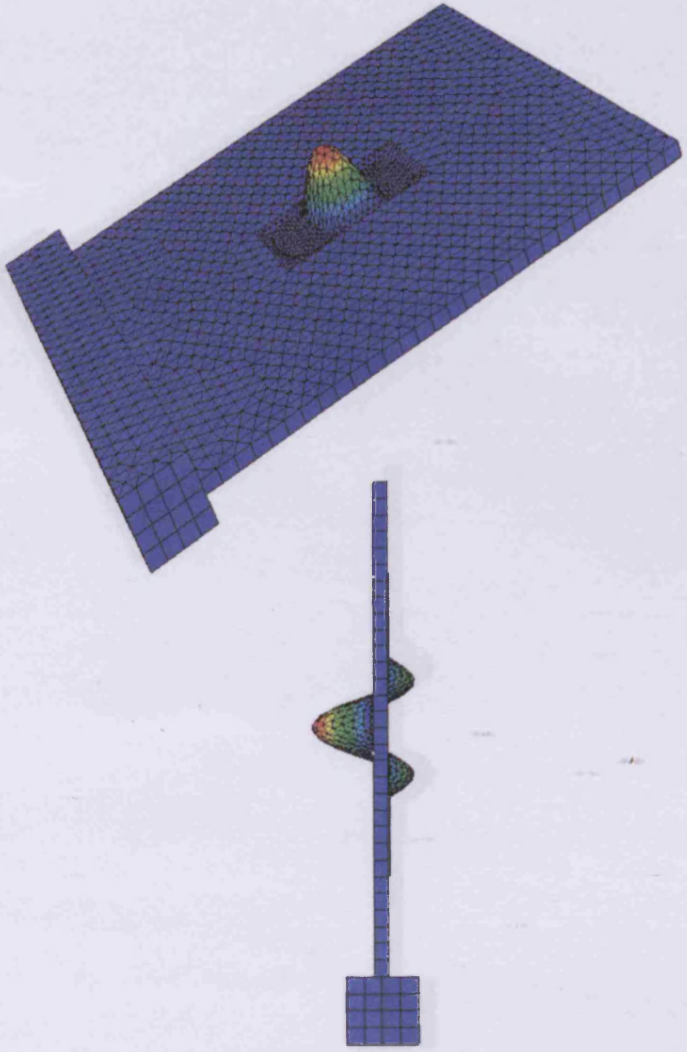

VICONOPT

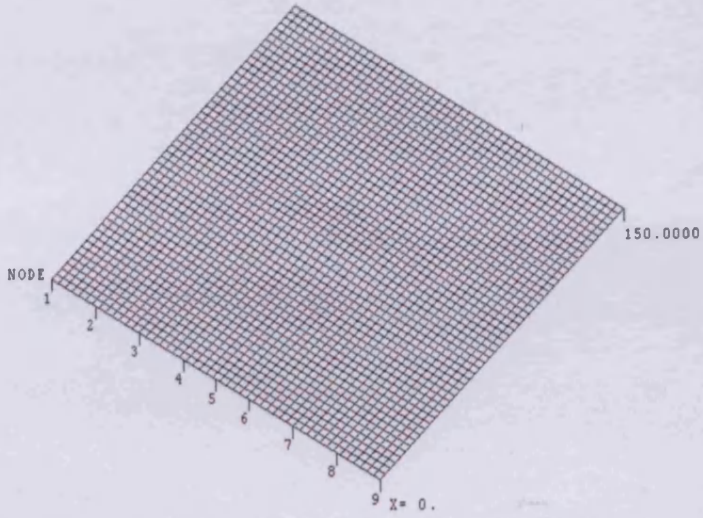

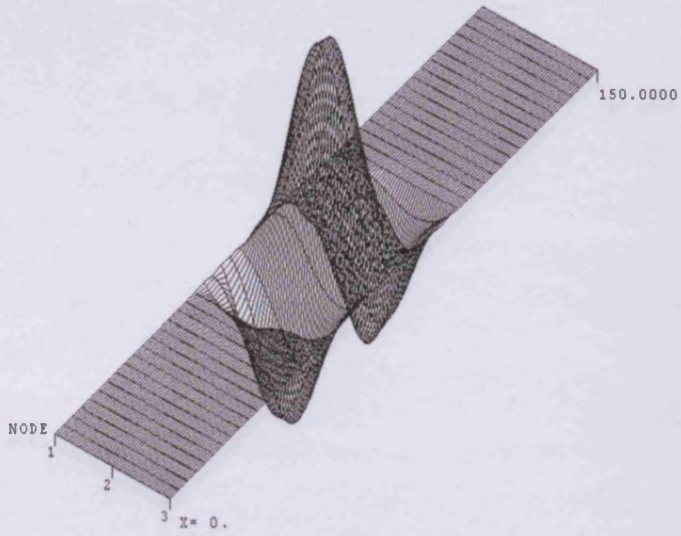

(e)

ABAQUS

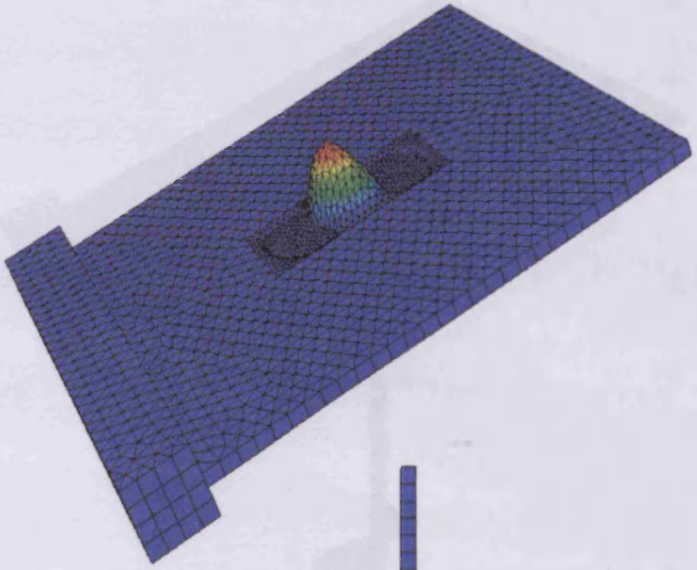

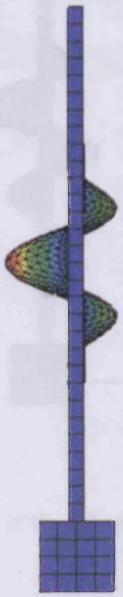

VICONOPT

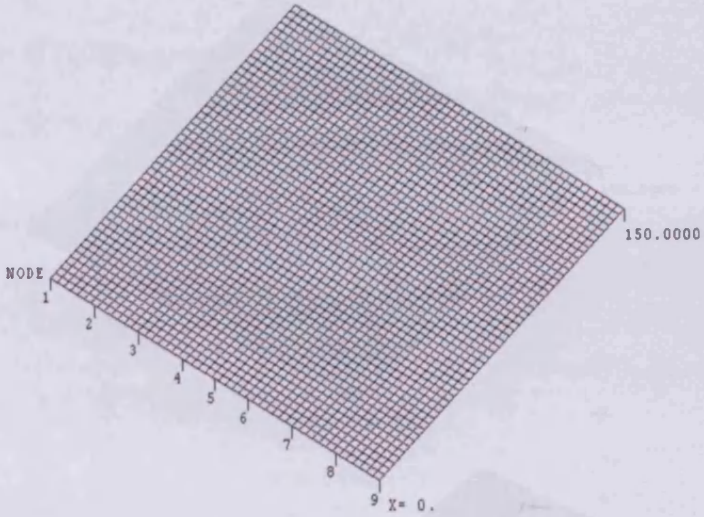

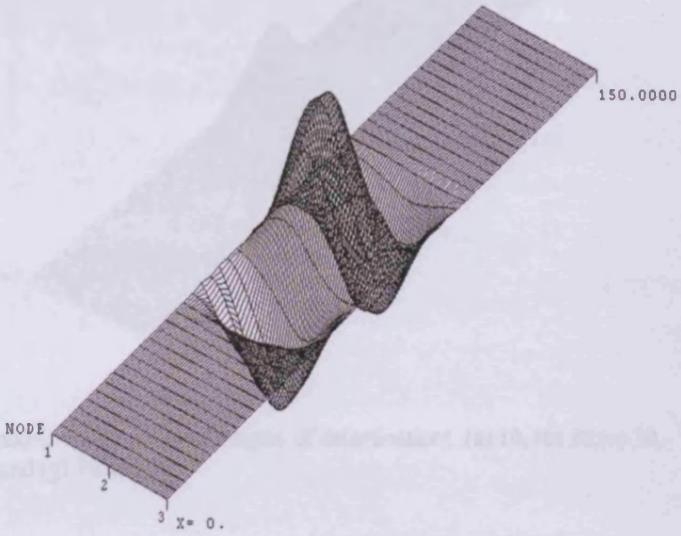

(f)

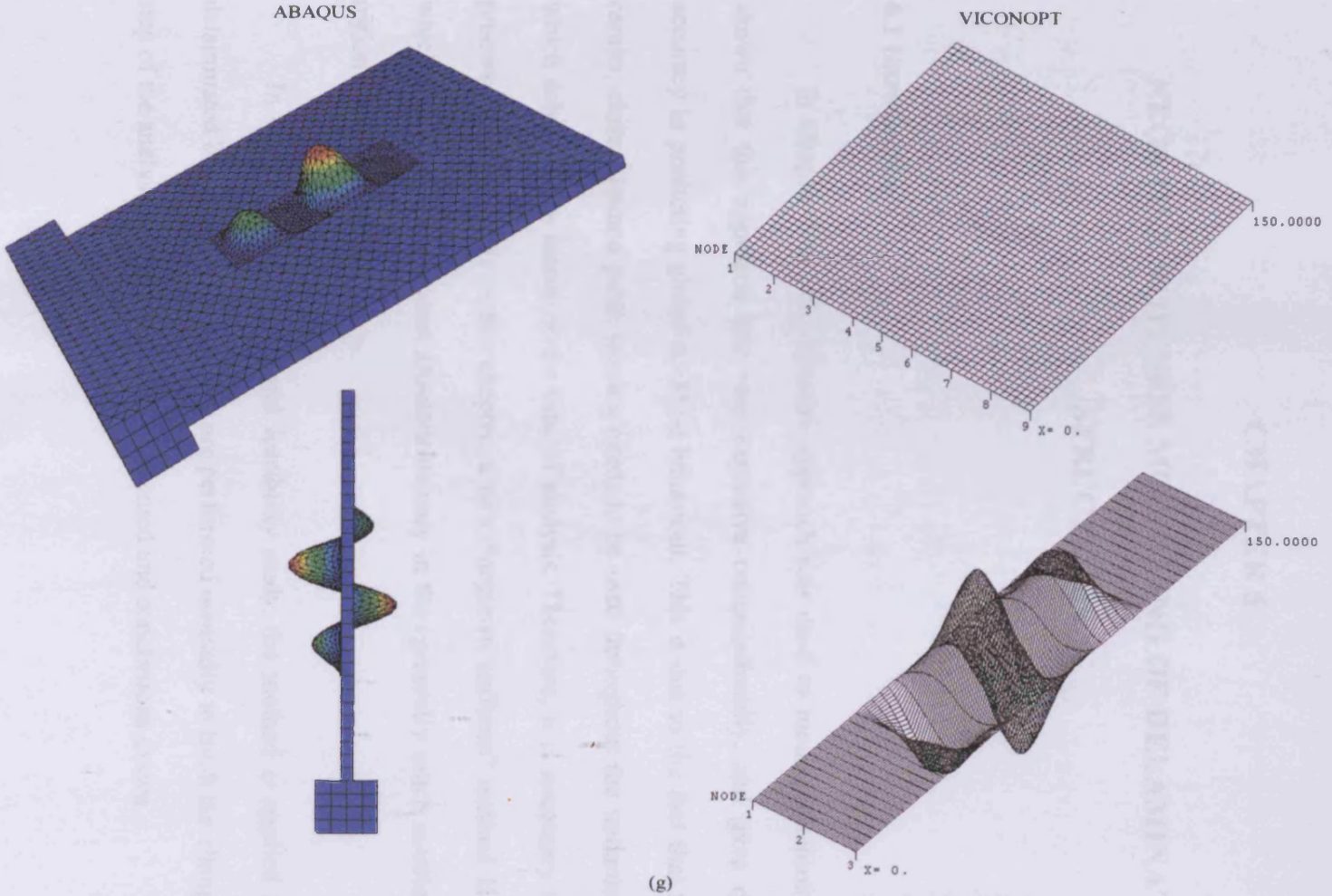

(g)

Figure 5.6: Mode shapes of the delaminated plate using multi-structure modelling for different lengths of delamination: (a) 10, (b) 20,(c) 30, (d) 40, (e) 50,(f) 60 and (g) 70 mm.

CHAPTER 6

NEGATIVE STIFFNESS MODELLING OF DELAMINATED STRUCTURES

6.1 Introduction

In Chapter 5 a multi-structure approach was used to model delamination. It was shown that this approach was very expensive computationally, and gave only limited accuracy in predicting global buckling behaviour. This is due to the fact that for accurate results, close common point spacing needs to be used throughout the undamaged region, which subsequently increases the time of analysis. Therefore, it is necessary to make the process more efficient. In this chapter, a new "negative stiffness" method is introduced which requires common point attachments only in the (generally much smaller) damaged region.

In order to carry out a rapid feasibility study, the method is applied to a simple delaminated beam problem. Analyses are performed manually to track the changes in every step of the analysis. Finally, results are presented and conclusions drawn.

6.2 Delaminated beam model

A delaminated beam problem is considered as a simple means to evaluate the negative stiffness method. The idea is to obtain the J counts (Chapter 2) of a delaminated

beam indirectly from the J counts of equivalent structural configurations. In order to do this, it is necessary to introduce four different structures S_d, S_0, S_1 and S_2 (Figure 6.1). S_d is the delaminated beam which is divided into 6 elements. Elements 1 and 6 have length l, Young's modulus E, thickness t and second moment of area I. Elements 2 and 4 represent the top sub-laminate of the delaminated region having length $l/2$, Young's modulus E, thickness $t/2$ and second moment of area $I/8$. Elements 3 and 5 have the same properties as elements 2 and 4 but represent the bottom sub-laminate of the delaminated region. S_0 is a perfect beam divided into 4 elements with Young's modulus E, thickness t and second moment of area I. S_d and S_0 are clamped at their two ends and simply supported at $x = l$ and $x = 2l$, and carry a longitudinal compressive load P. S_1 and S_2 are essentially similar structures (the same portion) divided into two elements, which each have length $l/2$, Young's modulus E, thickness $t/2$ and second moment of area $I/8$ and carry a compressive load $P/2$. It is worth noting that in S_d, nodes 3 and 4 are not connected while nodes 2 and 5 are common between the top and bottom sub-laminates, to represent a delamination. At the next stage of modelling, the beam is studied using a more refined mesh ($n = 4$), i.e. with four elements across the delaminated region instead of two (Figure 6.2). In this study, example matrices are given for the rough mesh ($n = 2$) as the stiffness matrices are smaller and simpler to understand.

6.3 Methodology

The delaminated structure S_d can be regarded as the following combination of structures S_0, S_1 and S_2.

$$S_d = S_0 \underset{b,i}{-} S_2 \underset{b}{+} S_1 \tag{6.1}$$

where S_2 is detached (subtracted) from S_0 at the boundaries and interior, and then S_1 attached (added) only at the boundaries. In other words, nodes 1, 2 and 3 of S_2 are disconnected from nodes 2, 3 and 4 of S_0; and then nodes 1 and 3 of S_1 are connected to nodes 2 and 4 of S_0. The resultant of this operation is equivalent to the delaminated beam (S_d). Hence, instead of obtaining the J counts of the delaminated structure and possibly dealing with many common points outside the delaminated region, the J counts of an equivalent configuration (i.e. the right-hand side of Eq (6.1)) will be dealt with, considering a small number of common points in the delaminated region only. It is worth noting that the naming of the "negative stiffness" model is due to the subtraction of structure S_2 from $S_0 \underset{b}{+} S_1$ which is equivalent to adding S_2 with negative stiffness to $S_0 \underset{b}{+} S_1$. Prior to proceeding with such an analysis, it is essential to investigate whether such an approach would yield acceptable results. Therefore, refining Eq (6.1) gives

$$S_0 \underset{b}{+} S_1 = S_d \underset{b,i}{+} S_2 \tag{6.2}$$

Hereafter, Configurations 1 and 2 are regarded as the left- and right-hand sides of Eq (6.2), respectively. Each configuration represents an artificial problem which has additional elements in the central region. Since these two configurations are equivalent geometrically, similar J counts are expected to be obtained for each of them.

6.4 Theory and formulation

In 1980, Lightfoot [6.1] presented the exact member equations for a range of Bernoulli-Euler straight line elements in terms of a unified notation based on that of Blaszkowiak [6.2]. This notation is shown in Figure 6.3 and Eq (6.3).

$$\begin{bmatrix} F_1 l \\ F_2 \\ F_3 l \\ F_4 \end{bmatrix} = EI/l \begin{bmatrix} \gamma & \upsilon & -\epsilon & \delta \\ \upsilon & \alpha & -\delta & \beta \\ -\epsilon & -\delta & \gamma & -\upsilon \\ \delta & \beta & -\upsilon & \alpha \end{bmatrix} \begin{bmatrix} D_1/l \\ D_2 \\ D_3/l \\ D_4 \end{bmatrix} \tag{6.3}$$

Here, P, EI and l are the axial force, flexural rigidity and length of the member, F_1-F_4 are the transverse forces and moments at its ends and D_1-D_4 are the corresponding displacements. The Greek symbols are the appropriate stiffness coefficients, e.g. stability functions in a buckling problem. Timoshenko theory was used in ref. [6.3] to obtain the member equations for a vibrating beam-column. However, for the illustrative purposes of this study, the simpler Bernoulli-Euler theory has been used, giving

$$\alpha = \frac{p^2}{[2p(1-\cos p) - p^2 \sin p]}(\sin p - p\cos p)$$

$$\beta = \frac{p^2}{[2p(1-\cos p) - p^2 \sin p]}(p - \sin p)$$

$$\upsilon = \delta = \frac{p^2}{[2p(1-\cos p) - p^2 \sin p]}[(\sin p - p\cos p) + (p - \sin p)]$$

$$\gamma = \epsilon = \frac{p^4 \sin p}{[2p(1-\cos p) - p^2 \sin p]} \tag{6.4}$$

where $p^2 = Pl^2/EI$.

Once the stiffness parameters are calculated, the stiffness matrices for S_d, S_1, S_2 and S_0 can be formed. After formation of these matrices, the displacements and rotations of each structure are coupled to obtain the resulting stiffness of the two configurations, i.e. (1) S_d plus S_2 attached both at the boundaries and interior and (2) S_1 plus S_0 attached at just the boundaries. It should be mentioned that Eq (6.3) is applicable when no offsets have been applied to the beam elements. In case offset effects need to be considered, Eq (6.3) would have the form [6.4]

$$\begin{bmatrix} F_1 l \\ F_2 \\ F_3 l \\ F_4 \end{bmatrix} = EI/l \begin{bmatrix} \gamma & \upsilon & -\epsilon & \delta \\ \upsilon & \alpha + e^2F & -\delta & \beta - e^2F \\ -\epsilon & -\delta & \gamma & -\upsilon \\ \delta & \beta - e^2F & -\upsilon & \alpha + e^2F \end{bmatrix} \begin{bmatrix} D_1/l \\ D_2 \\ D_3/l \\ D_4 \end{bmatrix} \tag{6.5}$$

where e is the offset distance of the nodes of the beam element from their neutral axis (mid-plane of the beam) and F is the axial stiffness of beam element, i.e. EA/l . After calculating α, β, δ, υ, γ and ϵ and taking offset effects into account (i.e. for elements 2, 3, 4 and 5 of S and for elements 1 and 2 of S_1 and S_2), Eq (6.3) can be expanded in the following format

$$\begin{bmatrix} F_1 \\ F_2 \\ F_3 \\ F_4 \end{bmatrix} = \begin{bmatrix} M & N & Q & V \\ N & Y & -V & H \\ Q & -V & M & -N \\ V & H & -N & Y \end{bmatrix} \begin{bmatrix} D_1 \\ D_2 \\ D_3 \\ D_4 \end{bmatrix} \tag{6.6}$$

where

$$M = \gamma EI/l^3$$

$$N = \upsilon EI/l^2$$

$$Q = -\epsilon EI/l^3$$

$$V = \delta EI/l^2 \tag{6.7}$$

$$Y = (\alpha + e^2F)EI/l$$

$$H = (\beta - e^2F)EI/l$$

Omitting rows and columns corresponding to the constrained displacements at nodes 1 and 3, the stiffness matrix for structure S_2 can be obtained as

$$\begin{bmatrix} Y_{21} & V_{21} & H_{21} & 0 \\ V_{21} & M_{21}+M_{22} & N_{21}+N_{22} & V_{22} \\ H_{21} & N_{21}+N_{22} & Y_{21}+Y_{22} & H_{22} \\ 0 & V_{22} & H_{22} & Y_{22} \end{bmatrix} \tag{6.8}$$

where the subscripts (*ij*) on the stiffness parameters denotes element *j* of structure S_i. For example, Y_{21} is the parameter for element 1 of structure S_2 (Figure 6.1).

Knowing that elements 1 and 2 are identical, so that $Y_{21}=Y_{22}$, $H_{21}=H_{22}$, $V_{21}=V_{22}$, $M_{21}=M_{22}$ and $N_{21}=N_{22}$, Eq (6.8) can be simplified as

$$\begin{bmatrix} Y_{21} & V_{21} & H_{21} & 0 \\ V_{21} & 2\times M_{21} & 0 & V_{21} \\ H_{21} & 0 & 2\times Y_{21} & H_{21} \\ 0 & V_{21} & H_{21} & Y_{21} \end{bmatrix} \tag{6.9}$$

The stiffness matrix of S_1 is identical to that of S_2. Following the same procedure as that mentioned above gives the stiffness matrix of structure S_d as

$$\begin{bmatrix} Y_{d1}+2\times Y_{d2} & V_{d2} & H_{d2} & V_{d2} & H_{d2} & 0 \\ V_{d2} & 2\times M_{d2} & 0 & 0 & 0 & V_{d2} \\ H_{d2} & 0 & 2\times Y_{d2} & 0 & 0 & H_{d2} \\ V_{d2} & 0 & 0 & 2\times M_{d2} & 0 & V_{d2} \\ H_{d2} & 0 & 0 & 0 & 2\times Y_{d2} & H_{d2} \\ 0 & V_{d2} & H_{d2} & V_{d2} & H_{d2} & Y_{d1}+2\times Y_{d2} \end{bmatrix} \tag{6.10}$$

noting that elements 1 and 6 are identical, as are elements 2, 3, 4 and 5.

It is assumed that $EI/l = 100$ N. m and $l = 10$ m for the long elements (elements 1 and 6 in structure S_d); and consequently $EI/l = 25$ N. m and $l = 5$ m for the shorter elements (elements 2, 3, 4 and 5 of structure S_d).

Finally, in the perfect structure S_0, elements 1 and 4 are identical, as are elements 2 and 3, and the stiffness matrix is

$$\begin{bmatrix} Y_{01}+Y_{02} & V_{02} & H_{02} & 0 \\ V_{02} & 2\times M_{02} & 0 & V_{02} \\ H_{02} & 0 & 2\times Y_{02} & H_{02} \\ 0 & V_{02} & H_{02} & Y_{01}+Y_{02} \end{bmatrix} \tag{6.11}$$

Once all the stiffness matrices are formed, the displacements and rotations of the common nodes can be coupled to form configurations 1 and 2. The procedure and pattern of coupling degrees of freedom is similar to using common points which was explained in Chapters 2 and 4.

For example, the format of the assembled matrix for configuration 1, i.e. structures S_0 plus S_1 is given as below

$$\begin{bmatrix} Y_{01}+Y_{02} & V_{02} & H_{02} & 0 & 0 & 0 & 0 & 0 & 1 & 0 \\ V_{02} & 2M_{02} & 0 & V_{02} & 0 & 0 & 0 & 0 & 0 & 0 \\ H_{02} & 0 & 2Y_{02} & H_{02} & 0 & 0 & 0 & 0 & 0 & 0 \\ 0 & V_{02} & H_{02} & Y_{01}+Y_{02} & 0 & 0 & 0 & 0 & 0 & 1 \\ 0 & 0 & 0 & 0 & Y_{11} & V_{11} & H_{11} & 0 & -1 & 0 \\ 0 & 0 & 0 & 0 & V_{11} & 2M_{11} & 0 & V_{11} & 0 & 0 \\ 0 & 0 & 0 & 0 & H_{11} & 0 & 2Y_{11} & H_{11} & 0 & 0 \\ 0 & 0 & 0 & 0 & 0 & V_{11} & H_{11} & Y_{11} & 0 & -1 \\ 1 & 0 & 0 & 0 & -1 & 0 & 0 & 0 & -\text{Э} & 0 \\ 0 & 0 & 0 & 1 & 0 & 0 & 0 & -1 & 0 & -\text{Э} \end{bmatrix} \begin{bmatrix} D_{10} \\ D_{20} \\ D_{30} \\ D_{40} \\ D_{11} \\ D_{21} \\ D_{31} \\ D_{41} \\ P_{L1} \\ P_{L2} \end{bmatrix} = \begin{bmatrix} F_{10} \\ F_{20} \\ F_{30} \\ F_{40} \\ F_{11} \\ F_{21} \\ F_{31} \\ F_{41} \\ 0 \\ 0 \end{bmatrix} \tag{6.12}$$

(where D_{ij} and F_{ij} are the displacements/rotations and forces/moments of structure j, respectively. Subscript i can be 1, 2, 3 or 4 which relates to the four degrees of freedom of each structure, i.e. rotation at the two attachment nodes, displacement and rotation at the

central node. P_{L1} and P_{L2} are Lagrangian multipliers, and. $\Im$ is a small positive constant, e.g. 10^{-8}.

In Eq (6.12), the first four rows contain the 4×4 stiffness matrix of S_0, while the next four rows contain the stiffness matrix of S_1. In forming the stiffness matrices of each structure, rows and columns related to zero displacements and rotation are omitted, i.e. those relating to the displacement and rotation of nodes 1 and 5 and also the displacements at nodes 2 and 4 of structure S_0 are eliminated. The same applies to structure S_1 in which the matrix elements corresponding to vertical displacements of nodes 1 and 3 are left out. The last two rows contain the two (2×4) constraint matrices. Each constraint matrix has non-zero elements coupling degrees of freedom of S_0 and S_1. The (4×2) matrices in the last two columns are the transposes of these constraint matrices.

Having formed the global stiffness matrix for the problem, the eigenvalues can be obtained using W-W algorithm. In order to do this, it is necessary to obtain

$$J = s\{\mathbf{K}\} - r \tag{6.13}$$

Using analysis similar to that of Chapter 2, Eq (6.13) is further developed, for a problem with n coupled structures, to

$$J = \sum_{i=1}^{n} (J_{0i} + s\{\mathbf{K}_i\}) + s\{\mathbf{R}\} - r \tag{6.14}$$

In Eq (6.14) the first term can be obtained from the exact member equations, and **R** can also be obtained as [6.6]

$$\mathbf{R} = -\sum_{i=1}^{n} \mathbf{E}_i \mathbf{K}^{-1}{}_i \mathbf{E}_i^T \tag{6.15}$$

where $\mathbf{K}_i$ and $\mathbf{E}_i$ are the stiffness and constraint matrices, respectively, for structure i.

In Eq (6.14) J_{0i} is the number of eigenvalues for each element and is obtained from the formulae given in [6.5].

To further clarify how these formula are used to obtain J, sample upper triangulated stiffness matrices for structures S_0 and S_1 accompanied by the **R** matrix are

$$\mathbf{K}_0^{\Delta} = \begin{bmatrix} 250645.3 & -197.35 & 493.58 & 0 \\ 0 & -0.311 & 0.39 & 197.35 \\ 0 & 0 & 985.89 & 740.01 \\ 0 & 0 & 0 & 375227.4 \end{bmatrix}$$

$$\mathbf{K}_1^{\Delta} = \begin{bmatrix} 62538.04 & 0.04 & -62538.2 & 0 \\ 0 & -79.05 & 0.04 & -0.0395 \\ 0 & 0 & 62537.64 & -62538.2 \\ 0 & 0 & 0 & -0.79 \end{bmatrix}$$

$$\mathbf{R}^{\Delta} = \begin{bmatrix} 1.26 & 1.26 \\ 0 & -0.000035 \end{bmatrix} \tag{6.16}$$

Hence,

$$s\{\mathbf{K}_0\}=1;\ s\{\mathbf{K}_1\}=2;\ s\{\mathbf{R}\}=1;\ r=2 \text{ and } J_{00}=J_{0i}=0$$

$$J=s\{\mathbf{K}_0\}+s\{\mathbf{K}_1\}+s\{\mathbf{R}\}\text{-}r=(1+2)+1-2=2 \tag{6.17}$$

An analogous procedure is used for configuration 2, i.e. structures $S_d + S_2$. Here the stiffness matrix for S_d is of order 6 × 6, corresponding to rotations at nodes 2 and 5, and to displacements and rotations at nodes 3 and 4. The stiffness matrix for S_2 is of order 4 × 4, corresponding to rotations at nodes 1 and 3, and to displacement and rotation at node 2. There are 4 constraints, relating the degrees of freedom at nodes 2, 3 and 5 of structure S_d to those at nodes 1, 2 and 3 of structure S_2.

Once J counts are counted for both configurations, it is intended to obtain J counts of the delaminated structure from the configuration of Eq (6.2), i.e.

$$J(S_0 \underset{b}{+} S_1) = J(S_d \underset{b,i}{+} S_2) \tag{6.18}$$

where

$$J\left(S_0 \underset{b}{+} S_1\right) = (J_{00} + s\{\mathbf{K}_0\}) + (J_{01} + s\{\mathbf{K}_1\}) + (s\left\{\mathbf{R}_{0\,\underset{b}{+}\,1}\right\} - r_{0\,\underset{b}{+}\,1})$$

$$J\left(S_d \underset{b,i}{+} S_2\right) = (J_{0d} + s\{\mathbf{K}_d\}) + (J_{02} + s\{\mathbf{K}_2\}) + (s\left\{\mathbf{R}_{d\,\underset{bi}{+}\,2}\right\} - r_{d\,\underset{bi}{+}\,2}) \tag{6.19}$$

Here, $\mathbf{R}_{0\,\underset{b}{+}\,1}$ and $\mathbf{R}_{\mathrm{d}\,\underset{bi}{+}\,2}$ are the **R** matrices for configurations 1 and 2, respectively; $r_{0\,\underset{b}{+}\,1}$ and $r_{\mathrm{d}\,\underset{bi}{+}\,2}$ are their orders.

Substituting Eq (6.19) into Eq (6.18) yields

$$J(S_{\mathrm{d}}) = (J_{0\mathrm{d}} + s\{\mathbf{K}_{\mathrm{d}}\}) = \tag{6.20}$$

$$(J_{00} + s\{\mathbf{K}_0\}) + (J_{01} + s\{\mathbf{K}_1\}) - (J_{02} + s\{\mathbf{K}_2\}) + (s\left\{\mathbf{R}_{0\,\underset{b}{+}\,1}\right\} - r_{0\,\underset{b}{+}\,1}) - (s\left\{\mathbf{R}_{\mathrm{d}\,\underset{bi}{+}\,2}\right\} - r_{\mathrm{d}\,\underset{bi}{+}\,2})$$

Since structures S_1 and S_2 are identical,

$$(J_{01} + s\{\mathbf{K}_1\}) = (J_{02} + s\{\mathbf{K}_2\}) \tag{6.21}$$

and so Eq (6.34) is simplified to

$$J(S_{\mathrm{d}}) = (J_{0\mathrm{d}} + s\{\mathbf{K}_{\mathrm{d}}\}) = \tag{6.22}$$

$$(J_{00} + s\{\mathbf{K}_0\}) + (s\left\{\mathbf{R}_{0\,\underset{b}{+}\,1}\right\} - r_{0\,\underset{b}{+}\,1}) - (s\left\{\mathbf{R}_{\mathrm{d}\,\underset{bi}{+}\,2}\right\} - r_{\mathrm{d}\,\underset{bi}{+}\,2})$$

The idea of the negative stiffness method is to replace analysis of structure S_d by analysis of the simpler structures S_0, S_1 and S_2. Thus the term $(s\left\{\mathbf{R}_{d\,\underset{bi}{+}\,2}\right\} - r_{d\,\underset{bi}{+}\,2})$ in Eq (6.22) is unknown but, it is proposed to approximate it to $(s\left\{\mathbf{R}_{0\,\underset{bi}{+}\,2}\right\} - r_{0\,\underset{bi}{+}\,2})$. Doing this would significantly facilitate the process for obtaining the J counts of the delaminated structure and thereby finding its critical buckling load.

6.5 Results

Based on the procedure outlined above values of J for both configurations have been obtained (using Microsoft Excel software [6.8]) which are plotted against the applied load in Figure 6.4. Two mesh patterns, a rough mesh ($n = 2$) and a more refined mesh ($n = 4$) were adopted. As stated earlier, since $S_0 + S_1$ and $S_d + S_2$ represent physically equivalent structures they should have the same J. As Figure 6.4 shows, despite using a more refined mesh ($n = 4$) there are discrepancies between the J values of the two configurations. For example for the case studied the first, second and third eigenvalues are located at 68.07, 101.06 and 135.8 (N), respectively. In considering a load factor of up to 290 (N), it was found that 6 eigenvalues are exceeded (represented by the number of changes in the value of J) for $S_d + S_2$ while only 4 eigenvalues are exceeded for $S_0 + S_1$. Occurrence of more eigenvalues for $S_d + S_2$ means more local effects are captured.

Figure 6.5 illustrates the first three buckling loads for the structure. Trends related to the more refined mesh are shown with a dashed line. It can be seen that in each configuration the case of $n = 4$ gives a higher critical load. This can be related to the use

of more constraints which to some extent prevents local buckling behaviour between successive attachment points and consequently introduces a stiffer model. It can also be noticed that in configuration $S_0 + S_1$, the eigenvalues are always higher than those of the other configuration which can be regarded as due to the existence of the perfect beam structure. The perfect beam has no geometric and material discontinuity; so it adds to the stiffness of the whole structure. On the other hand, $S_d + S_2$ has less continuity than the other configuration; it seems to have local effects that introduce additional eigenvalues.

It should be noted that this approach could have been tried with much finer mesh (i.e. $n = 10$ or 20), but the initial analysis of the problem for mesh density of $n = 2$ and 4 reveals that there are some doubts regarding approximating $(s\{\mathbf{R}_{d\,\overset{+}{bi}\,2}\} - r_{d\,\overset{+}{bi}\,2})$ with $\left(s\{\mathbf{R}_{0\,\overset{+}{bi}\,2}\} - r_{0\,\overset{+}{bi}\,2}\right)$.

6.6 Conclusions

The buckling behaviour of a beam structure modelled by two different configurations has been investigated analytically. The examined structure was assembled from two Bernoulli-Euler beams which were attached to each other at discretely constrained intervals. Results of the analysis are compared for both configurations. As both idealisations represent the same physical structure, it is expected to obtain similar J counts and buckling behaviour, but this does not happen. The reason is the attachment of the constituents of the final structure at discrete points which brings about geometric discontinuity in the problem of study. Basically, it is expected that good results (equal

buckling behaviour for both idealisations) could be obtained by increasing the number of attachment points, but this leads to increased time of analysis, and is expected to overweigh the benefit of the usage of W-W algorithm. This finding can be generalised and applied to the problem of delaminated composite plates, i.e. the usage of negative stiffness modelling to represent a delaminated composite plate is not a practical method of analysis. It should be noted that this does not mean that the use of common points is incapable of dealing with delamination, theoretically. This method can be efficient when dealing with just a few constraints in the problem. However in larger problem it is too computationally expensive. Hence, we can conclude that for predicting the buckling behaviour of a given delaminated composite plate, recourse must be made to an efficient and practical model which can deal with the problem in the least time within a good range of accuracy. The common point approach can not therefore be used for such problems in general.

6.7 References

[6.1] E. Lightfoot, Exact straight-line elements, *J. Strain Anal.*, **15** (2), 89-96 (1980).

[6.2] S. Blaszkowiak and Z. Kaczkowski, Iterative Methods in Structural Analysis Pergamon Press, Oxford (1966).

[6.3] W. P. Howson and F. W. Williams, Natural frequencies of frames with axially loaded Timoshenko members, *J. Sound Vib.*, **26** (4), 503 (1973).

[6.4] W. H.Wittrick and F. W. Williams, Buckling and vibration of anisotropic and isotropic plate assemblies under combined loadings, *int. J. Mech. Sci*, **16** (4), 209-239 (1974).

[6.5] W. P. Howson, J. R. Banerjee and F. W. Williams, Concise equations and program for eigensolutions of plane frames including member shear, *Adv. Eng. Software*, **5** (3), 137-141 (1983).

[6.6] F. W. Williams and M. S. Anderson, Incorporation of lagrangian multipliers into an algorithm for finding exact natural frequencies or critical buckling loads, *int. J. Mech. Sci*, **25** (8), 579-584 (1983).

[6.7] M. S. Anderson, F. W. Williams, Buckling and vibration of any prismatic assembly of shear and compression loaded anisotropic plates with an arbitrary supporting structure, *int. J. Mech. Sci*, **25** (8), 585-596 (1983).

[6.8] Microsoft Office Excel 2007, Microsoft Corporation (2007).

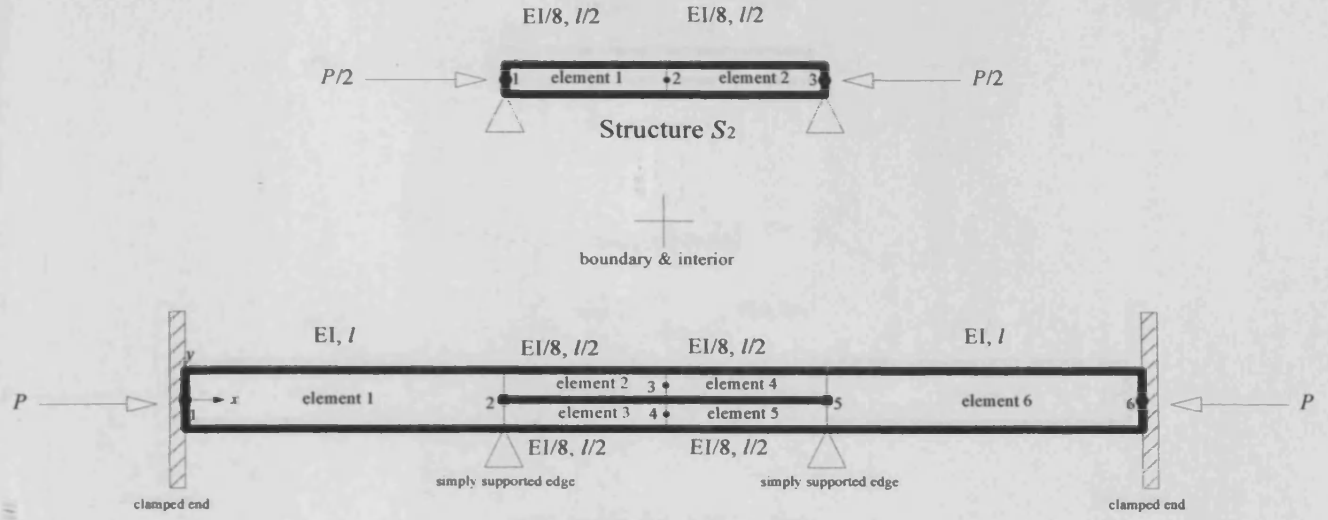

(a)

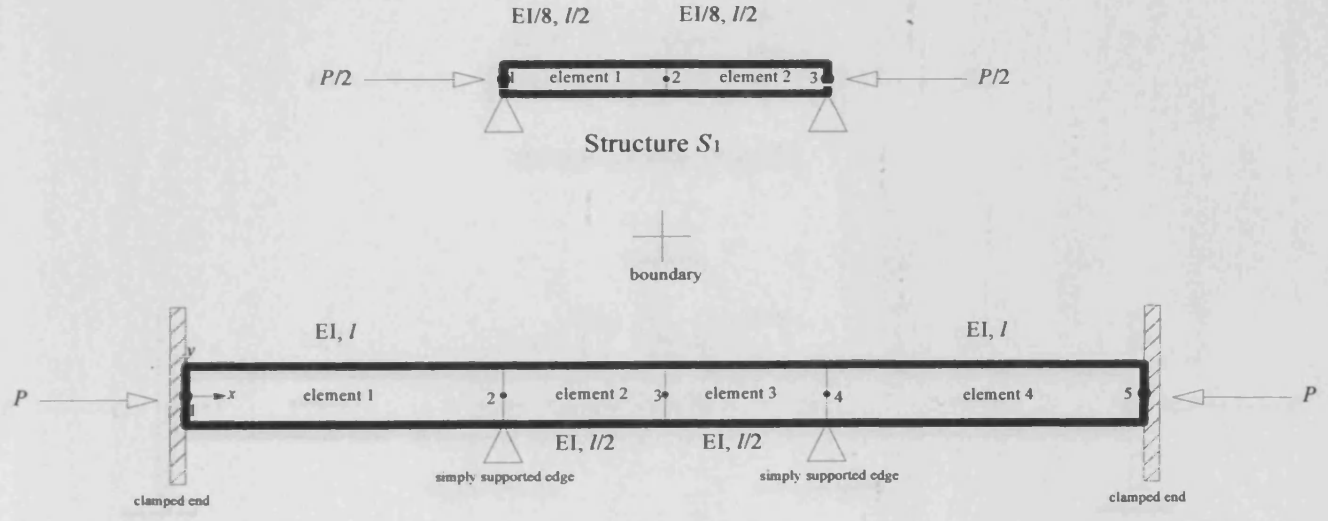

(b)

Figure 6.1: Schematic representation of present study for rough meshing, i.e. $n = 2$,

(a) S_d and S_2 are connected at the boundary and interior, (b) S_0 and S_1 are connected at the boundary only.

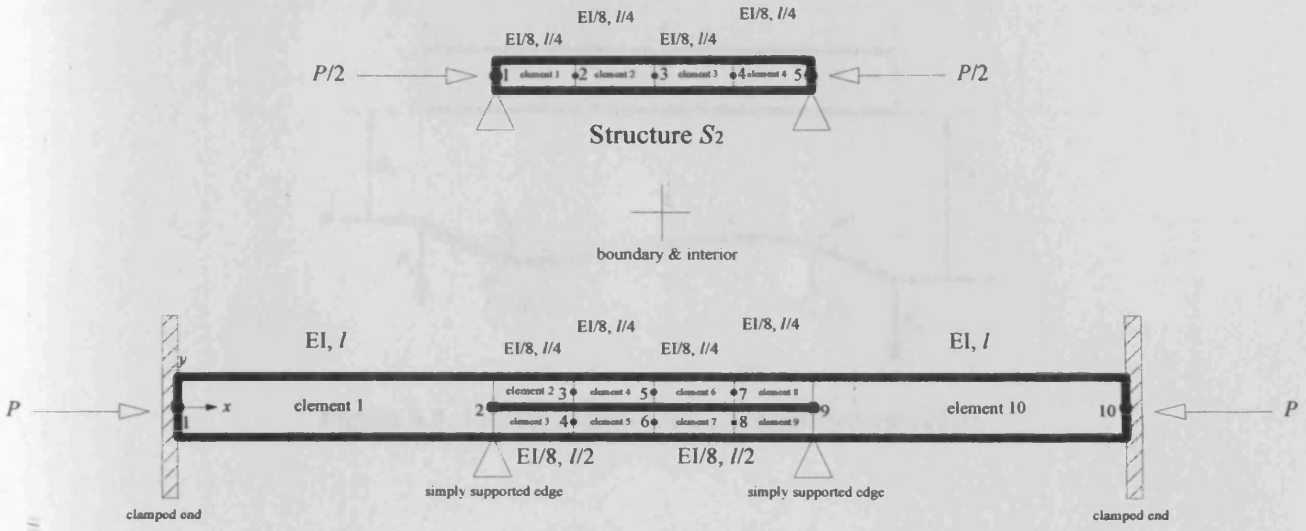

(a)

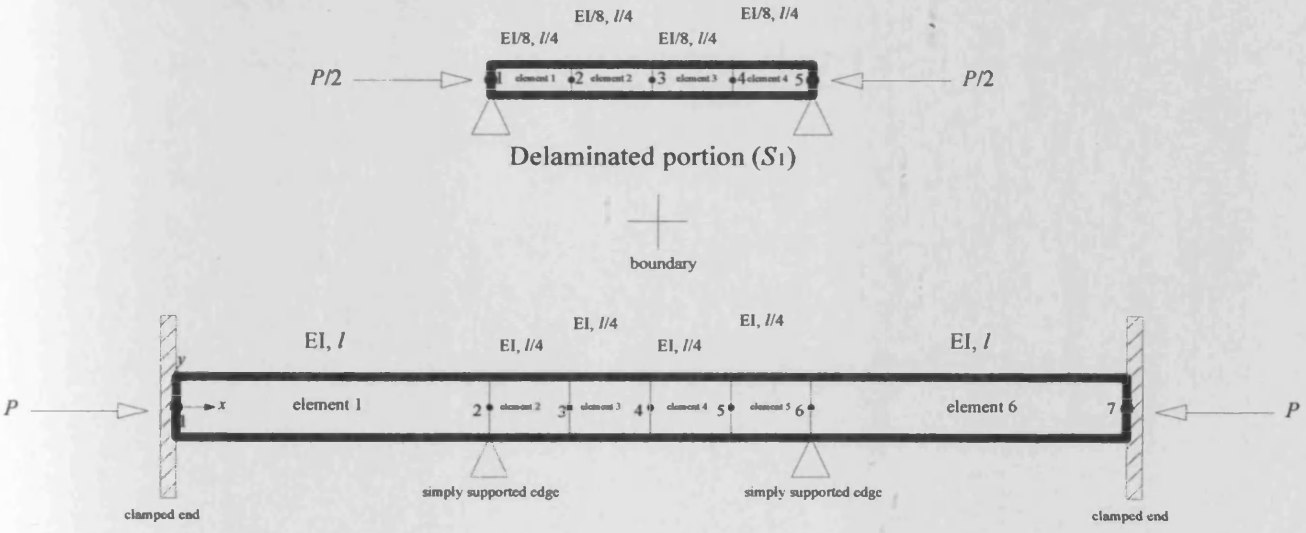

(b)

Figure 6.2: Schematic representation of present study for rough meshing, i.e. $n = 4$,

(a) S_d and S_2 are connected at the boundary and interior, (b) S_0 and S_1 are connected at the boundary only.

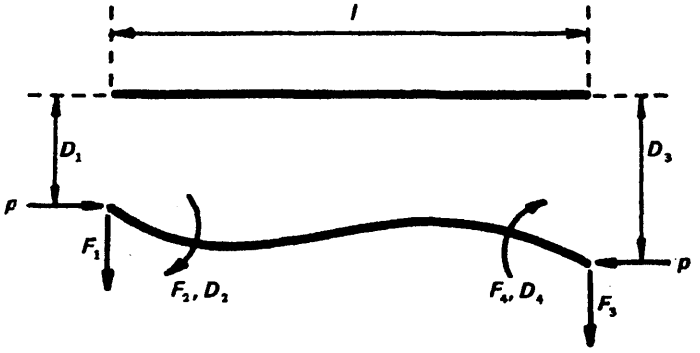

Figure 6.3: Member end forces and displacements [6.3]

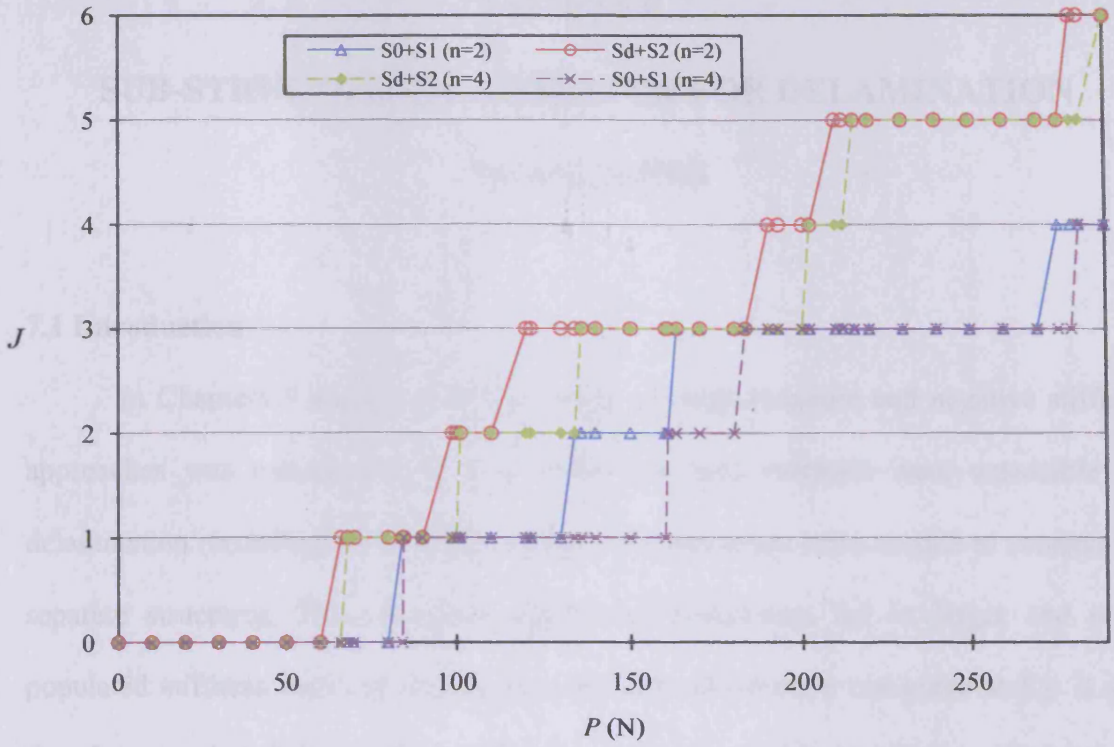

Figure 6.4: J_L versus compressive load for S_d and S_2 connected at the boundary and interior, and S_0 and S_1 connected at the boundary only.

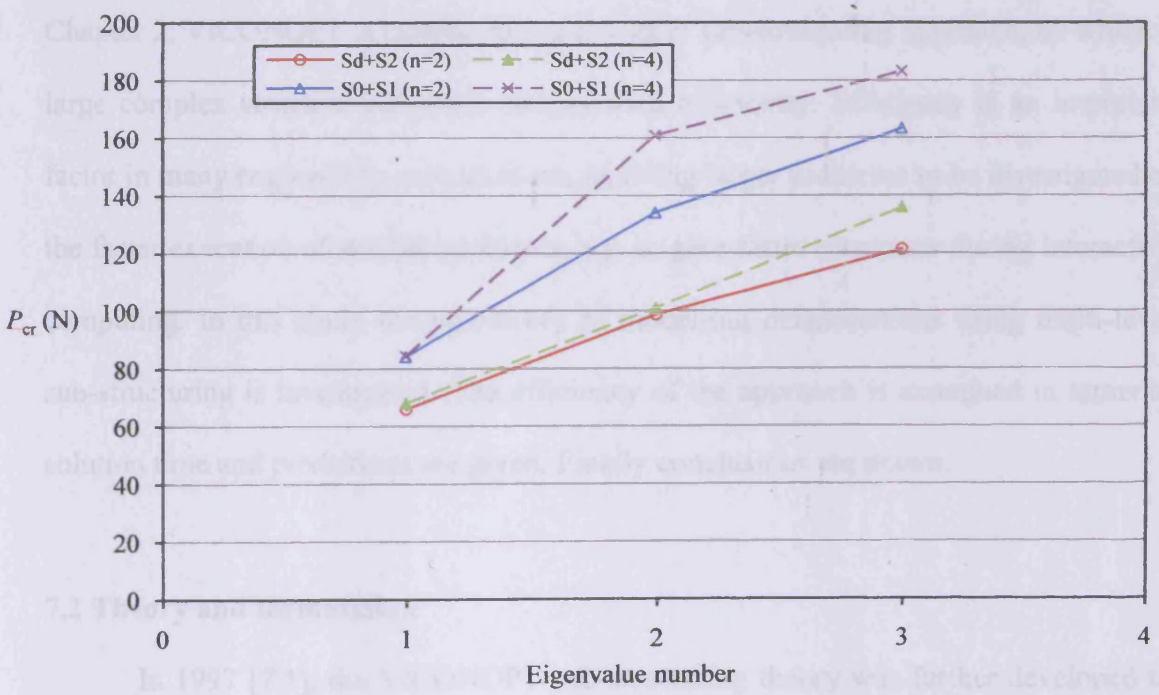

Figure 6.5: Lowest three eigenvalues (i.e. buckling loads) for two configurations.

CHAPTER 7

SUB-STRUCTURING APPROACH FOR DELAMINATION MODELLING

7.1 Introduction

In Chapters 5 and 6 a thorough study of multi-structure and negative stiffness approaches was carried out. It was found that both methods were unsuitable for delamination modelling since large numbers of constraints were needed to connect the separate structures. This increased number of constraints led to larger and more populated stiffness matrices making the methods unattractive computationally. It was therefore concluded that further approaches must be considered which might keep the size of the stiffness matrix and therefore the time of analysis small. As explained in Chapter 2, VICONOPT is capable of a multi-level sub-structuring approach, by which a large complex structure can often be modelled efficiently. Efficiency is an important factor in many engineering computations, enabling larger problems to be investigated or the faster execution of smaller problems, e.g. to give faster responses during interactive computing. In this study the possibility of modelling delaminations using multi-level sub-structuring is investigated. The efficiency of the approach is examined in terms of solution time and predictions are given. Finally conclusions are drawn.

7.2 Theory and formulation

In 1997 [7.1], the VICONOPT sub-structuring theory was further developed to allow the inclusion of point constraints at the internal or external degrees of freedom of the sub-structures. After elimination of the internal nodes of the sub-structures, this

theory gives the following matrices for the parent structure (in this example three sub-structures are assumed) for one typical half-wavelength λ_m :

$$\mathbf{K}_{mf}=\begin{bmatrix} \mathbf{K}_{cm1}{}^{*}+\mathbf{K}_{pm1} & \mathbf{K}_{qm12} & \mathbf{K}_{qm13} & \mathbf{K}_{rm1} \\ \mathbf{K}_{qm12}{}^{H} & \mathbf{K}_{cm2}{}^{*}+\mathbf{K}_{pm2} & \mathbf{K}_{qm23} & \mathbf{K}_{rm2} \\ \mathbf{K}_{qm13}{}^{H} & \mathbf{K}_{qm23}{}^{H} & \mathbf{K}_{cm3}{}^{*}+\mathbf{K}_{pm3} & \mathbf{K}_{rm3} \\ \mathbf{K}_{rm1}{}^{H} & \mathbf{K}_{rm2}{}^{H} & \mathbf{K}_{rm3}{}^{H} & \mathbf{K}_{umf} \end{bmatrix} \tag{7.1}$$

$$\mathbf{D}_{m_f}=\begin{bmatrix} \mathbf{D}_{cm1} \\ \mathbf{D}_{cm2} \\ \mathbf{D}_{cm3} \\ \mathbf{D}_{umf} \end{bmatrix} \tag{7.2}$$

$$\mathbf{e}_{m_f}=\begin{bmatrix} \mathbf{A}_{m1} & \mathbf{0} & \mathbf{0} & \mathbf{0} \\ \mathbf{e}_{cm1} & \mathbf{0} & \mathbf{0} & \mathbf{0} \\ \mathbf{e}_{pm1} & \mathbf{0} & \mathbf{0} & \mathbf{0} \\ \mathbf{0} & \mathbf{A}_{m2} & \mathbf{0} & \mathbf{0} \\ \mathbf{0} & \mathbf{e}_{cm2} & \mathbf{0} & \mathbf{0} \\ \mathbf{0} & \mathbf{e}_{pm2} & \mathbf{0} & \mathbf{0} \\ \mathbf{0} & \mathbf{0} & \mathbf{A}_{m3} & \mathbf{0} \\ \mathbf{0} & \mathbf{0} & \mathbf{e}_{cm3} & \mathbf{0} \\ \mathbf{0} & \mathbf{0} & \mathbf{e}_{pm3} & \mathbf{0} \\ \mathbf{0} & \mathbf{0} & \mathbf{0} & \mathbf{e}_{umf} \end{bmatrix} \tag{7.3}$$

$$\gamma_f = \begin{bmatrix} \gamma_{i1} \\ \gamma_{c1} \\ \gamma_{p1} \\ \gamma_{i2} \\ \gamma_{c2} \\ \gamma_{p2} \\ \gamma_{i3} \\ \gamma_{c3} \\ \gamma_{p3} \\ \gamma_{uf} \end{bmatrix} \tag{7.4}$$

$$\mathbf{R}_{0f} = \text{Diag}\,[\mathbf{B}_{m1}, \mathbf{0}, \mathbf{0}, \mathbf{B}_{m2}, \mathbf{0}, \mathbf{0}, \mathbf{B}_{m3}, \mathbf{0}, \mathbf{0}, \mathbf{0}, \mathbf{0}, \mathbf{0}] \tag{7.5}$$

$\mathbf{D}_{cms}$ is related to the degrees of freedom of the nodes in sub-structure s (s = 1, 2, 3) which are connected to the parent structure, and $\mathbf{D}_{umf}$ is associated with those degrees of freedom of the nodes of the parent structure which are not connected to the sub-structure. $\mathbf{K}_{cms}^{*}$ is the matrix resulting from partial triangulation of the stiffness matrix of sub-structure s; $\mathbf{A}_{ms}$ is the correspondingly modified constraint matrix for sub-structure s; and $\mathbf{B}_{ms}$ is the consequent contribution to the **R** matrix of Eq (2.27). The remaining term in $\mathbf{K}_{mf}$ arise from partitioning of the parent structure's stiffness matrix. $\mathbf{e}_{cms}$ and $\mathbf{e}_{pms}$ relate to constraints applied to sub-structure s and the parent structure, respectively, at the connection nodes; $\mathbf{e}_{umf}$ relates to constraints applied elsewhere to the parent structure. γ_{is}, γ_{cs}, γ_{ps} and γ_{uf} are vectors of Lagrangian multipliers related to constraints at the internal nodes of sub-structure s, the nodes of sub-structure s which are connected to the parent structure, the nodes of the parent structure and the nodes of parent structure which are not connected to any sub-structure, respectively. The reader

is referred to reference [7.1] for comprehensive information regarding sub-structuring in VICONOPT.

As mentioned earlier, the purpose of sub-structuring is to reduce the time of analysis and data preparation. The amount of work required to obtain the solution of Eq (2.24) is attributed to the following

1- Gauss elimination of the $\mathbf{K}_m$ matrix.

2- Gauss elimination of the **R** matrix.

3- Work done to assemble and arrange the stiffness and constraint matrices.

Computational time is chiefly governed by the Gauss elimination process. In other words, W_L, the total number of multiplications required to change $\mathbf{K}_m$ and **R** to triangular form, can be valued as an approximate criterion of the computational effort engaged at each trial frequency or load factor φ_t.

The approximate work W_F [7.1] involved in triangulating each parent structure stiffness matrix $\mathbf{K}_{mf}$ of Eq (7.1) is calculated as

$$W_F = 32NC\left(C + \frac{r}{4}\right) + \frac{2}{3}Nr^2 \tag{7.6}$$

where N is the number of nodes, C is one plus the maximum difference between the node numbers of any two connected nodes and r is the total number of constraints, including those in contained sub-structures. For singly and doubly connected sub-structures $C = 2$ and $C = 3$, respectively. Replacing suitable C and r in Eq (7.6) will give

$$W_s = 16N_s(8 + r_s) + \frac{2}{3}Nr_s^2 \tag{7.7}$$

for singly connected sub-structures and

$$W_D = 24N_s(12 + r_s) + \frac{2}{3} Nr_s^2 \tag{7.8}$$

for doubly connected sub-structures, where N_s is the number of internal nodes of the sub-structure, and r_s is the total number of constraints on the internal nodes, including those in contained sub-structures.

Finally the number of multiplications required to triangulate **R** is approximately

$$W_R = \frac{1}{6} r^3 \tag{7.9}$$

Hence, the total computational effort for one trial value φ_t is estimated by

$$W_L = m'(\sum W_s + \sum W_D + W_F) + W_R \tag{7.10}$$

Where m' is the total number of half-wavelengths used in the analysis.

7.3 Methodology

It was considered advisable in examining the possibility of using sub-structuring to model delamination to first investigate whether such a method would allow solution times to be reduced in comparison with more conventional methods (i.e. those presented in Chapters 3, 5 and 6).

As stated earlier, the rectangular delamination of Chapter 5 can be modelled as shown in Figure 7.1 (with dimensions and stacking sequence which for the purposes of this study are abitrary). Modelling the delamination in this way however increases the time of analysis due to the number of constraints (for this example 103 constraints; i.e.

9 at each of the 7 internal nodes and 20 at each of the 2 edges of the delamination) added to the problem. (In this method the degrees of freedom of structure 1 (containing nodes 1, ..., 9) are coupled with those of structure 2 (at nodes 4, ... , 12) everywhere except in the rectangular delaminated portion area using the multi-structure approach.)

An alternative method is shown in Figure 7.2. Structure 1 (the top sub-laminate) and that part of structure 2 which contains nodes 4, 5, ... , 19 (the bottom sub-laminate) are modelled using three levels of sub-structuring. In level i (=1, 2), there are sub-structures of level $i + 1$ between nodes 2 and 1, and between nodes 1 and 3. Node 1 is an internal node whilst nodes 2 and 3 are points of connection to the parent structure/sub-structure. All the levels of sub-structuring consist of doubly connected sub-structures. Those portions of Figure 7.2 that are located between nodes 1, ... , 4 and 19, ... , 22 are the parent structure. Each sub-structure includes parts of the top and bottom sub-laminates, which are connected together using attachment points (cross marks in Figure 7.2) in their un-delaminated regions.

7.4 Results

The amount of work needed to model delamination using the multi-structure approach (Figure 7.1) is calculated and compared with that of the multi-level sub-structuring method (Figure 7.2). The amount of work required to solve the problem using both methods is estimated in Tables 7.1 and 7.2.

Here N is the number of nodes, C is one plus the maximum difference between the node numbers of any two connected nodes and r is the total number of constraints, including those in contained sub-structures. Subscript i in Table 7.1 represents the structure number, i.e. N_1 is the number of nodes in structure 1. m' is the number of half-wavelengths used for analysis.

W_F is the work involved in triangulating each parent structure stiffness matrix. W_R is the number of multiplications required to triangulate the **R** matrix. W_L is the estimated total computational effort for one trial value φ_t.

The numbers in Table 7.1 are obtained from Eq (7.6) for each structure, and then used in Eq (7.9) and (7.10) to obtain the final W_L. The calculation is done for 10 half-wavelengths.

Since the existing sub-structures are doubly connected sub-structures, Eq (7.8) is used to estimate the amount of work required for the sub-structure analysis. For the sake of clarity a typical calculation for the sub-structuring of level 1 is as

$$W_{D1} = \left[24 \times 1 \times (12 + 9) + \frac{2}{3} \times 3 \times 9^2\right] \tag{7.11}$$

Comparing the results of Tables 7.1 and 7.2 shows that using the sub-structuring method would decrease the amount of work to analyze the model by about 56%, but it is necessary to point out that even then the solution time is estimated to be considerably higher than would be associated with using the FE method for example with the ABAQUS package, e.g. see Figure 5.5.

7.5 Conclusions

A feasibility study for using multi-level sub-structuring was carried out. It was found that sub-structuring can decrease the time of analysis for multi-structure delamination modelling substantially, but not enough to render this approach competitive against FEA. Alternative methods are required to produce results with good accuracy and acceptable analysis time.

7.6 References

[7.1] S. M. Powell, D. Kennedy and F. W. Williams, Efficient multi-level substructuring with constraints for buckling and vibration analysis of prismatic plate assemblies, *Int. J. Mech. Sci.*, **39**(7), 795 805 (1997).

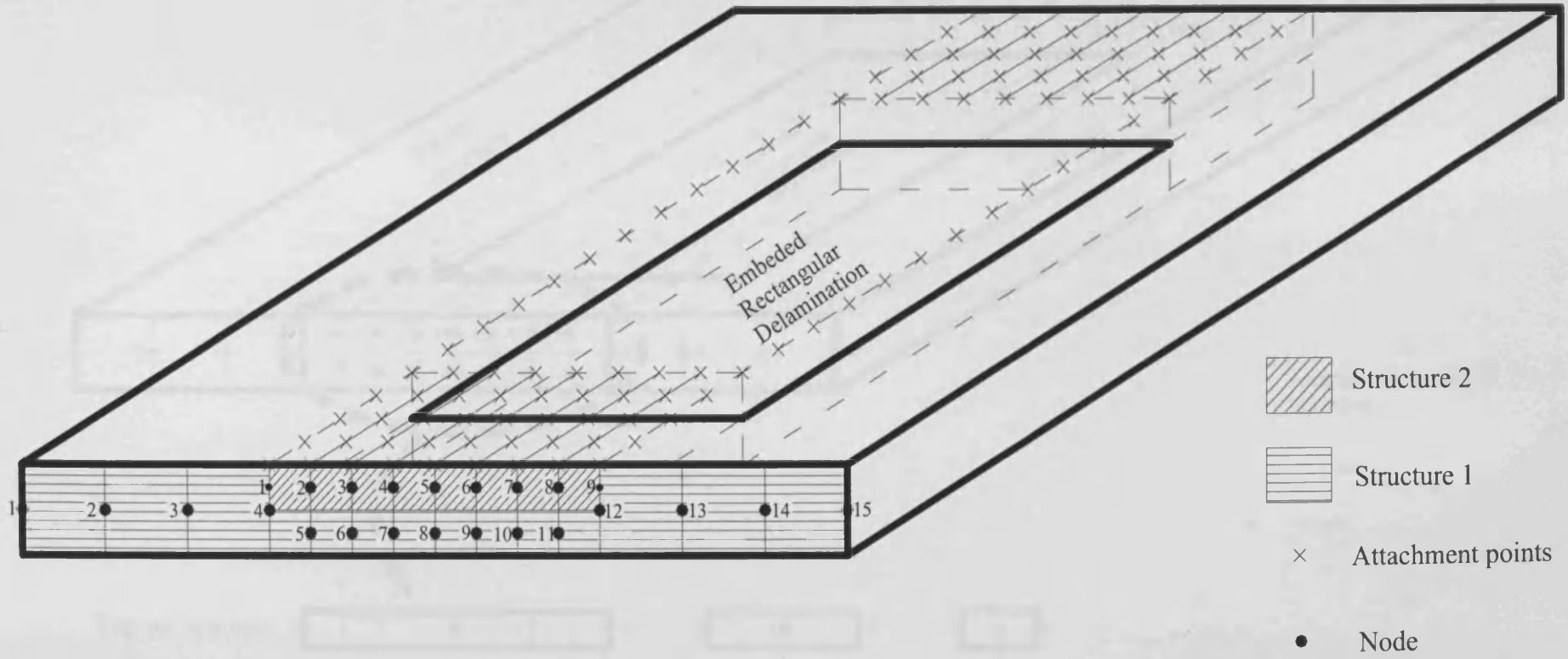

Figure 7.1: Illustration of a typical composite plate with central rectangular delamination; cross marks represent the Common Points between upper and lower sub-laminates in the delaminated strip (numbers in the figure represent node numbers).

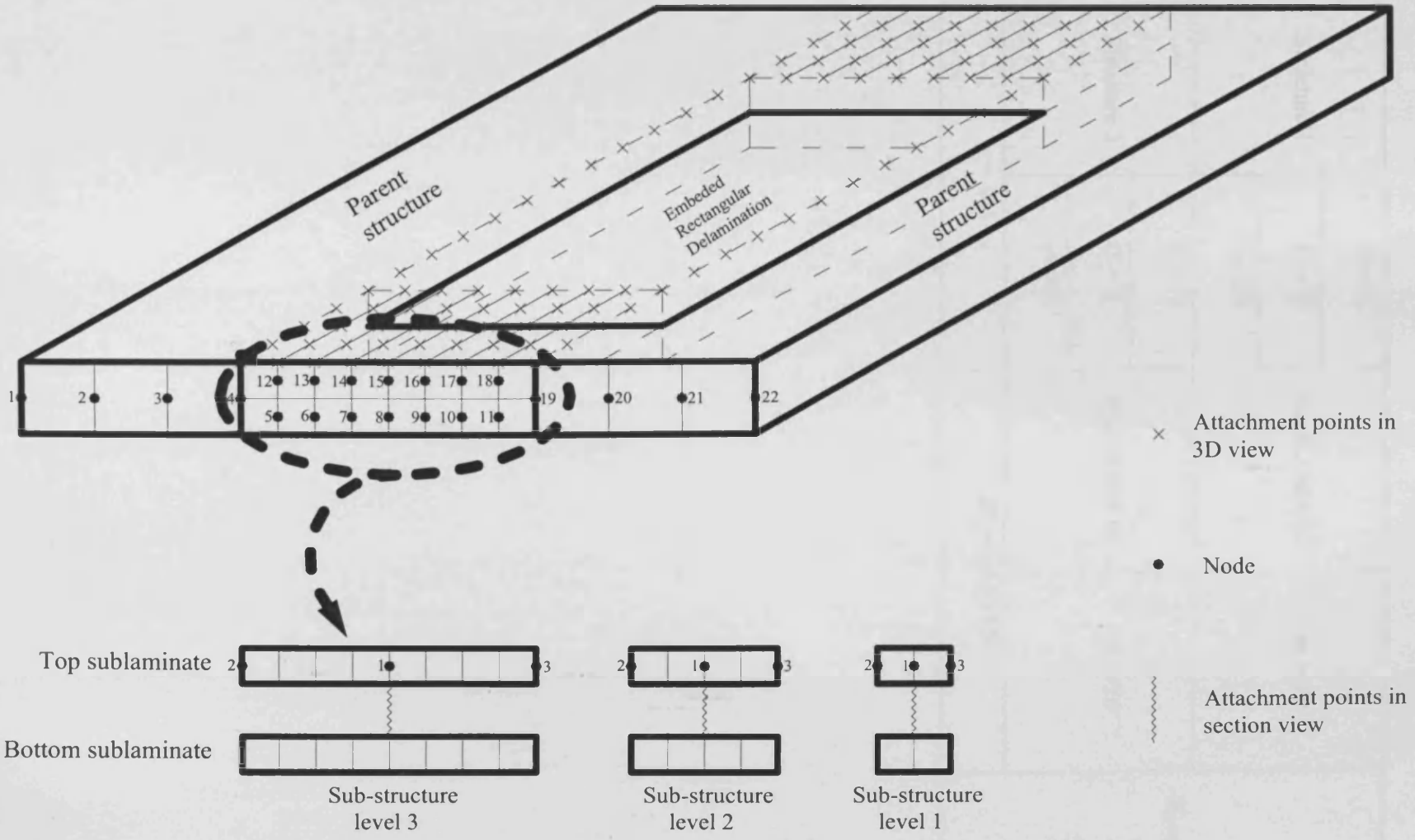

Figure 7.2: Illustration of multi-level sub-structuring of delaminated composite plate (numbers in the figure represent node numbers).

Table 7.1: The amount of work required to triangulate the stiffness matrix of a delaminated composite plate using the multi-structure approach.

<table>
<tr><td rowspan="3">Structure 1</td><td>$N_1 = 9$</td><td rowspan="3">$W_{F2} = 7.96\times10^4$</td><td rowspan="3">$m' = 10$</td><td rowspan="6">$W_L = 2.32\times10^6$</td></tr>
<tr><td>$C_1 = 2$</td></tr>
<tr><td>$r_1 = 103$</td></tr>
<tr><td rowspan="3">Structure 2</td><td>$N_2 = 15$</td><td rowspan="3">$W_{F1} = 1.33\times10^5$</td><td rowspan="3">$m' = 10$</td></tr>
<tr><td>$C_2 = 2$</td></tr>
<tr><td>$r_2 = 103$</td></tr>
<tr><td colspan="2">$r = 103$</td><td colspan="2">$W_R = 1.82\times10^5$</td></tr>
</table>

Table 7.2: The amount of work required to triangulate the stiffness matrix of a delaminated composite plate using multi-level sub-structuring.

<table>
<tr><td rowspan="10">Sub-structure</td><td rowspan="3">Level 1</td><td>$N_{s1} = 1$</td><td rowspan="3">$W_{D1} = 6.66\times10^{2}$</td><td rowspan="10">$m'=10$</td><td rowspan="13">$W_L=1.02\times10^{6}$</td></tr>
<tr><td>$N_1 = 3$</td></tr>
<tr><td>$r_{s1} = 9$</td></tr>
<tr><td rowspan="3">Level 2</td><td>$N_{s2} = 1$</td><td rowspan="3">$W_{D2} = 2.39\times10^{3}$</td></tr>
<tr><td>$N_2 = 3$</td></tr>
<tr><td>$r_{s2} = 27$</td></tr>
<tr><td rowspan="3">Level 3</td><td>$N_{s3} = 1$</td><td rowspan="3">$W_{D3} = 9.74\times10^{3}$</td></tr>
<tr><td>$N_3 = 3$</td></tr>
<tr><td>$r_{s3} = 63$</td></tr>
<tr><td colspan="2" rowspan="3">Parent structure</td><td>$N_p = 8$</td><td rowspan="3">$W_{FP} = 7.08\times10^{4}$</td></tr>
<tr><td>$C = 2$</td><td rowspan="2">$m'=10$</td></tr>
<tr><td>$r_p = 103$</td></tr>
<tr><td colspan="2"></td><td>$r = 103$</td><td colspan="2">$W_R = 1.82\times10^{5}$</td></tr>
</table>

CHAPTER 8

SIMPLE SMEARING METHOD FOR DELAMINATION MODELLING

8.1 Introduction

So far a number of different methods have been used to model delamination in VICONOPT including conventional modelling (Chapter 3), the use of a multi-structure approach (Chapters 4 and 5), a negative stiffness approach (Chapter 6) and multi-level sub-structuring (Chapter 7). Each of the methods used has had advantages and disadvantages. For example, conventional modelling gives good results which are comparable with those obtained from FE analysis, but can only be used for through-the-length (strip) delaminations and certain boundary conditions. The multi-structure approach gives accurate results (but at the expense of significantly increased time of analysis) and can be applied to any delamination shape - rectangular, circular, elliptical and triangular. It is particularly useful when the size of the delamination is large compared to the dimensions of the 'parent' plate, since the computational disadvantage is reduced. But as the size of delamination decreases, more constraints are required in order to attach the two constituent structures which form the model and the time of analysis increases drastically. An attempt to remedy this by using a 'negative stiffness' approach proved to be inaccurate, due to approximations introduced in the analysis. Finally although sub-structuring was predicted to provide some time savings when compared to the standard multi-structure approach, the method was still not competitive and therefore was ruled out for delamination modelling. Hence, alternative methods of modelling delaminations with any shape and position within a structure but which require less solution time are needed. These need to be consistent with the requirement

that in VICONOPT, all assemblies must be or must be approximated to be prismatic or modelled by one or more prismatic structures.

Previous researchers have modelled delamination by reducing element material properties E_{11}, E_{22}, E_{12} and G_{12} to effectively alter the membrane stiffness of the structure while the bending stiffness is barely affected. In the present study it is intended to use a method introduced by Zhang et al. [8.1] to model the delaminated portion of a structure. However whilst in Zhangs method material properties were kept intact, the proposed method in contrast alters the stiffness matrix to model delamination, as elaborated in the following sections.

8.2 Theory

In Zhang's method [8.1], instead of changing material properties, an equivalent degraded bending stiffness is deduced as follows.

The elasticity law for the laminate is

$$\begin{bmatrix} \mathbf{N} \\ \mathbf{M} \end{bmatrix} = \begin{bmatrix} \mathbf{A} & \mathbf{B} \\ \mathbf{B} & \mathbf{D} \end{bmatrix} \begin{bmatrix} \varepsilon^0 \\ \kappa \end{bmatrix} \tag{8.1}$$

where **A**, **B** and **D** are the membrane, coupling and bending stiffness matrices, respectively. **N** and **M** are laminate stress and moment resultants while ε^0 and κ are the strains and curvatures of the laminate's reference surface. It is presumed that there is a delamination in the laminate as shown in Figure 8.1, dividing the laminate into two sub-laminates. An equivalent laminate will be defined to simulate the influence of the delamination. The mid-plane of the equivalent laminate will be the same as that of the undelaminated laminate. The delamination will have little effect on the in-plane load-carrying ability and, for the sake of simplicity; it is further assumed that the coupling

matrix does not alter as the result of delamination [8.1-8.2]. The new membrane stiffness $\mathbf{A}^*$ and coupling stiffness $\mathbf{B}^*$ can be obtained using the parallel axis theorem, which can be written as

$$\mathbf{A}^* = \mathbf{A}_1 + \mathbf{A}_2 = \mathbf{A}; \mathbf{B}^* = \mathbf{B}_1 + \mathbf{A}_1 z_1 + \mathbf{B}_2 + \mathbf{A}_2 z_2 = \mathbf{B} \tag{8.2}$$

Subscripts 1 and 2 denote the top and bottom sub-laminate, respectively. z_1 and z_2 are the mid-plane coordinates of each sub-laminate in the z-direction.

It is further assumed that both sub-laminates have the same curvature κ and they are under pure bending, i.e. $\mathbf{N} = 0$. The moments of the components can now be calculated based on Eq (8.1). In this way the laminate strains in the top sub-laminate can be expressed in terms of the curvature by

$$\varepsilon_0^{\,l} = -\mathbf{A}_1^{-1}\mathbf{B}_1\kappa \tag{8.3}$$

The moments in the top sub-laminate then take the form

$$\mathbf{M}_1 = \mathbf{B}_1\,\varepsilon_0^{\,l} + \mathbf{D}_1\,\kappa \tag{8.4}$$

Finally, inserting Eq (8.3) into Eq (8.4), the moments are rewritten as

$$\mathbf{M}_1 = \mathbf{D}_1^*\kappa \tag{8.5}$$

where $\mathbf{D}_1^* = \mathbf{D}_1 - \mathbf{B}_1\mathbf{A}_1^{-1}\mathbf{B}_1$.

Similarly, the moments of the second sub-laminate can be written as

$$\mathbf{M}_2 = \mathbf{D}_2^*\kappa \tag{8.6}$$

where $\mathbf{D}_2^* = \mathbf{D}_2 - \mathbf{B}_2\mathbf{A}_2^{-1}\mathbf{B}_2$.

The total moments are then

$$\mathbf{M} = \mathbf{M}_1 + \mathbf{M}_2 \tag{8.7}$$

It should be noted that $\mathbf{A}_1$, $\mathbf{B}_1$, $\mathbf{D}_1$, $\mathbf{A}_2$, $\mathbf{B}_2$ and $\mathbf{D}_2$ are defined around the mid-planes of the first and the second sub-laminate, respectively.

Comparing Eq (8.5) and (8.6), provides a relationship between total moments and the curvature

$$\mathbf{M} = \mathbf{D}^{*}\kappa \tag{8.8}$$

where $\mathbf{D}^{*} = \mathbf{D}_1^{*} + \mathbf{D}_2^{*}$.

However, as mentioned earlier, structures must be prismatic in order to be modelled in VICONOPT., Replacing the delaminated portion of a structure with an equivalent laminate with reduced properties will create a non-prismatic structure whose stiffness is not uniform in the longitudinal direction. Hence, a method to combine the stiffnesses of an equivalent laminate and the remaining undelaminated portions of strips which contain the equivalent laminate must be found. This method will be called 'smearing'. The process described above is shown schematically in Figure 8.2.

Once $\mathbf{A}^{*}$, $\mathbf{B}^{*}$ and $\mathbf{D}^{*}$ matrices are defined for the equivalent laminate, 'smearing' will be implemented in one of three ways, as follows,

1- Linear smearing based on the length of delamination (d) and the length of the plate (l);

In this case, the strip with reduced stiffness (the hatched strip in stage 3 of Figure 8.2) will have the same **A** and **B** matrices as that of the equivalent laminate (based on the assumptions of ref [8.1]), i.e. essentially similar to those of a perfect laminate but its **D** matrix will be altered ;

$$\begin{aligned} \mathbf{A}_r &= (d/l)\,\mathbf{A}^{*} + (1-d/l)\mathbf{A} = \mathbf{A} \\ \mathbf{B}_r &= (d/l)\,\mathbf{B}^{*} + (1-d/l)\mathbf{B} = \mathbf{B} \\ \mathbf{D}_r &= (d/l)\,\mathbf{D}^{*} + (1-d/l)\,\mathbf{D} \end{aligned} \tag{8.9}$$

where $\mathbf{A}_r$, $\mathbf{B}_r$ and $\mathbf{D}_r$ are the membrane, coupling and bending stiffnesses of the strip with reduced stiffness, respectively and l and d are shown in Figure 8.3. This assumption will also satisfy the condition of a strip delamination in

which $d/l = 1$ and the strip with reduced stiffness will have the stiffness of the equivalent laminate which is $\mathbf{D}^*$.

2- Linear smearing based on half-wavelength (λ);

In this case, the **A** and **B** matrices are calculated in a similar way to case (1), but the **D** matrix has the form

$$\mathbf{D}_r = (d/\lambda)\,\mathbf{D}^* + (1 - d/\lambda)\,\mathbf{D} \text{ for } d \leq \lambda$$

$$\mathbf{D}_r = \mathbf{D}^* \text{ for } d > \lambda \qquad (8.10)$$

when $d \leq \lambda$, the whole delamination is assumed to be included within one half-wavelength and therefore a global buckling behaviour is considered. In this situation the strip with reduced stiffness should benefit somewhat from the stiffness of the perfect laminate. When $d > \lambda$, the delamination extends over more than one half-wavelength and so local buckling behaviour is expected to dominate the behaviour. In this case, the stiffness of the equivalent laminate is more predominant.

3- Linear smearing based on a revised half-wavelength;

In this case, the ratio of d/λ is revised depending on how much of the length of delamination is included in any one half-wavelength (Figure 8.4), i.e. if $d/\lambda \leq 1$ then the coefficient d/λ will be multiplied by another coefficient (α) and Eq (8.10) will change to

$$\mathbf{D}_r = (\alpha\, d/\lambda)\,\mathbf{D}^* + (1 - \alpha\, d/\lambda)\,\mathbf{D} \text{ for } d \leq \lambda$$

$$\mathbf{D}_r = \mathbf{D}^* \text{ for } d > \lambda \qquad (8.11)$$

where α is the ratio of the greatest delamination length located in any one half-wavelength to the total length of delamination.

It is also worth noting that using the half-wavelength λ instead of l is intended for a VIPASA analysis. Since VICON analysis uses combinations of

different half-wavelengths, it is excluded from the focus of the current study. Hence, only problems with simply supported end conditions are considered in this study. It should be mentioned that case (2) or case (3) could easily be studied using VICON analysis by using Eq (8.10) or (8.11) to obtain a different matrix $\mathbf{D}_r$ for each half-wavelength λ.

8.3 Examples

Two problems are investigated. The material used for both problems has the properties $E_1 = 130\,\text{kNmm}^{-2}$, $E_2 = 10\,\text{kNmm}^{-2}$, $G_{12} = 5\,\text{kNmm}^{-2}$, $\nu_{12} = 0.3$. In problem 1 a composite plate of length l = 100 mm, width B = 100 mm and thickness h = 2 mm with a stacking sequence of $[0/+45/-45/90/0/+45/-45/90]_s$ is studied. A strip delamination of length d = 100 mm and variable width b is located between the fourth and the fifth plies. It is worth mentioning that the use of a strip delamination in this problem is designed to enable comparison of the results with those already obtained in Chapter 3 and to obtain a better understanding of the performance of the smearing method.

In problem 2 the length is increased to l = 200 mm and the effect of an *embedded rectangular delamination* is studied. For this problem the length of delamination (d) is kept at the constant value of 60 mm whilst its width (b) is varied from 10 mm to 90 mm. The composite plate is simply supported on four edges and is loaded longitudinally in the direction of the x axis. For each of the problems mentioned above, all three cases of the smearing method are applied.

8.4 Results and discussion

Figure 8.5 shows that a linear eigenvalue analysis using either the proposed technique incorporated into VIPASA or ABAQUS, as in Chapter 3, reflects the transition between global and local behaviour of a delaminated composite plate, i.e. that the mode is initially global, but as the width of delamination increases the stiffness of the delaminated portion reduces and the load factor relates to the local buckling of the delaminated portion. It is evident that this load factor does not mirror the load carrying capacity of the whole structure, as the delaminated composite plate is easily capable of resisting load factors much higher than the load factor related to the buckling of the delaminated portion. Obtaining the load factor for the whole structure requires the use of either a nonlinear FE analysis or an efficient smearing method in VICONOPT. A nonlinear FE analysis is expensive computationally but is a good base for comparative study. The smearing method is a very efficient way of predicting the load factor, providing a correct smearing model is utilised. The results presented in Figure 8.5 represent buckling loads calculated using the three different smearing methods described above. For this particular example, cases 1, 2 and 3 overlap exactly. This is because the plate buckles with half-wavelength $\lambda = l$, and the delamination length $d = l$, which gives $\alpha\ (d/\lambda) = d/l = (d/\lambda)$. All three smearing methods (cases 1, 2 and 3) under-predict global buckling behaviour by maximum 20%, i.e. when $/B \leq 0.2$, but give a more realistic buckling residual strength than FE eigenvalue analysis and VIPASA when local buckling occurs , i.e. $b/B > 0.2$.

Figure 8.6 illustrates the results of applying the smearing method compared to FE analysis for problem 2, for which critical buckling occurs with $\lambda = l/2$. In this particular example cases 2 and 3 overlap exactly. As can be seen there is excellent agreement when $b/B \leq 0.4$. As the size of delamination increases, i.e. $b/B > 0.4$, the

discrepancy between the results increases and the smearing methods give different results. For $b/B > 0.4$ case 1 over predicts the results obtained by FEA because the mode shapes are assumed to remain sinusoidal with two half-wavelengths, i.e. $\lambda = l/2$ whilst the mode shape in FE analysis is more general. For $b/B > 0.4$ cases 2 and 3 under-estimate the FEA results because they force the structure to buckle with a half-wavelength $\lambda = l/3$ with $\mathbf{D}_r$ taking smaller values than in case 1.

The reason for the discrepancy could be attributed to the calculation of the $\mathbf{A}^*$, $\mathbf{B}^*$ and $\mathbf{D}^*$ matrices using ref [8.1] which is based on some assumptions, such as that of equal curvature in both base plate and delaminated portions. This assumption does not necessarily apply. As it is mentioned in ref [8.3], the deformation of two sub-laminates which are under pure bending and have no contact between their interfaces would look like Figure 8.7a. It can be seen there is misalignment (Δ) at the end faces of the sub-laminates. In a delamination problem, the ends of the sub-laminates must be aligned and have equal slope to that of the base structure (see [1.7]). In order to align the end faces of each sub-laminate there must exist an axial force (N) to allow for displacement of the end faces to the amount Δ (see Figure 8.7b). This suggests the existence of axial forces (N_1 and N_2, i.e. axial forces in the top and the bottom sub-laminates, respectively) as well as bending moments is essential in the delaminated portion.

As a physical example, when mixed-mode buckling (see Chapter 1) occurs the curvature of the delamination is essentially different from that of the base plate. This will certainly lead to inaccuracies in calculation of the stiffness of the equivalent laminate and the smearing method, accordingly.

8.5 Conclusion

Three different smearing methods (cases 1, 2 and 3) have been introduced. It has been shown that where local behaviour of the delaminated portion is more predominant, case 1 gives higher results than cases 2, 3 and ABAQUS. Using case 1 does not change the mode shape of the structure and does not allow for the longitudinal position of the delamination, whilst cases 2 and 3 depending on the sizes of delamination and structure may alter the mode shape and allow for the longitudinal position of the delamination in an approximate way. In other words, as cases 2 and 3 are obtained by manipulating half-wavelength λ, the load factors may not reflect the correct value. It can also be concluded that in order to increase the accuracy of such a technique, the $\mathbf{A}^*$, $\mathbf{B}^*$ and $\mathbf{D}^*$ matrices for the equivalent laminate need to be calculated with more realistic assumptions such as different curvature for top and bottom sub-laminates and allowing for axial forces in the delaminated region as elaborated in ref [8.3]. The smearing method also requires nonlinear FE analysis results for comparison purposes.

8.6 References

[8.1] Z. Zhang, H. Chen, L. Ye, Progressive failure analysis for advanced grid stiffened composite plates/shells, *Composite Structures*, **86**, 45-54 (2008).

[8.2] J. Lee, Free vibration analysis of delaminated composite beams, *Computers and Structures*, **74**, 121-129 (2000).

[8.3] C. Harrison, R. Butler, Locating delaminations in composite beams using gradient techniques and a genetic algorithm, *AIAA Journal*, **39** (7), 1383-1389 (2001).

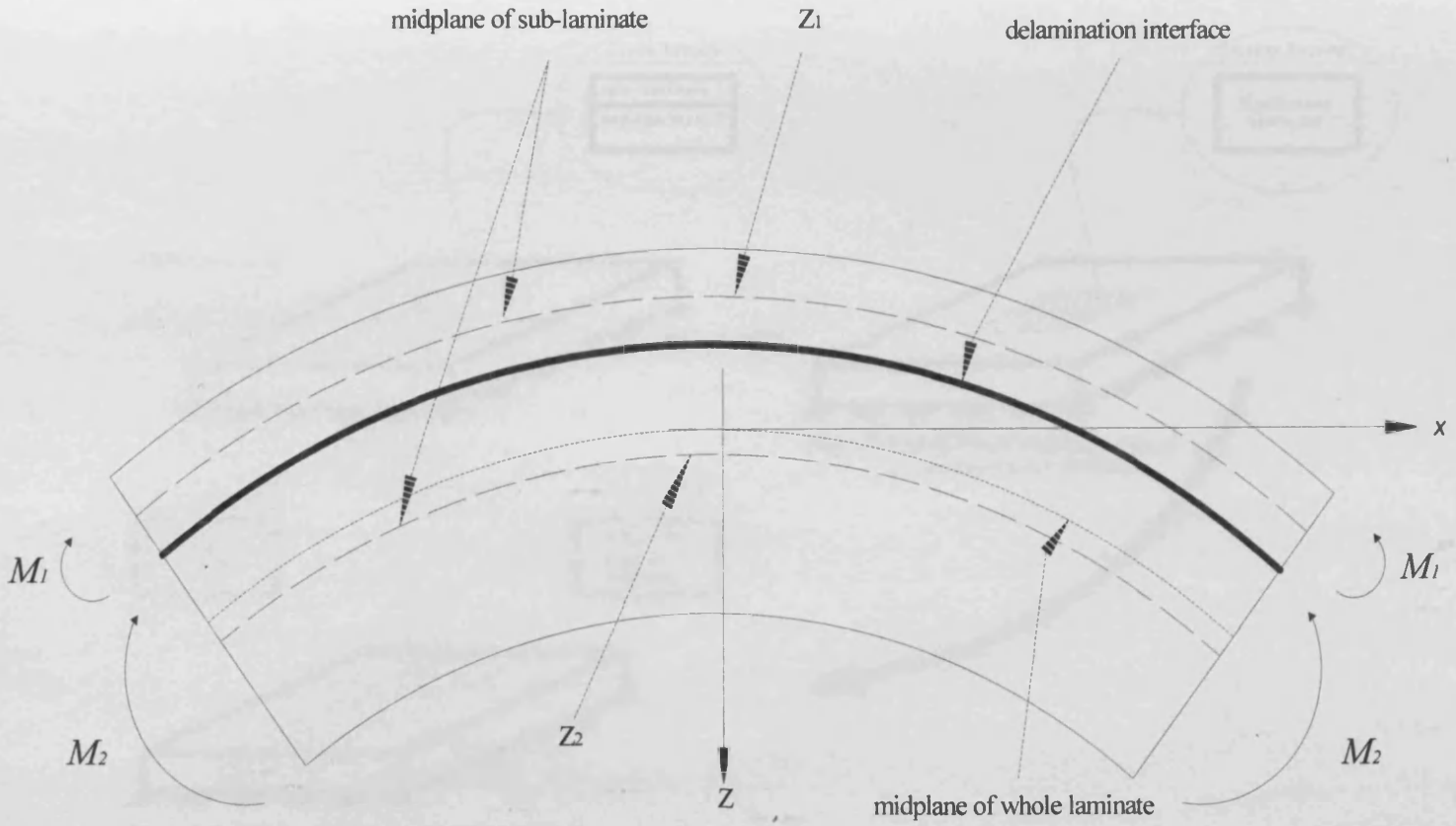

Figure 8.1: Schematic representation of a delaminated composite plate within the delaminated region.

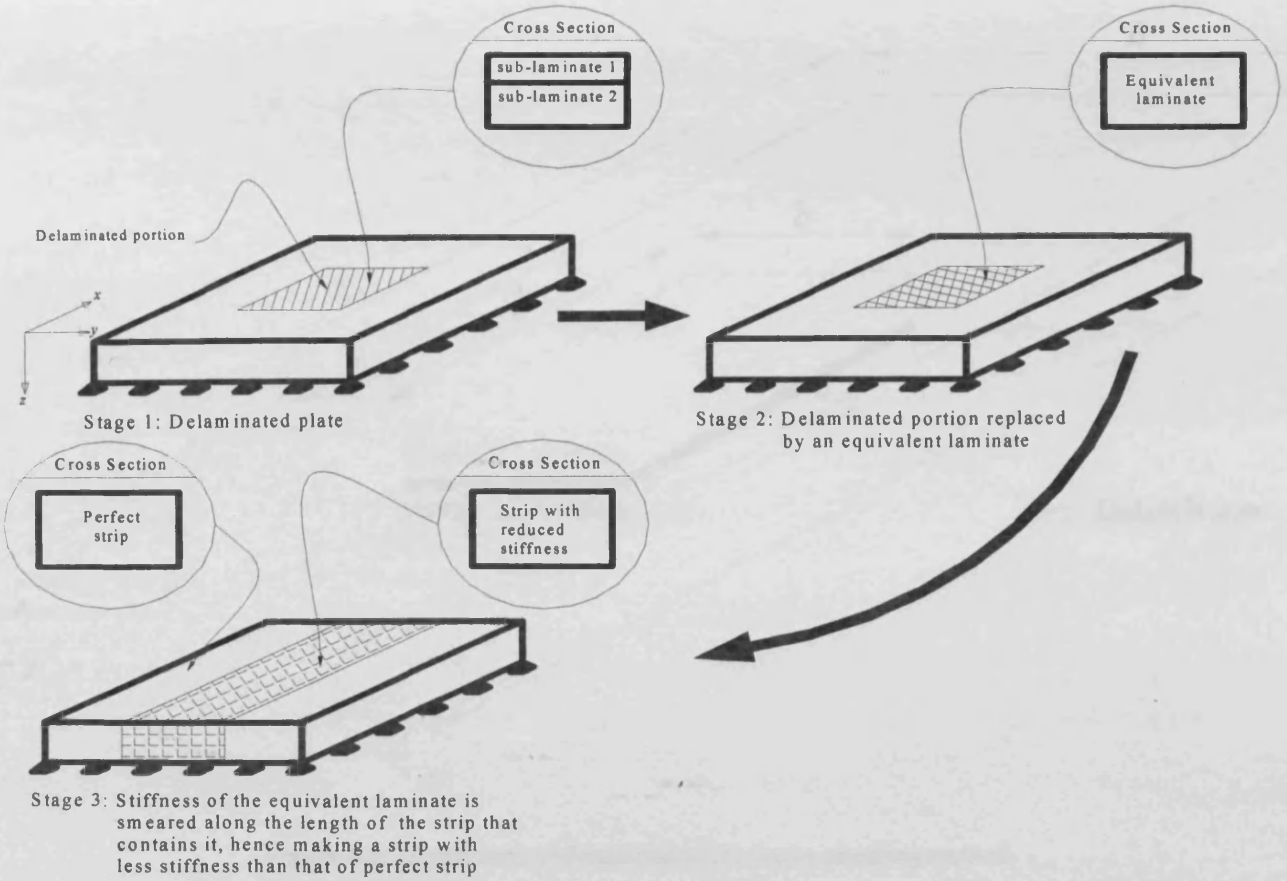

Figure 8.2: Schematic representation of the problem.

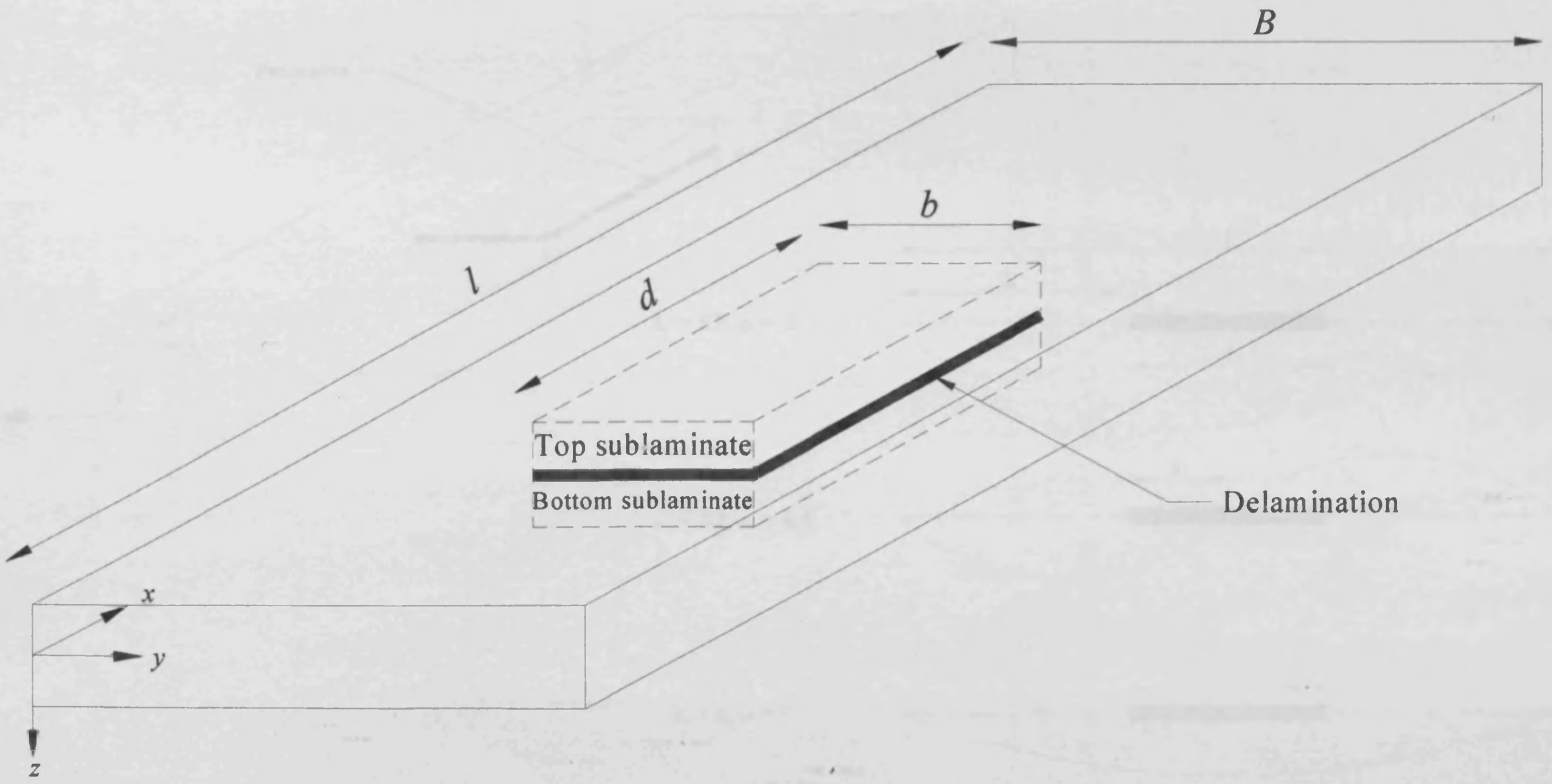

Figure 8.3: Dimensions of delamination for use in smearing method.

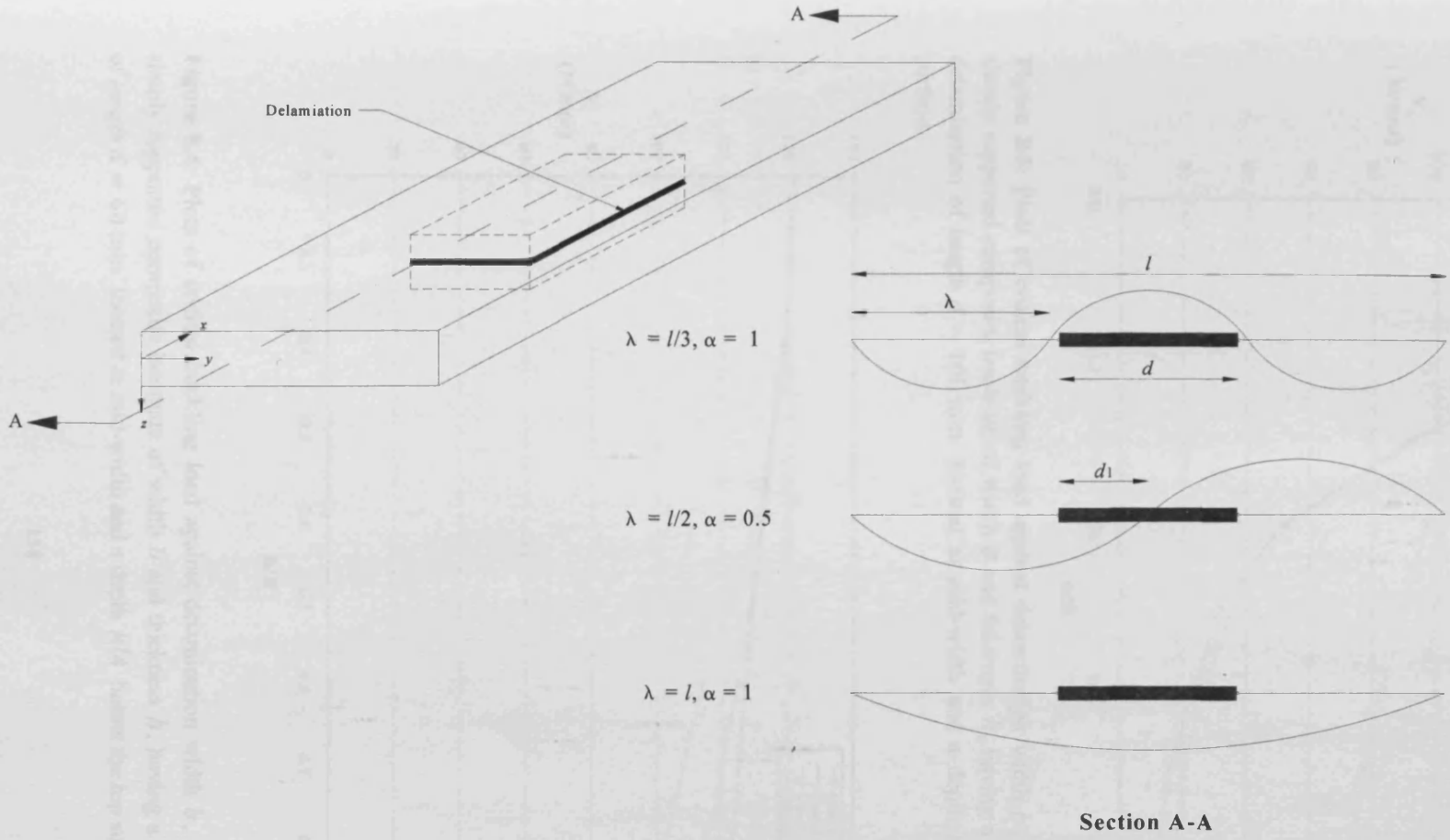

Figure 8.4: Schematic representation of case 3.

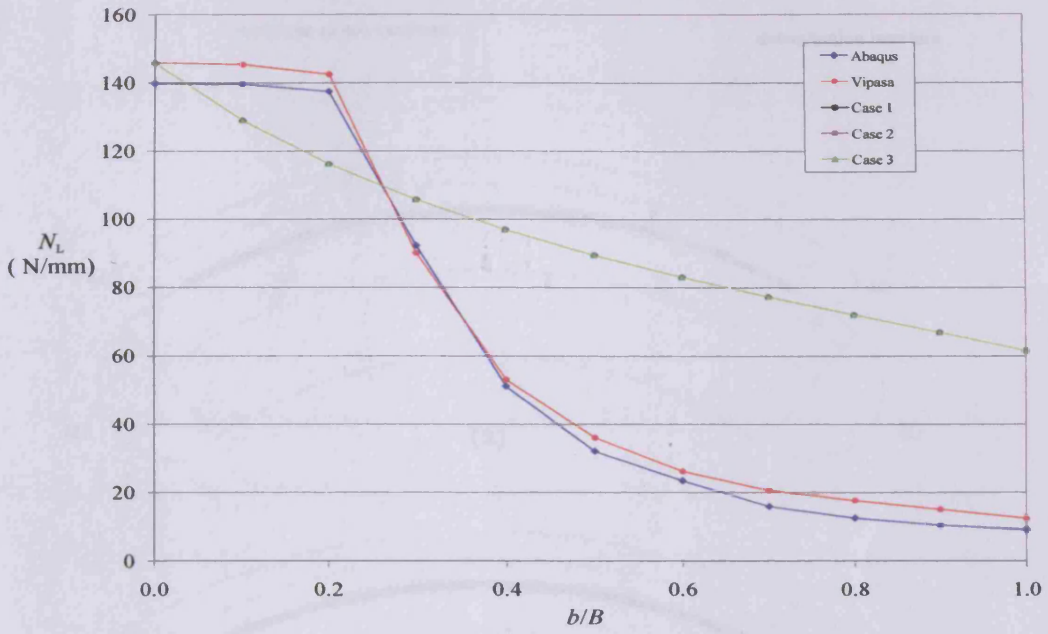

Figure 8.5: Plots of critical buckling load against delamination width b, for problem 1, a simply supported composite laminate of width B and thickness h, having a through-the-length delamination of length $d = 100$ mm located at mid-width and a depth $h/4$ below the top surface.

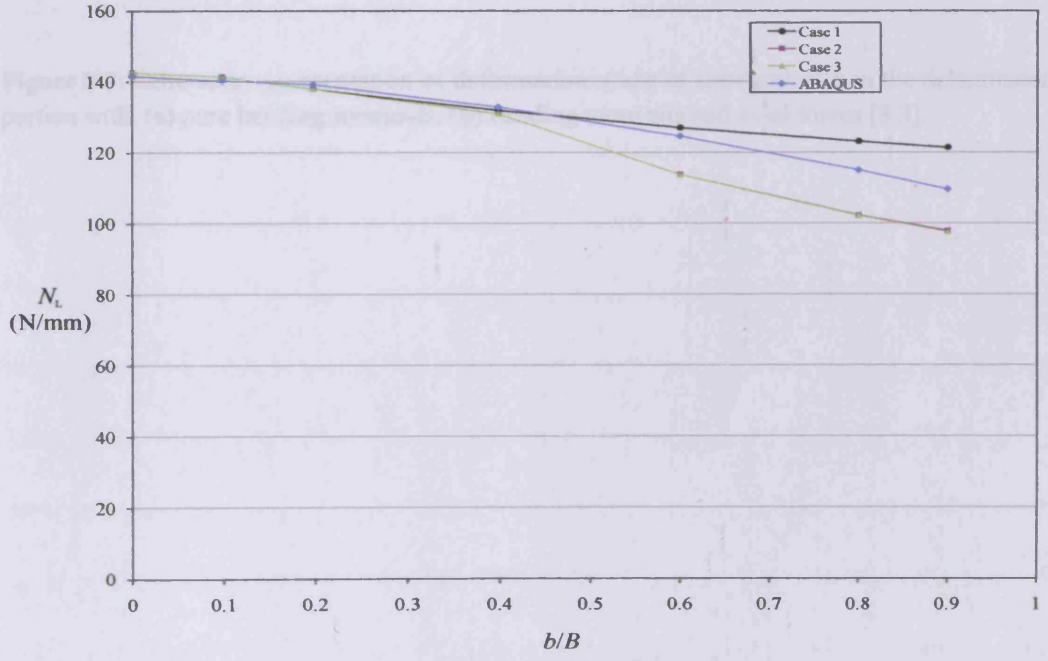

Figure 8.6: Plots of critical buckling load against delamination width b, for problem 2, a simply supported composite laminate of width B and thickness h, having a strip delamination of length $d = 60$ mm located at mid-width and a depth $h/4$ below the top surface.

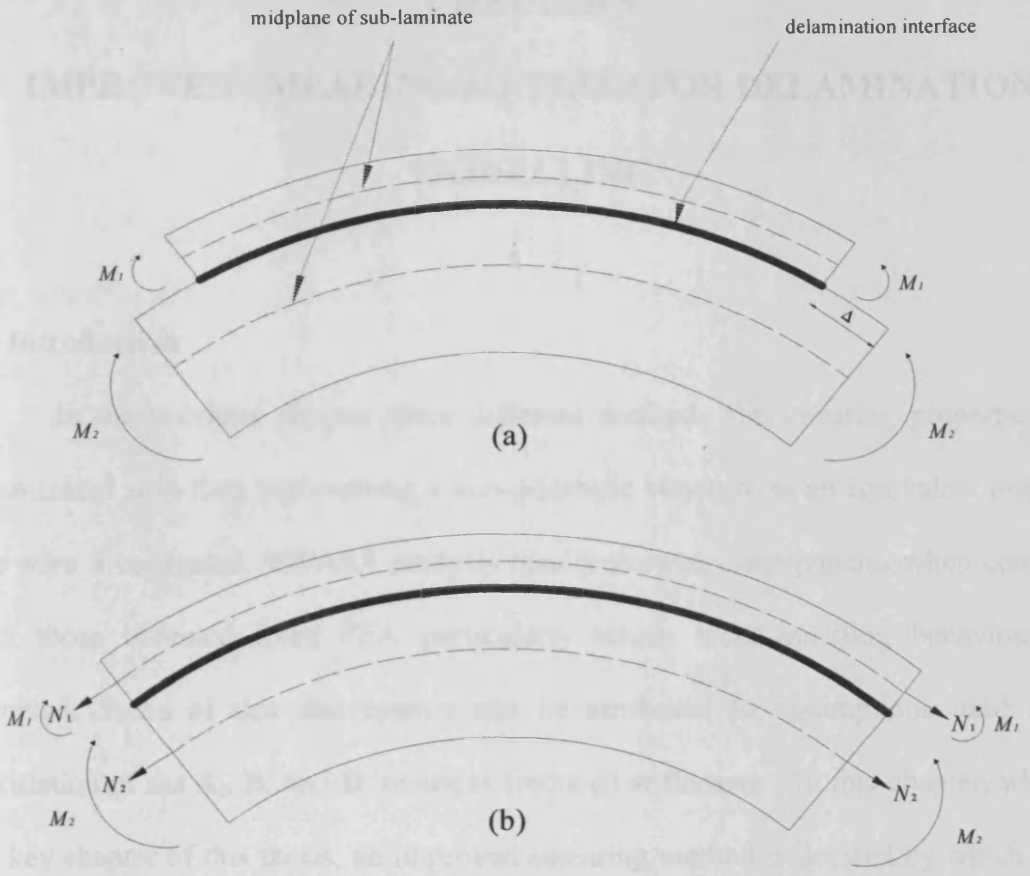

Figure 8.7: Schematic representation of deformation shape of sub-laminates in the delaminated portion with, (a) pure bending moments, (b) bending moments and axial forces [8.3].

CHAPTER 9

IMPROVED SMEARING METHOD FOR DELAMINATION MODELLING

9.1 Introduction

In the previous chapter three different methods for smearing properties in a delaminated strip thus representing a non-prismatic structure as an equivalent prismatic one were investigated. VIPASA analysis results showed discrepancies when compared with those obtained from FEA particularly where local buckling behaviour was involved. Some of this discrepancy can be attributed to assumptions used in the calculation of the $\mathbf{A}_r$, $\mathbf{B}_r$ and $\mathbf{D}_r$ matrices (reduced stiffnesses). In this chapter, which is the key chapter of this thesis, an improved smearing method is devised by which $\mathbf{A}_r$, $\mathbf{B}_r$ and $\mathbf{D}_r$ can be calculated using modified VICONOPT data.

The concepts introduced in Chapter 8 are now developed to model non-prismatic structures (such as delamination problems) by expanding the total energy term in VICONOPT software. The proposed method is initially verified for a simply supported delaminated plate problem using VIPASA analysis. It is then used to carry out VICON analyses for a wider range of problems and boundary conditions. Results of the verified method are compared with nonlinear FEA to validate the results obtained. It is worth noting that the results of this chapter have been accepted for presentation at the CEAS2009 European Air and Space Conference [9.1] and prepared for submission as a journal paper to *Computers and Structures*.

9.2 Problem definition and theory

9.2.1 Physical basis

The aim of this chapter is to represent a non-prismatic problem (delamination) by a prismatic problem in which each of the constituents of the plate assembly would take equal length l and have constant material properties along their longitudinal direction (x direction) whilst maintaining their original stiffnesses, i.e. the overall stiffness of the prismatic structure would be equal to that of original non-prismatic structure. This representation would enable us to model delamination using VICONOPT and study the buckling behaviour of such a problem. It should be mentioned that due to inherent assumption in VICONOPT, each of the constituents of the plate assembly are assumed to be infinitely long and their mode shapes repeat over length $L = Ml$ (see Chapter 2). Therefore there is always some degree of approximation if the structure to be studied is not infinitely long and the boundary conditions are not clamped at $x = 0$ and $x = l$.

9.2.2 Theory

As stated in Chapter 8, the assumption of equal curvature in both sub-laminates of a region of delamination imposes inaccuracies in solving for the buckling of delaminated composite plates. An alternative method for calculating the $\mathbf{A}_r$, $\mathbf{B}_r$ and $\mathbf{D}_r$ matrices, not based on this assumption, is therefore required.

The present study examines a rectangular composite laminated plate containing an embedded rectangular delamination. The longitudinal portion of the plate containing the delamination (which will be termed the delaminated strip) is divided into 4 different regions (Figure 9.1 and 9.2). Regions 1 and 2 are the top and bottom sub-laminates

having length $d(=\mu l)$, width b, thickness h_1 and h_2, and stiffness $\mathbf{K}_1$ and $\mathbf{K}_2$, respectively.

Including sub-laminates in a VICONOPT model is only accurate and computationally efficient if they are prismatic and have the same length (l) as the rest of the structure. Hence, the proposed methods are based on manipulating the properties of the sub-laminates so that they can take length l instead of d, thickness h_1 or h_2 $(= h - h_1)$ and width b while maintaining their original stiffnesses, i.e. $\mathbf{K}_1$ and $\mathbf{K}_2$, are required.

The total energy of a length $L\,(= Ml$, for some integer $M\,)$ of a plate assembly is given by

$$V = \frac{1}{2}\int_0^L \mathbf{D}_A^T \mathbf{P}_A \, dx \tag{9.1}$$

where $\mathbf{D}_A^T$ and $\mathbf{P}_A$ and M are perturbation displacements and forces at the nodes (see Chapter 2). In the present study, for the sake of brevity, $M \doteq 1$ is considered, i.e. the mode shape is assumed to repeat over length $2l$. Replacing the terms for $\mathbf{D}_A^T$, $\mathbf{P}_A$ for a VICON type analysis and putting $L = l$ gives the total energy as

$$V = \frac{1}{2}\int_0^L \sum_q \mathbf{D}_q \exp(2i\pi qx/l) \sum_m \mathbf{K}_m \mathbf{D}_m \exp(2i\pi mx/l)\, dx \tag{9.2}$$

In order to expand Eq (9.2), three different kinds of term arise, as follows

1- Case 1 $(m+q=0)$.

2- Case 2 $(m-q=0)$.

3- Case 3 $(m+q\neq 0, m-q\neq 0)$.

Integrating over the length of a non-prismatic plate (Figure 9.3) gives the following contributions to the potential energy of each case as follows.

1- Case 1 terms which represent the potential energy of the non-prismatic strip of Figure 9.3, without allowing for the longitudinal position of the delamination.

$$V_1 = [\frac{l}{2}][\sum_q \mathbf{D}_q^H [\mathbf{K}_q (1-\mu) + \mathbf{K'}_q \, \mu] \mathbf{D}_q] \tag{9.3}$$

where $\mathbf{K'}$ is the stiffness of the delaminated portion (obtained from the stiffness of regions 1 and 2, i.e. $\mathbf{K}_1$ and $\mathbf{K}_2$ respectively, with appropriate offset transformations).

2- Case 2 terms which allow for the change of the position of delamination (i.e. the portion with stiffness $\mathbf{K'}$ in Figure 9.3) along the longitudinal direction.

$$V_2 = [\frac{l}{2}][\sum_q \frac{1}{2\pi q} \mathbf{D}_q^H (\mathbf{K}_q - \mathbf{K'}_q) \sin 2\pi q\mu \left\{ \cos \frac{4\pi qD}{l} - i \sin \frac{4\pi qD}{l} \right\} \mathbf{D}_q] \tag{9.4}$$

3- Case 3 terms which allow for coupling of various half-wavelengths in VICON type analysis.

$$V_3 = [\frac{l}{2}][\sum_q \sum_m \frac{1}{\pi(m+q)} \mathbf{D}_q^H (\mathbf{K}_m - \mathbf{K'}_m) \sin \pi(m+q)\mu \left\{ \cos \frac{2\pi(m+q)D}{l} - i \sin \frac{2\pi(m+q)D}{l} \right\} \mathbf{D}_m] \tag{9.5}$$

where D is the distance between the centre of delamination and the edge of the plate (see Figure 9.2). Full details of the derivations of V_1, V_2 and V_3 are given in Appendix 1. Finally, the total potential energy for a non-prismatic plate assembly for a VICON type analysis becomes

$$V = V_1 + V_2 + V_3$$

$$= [\frac{l}{2}][\sum_q \mathbf{D}_q^H [\mathbf{K}_q (1-\mu) + \mathbf{K'}_q (\mu)] \mathbf{D}_q]$$

$$+$$

$$[\frac{l}{2}][\sum_q \frac{1}{2\pi q}\mathbf{D}_q^H(\mathbf{K}_q - \mathbf{K'}_q)\sin 2\pi q\mu\left\{\cos\frac{4\pi qD}{l} - i\sin\frac{4\pi qD}{l}\right\}\mathbf{D}_q]$$

$$+$$

$$[\frac{l}{2}][\sum_q\sum_m \frac{1}{2i\pi(m+q)}\mathbf{D}_q^H(\mathbf{K}_m - \mathbf{K'}_m)\mathbf{D}_m\{\exp(2i\pi(m+q)l_1/l) - \exp(2i\pi(m+q)l_2/l)\}] \tag{9.6}$$

The stiffnesses for the three cases mentioned above are

$$\mathbf{K}_{q1} = \mathbf{K}_q(1-\mu) + \mathbf{K'}_q(\mu)$$

$$\mathbf{K}_{q2} = \frac{1}{2\pi q}(\mathbf{K}_q - \mathbf{K'}_q)\sin 2\pi q\mu\left\{\cos\frac{4\pi qD}{l} - i\sin\frac{4\pi qD}{l}\right\}$$

$$\mathbf{K}_{q3} = \sum_m \frac{1}{2i\pi(m+q)}(\mathbf{K}_m - \mathbf{K'}_m)\{\exp(2i\pi(m+q)l_1/l) - \exp(2i\pi(m+q)l_2/l)\} \tag{9.7}$$

where $\mathbf{K}_{qi}\,(i=1,2,3)$ is the stiffness for case i and half-wavelength q.

Using the stiffnesses above gives the exact equivalent stiffness for the delaminated strip as

$$\mathbf{K}_{q(eq)} = \mathbf{K}_{q1} + \mathbf{K}_{q2} + \mathbf{K}_{q3} \tag{9.8}$$

As will be shown later (section 9.4.1), $\mathbf{K}_{q2}$ and $\mathbf{K}_{q3}$ are small compared to $\mathbf{K}_{q1}$ and therefore can be ignored for the sake of simplicity. Hence, the equivalent stiffness of the delaminated strip can be approximated by

$$\mathbf{K}_{q(approx)} = \mathbf{K}_{q1} = \mathbf{K}_q(1-\mu) + \mathbf{K'}_q(\mu) \tag{9.9}$$

which matches case (1) of Chapter 8.

Following a similar procedure for a VIPASA type analysis and assuming a displacement field of $\mathbf{D} = \mathbf{D}_0 \sin(\pi x / l)$ gives the total potential energy term for one typical half-wavelength $\lambda = \frac{l}{n}$ as

$$V = \frac{l}{4}\mathbf{D}_0{}^T\{\mathbf{K}(1-\mu)+\mathbf{K}'(\mu)\}\mathbf{D}_0 + \frac{l}{4n\pi}\{\mathbf{D}_0{}^T(\mathbf{K}-\mathbf{K}')\mathbf{D}_0 \cos\frac{2n\pi D}{l}\sin\mu n\pi\} \quad (9.10)$$

The reader is referred to Appendix 2 for the derivation of Eq (9.10). Finally the exact equivalent stiffness for a plate assembly for a VIPASA type analysis becomes

$$\mathbf{K}_{(eq)} = (1-\mu)\mathbf{K} + (\mu)\mathbf{K}' + (\mathbf{K}-\mathbf{K}')\frac{1}{\pi n}\cos\frac{2n\pi D}{l}\sin n\mu\pi \quad (9.11)$$

As for VICON analysis, since the value of the last term is small compared to the first two terms it can be ignored and the equivalent stiffnesses for delaminated strips for VIPASA analyses can be approximated by

$$\mathbf{K}_{(approx)} = (1-\mu)\mathbf{K} + (\mu)\mathbf{K}' \quad (9.12)$$

9.2.3 Problem definition and theory application

In order to apply the above mentioned procedure to delamination modelling, it is assumed that the top and bottom sub-laminates are replaced by two prismatic strips 1 and 2 with length l, width b and thickness h_1 and h_2, respectively. These have material properties E_1^i, E_2^i, G_{12}^i and $\nu_{12}^i (i = 1,2)$, where

$$E_1^1 = E_1^2 = \mu E_1$$

$$E_2^1 = E_2^2 = \mu E_2$$

$$G_{12}^1 = G_{12}^2 = \mu G_{12}$$

$$\nu_{12}^1 = \nu_{12}^2 = \nu_{12} \tag{9.13}$$

E_1 and E_2 are Young's moduli parallel and normal to the fibre direction, G_{12} is the shear modulus and ν_{12} is Poisson's ratio. Regions 3a and 3b are replaced by a single strip 3 which has length l, width b and thickness h and the material properties of this strip are

$$E_1^3 = (1-\mu)E_1$$

$$E_2^3 = (1-\mu)E_2$$

$$G_{12}^3 = (1-\mu)G_{12}$$

$$\nu_{12}^3 = \nu_{12} \tag{9.14}$$

Replacement strips 1, 2 and 3 are modelled with stacking sequences and geometric offsets corresponding to those of the three regions shown in Figure 9.1.

In terms of stiffness, if the material properties E_1, E_2 and G_{12} are all multiplied by the same factor then the $\mathbf{K}$ matrix will be scaled accordingly, i.e.

$$\mathbf{K}_r^1 = \mu\mathbf{K}^1 \quad \mathbf{K}_r^2 = \mu\mathbf{K}^2 \quad \mathbf{K}_r^3 = (1-\mu)\mathbf{K}^3 \tag{9.15}$$

where $\mathbf{K}_r^i$ $(i = 1,2,3)$ are the stiffness matrices for the replacement strips and $\mathbf{K}^i$ are the corresponding original stiffnesses for these strips.

Finally, the equivalent smeared stiffnesses of the delaminated strip (i.e. the union of regions 1, 2 and 3) is defined by

$$\mathbf{K}_{q(approx)} = \mathbf{K}_r^1 + \mathbf{K}_r^2 + \mathbf{K}_r^3 = \mu\left(\mathbf{K}^1 + \mathbf{K}^2\right) + (1-\mu)\mathbf{K}^3 \tag{9.16}$$

This approach enables the approximate smearing model to be used in VICONOPT simply by making changes to the material properties in the input data.

9.3 Numerical study

In the present work, validation analyses are carried out using VIPASA. Then analyses are performed for both delaminated and perfect composite plates subjected to in-plane longitudinal loading N_L per unit width (Figure 9.2). Linear (eigenvalue) and nonlinear FEA and VICONOPT analyses are used to determine the eigenvalues and eigenvectors for the delaminated composite plate. Transverse shear effects are included in both analyses but contact effects in the delaminated portion are ignored, therefore giving potentially conservative results.

9.3.1 Properties of the composite plate and delamination

The composite plate examined has length l =200mm, width B =100mm and thickness h =2mm and is constructed from material having properties E_1 =130 kN/mm^{-2}, E_2 =10kNmm^{-2}, G_{12} =5KNmm^{-2} and ν_{12} =0.3. The plate is laid up in 16 layers with stacking sequence [0, +45, -45, 90, 0, +45, -45, 90]$_s$. Each ply has thickness $t = 0.125\,\text{mm}$.

In the parametric study presented, the length d, width b and the position of a single rectangular delamination are variables. β and D are the distances between the edges of the plate and the centre of the delamination (see Figure 9.2). Dimensionless parameters β/b, D/l and h_1/h represent the widthwise, lengthwise and depthwise positions of the delamination, respectively.

9.3.2 Validation analysis

In order to investigate the effects of approximating the equivalent stiffness matrix of the delaminated strip with Eq (9.11), a parametric study is carried out on a composite plate with the dimensions given containing a central delamination with varying length and width located between the 6^{th} and 7^{th} plies under longitudinal compressive loading. The plate is assumed to be simply supported on all four edges. A VIPASA type analysis is chosen to compare the critical buckling loads of the delaminated plate using $\mathbf{K}_{(eq)}$ and $\mathbf{K}_{(approx)}$.

9.3.3 FE analysis

Delaminated rectangular plates are also analysed using ABAQUS 6.8 [9.2] in order to validate the results obtained by the exact strip method suggested in this study, using both a linear eigenvalue analysis to predict initial buckling loads and postbuckling analysis to examine nonlinear behaviour.. Linear buckling analyses in ABAQUS consist of two steps. The first step involves performing a general linear static analysis which provides a base state, i.e. the stiffness matrix and stresses for the next step of analysis. The second step is an eigenvalue analysis which provides results in terms of load factors (eigenvalues) and mode shapes (eigenvectors). Depending on the size of delamination, the result of an eigenvalue analysis can be global, or local, i.e. affecting the delaminated

portion only. In cases where local buckling occurs, an iterative nonlinear static analysis is required to capture global buckling behaviour and the buckling load factor which is identified as the load proportionality factor at the point of buckling. Nonlinear static analysis takes the effects of large deformations into account. In this analysis the Riks method, which is generally used to predict unstable geometrically nonlinear collapse of structures, is employed. This method enables the solution of nonlinear equations using the Newton-Raphson method in conjunction with a variable arc-length constraint to trace instability problems associated with local delamination [9.3]. In order to carry out an iterative static nonlinear analysis, an initial geometric imperfection should be introduced to the model. In the absence of geometric data, this is normally achieved by running an eigenvalue analysis and using the first mode shape scaled to achieve an appropriate maximum amplitude representative of the postulated imperfections. An iterative nonlinear post-local-buckling analysis is then performed.

Models were constructed using the SC6R continuum shell elements shown in Figure 9.4, which can be used both for linear and complex nonlinear analyses involving contact, plasticity and large deformations. In contrast to many other shell elements, thickness in these elements is determined from the nodal geometry. They have only displacement degrees of freedom at each node and from a modelling point of view look like three-dimensional continuum solids. SC6R elements are linear 6-node triangular in-plane general-purpose continuum shell wedge elements which use the reduced integration method. Mesh details and boundary conditions are shown in Figure 9.4.

9.4 Results and discussion

Buckling loads were calculated using the proposed technique for composite plates, (1) simply supported on all four edges, and (2) clamped on the loaded ends and free on the unloaded edges, containing an embedded rectangular delamination of varying size, and varying position along the length, across the width and through the thickness. Results are given in Figures 9.5−9.13. Figure 9.5 illustrates the results of VIPASA validation analyses for a simply supported plate and investigates the effects of inherent approximation in smearing method (see section *9.4.1*). Figures 9.6 − 9.13 demonstrate the results of adopting the smearing method for VICON analyses, includes results from three-dimensional FEA for comparison purposes and are for a plate with clamped ends and free edges (see sections *9.4.2−9.4.5*). Good agreement between the FEA results and those obtained by the present numerical method is clearly seen in the majority of cases.

9.4.1 Effects of approximating $\mathbf{K}_{(eq)}$ by $\mathbf{K}_{(approx)}$.

Figure 9.5 demonstrates the effect of using VIPASA models incorporating both exact and approximate delaminated strip stiffnesses to investigate the buckling loads of plates with a single central rectangular delamination of increasing length. . Whilst both methods demonstrate the decrease in buckling load with increasing delamination length is almost insensitive to the width of delamination, due to the simple supports on all the edges of the plate, the approximate smeared stiffness method gives slightly lower results for $\mu < 0.5$ and over-predicts the buckling load for $\mu > 0.5$ by a maximum of 1%. This is due to the effect of the term $\frac{1}{\pi n}\cos\frac{2n\pi D}{l}\sin n\mu\pi$ in Eq (9.11) for different values of μ.

For $\mu = 0.5$, this term becomes zero, so that $\mathbf{K}_{(approx)} = \mathbf{K}_{(eq)}$ and therefore the results of both methods match perfectly. Here, critical buckling occurs for $n = 2$. Therefore, if $\mu < 0.5$ then the additional term $\frac{1}{\pi n}\cos\frac{2n\pi D}{l}\sin n\mu\pi$ in the exact smeared stiffness will be positive, and hence the exact smeared stiffness method gives a higher critical buckling load than the approximate smeared stiffness method. Conversely, when $\mu > 0.5$, the additional term in the exact smeared stiffness is negative and a lower critical buckling load is obtained. Hence, although there are differences between the results obtained using the two methods, these are negligibly small in all cases, reading a maximum of about 3% for very large delaminations. This confirms that the proposed approximate method gives results of good accuracy and suggests that it can be generalised to VICON type analyses, without including the second term (V_2) of Eq (9.6).

For a VICON type analyses Eq (9.6) contains a third term which should also be added for exact analysis. This will be of the same order as the second term and, by a similar argument to that used for VIPASA analysis, can also be ignored. Therefore for a VICON analysis, only the first term of Eq (9.6), which corresponds to $\mathbf{K}_{q(approx)}$ in Eq (9.9) will be included. Considering the effects of the third term would add cross stiffness elements to the final stiffness matrix for VICON analysis, and would therefore increase the amount of work for Gauss elimination, which dominates the solution time.

9.4.2 Effects of width and depth of delamination.

As shown in Figure 9.6, the buckling load of a plate with a single central rectangular delamination decreases with increasing width of delamination. Figure 9.6 demonstrates that the deeper the delamination the lower the initial load bearing capacity of the plate and the greater the effect of the delamination. Both FEA and VICONOPT analyses

illustrate similar trends but the VICONOPT results are seen to be higher than those calculated using FEA. For example when $b/B = 0.9$ and $h_1/h = 0.375$, the critical buckling loads N_L from VICONOPT and ABAQUS are 38.35 N/mm and 36.82 N/mm, respectively. Comparison of the time taken to complete each analysis on a 2.4GHz PC for both methods (Table 9.1) shows that on average VICONOPT analyses are 3.4 and 62.9 times faster for deep ($h_1/h = 0.5$ and 0.375) and near-surface delaminations ($h_1/h = 0.25$ and 0.125), respectively. As the delamination moves closer to the surface, an eigenvalue analysis in ABAQUS will give a local buckling mode and obtaining a global load factor (N_L) requires the running of a nonlinear post-local-buckling analysis, hence the time of analysis increases significantly. For example, when $b/B =$ 0.9 and $h_1/h = 0.25$, ABAQUS required 382.6 seconds while VICONOPT required just 1.96 seconds. Figure 9.7 presents typical post-local-buckling paths at the centre of the delaminated plate. Figure 9.8 shows the mode shapes obtained from VICONOPT and ABAQUS for comparison purposes. It can be seen that there is a good agreement between the predicted modes shapes except for Figure 9.8b. This is due to the inability of the smeared VICONOPT model to capture local effects.

9.4.3 Effects of length and depth of delamination.

Figure 9.9 shows the effect of the length of a delamination on the critical buckling load of a delaminated composite plate. The figure clearly illustrates that buckling is initiated earlier when the delamination is longer. Once again, deeper delaminations show greater vulnerability to buckling than near-surface delaminations. VICONOPT follows an almost linear trend and slightly over-estimates the ABAQUS results except in the case of the larger delaminations for which an almost perfect match

can be confirmed, i.e. for $d/l \geq 0.45$. This is due to the fact that as the length of delamination increases the value of stiffness terms from Cases 2 and 3 becomes small compared to Case 1 and therefore less approximation is assumed by ignoring these terms. In other words, the stiffness obtained from smeared method would match those obtained by ABAQUS and an almost perfect match is obtained, accordingly. The average discrepancy in predicted buckling load factor between VICONOPT and ABAQUS is 0.96% and 0.29% for deep and near-surface delaminations, respectively.

9.4.4 Effects of the lengthwise position and depth of delamination.

The ABAQUS plots presented in Figure 9.10 clearly show a reduction in the buckling load as the delamination moves toward the centre of plate. However the limitations of the approximate smeared stiffness method render it unable to model a change in the position of delamination along the length of the plate. Thus VICONOPT predicted no variation with longitudinal position, since structural degradation effects due to delamination are reflected in the smeared material properties which were kept constant for each individual strip to ensure the structure remains prismatic. It is worth mentioning that using the energy term of Case 2 would enable us to capture the effects of changing the position of delamination along the longitudinal direction. However, ignoring this term gives lower results for some longitudinal positions and over-estimates some other. It seems as delamination moves from the centre to the clamped end, it is moving to a region where displacement is lower as can be seen in Figure 9.11 (obtained from ABAQUS) and therefore it has less effect on the critical buckling load. It is worth mentioning if the delamination was located on the nodal line, i.e. x=0, then the critical buckling load would be less sensitive compared to a delamination where displacements are large. The advantages in terms of significant reduction of time of analysis however

can be seen from Table 9.2. The times listed each represent a summation over all the depths of delamination investigated, i.e. h_1/h = 0.125, 0.25, 0.375 and 0.5. Once again, it can be seen that as the delamination becomes larger, the method used in the present study proves to be much less expensive and more efficient computationally than FEA.

9.4.5 Effects of the widthwise position and depth of delamination.

Figure 9.12 shows the variation of critical buckling load with the non-dimensional position of the delamination across the width of the plate. As both FEA and VICON analyses show, buckling is initiated at a slightly lower load factor when the delamination moves toward the edge of the plate. It seems as delamination moves from the centre to the edge, it is moving to a region where displacement is higher as can be seen in Figure 9.13 (obtained from ABAQUS) and therefore it has more effect on the critical buckling load. VICON analyses slightly overestimate the buckling load by about 0.59% and 2.15% in near-surface and deep delaminations, respectively.

9.5 Conclusions

A smeared method for modelling delamination has been proposed. The method has been validated for a simply supported plate using VIPASA analysis. The validated smeared method has then been generalized to a VICON type analysis, and the critical buckling behaviour of a composite plate with a single rectangular delamination has been studied parametrically. The method has demonstrated its capability in predicting good results with significantly lower times of analysis than FEA. The following can be concluded:

- Buckling loads of plates with a single rectangular delamination decrease as the length of delamination is increased.

- Buckling loads of plates with a single rectangular delamination decrease as the width of delamination is increased.
- Buckling loads of clamped-free plates with a single rectangular delamination decrease slightly by moving the central delamination towards the edge.
- Buckling loads of clamped-free plates with a single rectangular delamination decrease by moving the delamination along the length towards the centre, although this effect is not captured by the smeared model used.
- For delaminations of the same size and location, deeper delaminations will exhibit a lower buckling load factor.

The method used in this study gives results within a good accuracy range (2%-3%) compared to FEA and also has very low solution time, specifically for larger delaminations where post-local-buckling analysis is required to find the global buckling load using FEA. It is therefore a highly attractive method for the preliminary design and optimisation for composite components of aerospace structures.

9.6 Refrences

[9.1] M. Damghani, D. Kennedy and C. A. Featherston, Effects of Embedded Rectangular Delamination on Buckling Behaviour of Composite Plates Using Exact Stiffness Method and the Wittrick-Williams Algorithm , *CEAS 2009 European Air and Space Conference* (2009).

[9.2] ABAQUS theory manual. Version 6.8 Hibbitt. Pawtucket (RI): Karlsson and Sorensen, Inc., 2008.

[9.3] A. D. Lanzo, Nonlinear analysis of elastic high-shear deformable plane frames by a mixed FEM path-following approach, *International Journal of Solids and Structures*, **46**, 1764–1771(2009).

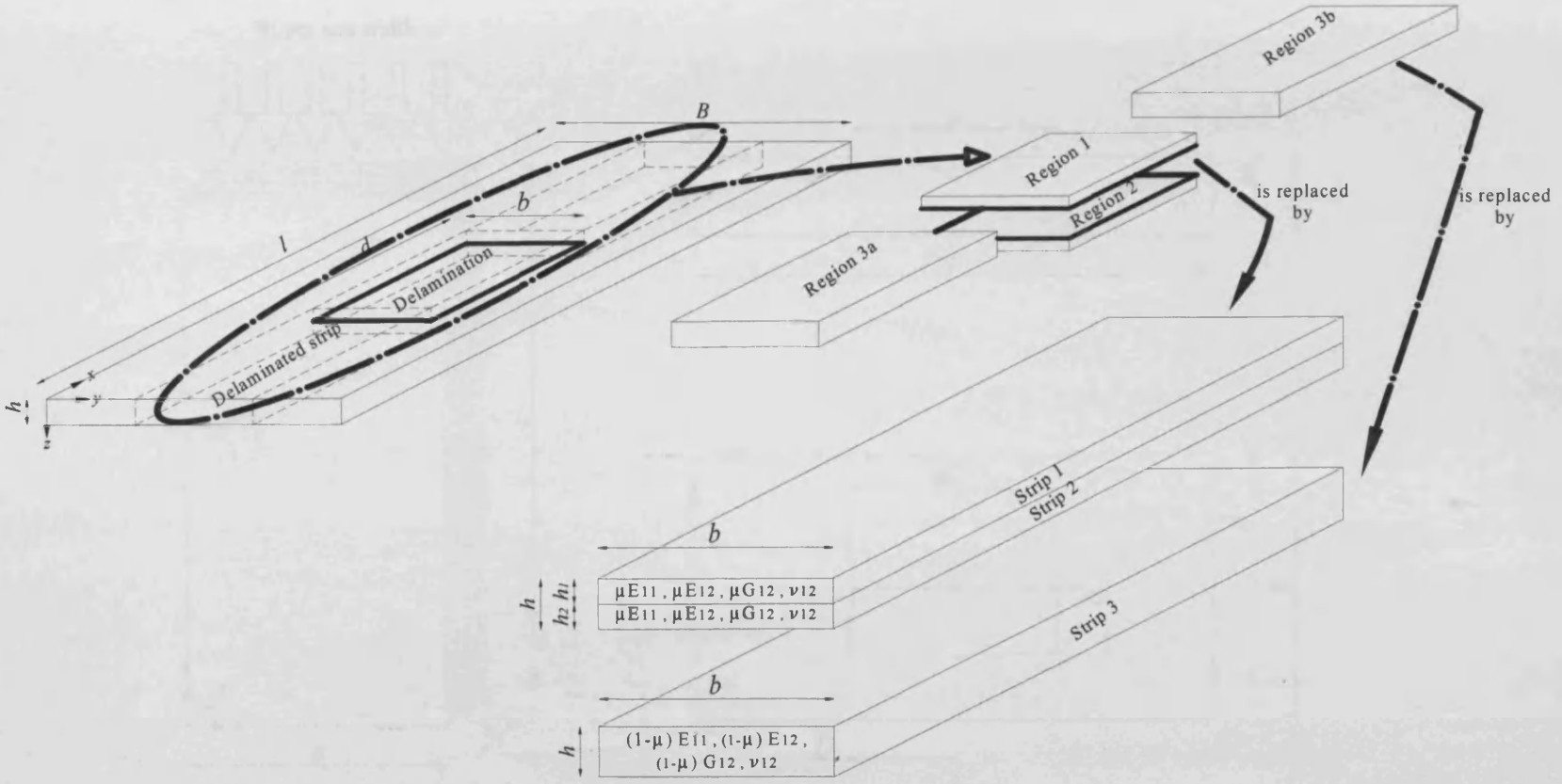

Figure 9.1: Sketch of VICONOPT model for a laminate of width B and thickness h, having an embedded rectangular delamination of length d and width b.

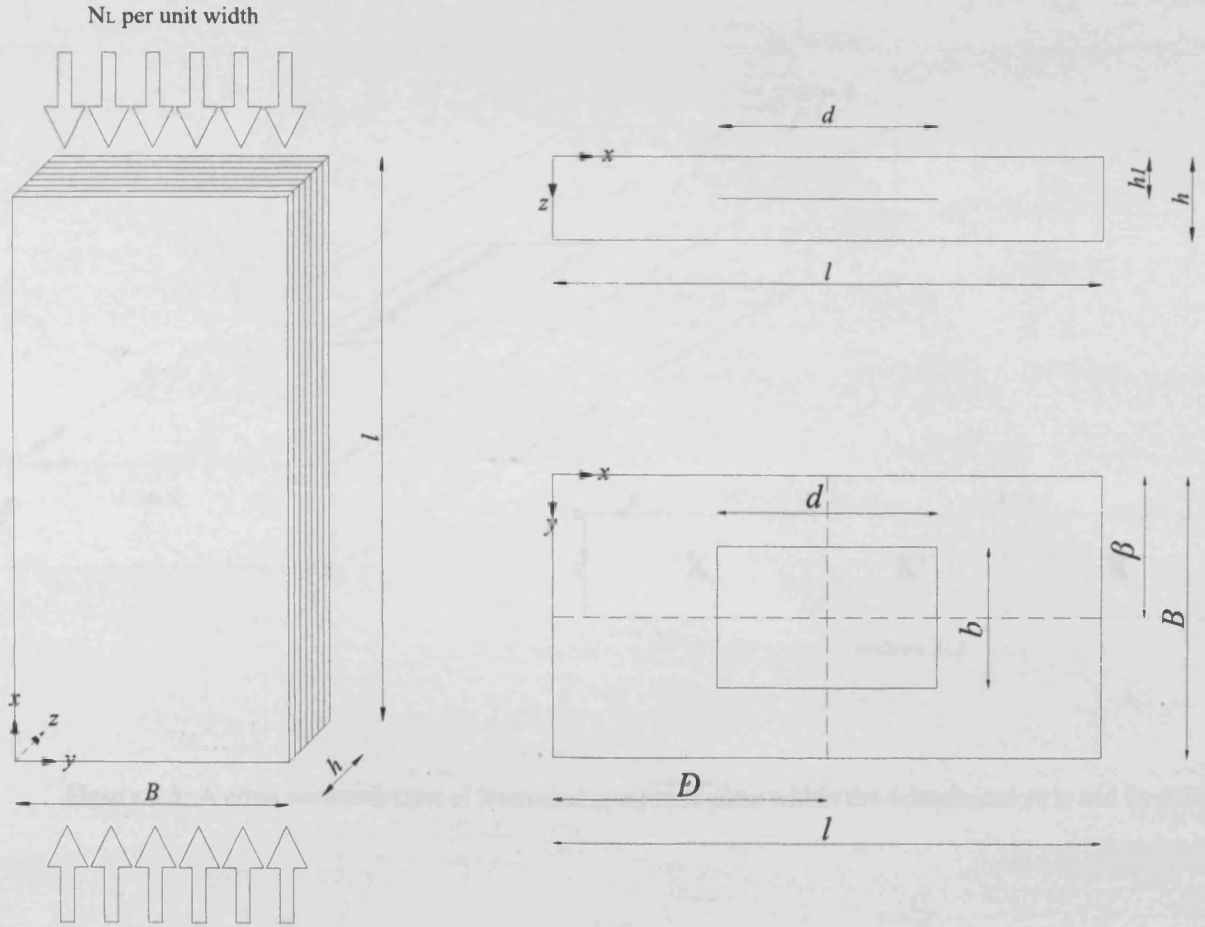

Figure 9.2: (a) 3D geometric properties of the composite plate. (b) & (c) Positions and dimensions of the single rectangular delamination.

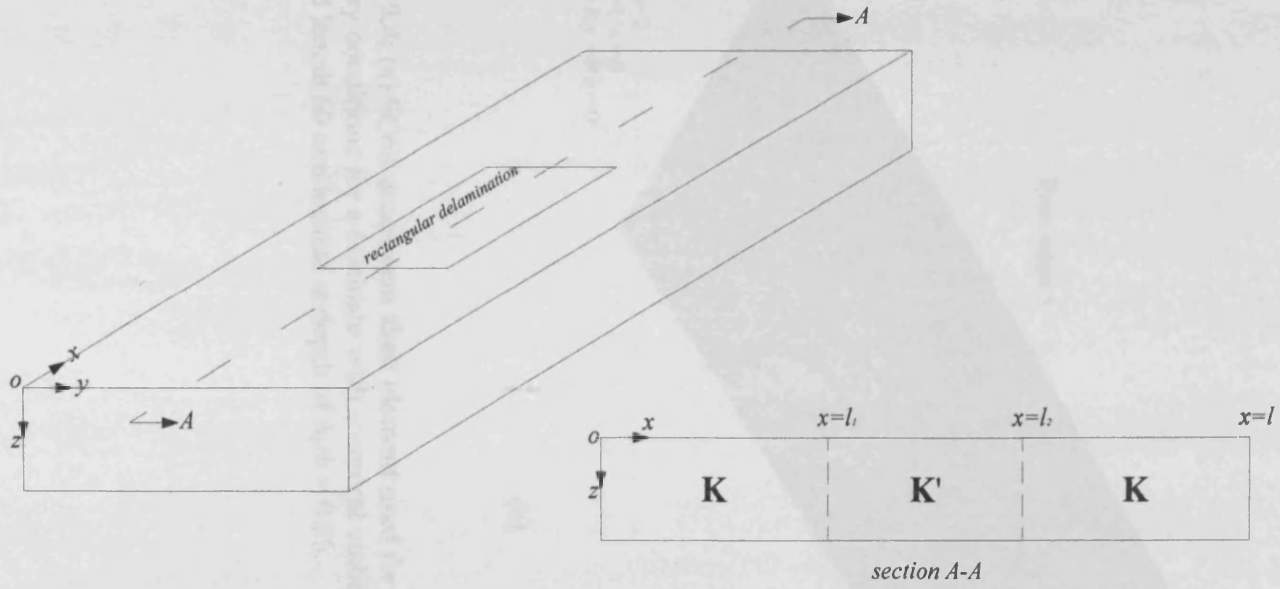

Figure 9.3: A cross sectional view of laminated composite plate within the delaminated strip and its stiffnesses.

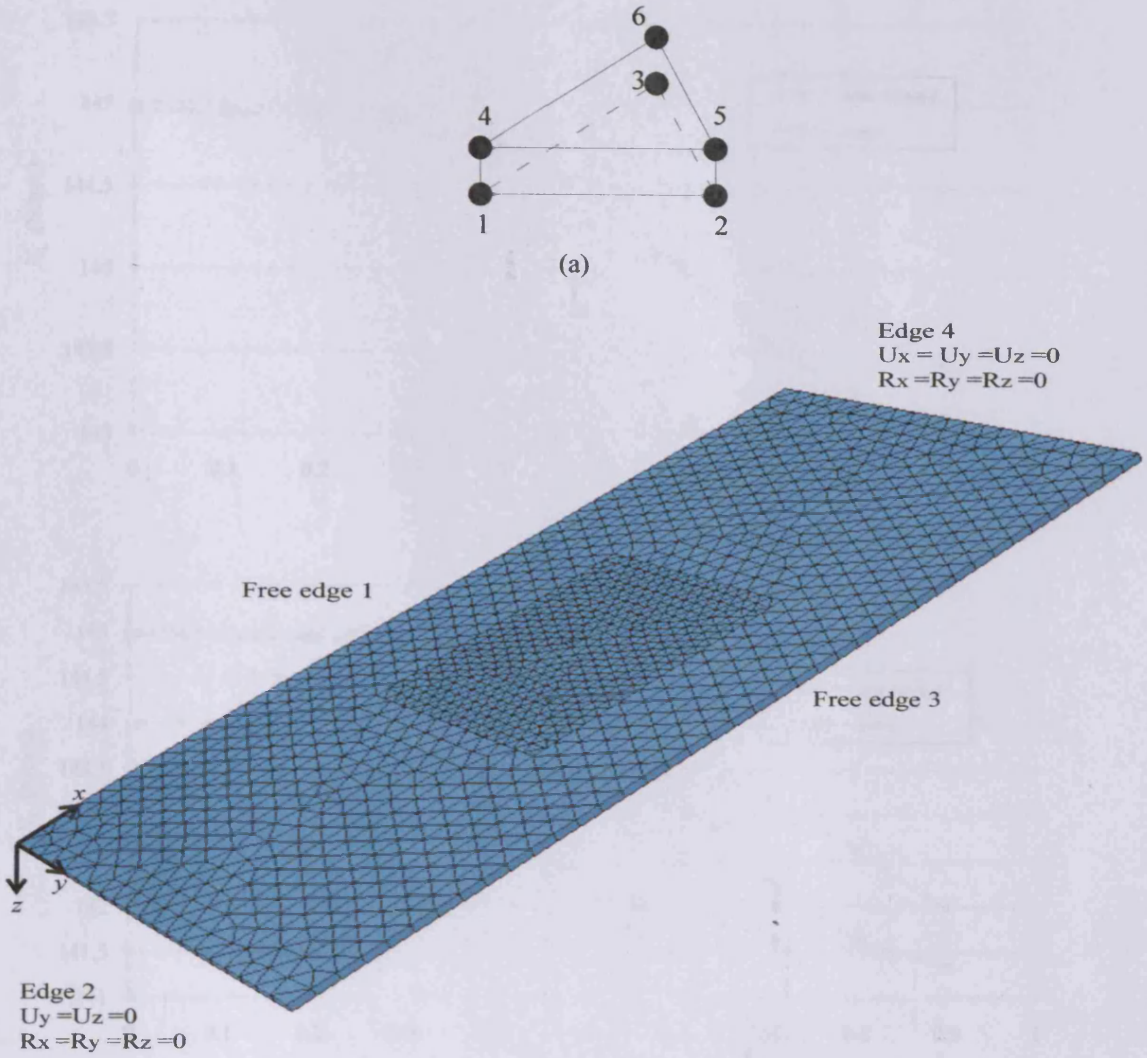

Figure 9.4: (a) SC6R continuum shell element used for meshing the model. (b) A typical mesh and boundary conditions for a laminate with a central embedded rectangular delamination of width 50 mm and length 60 mm located at depth of $h_1/h = 0.25$.

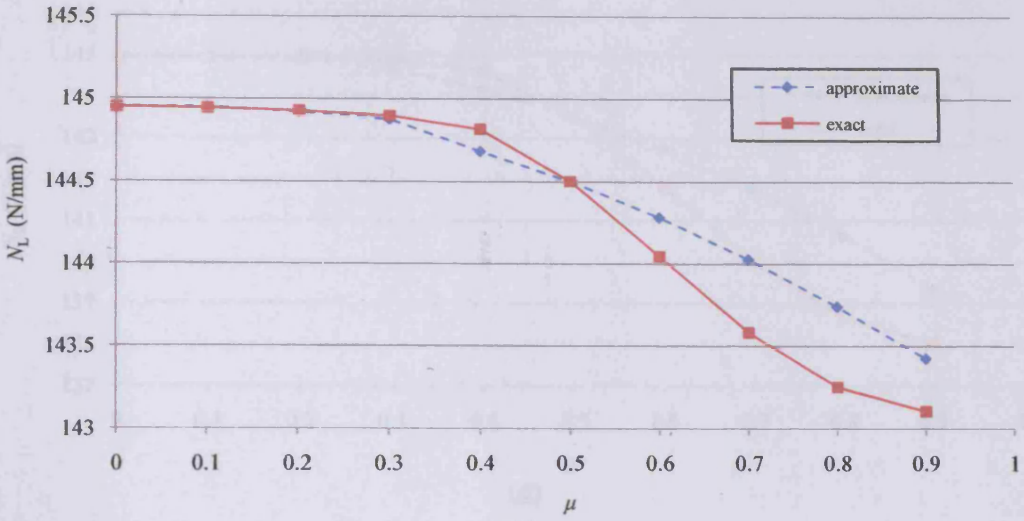
145.5
145
144.5
144
143.5
143
N_L (N/mm)
0
0.1
0.2
0.3
0.4
0.5
0.6
0.7
0.8
0.9
1
μ
approximate
exact

(a)

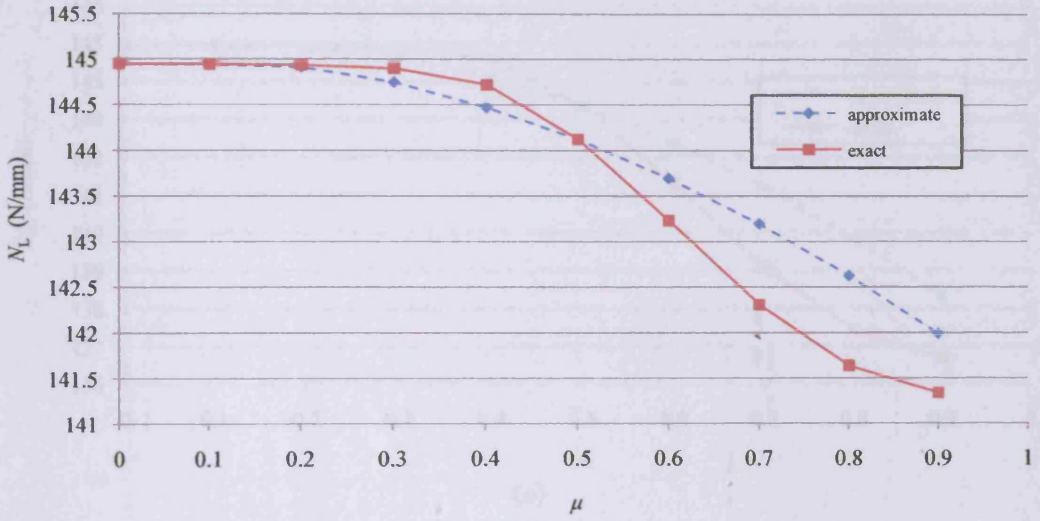
145.5
145
144.5
144
143.5
143
142.5
142
141.5
141
N_L (N/mm)
0
0.1
0.2
0.3
0.4
0.5
0.6
0.7
0.8
0.9
1
μ
approximate
exact

(b)

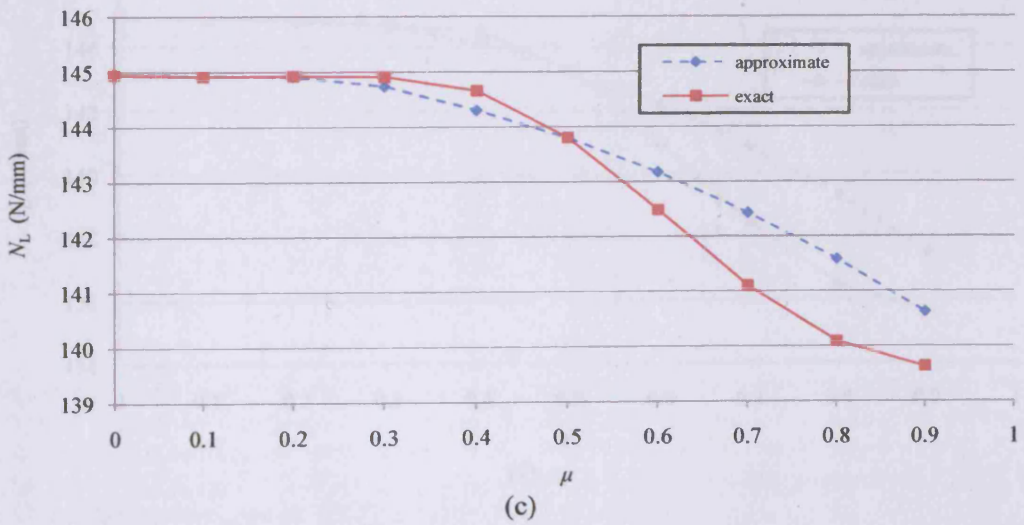
146
145
144
143
142
141
140
139
N_L (N/mm)
0
0.1
0.2
0.3
0.4
0.5
0.6
0.7
0.8
0.9
1
μ
approximate
exact

(c)

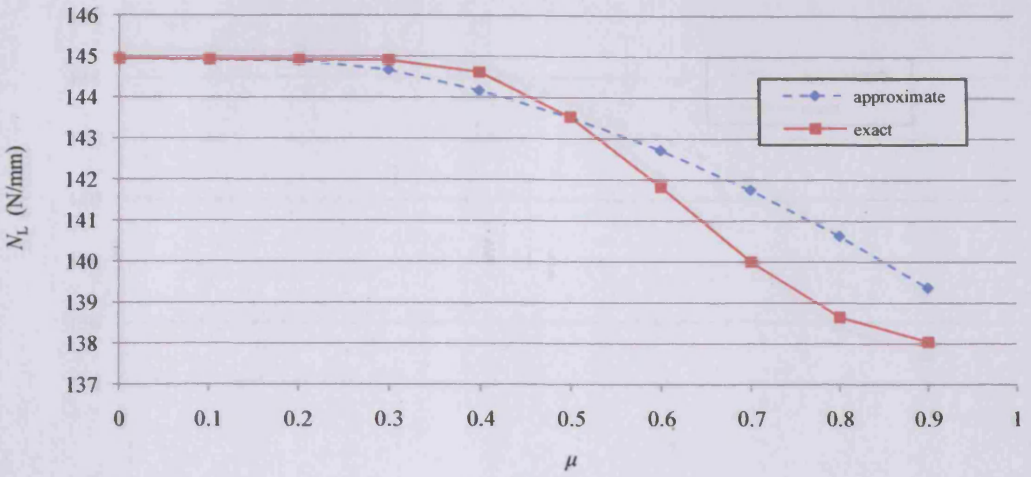
146
145
144
143
142
141
140
139
138
137
N_L (N/mm)
0
0.1
0.2
0.3
0.4
0.5
0.6
0.7
0.8
0.9
1
μ
approximate
exact

(d)

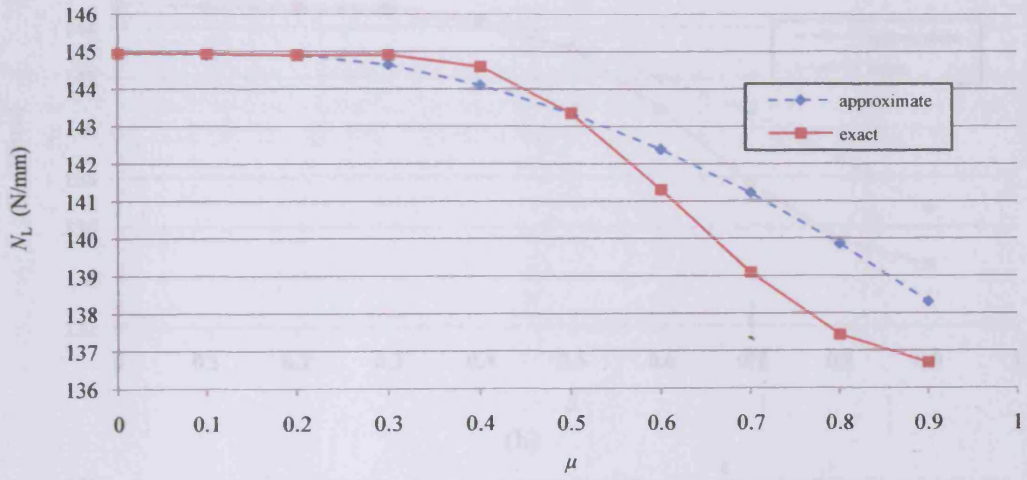
146
145
144
143
142
141
140
139
138
137
136
N_L (N/mm)
0
0.1
0.2
0.3
0.4
0.5
0.6
0.7
0.8
0.9
1
μ
approximate
exact

(e)

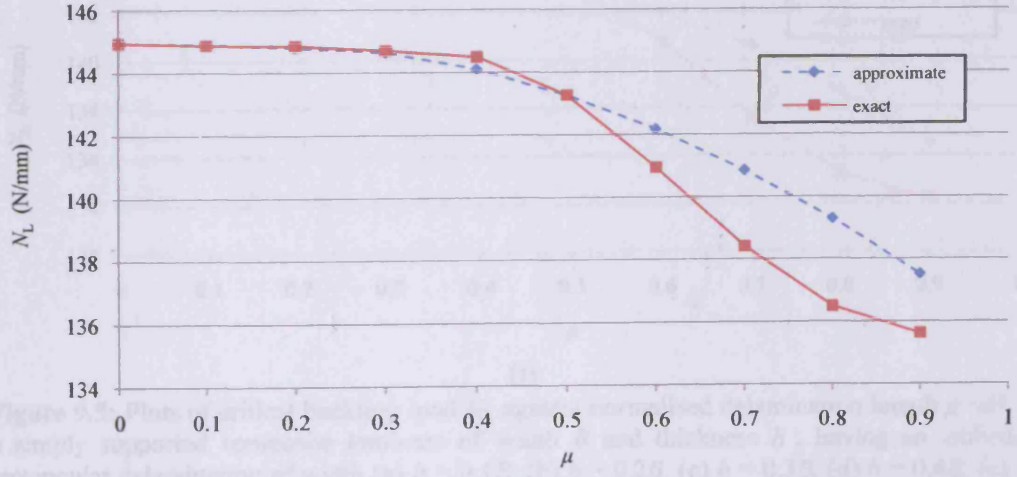
146
144
142
140
138
136
134
N_L (N/mm)
0
0.1
0.2
0.3
0.4
0.5
0.6
0.7
0.8
0.9
1
μ
approximate
exact

(f)

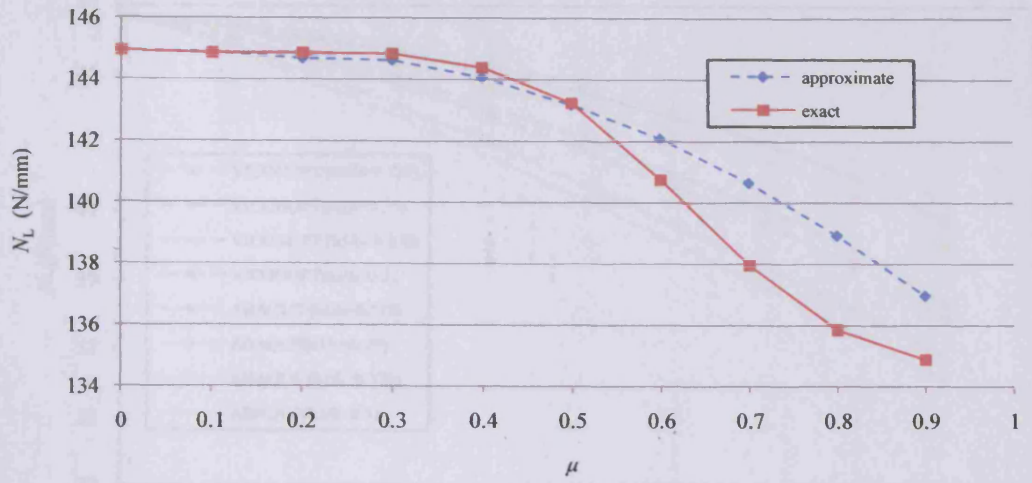

(g)

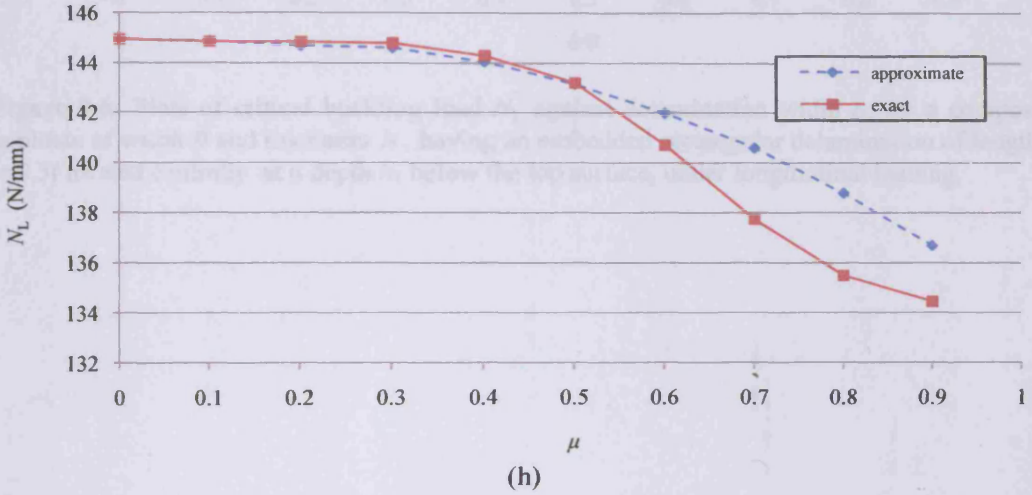

(h)

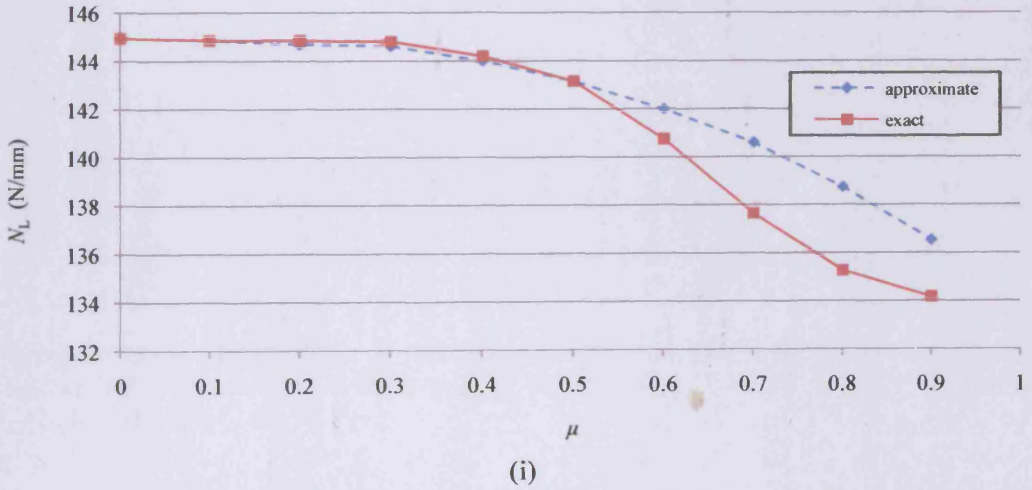

(i)

Figure 9.5: Plots of critical buckling load N_L against normalised delamination length $\mu=d/l$, for a simply supported composite laminate of width B and thickness h, having an embedded rectangular delamination of width (a) $b = 0.1B$, (b) $b = 0.2B$, (c) $b = 0.3B$, (d) $b = 0.4B$, (e) $b = 0.5B$, (f) $b = 0.6B$, (g) $b = 0.7B$, (h) $b = 0.8B$ and (i) $b = 0.9B$ located centrally at a depth $h_1 = 0.375h$ below the top surface, under longitudinal loading.

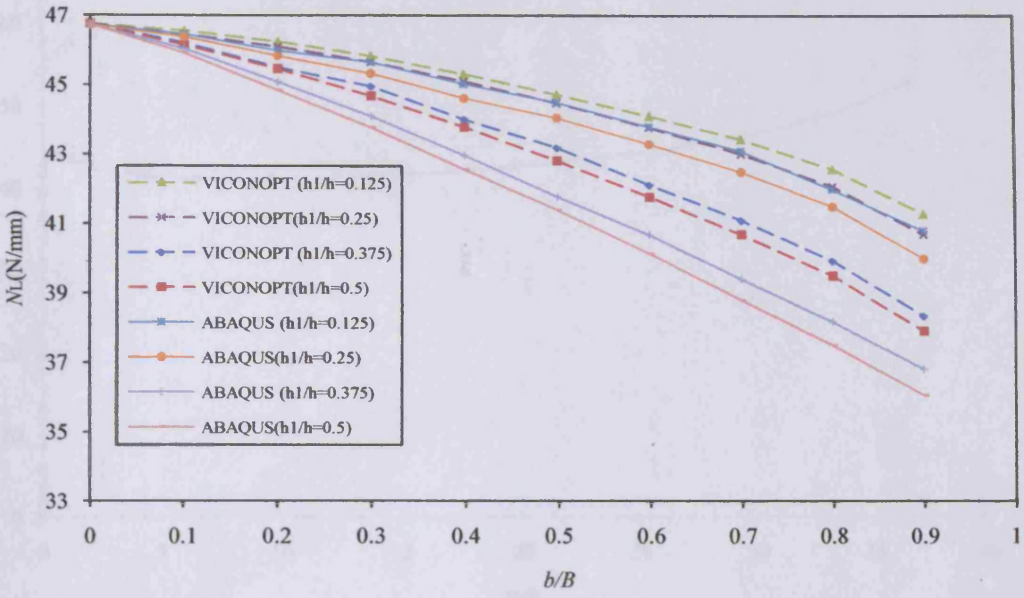

Figure 9.6: Plots of critical buckling load N_L against delamination width b, for a composite laminate of width B and thickness h , having an embedded rectangular delamination of length $d = 0.3l$ located centrally at a depth h_1 below the top surface, under longitudinal loading.

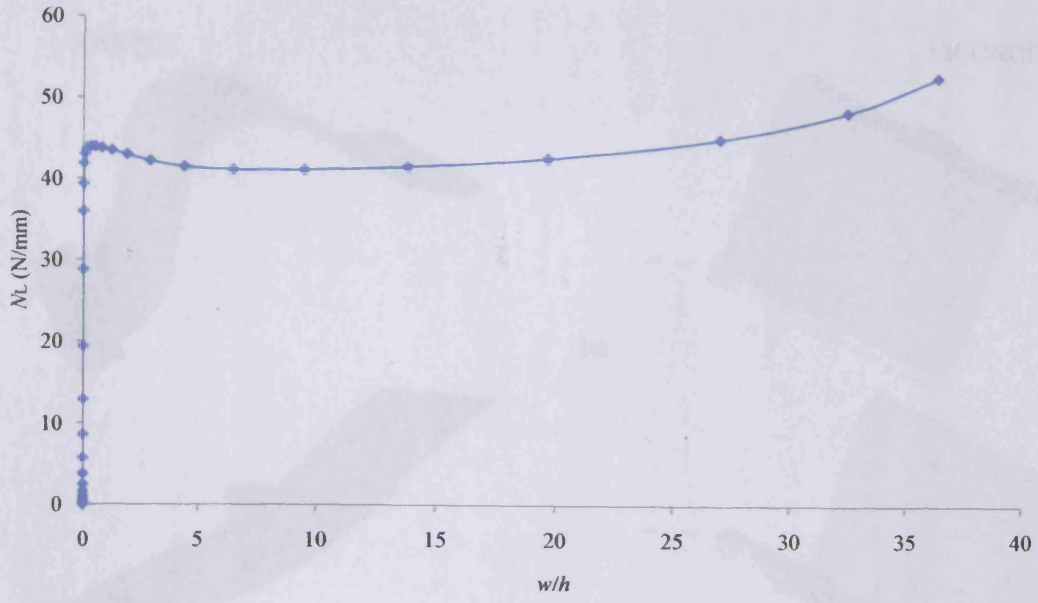

(a)

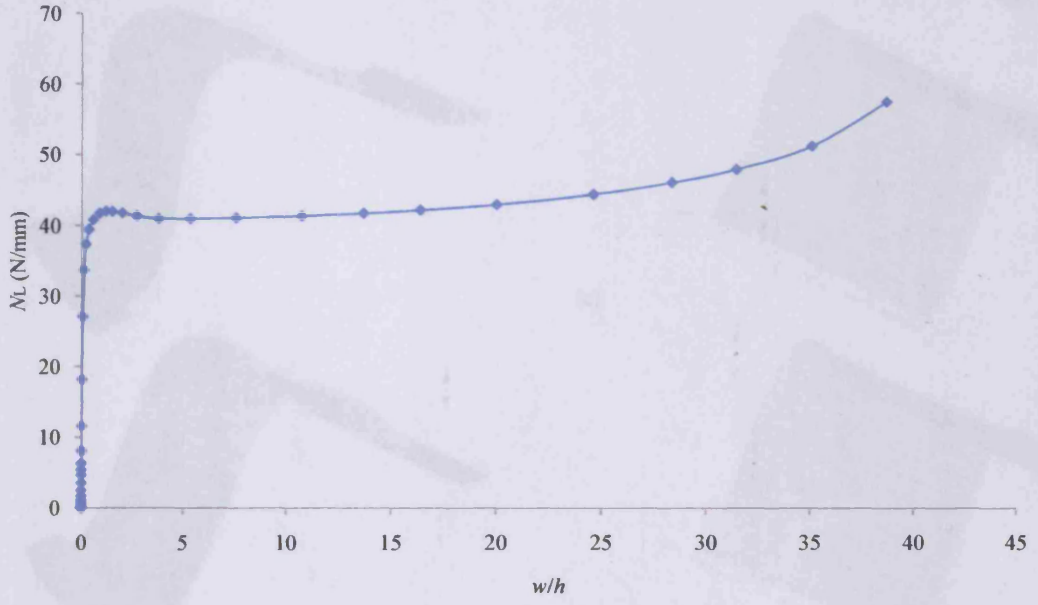

(b)

Figure 9.7: Plots of central out of plane displacement w against longitudinal load N_L, for a clamped-free plate with a central rectangular delamination of length $d=0.3l$. (a) $b=0.6B$, $h_1=0.25h$. (b) $b=0.9B$, $h_1=0.125h$.

Figure 9.8: Plots of mode shapes of delaminated composite plate of width B and thickness h, having a centrally located embedded rectangular delamination of length d=0.3l, under longitudinal loading. (a) b=0.5B, h_1=0.125h. (b) b=0.6B, h_1=0.25h. (c) b=0.4B, h_1=0.375h. (d) b=0.3B, h_1=0.5h.

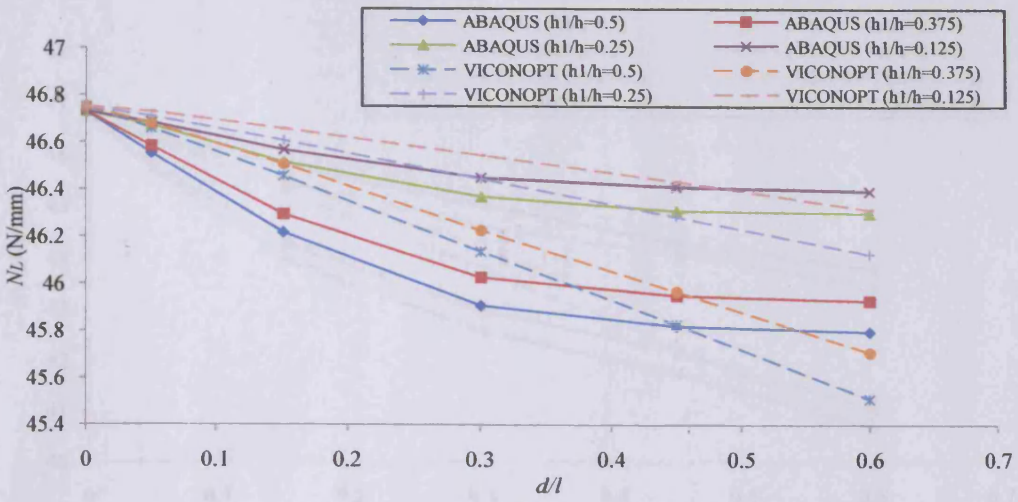
ABAQUS (h1/h=0.5)
ABAQUS (h1/h=0.375)
ABAQUS (h1/h=0.25)
ABAQUS (h1/h=0.125)
VICONOPT (h1/h=0.5)
VICONOPT (h1/h=0.375)
VICONOPT (h1/h=0.25)
VICONOPT (h1/h=0.125)
NL (N/mm)
47
46.8
46.6
46.4
46.2
46
45.8
45.6
45.4
0
0.1
0.2
0.3
0.4
0.5
0.6
0.7
d/l

(a)

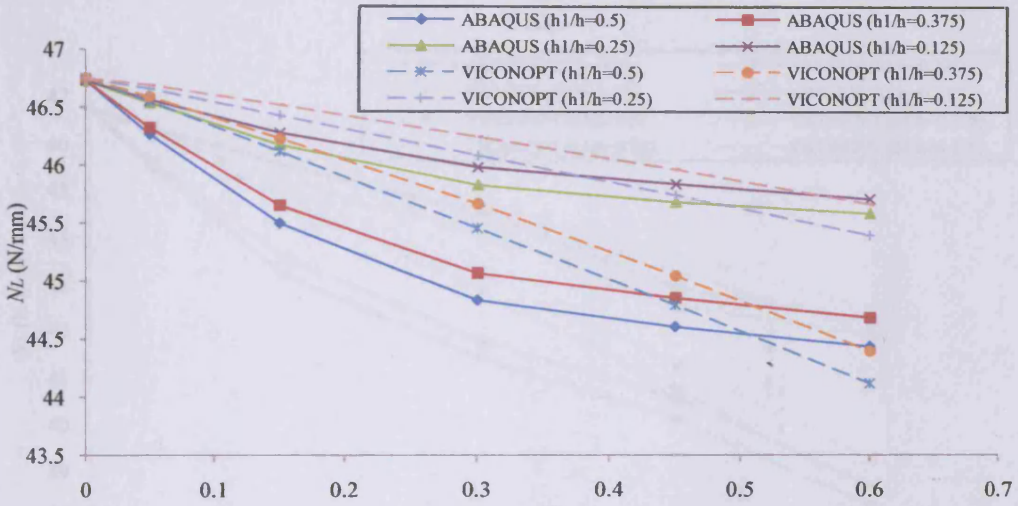
ABAQUS (h1/h=0.5)
ABAQUS (h1/h=0.375)
ABAQUS (h1/h=0.25)
ABAQUS (h1/h=0.125)
VICONOPT (h1/h=0.5)
VICONOPT (h1/h=0.375)
VICONOPT (h1/h=0.25)
VICONOPT (h1/h=0.125)
NL (N/mm)
47
46.5
46
45.5
45
44.5
44
43.5
0
0.1
0.2
0.3
0.4
0.5
0.6
0.7
d/l

(b)

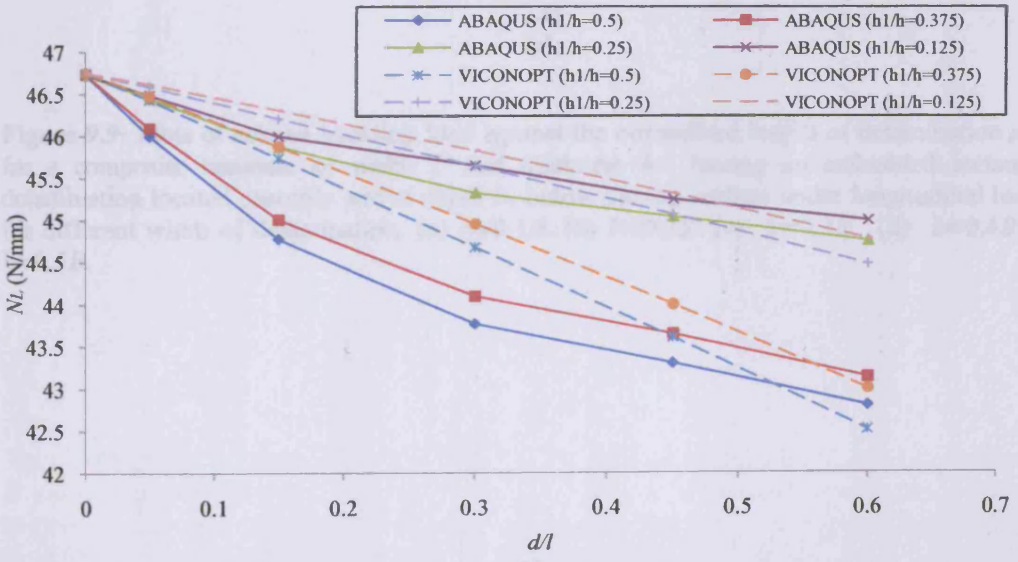
ABAQUS (h1/h=0.5)
ABAQUS (h1/h=0.375)
ABAQUS (h1/h=0.25)
ABAQUS (h1/h=0.125)
VICONOPT (h1/h=0.5)
VICONOPT (h1/h=0.375)
VICONOPT (h1/h=0.25)
VICONOPT (h1/h=0.125)
NL (N/mm)
47
46.5
46
45.5
45
44.5
44
43.5
43
42.5
42
0
0.1
0.2
0.3
0.4
0.5
0.6
0.7
d/l

(c)

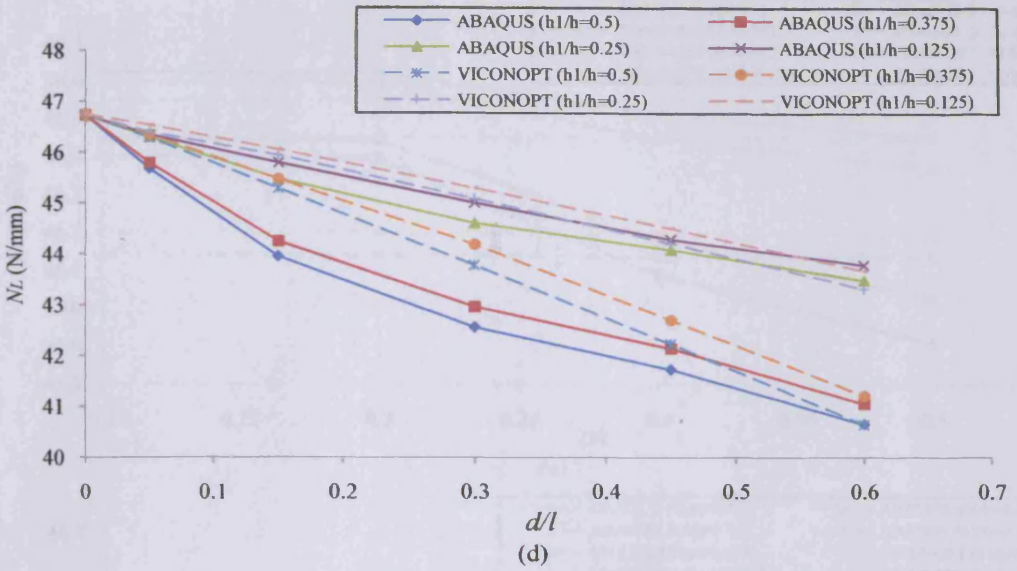

(d)

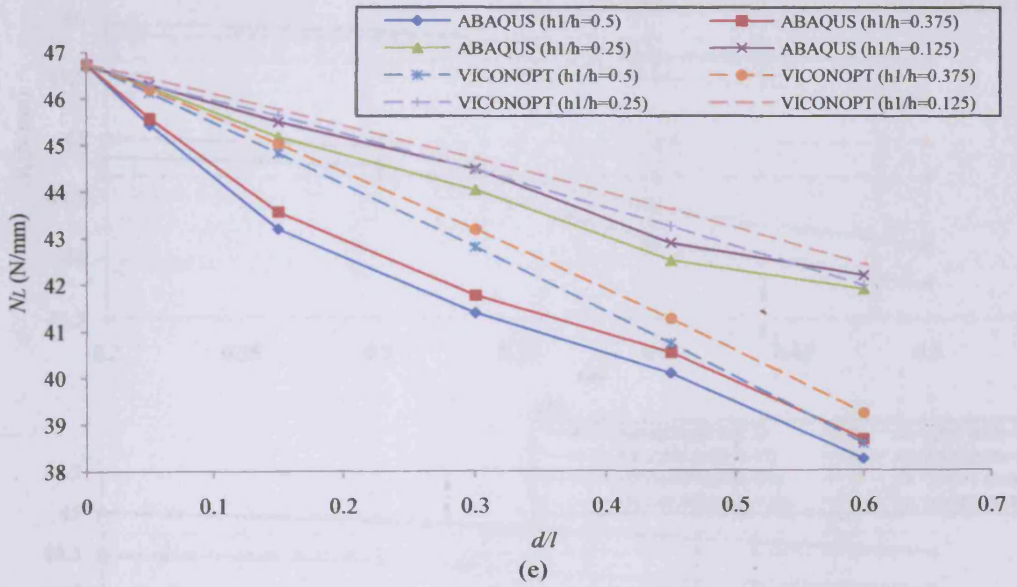

(e)

Figure 9.9: Plots of critical buckling load against the normalised length of delamination $\mu=d/l$, for a composite laminate of width B and thickness h, having an embedded rectangular delamination located centrally and at depth h_1 below the top surface under longitudinal loading for different width of delamination. (a) $b=0.1B$. (b) $b=0.2B$. (c) $b=0.3B$. (d) $b=0.4B$. (e) $b=0.5B$.

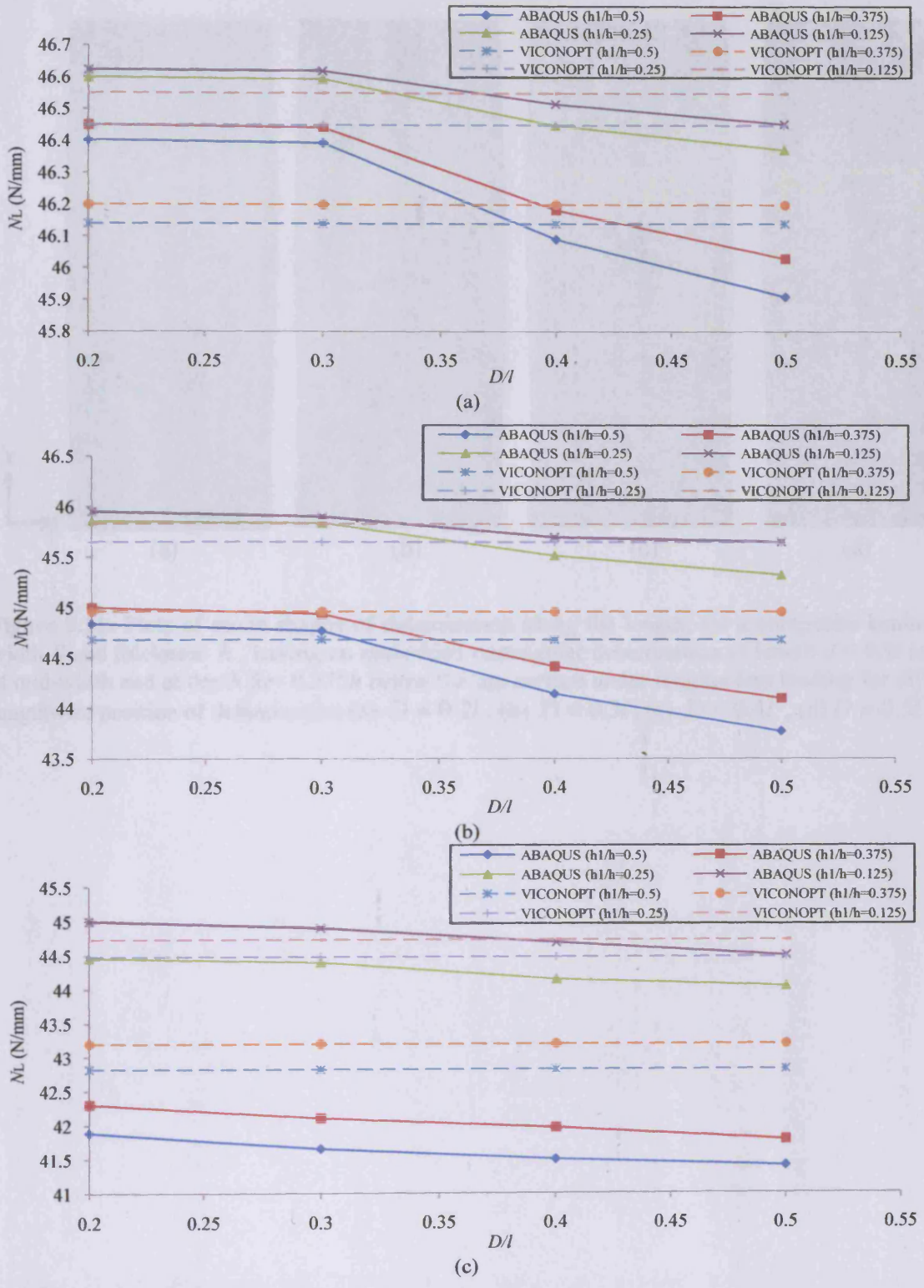

Figure 9.10: Plots of critical buckling load against position of delamination along the length, for a composite laminate of width B and thickness h, having an embedded rectangular delamination of length d=0.3l located at mid-width and at depth h_1 below the top surface under longitudinal loading for different width of delamination (a) b=0.1B. (b) b=0.3B. (c) b=0.5B.

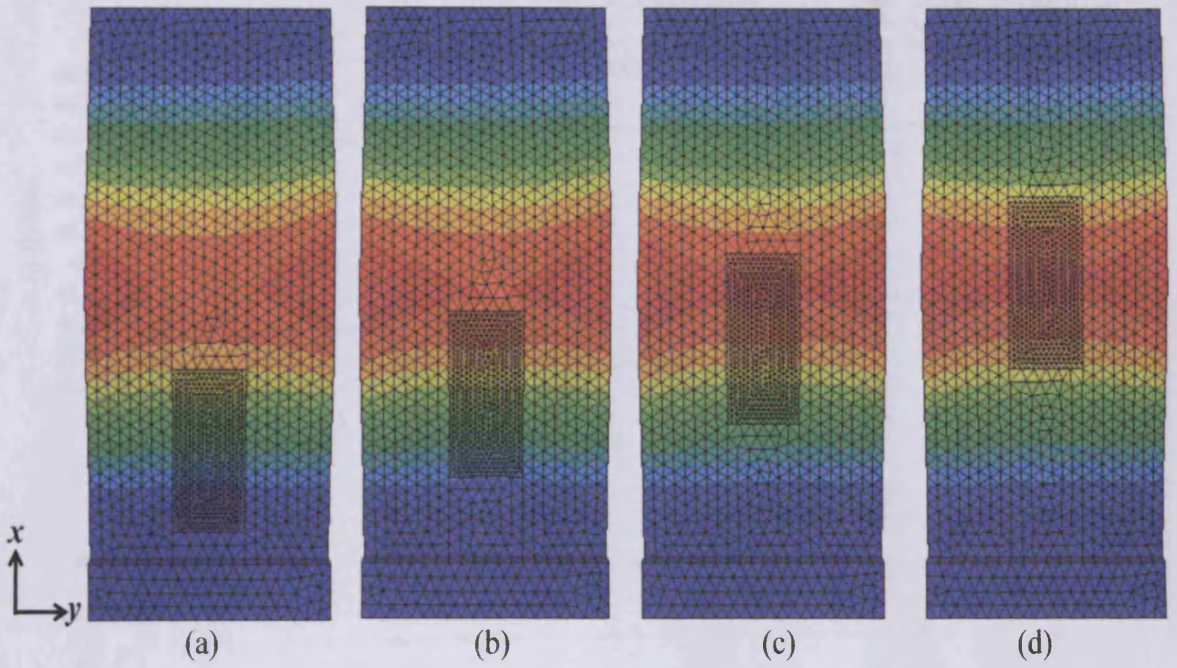

Figure 9.11: Plots of mode shapes of delamination along the length, for a composite laminate of width B and thickness h, having an embedded rectangular delamination of length $d = 0.3l$ located at mid-width and at depth $h_1 = 0.375h$ below the top surface under longitudinal loading for different lengthwise position of delamination (a) $D = 0.2l$, (b) $D = 0.3l$, (c) $D = 0.4l$, (d) $D = 0.5l$.

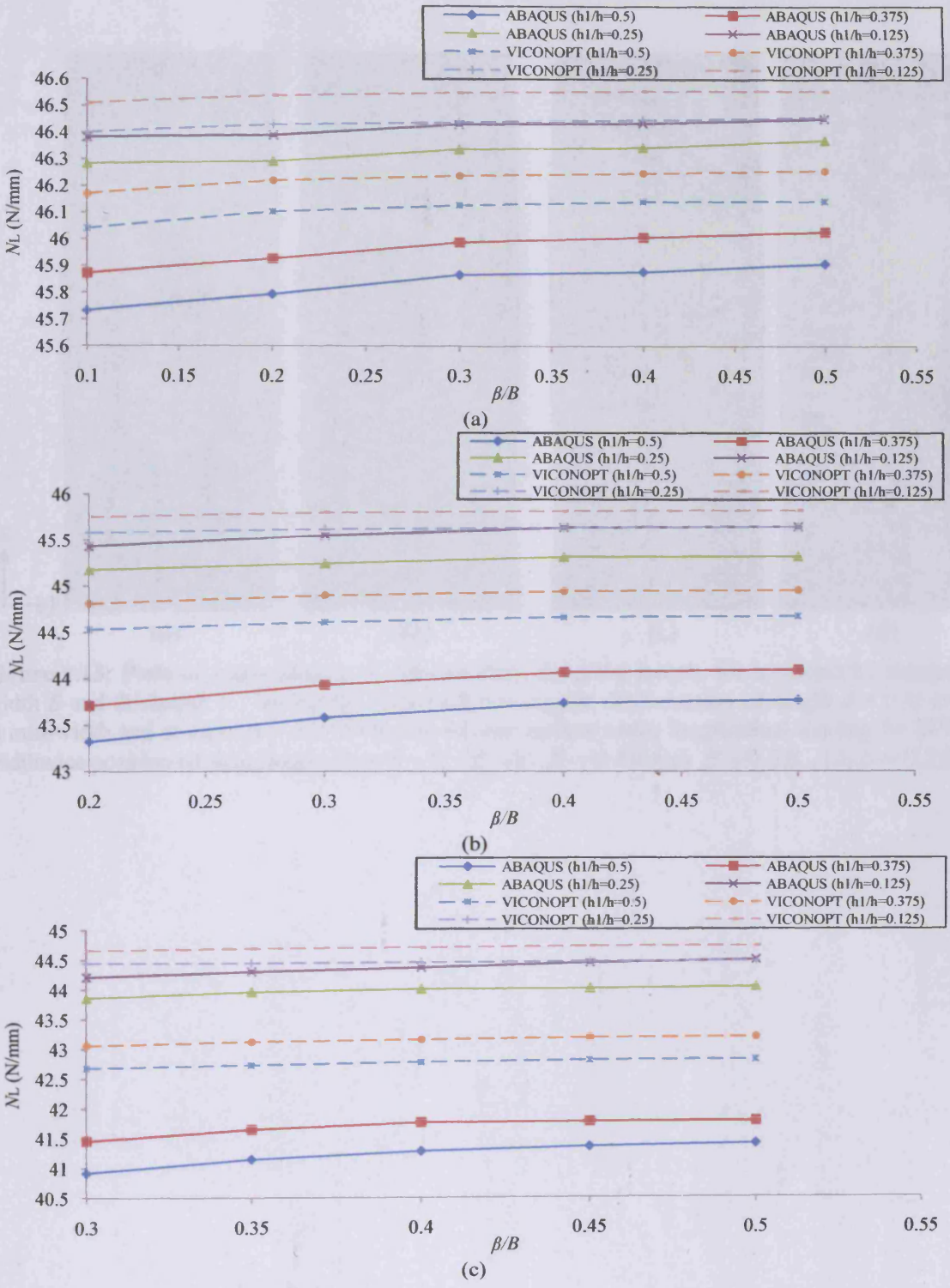

Figure 9.12: Plots of critical buckling load against position of delamination across the width, for a composite laminate of width B and thickness h , having an embedded rectangular delamination of length $d = 0.3l$ located at mid-length and at depth h_1 below the top surface under longitudinal loading for different width of delamination (a) b=0.1B. (b) b=0.3B. (c) b=0.5B.

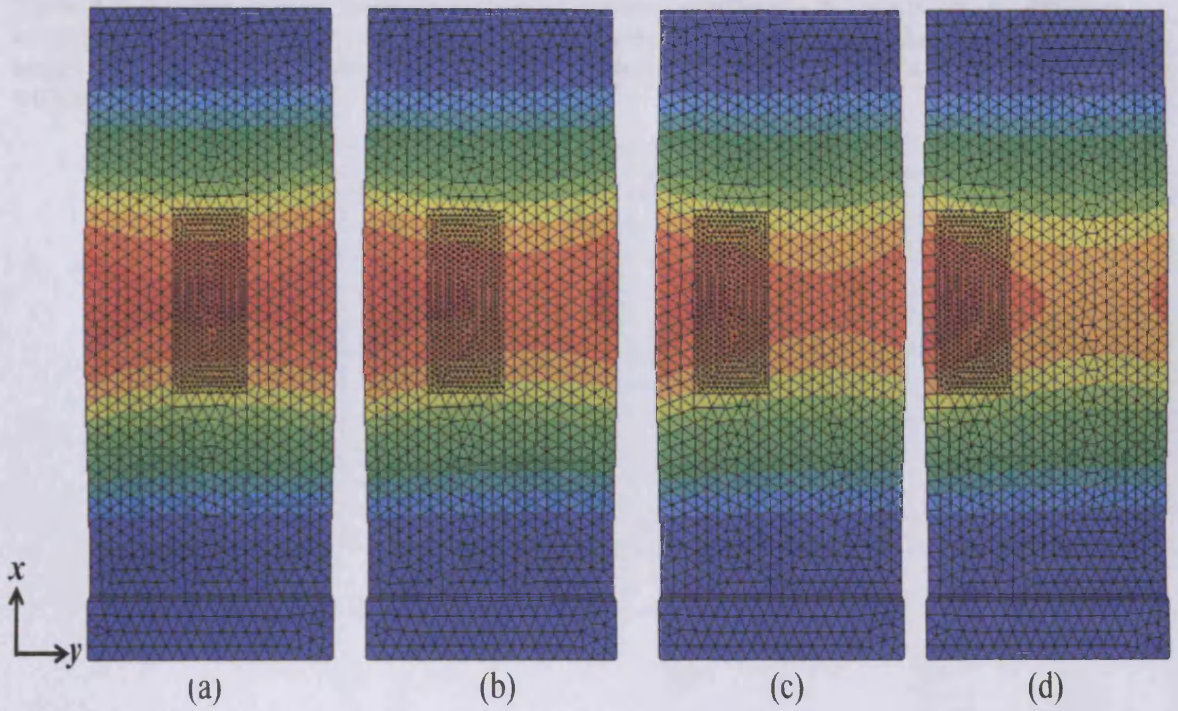

Figure 9.13: Plots of mode shapes of delamination along the length, for a composite laminate of width B and thickness h, having an embedded rectangular delamination of length $d = 0.3l$ located at mid-width and at depth $h_1 = 0.375h$ below the top surface under longitudinal loading for different widthwise position of delamination (a) $\beta = 0.5B$, (b) $\beta = 0.4B$, (c) $\beta = 0.3B$, (d) $\beta = 0.2B$.

Table 9.1: Solution time (in seconds) for various delamination widths b, for a composite laminate of width B and thickness h, having a centrally located embedded rectangular delamination of length $d = 0.3l$ at depth h_1 below the top surface, under longitudinal loading. (A): ABAQUS. (V): VICONOPT.

b/B	$h_1/h = 0.125$		$h_1/h = 0.25$		$h_1/h = 0.375$		$h_1/h = 0.5$	
	(A)	(V)	(A)	(V)	(A)	(V)	(A)	(V)
0	3.7	0.27	3.7	0.27	3.7	0.27	3.7	0.27
0.1	3.8	1.43	3.6	1.43	3.8	1.43	3.8	1.60
0.2	7.9	1.76	7.9	1.87	3.6	1.79	3.5	1.84
0.3	148.2	1.79	4.5	1.79	3.6	1.73	3.7	1.81
0.4	202.4	1.81	21.0	1.67	4.1	1.64	3.9	1.81
0.5	147.1	1.50	141.6	1.68	4.1	1.75	3.9	1.68
0.6	142.1	1.75	161.5	1.75	4.2	1.75	4.2	1.45
0.7	155.7	1.68	172.7	1.70	4.3	1.76	4.2	1.75
0.8	162.6	2.43	248.7	2.42	4.7	2.31	4.3	2.26
0.9	179.7	1.96	382.6	1.96	4.6	1.95	4.5	2.17

Table 9.2: Solution time (in seconds) for various delamination widths b, for a composite laminate of width B and thickness h, having an embedded rectangular delamination of length $d = 0.3l$ at depth h_1 below the top surface, under longitudinal loading. (A)=ABAQUS. (V)=VICONOPT.

D/l	$b = 0.1B$		$b = 0.3B$		$b = 0.5B$	
	(A)	(V)	(A)	(V)	(A)	(V)
0.2	14.0	5.89	150.0	7.18	158.9	6.61
0.3	15.0	5.89	149.1	7.18	163.8	6.61
0.4	14.5	5.89	137.3	7.18	151.4	6.61
0.5	15.0	5.89	160.0	7.18	296.7	6.61

CHAPTER 10

OVERALL CONCLUSIONS AND FUTURE WORK

10.1 Summary of conclusions

In this thesis the goal was to study local and global buckling behaviour of composite plates containing delamination using the efficient exact strip software VICONOPT. Different methods were employed to model delamination including:

1- Offset method (Chapter 3).

2- Multi-structure approach using common points (Chapters 4 and 5).

3- Negative stiffness approach (Chapter 6).

4- Sub-structuring approach (Chapter 7).

5- Smearing method (Chapters 8 and 9).

The offset method proved to be a reliable approach for certain shape of delamination (i.e. strip delamination only) but was incapable of dealing with reserve strength of structure after local buckling.

The multi-structure method using common points could give potentially accurate results at the expense of considerably high time of analysis. This approach was capable of dealing with very general cases, i.e. various boundary conditions and shapes of delaminations.

Using a negative stiffness approach demonstrated the possibility of missing of some eigenvalues. This method also required common point usage which does not work in favour can greatly increase time of analysis.

The sub-structuring approach did not prove to be time efficient compared to the multi-structure approach so was ruled out as a means to model delamination.

In Chapter 8 several possible smearing methods were introduced. Results obtained from each method were then compared with each other and those of FEA. The smearing method which gave better and closer results to FEA (i.e. smearing based on the length of delaminated region) was adopted as the proposed method.

The proposed smearing method (Chapters 8 and 9) was very time efficient yet capable of dealing with global buckling behaviour. The accuracy of this method was validated by comparing results with those of FEA. This method is very general and thus could handle delaminations of any shape or size. The mere shortcoming of this method was its failure to take into account the position of delamination along the length of the structure, i.e. it gives the same results irrespective of the position of delamination along the length of structure.

10.2 Future work

Based on research executed in this thesis the following topics are suggested for future study:

1- Further development of smearing method so that it can handle the effects of position of delamination along the length of structure.
2- Development of smearing method to take into account the contact effects in delaminated region.

3- A parametric study on delaminated composite plates with various shapes of delamination, i.e. circular, triangular and elliptical delaminations, and also considering the effects of different boundary conditions and stacking sequences using smearing method.

4- A thorough parametric study on composite plates with multiple delaminations.

5- Investigation of the effect of delamination on the natural frequency of delaminated composite plates and considering different boundary conditions, various delamination shapes and stacking sequences employing smearing method.

Items 3, 4 and 5 mentioned above have a great potential for publication as well.

APPENDIX 1

The following gives the derivation of Eqs (9.3)-(9.5).

1- Case 1 ($m+q=0$);

$$V_1 = \frac{1}{2}\int_0^L \sum_q \mathbf{D}_q \exp(2i\pi qx/l)\mathbf{K}_q\mathbf{D}_q \exp(2i\pi mx/l)dx$$

$$=$$

$$\frac{1}{2}\int_0^L \sum_q \mathbf{D}_q^H\mathbf{K}_q\mathbf{D}_q dx$$

$$=$$

$$[\frac{1}{2}][\sum_q \mathbf{D}_q^H\mathbf{K}_q\mathbf{D}_q x\Big|_0^l$$

$$=$$

$$[\frac{1}{2}][\sum_q \mathbf{D}_q\mathbf{K}_q\mathbf{D}_q x\Big|_0^{l_1} + \sum_q \mathbf{D}_q^H\mathbf{K'}_q\mathbf{D}_q x\Big|_{l_1}^{l_2}$$

$$+$$

$$\sum_q \mathbf{D}_q^H\mathbf{K}_q\mathbf{D}_q x\Big|_{l_2}^{ll_3}]$$

$$=$$

$$[\frac{l}{2}][\sum_q \mathbf{D}_q^H\mathbf{K}_q\mathbf{D}_q \frac{l_1}{l} + \mathbf{D}_q^H\mathbf{K'}_q\mathbf{D}_q(\frac{l_2-l_1}{l}) + \mathbf{D}_q^H\mathbf{K}_q\mathbf{D}_q(\frac{l-l_2}{l})]$$

$$=$$

$$[\frac{l}{2}][\sum_q \mathbf{D}_q^H\mathbf{K}_q\mathbf{D}_q \frac{l_1}{l} + \mathbf{D}_q^H\mathbf{K'}_q\mathbf{D}_q(\frac{l_2-l_1}{l}) + \mathbf{D}_q^H\mathbf{K}_q\mathbf{D}_q(\frac{l-l_2}{l})]$$

Considering $\mu = \frac{l_2 - l_1}{l} = \frac{d}{l}$ then

$$V_1 = [\frac{l}{2}][\sum_q \mathbf{D}_q^H \{\mathbf{K}_q (1-\mu) + \mathbf{K'}_q (\mu)\}\mathbf{D}_q] \tag{9.3}$$

2- Case 2 ($m - q = 0$);

$$V_2 = [\frac{l}{2}][\sum_q \frac{1}{4i\pi q}\mathbf{D}_q^H \mathbf{K}_q \mathbf{D}_q \{\exp(4i\pi q l_1 / l) - 1\}$$

$$+$$

$$\sum_q \frac{1}{4i\pi q}\mathbf{D}_q^H \mathbf{K'}_q \mathbf{D}_q \{\exp(4i\pi q l_2 / l) - \exp(4i\pi q l_1 / l)\}$$

$$+$$

$$\sum_q \frac{1}{4i\pi q}\mathbf{D}_q^H \mathbf{K}_q \mathbf{D}_q \{\exp(4i\pi q l / l) - \exp(4i\pi q l_2 / l)\}]$$

$$=$$

$$[\frac{l}{2}][\sum_q \frac{1}{4i\pi q}\mathbf{D}_q^H (\mathbf{K}_q - \mathbf{K'}_q)\{\exp(4i\pi q l_1 / l) - \exp(4i\pi q l_2 / l)\}\mathbf{D}_q]$$

$$=$$

$$[\frac{l}{2}][\sum_q \frac{1}{4i\pi q}\mathbf{D}_q^H (\mathbf{K}_q - \mathbf{K'}_q)\left\{\cos\frac{4\pi q l_1}{l} + i\sin\frac{4\pi q l_1}{l} - \cos\frac{4\pi q l_2}{l} - i\sin\frac{4\pi q l_2}{l}\right\}\mathbf{D}_q]$$

$$=$$

$$[\frac{l}{2}][\sum_q \frac{1}{2i\pi q}\mathbf{D}_q^H (\mathbf{K}_q - \mathbf{K'}_q)\{\sin\frac{2\pi q(l_1 + l_2)}{l}\sin\frac{2\pi q(l_2 - l_1)}{l}$$

$$-$$

$$i\cos\frac{2\pi q(l_1 + l_2)}{l}\sin\frac{2\pi q(l_2 - l_1)}{l}\}\mathbf{D}_q]$$

$$=$$

$$[\frac{l}{2}][\sum_q \frac{1}{2\pi q}\mathbf{D}_q^H (\mathbf{K}_q - \mathbf{K'}_q)\sin 2\pi q\mu\left\{\cos\frac{4\pi q D}{l} - i\sin\frac{4\pi q D}{l}\right\}\mathbf{D}_q] \tag{9.4}$$

3- Case 3 ($m+q\neq 0, m-q\neq 0$);

$$V_3=[\frac{l}{2}][\sum_q\sum_m \frac{1}{2i\pi(m+q)}\mathbf{D}_q^H\mathbf{K}_m\mathbf{D}_m\{\exp(2i\pi(m+q)l_1/l)-1\}$$

$$+$$

$$\sum_q\sum_m \frac{1}{2i\pi(m+q)}\mathbf{D}_q^H\mathbf{K'}_m\mathbf{D}_m\{\exp(2i\pi(m+q)l_2/l)-\exp(2i\pi(m+q)l_1/l)\}$$

$$+$$

$$\sum_q\sum_m \frac{1}{2i\pi(m+q)}\mathbf{D}_q^H\mathbf{K}_m\mathbf{D}_m\{\exp(2i\pi(m+q)l/l)-\exp(2i\pi(m+q)l_2/l)\}]$$

$$=$$

$$[\frac{l}{2}][\sum_q\sum_m \frac{1}{2i\pi(m+q)}\mathbf{D}_q^H(\mathbf{K}_m-\mathbf{K'}_m)\mathbf{D}_m\{\exp(2i\pi(m+q)l_1/l)-\exp(2i\pi(m+q)l_2/l)\}]$$

$$=$$

$$[\frac{l}{2}][\sum_q\sum_m \frac{1}{\pi(m+q)}\mathbf{D}_q^H(\mathbf{K}_m-\mathbf{K'}_m)\sin\pi\pi(m+q)\mu\left\{\cos\frac{2\pi(m+q)D}{l}-i\sin\frac{2\pi(m+q)D}{l}\right\}\mathbf{D}_m] \quad (9.5)$$

APPENDIX 2

The following gives the derivation of Eq (9.10).

$$V = \frac{1}{2}\int_0^{l_1} \mathbf{D}_0{}^T \mathbf{K} \sin^2(n\pi x/l)\mathbf{D}_0 dx$$

$$+$$

$$\frac{1}{2}\int_{l_1}^{l_2} \mathbf{D}_0{}^T \mathbf{K}' \sin^2(n\pi x/l)\mathbf{D}_0 dx$$

$$+$$

$$\frac{1}{2}\int_{l_2}^{l} \mathbf{D}_0{}^T \mathbf{K} \sin^2(n\pi x/l)\mathbf{D}_0 dx$$

$$=$$

$$\frac{1}{4}\int_0^{l_1} \mathbf{D}_0{}^T \mathbf{K}(1-\cos(2n\pi x/l))\mathbf{D}_0 dx$$

$$+$$

$$\frac{1}{4}\int_{l_1}^{l_2} \mathbf{D}_0{}^T \mathbf{K}'(1-\cos(2n\pi x/l))\mathbf{D}_0 dx$$

$$+$$

$$\frac{1}{4}\int_{l_2}^{l} \mathbf{D}_0{}^T \mathbf{K}(1-\cos(2n\pi x/l))\mathbf{D}_0 dx$$

$$=$$

$$\frac{1}{4}[\mathbf{D}_0{}^T \mathbf{K}(x - \frac{l}{2\pi}\sin(2n\pi x/l))\Big|_0^{l_1} \mathbf{D}_0]$$

$$+$$

$$\frac{1}{4}[\mathbf{D}_0{}^T \mathbf{K}'(x - \frac{l}{2\pi}\sin(2n\pi x/l))\Big|_{l_1}^{l_2} \mathbf{D}_0]$$

$$+$$

$$\frac{1}{4}[\mathbf{D}_0{}^T \mathbf{K}(x - \frac{l}{2\pi}\sin(2n\pi x/l))\Big|_{l_2}^{l} \mathbf{D}_0]$$

$$=$$

$$\frac{1}{4}[\mathbf{D}_0{}^T \mathbf{K}(l_1 - \frac{l}{2n\pi}\sin(2n\pi l_1/l))\mathbf{D}_0]$$

$$+$$

$$\frac{1}{4}[\mathbf{D}_0{}^T \mathbf{K}'(l_2 - \frac{l}{2n\pi}\sin(2n\pi l_2/l) - l_1 + \frac{l}{2n\pi}\sin(2n\pi l_1/l))\mathbf{D}_0]$$

$$+$$

$$\frac{1}{4}[\mathbf{D}_0{}^T\mathbf{K}(l-l_2+\frac{l}{2n\pi}\sin(2n\pi l_2/l))\mathbf{D}_0]$$

$$=$$

$$\frac{1}{4}\{\mathbf{D}_0{}^T\mathbf{K}(l_1)\mathbf{D}_0+\mathbf{D}_0{}^T\mathbf{K}'(l_2-l_1)\mathbf{D}_0+\mathbf{D}_0{}^T\mathbf{K}(l-l_2)\mathbf{D}_0\}$$

$$+$$

$$\frac{1}{4}\{\mathbf{D}_0{}^T(\mathbf{K}-\mathbf{K}')(-\frac{l}{2n\pi}\sin(2n\pi l_1/l))+\frac{l}{2n\pi}\sin(2n\pi l_2/l)\mathbf{D}_0\}$$

$$=$$

$$\frac{l}{4}\mathbf{D}_0{}^T\{\mathbf{K}(1-\mu)+\mathbf{K}'(\mu)\}\mathbf{D}_0-\frac{l}{8n\pi}\{\mathbf{D}_0{}^T(\mathbf{K}-\mathbf{K}')\mathbf{D}_0(\sin(2n\pi l_1/l)-\sin(2n\pi l_2/l)\}$$

$$=$$

$$\frac{l}{4}\mathbf{D}_0{}^T\{\mathbf{K}(1-\mu)+\mathbf{K}'(\mu)\}\mathbf{D}_0+\frac{l}{4n\pi}\{\mathbf{D}_0{}^T(\mathbf{K}-\mathbf{K}')\mathbf{D}_0\cos\frac{n\pi(l_1+l_2)}{l}\sin\frac{n\pi(l_2-l_1)}{l}\}$$

$$=$$

$$\frac{l}{4}\mathbf{D}_0{}^T\{\mathbf{K}(1-\mu)+\mathbf{K}'(\mu)\}\mathbf{D}_0+\frac{l}{4n\pi}\{\mathbf{D}_0{}^T(\mathbf{K}-\mathbf{K}')\mathbf{D}_0\cos\frac{2n\pi D}{l}\sin\mu n\pi\} \quad (9.10)$$